

# **Bridging Mesoscale Phenomena and Macroscopic Properties in Block Copolymers Containing Ionic Interactions and Hydrogen Bonding**

Mingtao Chen

Dissertation submitted to the faculty of the Virginia Polytechnic Institute and State  
University in partial fulfillment of the requirements for the degree of

Doctor of Philosophy  
In  
Chemistry

Timothy E. Long, chair  
Robert B. Moore  
Shengfeng Cheng  
Michael D. Schulz

May 30<sup>th</sup>, 2018  
Blacksburg, VA

Keywords: poly(ionic liquid)s, electrostatic interactions, block copolymers, hydrogen  
bonding, RAFT polymerization, anionic polymerization

Copyright 2018 Mingtao Chen

# **Bridging Mesoscale Phenomena and Macroscopic Properties in Block Copolymers Containing Ionic Interactions and Hydrogen Bonding**

Mingtao Chen

## **ABSTRACT**

Anionic polymerization and controlled radical polymerization enabled the synthesis of novel block copolymers with non-covalent interactions (electrostatic interaction and/or hydrogen bonding) to examine the relationships between mesoscale phenomenon and macroscopic physical properties. Non-covalent interactions offer extra intra- and inter-molecular interactions to achieve stimuli-responsive materials in various applications, such as artificial muscles, thermoplastic elastomers, and reversible biomacromolecule binding. The relationship between non-covalent interaction promoted mesoscale phenomenon (such as morphology) and consequent macroscopic physical properties is the key to optimize material design and improve end-use performance for emerging applications.

Pendant hydrogen bonding in ABA block copolymers promoted microphase separation and delayed the order-disorder transition, resulting in tunable morphologies (through composition changes) and extended rubbery plateaus. Reversible addition-fragmentation chain transfer (RAFT) polymerization afforded a facile synthesis of ABA triblock copolymers with hydrogen bonding (urea sites) and electrostatic interactions (pyridinium groups). Pyridine groups facilitated hydrogen bonding through a preorganization effect, leading to highly ordered, long-range lamellar morphology and a significant increase of flow temperature ( $T_f$ ) 80 °C above the hard block  $T_g$ . After

quaternization of pyridine groups, electrostatic interaction, as a second physical crosslinking mechanism, disrupted ordered lamellar morphology and decreased  $T_f$ . Yet, extra physical crosslinking from electrostatic interactions pertained ordered hydrogen bonding at high temperature and exhibited improved stress-relaxation properties.

Both conventional free radical polymerization and RAFT polymerization generated a library of poly(ionic liquid) (PIL) homopolymers with imidazolium groups as bond charge moieties. A long chain alkyl spacer between imidazolium groups and the polymer backbones ensured a low glass transition temperature ( $T_g$ ), which is beneficial to ion conductivity. Four different counter anions enabled readily tunable  $T_g$ s all below room temperature and showed promising ion conductivities as high as  $2.45 \times 10^{-5}$  S/cm at 30 °C. For the first time, the influence of counter anions on radical polymerization kinetics was observed and investigated thoroughly using *in situ* FTIR, NMR diffusometry, and simulation. Monomer diffusion and aggregation barely contributed to the kinetic differences, and the Marcus theory was applied to explain the polymerization kinetic differences which showed promising simulation results. RAFT polymerization readily prepared AB diblock, ABA triblock and  $(AB)_3$  3-arm diblock copolymers using the ionic liquid (IL) monomers discussed above and deuterated/hydrogenated styrene. We demonstrated the first example of *in situ* morphology studies during an actuation process, and counter anions with varied electrostatic interactions showed different mesoscale mechanisms, which accounted for macroscopic actuation. The long chain alkyl spacer between imidazolium groups and polymer backbones decoupled ion dynamics and structural relaxation. For the first time, composition changes of block copolymers achieved tunable viscoelastic properties without altering ion conductivity, which

provided an ideal example for actuation materials, solid electrolytes, and ion exchange membranes.

# **Bridging Mesoscale Phenomena and Macroscopic Properties in Block Copolymers Containing Ionic Interactions and Hydrogen Bonding**

Mingtao Chen

## **GENERAL AUDIENCE ABSTRACT**

My research focuses on the synthesis of novel soft materials with a special interest in responsive polymers. The incorporation of responsive chemistry, such as hydrogen bonding and ionic interactions, enables soft materials with complex responsive behavior were achieved. Polymers with ion pairs promise great potential as solid-state electrolytes (which transfer ions to generate current) to eliminate potential fire hazard in batteries, which has been an arising concern for modern cellphone and electric car industry. The introduction of strong dipoles into polymers allows the fabrication of actuators, which convert electric signals to physical movement. Under applied voltage, polymers bend within seconds while holding physical loads. Actuator studies in polymers paves the way towards artificial muscles as well as soft robotics. Temperature responsive hydrogen bonding in polymers offers drastically different viscoelastic properties at different temperature and serves as the key mechanism in holt-melt adhesives, controlled drug release, and high performance materials.

## Acknowledgements

First and foremost, I would like to thank and acknowledge my Ph.D. advisor, Dr. Timothy E. Long, for his kind and patient support and guidance throughout my graduate career in Virginia Tech. As an excellent scientist, he constantly contributes to all of my research projects as well as teaches me other related scientific skills, which I think is crucial for the rest of my career. These skills included critical thinking, design and evaluation of research plans, and cautious examination of experimental data. Especially, as a student from a non-English speaking country, I deeply appreciate his contribution and encouragement of my endeavor to improve my oral presentation skills and scientific writing. I also thank my committee members for their discussion and input: Dr. Robert B. Moore, Dr. Shengfeng Cheng, Dr. Michael D. Schulz, and Dr. S. Richard Turner (former committee member). They challenged me to be the best that I could possibly be.

I acknowledge funding and collaboration from other research groups as well as federal and industry partners. I thank Max Heres and Dr. Joshua Sangoro in University of Tennessee for the collaboration on the ion conductivity study. I also acknowledge the funding from Carlisle Construction Materials and Oak Ridge National Laboratory (ORNL). Especially, I thank Dr. Bradley S. Lokitz in ORNL for introducing me to the GO program and funding me for two years of amazing fundamental research. I also thank Dr. Jason W. Dugger for his great contribution and collaboration on the GO program.

All my research endeavors would not be realized without the support of the whole Long group. The Long group, to me, is a supportive team always full of excellent discussion and suggestions. I would like to thank Dr. David L. Inglefield and Dr. Alison

R. Schultz as they are my graduate mentors. David trained me on RAFT polymerization and various characterization instruments. He always guided me to become a scientist with broad background knowledge and novel ideas. Alison taught me anionic polymerization and always reminded me to consider the significance of a project besides novelty. I also owe my thanks to Dr. Keren Zhang, Dr. Evan Margareta, Dr. Joseph Dennis, Dr. Maruti Hegde and Phillip Scott for intensive discussion on physical crosslinking, rheology and ion-containing polymers. I thank Christopher Kasprzak for his great help in the lab during my last year. Finally, I thank the rest of Long group: Justin Serrine, Ryan Mondschein, Katerine Heifferon, Xi Chen, Dr. Orlor Bruce, Dr. Jana Herzberger, Dr. Chixia Tian, Tyler While, Clay Arrington, Emily Wilts, Josh Wolfgang, Keven Drummey, and Mark Cashman. They have been the kindest group members and contributed tremendously to my graduate career.

Finally and most importantly, I thank my family members for their constant support and love without which I could not become who I am today. I have been away from home studying ever since high school, spending half of my life so far on the road. My parents, Jin Liu and Jiayi Chen, grant me all their love to support me both financially and mentally. I couldn't be more lucky to be a member of this family, and deeply, I know I owe them more than I can give back for the rest of my life. I have the best sisters, Shan Luo and Yu Chen, as an important part of my life. I cannot wait to see my two nieces for the first time when I go back to China for vacation after graduation. Finally, I want to dedicate this dissertation to my grandma who passed away during my graduate study. I know even at the last moment in her life, she loved me and supported me. Now, I am

ready for the next trip of my life, I am sure I will still be blessed by the support of all my family members and friends, and I will always love them from my heart.

### **Attributions**

Professor Timothy E. Long (Research Advisor)

Professor of Chemistry at Virginia Tech

Director of Macromolecules Innovation Institutes

Professor Robert B. Moore

Professor of Chemistry at Virginia Tech and collaborator on Chapter 6, 7, and 9

Dr. Bradley S. Lokitz

Research and Development staff in ORNL and research advisor on GO program

Dr. Jason W. Dugger

Postdoc in ORNL and collaborator on Chapter 8 and 9

Dr. Wei Li

Postdoc in ORNL and collaborator on Chapter 8 and 9

Dr. Rajeev Kumar

Research staff in ORNL and collaborator on Chapter 8 and 9

Professor Louis A. Madsen

Professor of Chemistry at Virginia Tech and collaborator on Chapter 8

Xiuli Li

Graduate student in Dr. Madsen's group and collaborator on Chapter 8

Dr. David L. Inglefield

Former graduate student in Dr. Long's group and collaborator on Chapter 6

Dr. Keren Zheng

Former graduate student in Dr. Long's group and collaborator on Chapter 6 and 7

Dr. Maruti Hegde

Former postdoc in Dr. Long's group and collaborator on Chapter 2 and 7

Samantha J. Talley

Graduate student in Dr. Moore's group and collaborator on Chapter 6, 7 and 9

Amanda G. Hudson

Former graduate student in Dr. Moore's group and collaborator on Chapter 6

Lindsey J. Anderson

Graduate student in Dr. Moore's group and collaborator on Chapter 7

Max Heres

Graduate student in Dr. Sangoro's group and collaborator on Chapter 9

Prof. Joshua Sangoro

Assistant Professor at Chemical & Biomolecular Engineering Department in University of Tennessee and collaborator on Chapter 9

Mike Scanish

Senior Chemist at Carlisle Construction Materials and collaborator on Chapter 4

# Table of Contents

<b>Chapter 1: Introduction</b> .....	1
1.1 Dissertation overview.....	1
<b>Chapter 2: Probing Nothing: A Review of Free Volume and its Role in Polymer Structure-Property Relationships (literature review)</b> .....	4
2.1 Abstract.....	4
2.2 Introduction.....	4
2.3 Theoretical developments of free volume theory.....	6
2.4 Techniques for evaluating free volume in polymers.....	10
2.4.1 Melt rheology.....	11
2.4.2 Density study and Bondi's group contribution theory.....	11
2.4.3 Fluorescent probe.....	12
2.4.4 Positron Annihilation Lifetime Spectroscopy (PALS).....	13
2.4.5 Other approaches.....	14
2.5 Structure-property relationships affected by free volume.....	15
2.5.1 Application of free volume: general overview.....	15
2.5.2 The variation in free volume with temperature and pressure.....	19
2.5.3 Effect of polymer structure on free volume.....	22
2.5.4 Effect of molecular weight and molecular weight distribution on free volume.....	31
2.5.5 Effect of pendant groups and branching on free volume.....	35
2.5.6 Effect of crosslinking on free volume.....	41
2.5.7 Effect of polymer blends and additives on free volume.....	52

2.6 Conclusions.....	63
2.7 References.....	64
<b>Chapter 3: Advances in Electrolytes Phosphonium-based Ionic Liquids and Poly(Ionic Liquid)s (literature review).....</b>	<b>74</b>
3.1 Abstract.....	74
3.2 Introduction.....	74
3.3 Phosphonium-based ionic liquids.....	78
3.4 Phosphonium-based poly(ionic liquid)s.....	88
3.5 Future perspectives.....	97
3.6 References.....	98
<b>Chapter 4: Room Temperature Michael Addition Reactions for Structural Adhesives.....</b>	<b>105</b>
4.1 Abstract.....	105
4.2 Introduction.....	105
4.3 Experimental.....	108
4.3.1 Materials.....	108
4.3.2 Synthesis of hydrogenated polybutadiene diacrylate (hPBDA).....	108
4.3.3 Synthesis of hydrogenated polybutadiene bisacetoacetate (hPBbisAcAc).....	109
4.3.4 Preparation of adhesive samples.....	109
4.3.5 Sample preparation for peel tests.....	110
4.3.6 Analytic methods.....	111
4.4 Results and Discussion.....	111

4.5 Conclusion.....	119
4.6 Acknowledgment.....	120
4.7 References.....	120
4.8 Supporting Information.....	121
<b>Chapter 5: Polyisoprene Microstructure Control through Anionic Polymerization: Synthesis of 4-vinylbenzyl Piperidine-Containing ABC Triblock Copolymers.....</b>	<b>122</b>
5.1 Abstract.....	122
5.2 Introduction.....	123
5.3 Experimental.....	125
5.3.1 Materials.....	125
5.3.2 Instrumentation.....	126
5.3.3 Monitoring of poly(4VBP-I-S) anionic polymerization through <i>in situ</i> FTIR.....	126
5.3.4 Anionic polymerization of 4VBP containing block copolymers.....	127
5.3.5 Film casting.....	128
5.4 Results and discussion.....	128
5.4.1 Anionic polymerization of 4VBP-containing block copolymers.....	128
5.4.2 Polyisoprene microstructure study.....	131
5.4.3 Thermal and thermomechanical analysis.....	134
5.5 Conclusions.....	138
5.6 References.....	138
5.7 Supporting information.....	142

**Chapter 6: Synthesis of Urea-Containing ABA Triblock Copolymers: Influence of Pendant Hydrogen Bonding on Morphology and Thermomechanical Properties..145**

6.1 Abstract.....	145
6.2 Introduction.....	146
6.3 Experimental.....	149
6.3.1 Materials.....	149
6.3.2 Analytical methods.....	150
6.3.3 Synthesis of urea methacrylate monomers.....	151
6.3.4 Free radical polymerization for poly(HUrMA-co-PhUrMA).....	152
6.3.5 Difunctional CTA synthesis.....	153
6.3.6 Kinetic analysis of poly(DEGMEMA) macroCTA synthesis.....	154
6.3.7 Synthesis of polyDEGMEMA macroCTA using RAFT polymerization.....	154
6.3.8 Synthesis of poly(UrMA-b-DEGMEMA-b-UrMA) using RAFT polymerization.....	155
6.3.9 Film casting.....	156
6.4 Results and Discussion.....	156
6.5 Conclusions.....	169
6.6 Acknowledgements.....	170
6.7 References.....	170

**Chapter 7: Block Copolymers Containing Pyridinium and Urea: A Unique Example of Charged Hydrogen Bonding Materials.....174**

7.1 Abstract.....	174
-------------------	-----

7.2 Introduction.....	175
7.3 Results and Discussion.....	177
7.4 Conclusions.....	187
7.5 Experimental.....	188
7.5.1 Materials.....	188
7.5.2 Instruments.....	188
7.5.3 Synthesis of PyUrMA monomer.....	190
7.5.4 Synthesis of poly(DEGMEEMA) macroCTA.....	191
7.5.5 Synthesis of PyUr triblock copolymers.....	191
7.5.6 Synthesis of PyUrBr triblock copolymers.....	191
7.5.7 Film casting.....	192
7.6 References.....	192
7.7 Supporting information.....	195
<b>Chapter 8: Polymerized Ionic Liquid: Effect of Counter Ions on Ion Conduction and Polymerization Kinetics.....</b>	<b>198</b>
8.1 Abstract.....	198
8.2 Introduction.....	199
8.3 Experimental.....	204
8.3.1 Materials.....	204
8.3.2 Instrumentation.....	204
8.3.3 Synthesis of 1-butyl-3-(10'-hydroxydecyl)-1H-imidazolium bromide (1BDIBr).....	206

8.3.4	Synthesis of 1-butyl-3-(10'-hydroxydecyl)-1H-imidazolium tetrafluoroborate (1BDIBF <sub>4</sub> ), 1-butyl-3-(10'-hydroxydecyl)-1H-imidazolium hexafluorophosphate (1BDIPF <sub>6</sub> ), and 1-butyl-3-(10'-hydroxydecyl)-1H-imidazolium bis(trifluoromethane)sulfonimide (1BDITf <sub>2</sub> N).....	206
8.3.5	Synthesis of 1-[ $\omega$ -methacryloyloxydecyl]-3-( <i>n</i> -butyl)-imidazolium bromide (1BDIMABr), 1-[ $\omega$ -methacryloyloxydecyl]-3-( <i>n</i> -butyl)-imidazolium tetrafluoroborate (1BDIMABF <sub>4</sub> ), 1-[ $\omega$ -methacryloyloxydecyl]-3-( <i>n</i> -butyl)-imidazolium hexafluorophosphate (1BDIMAPF <sub>6</sub> ), and 1-[ $\omega$ -methacryloyloxydecyl]-3-( <i>n</i> -butyl)-imidazolium bis(trifluoromethane)sulfonimide (1BDIMATf <sub>2</sub> N).....	207
8.3.6	Conventional free radical polymerization of 1BDIMA IL monomers ( <i>in situ</i> FTIR).....	209
8.3.7	RAFT polymerization of 1BDIMA IL monomers ( <i>in situ</i> FTIR).....	210
8.3.8	Conventional free radical polymerization of 1BDIMABr (thermal properties and conductivity).....	210
8.3.9	Post-polymerization ion exchange of poly(1BDIMABr).....	211
8.3.10	NMR Diffusometry.....	211
8.4	Results and Discussion.....	212
8.4.1	Synthesis of IL monomer.....	212
8.4.2	Thermal properties and ion conductivity.....	215
8.4.3	Polymerization kinetics of ILs.....	219
8.5	Conclusion.....	228
8.6	Acknowledgments.....	230
8.7	Supporting information.....	230

8.8 References.....	238
<b>Chapter 9: Decoupling Ion Conduction and Mechanical Integrity: Imidazolium-Containing Poly(Ionic Liquid)s with Tunable Mechanical Properties.....</b>	<b>242</b>
9.1 Abstract.....	242
9.2 Introduction.....	243
9.3 Experimental.....	245
9.3.1 Materials.....	245
9.3.2 Instrumentation.....	246
9.3.3 Synthesis of poly(1BDIMABr) macroCTA.....	248
9.3.4 Synthesis of poly(S-b-1BDIMABr-b-S) triblock copolymers.....	248
9.3.5 Film casting.....	249
9.4 Results and Discussion.....	249
9.5 Conclusions.....	260
9.6 References.....	261
<b>Chapter 10: Polymerized Phosphorus Ylide: Fast Solid-State Charge Transfer ...</b>	<b>264</b>
10.1 Abstract.....	264
10.2 Introduction.....	265
10.3 Experimental.....	266
10.3.1 Materials.....	266
10.3.2 Instrumentation.....	266
10.3.3 Solid-state charge transfer.....	267
10.3.4 Synthesis of PY monomers.....	267
10.3.5 Free radical polymerization of PY monomers.....	267

10.4 Results and Discussions.....	268
10.5 Conclusions.....	274
10.6 References.....	275
10.7 Supplementary information.....	277
<b>Chapter 11: Overall Conclusions.....</b>	<b>279</b>
<b>Chapter 12: Suggested Future Work.....</b>	<b>283</b>
12.1 Ion-Containing 3-Arm (AB) <sub>3</sub> Diblock Copolymers Synthesis.....	283
12.2 Synthesis of Radical Block Copolymers.....	284
12.3 UV-Assisted Direct Writing of Ion Conduction Pathways.....	285
12.4 Tunable Anisotropy in Ion Conduction: Electro- and Light-Responsive Block Copolymers.....	287
12.5 References.....	290

## List of Figures

Figure 2.4.3-1 Fluorescence lifetime and intensity time traces of tetraphenoxyperylenetetracarboxy diimide (TPDI) molecules embedded in poly(n-butyl methacrylate) matrix. <sup>70</sup> .....	13
Figure 2.5.1-1 Correlation between the mean size of free volume elements ( $V_f$ ) from PALS and (a) CO <sub>2</sub> and CH <sub>4</sub> permeability and (b) H <sub>2</sub> and N <sub>2</sub> permeability at infinite dilution and 35 °C in PEGDA/PEGMEA (▼) and PEGDA/PEGA (△) copolymers. <sup>100</sup> ...	18
Figure 2.5.1-2 Influence of free volume size from PALS measurements on: (a) water and NaCl diffusivity and (b) diffusivity selectivity, $\alpha D$ in BPS (● and ○) and BPSH (■ and □) films. The dashed lines are provided to guide the eye. <sup>23</sup> .....	19
Figure 2.5.2-1 o-Ps life time (ns) (top) and o-Ps intensity (bottom) for different polyurethanes as a function of temperature. Open circle: 400 kDa molecular weight; open triangle: 1200 kDa molecular weight; open square: 2000 kDa molecular weight. <sup>106</sup> .....	20
Figure 2.5.2-2 Lifetime parameters of o-Ps annihilation in CYTOP at 298 K as a function of the pressure P: The mean lifetime $\tau_3$ , the mean dispersion $\sigma_3$ (standard deviation of the o-Ps lifetime distribution), and the relative intensity $I_3$ . The filled symbols: 1.3–2.6 million counts, and the open symbols: 3.8–6.3 million counts. The stars show the lifetime parameters of the last measurement done after finishing the pressure run and decreasing the pressure to the ambient value. The lines are exponential fits of first ( $\sigma_3, I_3$ ) or second order ( $\tau_3$ ). <sup>107</sup> .....	21
Figure 2.5.4-1 Free volume size (o-Ps lifetime) as a function of molecular weight (left) and polydispersity (right) in poly(methyl methacrylate). <sup>114</sup> .....	34

Figure 2.5.5-1 T<sub>g</sub> (a) determined from DSC and o-Ps lifetime  $\tau_3$  (b) determined from PALS against  $\alpha$ -olefin content (wt%) for ethylene copolymers containing: 1-propene (C3), 1-butene (C4) and 1-octene (C8). Solid lines are least-squares exponential fit.<sup>5</sup>....37

Figure 2.5.7-1 Measured oPs pickoff lifetimes for the PVOH/water system as a function of water content.<sup>29</sup>.....57

Figure 2.5.7-2 o-Ps lifetime (a) and o-Ps intensity (b) plotted as a function of relative humidity for the aromatic polyamide isolated from SW30.<sup>131</sup>.....59

Figure 3.1 Comparison between ILs and PILs in mechanical integrity and ion conductivity.....76

Figure 3.2 Ion conductivities and viscosity of phosphonium-based and ammonium based ILs with different substituents. T = 25 °C, counter ions = Tf<sub>2</sub>N<sup>-</sup>.<sup>39-40</sup>.....80

Figure 3.3 Comparison of P-based ILs with different counter anions (T = 25 °C).<sup>40, 54</sup>....82

Figure 3.4 Influence of lithium salt concentration on (a) viscosity and ion conductivities of P-based ILs;<sup>50</sup> (b) ion conductivities of various P-based ILs (T = 50 °C).<sup>55</sup>.....86

Figure 3.5 Temperature dependence of (a) viscosity and (b) ion conductivities in P-based ILs with different salt concentration.<sup>60</sup>.....87

Figure 3.6 Comparison of (a) thermal stability, (b) T<sub>g</sub>, (c) temperature dependent ion conductivities and (d) ion conductivities normalized with T<sub>g</sub> of P-based PILs and N-based PILs.<sup>15</sup>.....91

Figure 3.7 The influence of different counter cations on (a) T<sub>g</sub> and (b) ion conductivity (purple x is Na<sup>+</sup>, dark red solid diamond is Bu<sub>4</sub>N<sup>+</sup>, blue solid triangle is Bu<sub>4</sub>P<sup>+</sup>, olive green triangle is Me<sub>3</sub>(MOE)P<sup>+</sup>, red open circle is (MOEOE)<sub>3</sub>MeN<sup>+</sup>).<sup>48</sup>.....93

Figure 3.8 The influence of counter ions and ion concentration on (a) $T_g$ and (b) ion conductivity (at 30 °C). <sup>47</sup> .....	95
Figure 4.1 Influence of catalyst concentrations (a & b) and temperatures (c & d) on crosslinking kinetics through rheology at 25 °C for a and b while catalyst concentration was set to 3 wt% (to bisAcAc) in c & d.....	113
Figure 4.2 Influence of diacrylate molecular weight on crosslinking kinetics using rheology (a & b) and in situ FTIR (c). Rheology: T = 25 °C; catalyst concentration = 3 wt% (to the weight of bisAcAc).....	115
Figure 4.3 Michael network crosslinking kinetics with the addition of tackifiers. Rheology: T = 25 °C; catalyst concentration = 1 wt%.....	116
Figure 4.4 180° Peel test results: influence of diacrylate molecular weight (a & b) and tackifier addition (c & d) on adhesive properties. Rheology: T = 25 °C; catalyst concentration = 1 wt%.....	117
Figure 4.5 90° Peel test results on three different substrates (a) with different pre-cure time (b).....	118
Figure S4.1 Graphic illustration of 180° (a) and 90° (b) peel tests using Instron 5500...	121
Figure S4.2 Water contact angles on EPDM (a), TPO (b), and PVC (c).....	121
Figure 5.1 In situ Fourier transform infrared spectroscopy of poly(4VBP- <i>b</i> -I- <i>b</i> -S) block copolymers synthesized through living anionic polymerization.....	130
Figure 5.2 <sup>1</sup> H NMR spectroscopy allowed the calculation of the $M_n$ of poly(4VBP-I-S) (10-10-9 kg/mol shown). The existence of 4VBP segment led to higher 3, 4 addition percent in the isoprene block.....	131

Figure 5.3 DSC suggested micro-phase mixing of isoprene block with low molecular weight 4VBP block and micro-phase separation of isoprene block with high molecular weight 4VBP.....134

Figure 5.4 Dynamic mechanical analysis demonstrated similar  $T_g$ s to DSC from 4VBP containing block copolymers: solid line, storage modulus; dash line,  $\tan \delta$ .....137

Figure S5.1  $^1\text{H}$  NMR spectroscopy demonstrated high 3, 4 addition isoprene blocks in poly(4VBP-*b*-I-*b*-S) triblock copolymers in comparison to control polymers.....143

Figure S5.2 Quantitative  $^{13}\text{C}$  NMR for the polymer blends of polyisoprene (25 kg/mol) and poly4VBP (21 kg/mol).....144

Figure S5.3 Thermal annealing further promoted phase separation. Polymers shown: poly(4VBP-*b*-I-*b*-S) 25-10-10 kg/mol. Solid line: Storage modulus; Dash line:  $\tan \delta$ ...144

Figure 6.1 a) Thermal transitions of poly(HUrMA-co-PhUrMA) statistical copolymers. b)  $T_g$  of poly(HUrMA-co-PhUrMA) agreed with the Fox Equation.....158

Figure 6.2 SEC light scattering chromatograms exhibited an increase in molecular weight with time in poly(UrMA-*b*-DEGMEMA-*b*-UrMA) triblock synthesis. (Molecular weight of DEGMEMA macroCTA was determined using aqueous SEC, but shown for comparison in DMF + 0.05 M LiBr SEC).....160

Figure 6.3 Dynamic mechanical analysis of poly(UrMA-*b*-DEGMEMA-*b*-UrMA) with 25 and 50 wt% urea segment.....163

Figure 6.4 AFM revealed microphase-separated surface morphology: tapping mode, 42 N m-1 high spin constant cantilever.....164

Figure 6.5 SAXS of casted films exhibited distinct first-order interference peaks without higher order peaks.....165

Figure 6.6 Variable temperature Fourier transform infrared spectroscopy illustrated the transition from ordered hydrogen bonding to disordered hydrogen bonding with increasing temperature. (a, bidentate hydrogen bonding; b, mono-dentate hydrogen bonding).....167

Figure 6.7 Schematic illustration of the dissociation of main chain urea sites and pendant urea side sites.....169

Figure 7.1 Thermomechanical performance of PyUr and PyUrBr triblock copolymers: (a) DSC and (b) DMA of PyUr triblock copolymers; (c) DSC and (d) DMA of PyUrBr triblock copolymers. Homopolymer: poly(PyUrMA) homopolymer; Copolymer: poly(PyUrMA-co-DEGMEMA), 55 wt % of PyUrMA). Exo up for DSC.....180

Figure 7.2 Bulk morphologies of PyUr and PyUrBr triblock copolymer films: (a) SAXS and (b) WAXS of PyUr triblock copolymers; (c) SAXS and (d) WAXS of PyUrBr triblock copolymers. Copolymer: poly(PyUrMA-co-DEGMEMA), 55 wt% PyUrMA.....183

Figure 7.3 TEM images of PyUr<sub>2</sub> and PyUrBr<sub>2</sub> (scale bar: 500 nm).....185

Figure 7.4 VT-FTIR of PyUr<sub>2</sub> (a), PyUrBr (b), and the peak absorbance of carbonyl stretching at various temperature (c) coupled with corresponding stress-relaxation of PyUr<sub>2</sub> and PyUrBr<sub>2</sub> (d).....187

Figure S7.1 Size exclusion chromatography (SEC) trace of poly(DEGMEMA) macrCTA. Elution solvent: DMF + 0.05 M LiBr at 60 °C.....195

Figure S7.2 Molecular weight determination of poly(PyUrMA) block through <sup>1</sup>H NMR spectroscopy.....196

Figure S7.3 Comparison of <sup>1</sup>H NMR spectroscopies before and after quaternization....196

Figure S7.4 Second heat of differential scanning calorimetry (DSC) at different cooling rate: slow cool: 5 °C/min; quench cool: 100 °C/min.....	197
Figure S7.5 (a) Cooling traces of PyUr2 in DSC isotherming at 92 °C for 10, 30, and 60 min; (b) WAXS profiles of PyUr2 when annealed at 92 °C.....	197
Figure 8.1 <sup>1</sup> H NMR of imidazolium-containing precursors (1BDIBr) demonstrated complete ion-exchange from Br anion to Tf <sub>2</sub> N, BF <sub>4</sub> and PF <sub>6</sub> anions (500 MHz).....	214
Figure 8.2 Temperature dependent dc ionic conductivity of PIL homopolymers.....	219
Figure 8.3 Polymerization kinetics through <i>in situ</i> FTIR: (a) & (b) Free radical polymerization of IL monomer that shows similar polymerization kinetics. <i>In situ</i> FTIR: Matrix-MF, [1BDIMA] = 0.5 M, AIBN = 1 mol%, T = 65 °C, MeCN, 1289 - 1308 cm <sup>-1</sup> ; (c) & (d) RAFT polymerization of IL monomers that show obvious differences in polymerization kinetics. <i>In situ</i> FTIR: Matrix-MF, [1BDIMA] = 1 M, [CTA]/[I] = 3, T = 65 °C, MeCN, 1289 - 1308 cm <sup>-1</sup> .....	221
Figure 8.4 DMF accelerated RAFT polymerization of 1BIDMABr and 1BIDMATf <sub>2</sub> N compared to MeCN as solvent. <i>In situ</i> FTIR: [M] = 1 M, [CTA]/[I] = 3, T = 65 °C, 1289 - 1308 cm <sup>-1</sup> .....	223
Figure 8.5 Diffusion coefficients of IL monomers with different counter-anions and in different solvents. NMR diffusometry measurements were done at 21 °C and 62 °C, respectively. Errors in <i>D</i> values are ±5 %.....	225
Figure S8.1 Full <sup>1</sup> H NMR spectrum of 1BDIMABr (500 MHz).....	230
Figure S8.2 <sup>19</sup> F NMR spectra of the four IL precursors (470 MHz).....	231
Figure S8.3 SEC trace (dRI) of poly(1BIDMABr) homopolymers in DMF + 0.05 M LiBr. Blue solid line: 3 mol% AIBN; Red dash line: 1 mol% AIBN.....	231

Figure S8.4 Thermal degradation of PIL homopolymers. TGA: 10 °C/min heating rate, N <sub>2</sub> , isotherm at 120 °C for 30 min.....	232
Figure S8.5 T <sub>gs</sub> of PILs with different counter-ions. Solid line: 32.1 kg/mol (SEC, relative molecular weight); Dash line: 26.8 kg/mol (SEC, relative molecular weight). Blue: 1BIDMABr; Red: 1BDIMAPF <sub>6</sub> ; Green: 1BIDMABF <sub>4</sub> ; Purple: 1BIDMATf <sub>2</sub> N. Exo down.....	232
Figure S8.6 Conductivities of PIL homopolymers at similar chain mobility.....	233
Figure S8.7 Free radical polymerization showed similar kinetics regardless of the counter-ion species. Definition of t <sub>1/2</sub> : Time for the system to consume half of the initial monomers (50% of initial monomer intensity in <i>in situ</i> FTIR). <i>In situ</i> FTIR: [IBDIMA] = 0.5 M.....	233
Figure S8.8 <i>In situ</i> FTIR at 75 °C exhibited no monomer conversion during RAFT polymerization. <i>In situ</i> FTIR: [CTA]/[I] = 3, [M] = 1M. MacroCTA: poly(1BDIMATf <sub>2</sub> N) macro CTA.....	234
Figure S8.9 $k_{el}^{DMF}(\bar{r})/k_{el}^{MeCN}(\bar{r})$ obtained using Eq. 4 for the electron transfer occurring in DMF and MeCN. $n_{DMF} = 1.43$ , $n_{MeCN} = 1.34$ , $T = 293K$ , $\epsilon_{DMF}(0) = \epsilon_{MeCN} = 37$ , $r_a = r_d = 0.3nm$ were used. The top panel shows the ratio for $r \equiv \bar{r} = 0.4 nm$ and the bottom panel shows the ratio for various values of r on a semi-logarithmic plot to highlight changes in the ratio by orders of magnitude.....	237
Figure 9.1 Synthesis of poly(S- <i>b</i> -1BDIMABr- <i>b</i> -S) triblock copolymers through RAFT polymerization.....	250

Figure 9.2 (a) SEC traces of poly(S-*b*-1BDIMABr-*b*-S) triblock copolymers with different polymerization time; (b) thermal transitions monitored via DSC (15-34-15 kg/mol samples shown).....251

Figure 9.3 Real part (a) of complex conductivity  $\sigma = \sigma' + i\sigma''$  as a function of frequency for triblock copolymers with bromide (Br), tetrafluoroborate (BF<sub>4</sub>), and bis(trifluoromethyl sulfonyl)imide (Tf<sub>2</sub>N) anions at 310 K. Figure b) shows  $\sigma'$  and the dielectric loss modulus  $M''$  as a function of frequency. Red square mark the magnitude of the DC-ionic conductivity,  $\sigma_0$ , corresponding to the peak frequency of  $M''$  .....253

Figure 9.4 DC-ionic conductivity as a function of inverse temperature and T<sub>g</sub>-normalized temperature (ionic block T<sub>g</sub>). Blue and red lines indicate room temperature and the calorimetric glass transition temperature, respectively. An orange bar marks the range of T<sub>g</sub>s of polystyrene.....254

Figure 9.5 (a) Thermomechanical property of block copolymers with BF<sub>4</sub> counter anions in DMA; (b) shear storage modulus (G') as a function of frequency in block copolymers with BF<sub>4</sub> counter anions; (c) & (d) complex viscosity ( $\eta^*$ ) as a function of frequency at 180 °C (c) and 100 °C (d).....257

Figure 9.6 Time temperature superposition (TTS) of block copolymers with BF<sub>4</sub> counter anions (a) as a function of frequency and the WLF fitting (b) of TTS data (shown only 15-34-15 samples).....259

Figure 10.1 Fast solid-state charge transfer between DPPS and MA.....269

Figure 10.2 Synthesis of PY monomers with different DPPS/MA feed ratios.....270

Figure 10.3 Comparison of DPPS, ylide, and oxidized DPPS in <sup>31</sup>P NMR spectroscopy.....271

Figure 10.4 Light absorption (a) and fluorescence (b) of PPY1 and PPY3.....	273
Figure S10.1 <sup>1</sup> H NMR spectroscopy of PY3 monomer.....	277
Figure S10.2 <sup>13</sup> C NMR spectroscopy of PY3 monomer.....	277
Figure S10.3 <sup>1</sup> H NMR spectroscopy of PPY3 homopolymers.....	278
Figure 12.1 Schematic description of UV assisted direct writing of ion conduction pathways.....	286
Figure 12.2 Fabrication of electro-switchable anisotropic conductive devices.....	287
Figure 12.3 Schematic description of light-responsive polyampholytes.....	289

## List of Tables

Table 2.5.1-1 Thermal properties and free volume parameters of poly(ethylene- <i>co</i> - $\alpha$ -olefin) <sup>93</sup> .....	16
Table 2.5.3-1 Glass transition temperature and fractional free volume of high-vinyl polybutadiene and cis-isoprene <sup>89</sup> .....	23
Table 2.5.3-2 Glass transition temperature and free volume parameters in poly(styrene- <i>co</i> -acrylonitrile) <sup>32</sup> .....	24
Table 2.5.3-3 Fractional free volume and CO <sub>2</sub> permeability in poly(isoprene- <i>b</i> -vinyl trimethylsilane) <sup>109</sup> .....	25
Table 2.5.3-4 Glass transition temperature and free volume parameter between polyethylene terephthalate (PET) and polyethylene isophthalate (PEI) <sup>25</sup> .....	26
Table 2.5.3-5 Free volume parameters and water diffusivity of disulfonated poly(arylene ether sulfone) random copolymers <sup>23</sup> .....	28
Table 2.5.3-6 Glass transition temperature and free volume size of thermotropic liquid crystalline polymers <sup>86</sup> .....	29
Table 2.5.3-7 Fractional free volume and CO <sub>2</sub> permeability before and after thermal rearrangement <sup>110</sup> .....	30
Table 2.5.3-8 Free volume and permeability parameters of oriented PET films <sup>25</sup> .....	31
Table 2.5.4-1 Molecular weight, free volume size and spin-spin relaxation time of polystyrene <sup>113</sup> .....	32
Table 2.5.4-2 Molecular weight and free volume parameter of polystyrene and poly(methyl methacrylate) <sup>112</sup> .....	33
Table 2.5.5-1 Thermal properties and free volume results of poly(ethylene- <i>co</i> -olefin) <sup>93</sup> .....	35

Table 2.5.5-2 Thermomechanical properties and fractional free volume of poly(ethylene- <i>co</i> -norbornene) copolymers <sup>33</sup> .....	38
Table 2.5.5-3 Fractional free volume and gas permeability of triptycene-based polyimides <sup>26</sup> .....	39
Table 2.5.6-1 Thermal properties and free volume parameter for PEG based crosslinking system <sup>100</sup> .....	41
Table 2.5.6-2 Thermal properties and free volume parameters in PEG based crosslink system <sup>15</sup> .....	43
Table 2.5.6-3 Thermal properties and free volume parameters in PEG based crosslink system <sup>117-118</sup> .....	44
Table 2.5.6-4 Thermal properties and free volume parameters for crosslinked polybutadiene <sup>10</sup> .....	47
Table 2.5.6-5 Thermal properties and free volume parameters in crosslinked polyisoprene/polybutadiene blend initiated by dicumylperoxide <sup>89</sup> .....	47
Table 2.5.6-6 Thermal properties and free volume parameters in crosslinked unsaturated polymer ester <sup>119</sup> .....	48
Table 2.5.6-7 Thermal properties and free volume parameter in epoxy-polyether amine networks <sup>41</sup> .....	49
Table 2.5.6-8 Thermomechanical properties and fractional free volume in epoxy-amine crosslinking matrices <sup>120</sup> .....	50
Table 2.5.7-1 Thermal properties and free volume parameters of a polyimide matrix with various additives <sup>2</sup> .....	53

Table 2.5.7-2 Thermal properties and free volume parameters of polyimide with azide as additives <sup>128</sup> .....	55
Table 2.5.7-3 Free volume parameters of CS/Pebax® polymer blends <sup>37</sup> .....	56
Table 2.5.7-4 Free volume parameters of hydrated crosslinked PEG films with water as additives <sup>129</sup> .....	57
Table 2.5.7-5 Thermal properties and free volume of epoxy resin/polyurethane network and organophilic montmorillonite (oM) polymer nanocomposites <sup>8</sup> .....	59
Table 2.5.7-6 Thermal properties and free volume of poly(m-xylene adipamide)/montmorillonite nanocomposites <sup>71</sup> .....	60
Table 2.5.7-7 Free volume of phenol-formaldehyde resin using multi-wall carbon nanotubes (MWCNTs) as nanocomposites <sup>133</sup> .....	61
Table 3.1 Ion conductivity of P-based ILs with various alkyl substituents (T = 25 °C) <sup>51</sup> .....	81
Table 3.2 Ion conductivities of P-based ILs with different counter ions (T = 50 °C) <sup>55</sup> .....	83
Table 3.3 Viscosity and ion conductivities of P-based ILs with different counter ions (T = 25 °C) <sup>58</sup> .....	84
Table 3.4 Ion conductivities of P-based ILs with halide counter anions (T = 25 °C) <sup>41,59</sup> .....	85
Table 3.5 Hydroxide conductivity and water uptake of swelled phosphonium polymer films at different chloromethylation level. T = 20 °C <sup>78-80</sup> .....	96
Table 4.1 Tensile results of 180° peel tests on EPDM, PVC, and TPO membranes .....	117
Table 5.1 Isoprene microstructure study using <sup>1</sup> H NMR spectroscopy. Mn and isoprene 3,4 addition percent calculated from <sup>1</sup> H NMR: a. isoprene (3g) + poly4VBP homopolymers (1g); b. isoprene (3g) + N-methylpiperidine (3g) .....	132

Table 5.2 The results of quantitative $^{13}\text{C}$ NMR spectroscopy of 4VBP-containing triblock copolymers.....	133
Table 5.3 Thermomechanical study of 4VBP containing block copolymers and control polymers. $M_n$ , number average molecule weight, calculated from $^1\text{H}$ NMR. $T_g$ , glass transition temperature, obtained from DSC middle point and DMA $\tan \delta$ .....	136
Table 5.4 DMA exhibited one extra $T_g$ corresponding to 4VBP block compared to DSC, and further supported micro-phase behavior concluded from DSC data.....	138
Table S5.1 Polymers synthesized through anionic polymerization. Molecular weights were confirmed by $^1\text{H}$ NMR spectroscopy.....	142
Table 6.1. Molecular weight analysis of urea-containing ABA triblock copolymers....	161
Table 6.2. SAXS $q$ values and Bragg spacing for triblock copolymers with lamellar morphology in AFM.....	165
Table 7.1 Molecular weight and thermal analysis of triblock copolymers. $M_n$ was determined by aqueous SEC and $^1\text{H}$ NMR spectroscopy. $T_{d,5\%}$ was calculated using TGA. $T_g$ , endothermic transition, and exothermic transition were measured by DSC.....	179
Table 7.2 Bragg spacing and higher order peaks of triblock copolymers in SAXS.....	184
Table 8.1 Thermal properties and conductivity of PIL homopolymers with different counter-ions. $T_{d,5\%}$ , $T_g$ and $\sigma_{dc}$ were determined by TGA, DSC, and BDS, respectively. Samples were dried in a vacuum oven at $120\text{ }^\circ\text{C}$ overnight before the DSC and BDS tests.....	216
Table 8.2 Diffusion coefficients of solvents and sizes of monomers in different solutions at $62\text{ }^\circ\text{C}$ .....	226

Table 9.1 Molecular weights and $T_g$ s of triblock copolymers with different counter anions.....	252
Table 9.2 WLF fitting parameters and calculated viscoelastic properties from WLF equation and VFT equation of block copolymers with $BF_4$ counter anions. ( $T_{ref} = T_g = 100$ °C).....	260
Table 10.3 Excitation and emission properties of phosphonium ylide monomers and polymers.....	274

## List of Schemes

Scheme 4.1 Sample preparation for peel tests: (a) 180° peel tests between two identical rubber substrates; (b) 90° peel tests at the interfaces between rubber substrates and woods.....	110
Scheme 4.2 The synthesis of hPBDA (Michael acceptor) and hPBbisAcAc (Michael donor).....	112
Scheme 5.1. The synthesis of poly(4VBP- <i>b</i> -I- <i>b</i> -S) block copolymers using living anionic polymerization.....	129
Scheme 6.1. Urea-containing methacrylate monomer synthesis and free radical polymerization.....	157
Scheme 6.2. Synthesis of poly(UrMA- <i>b</i> -DEGMEMMA- <i>b</i> -UrMA) triblock in a divergent fashion using RAFT polymerization.....	159
Scheme 7.1 Synthesis of PyUrMA triblock copolymers and corresponding quaternization.....	178
Scheme 8.1 Synthesis of imidazolium-containing monomer with different counter-ions.....	213
Scheme 8.2 Synthesis of poly(1BIDMABr) and post-polymerization ion-exchange....	215
Scheme 10.1 Polymerization of PPYs through different synthetic strategies.....	272
Scheme 12.2 Synthesis of (AB) <sub>3</sub> diblock copolymers using RAFT polymerization.....	283
Scheme 12.3 Synthesis of radical-containing block copolymers through anionic polymerization and RAFT polymerization.....	284

# Chapter 1: Introduction

## 1.1 *Dissertation overview*

This dissertation primarily revolves around macromolecules with pendant non-covalent interactions (hydrogen bonding and electrostatic interaction), focusing on the influence of mesoscale phenomenon on macroscopic performances. Chapter 2 reviews the application of free volume theory in polymeric matrices. This comprehensive review intends to provide an understanding between structural elements and free volume and the corresponding thermomechanical and permeation properties. Chapter 3 reviews literature addressing phosphonium-containing ionic liquids (ILs) and poly(ionic liquid)s (PILs) as conductive materials. Phosphonium-containing ILs and PILs demonstrate significant advantages over conventional nitrogen-based counterparts (ammonium, imidazolium, etc.) in terms of ion conductivity and thermal and chemical stability.

Chapter 4 reports the application of Michael addition chemistry in solvent-free rooftop adhesives. Facile end-group functionization of hydrogenated polybutene diol allows the preparation of Michael donors and acceptors. With optimized stoichiometry and additives, the Michael addition adhesives at least double the performance of solvent-based commercial adhesive controls at three different interfaces.

Chapter 5 describes the utilization of piperidine functionalized styrene monomer to increase the 3,4 addition content in polyisoprene block during the synthesis of ABC triblock copolymers using anionic polymerization. The  $T_g$  of polyisoprene blocks varies from  $-60\text{ }^{\circ}\text{C}$  to  $-20\text{ }^{\circ}\text{C}$  due to 3,4 addition change. Due to increased polarity of polyisoprene block from high 3,4 addition content, polyisoprene blocks demonstrate microphase separation or mixing depending on their molecular weights. Chapter 6 and 7 examines the association of pendant hydrogen

bonding groups (urea sites) and its corresponding influence on microscopic morphologies and macroscopic thermomechanical properties. Specifically, Chapter 6 reports pendant urea hydrogen bonding sites promoted ordered morphologies and expanded rubbery plateau above the hard block  $T_g$ . Pendant hydrogen bonding remains ordered at high temperatures comparing to backbone hydrogen bonding, presumably due to the lack of cooperativity. Chapter 7 compares a library of ABA block copolymers containing either hydrogen bonding (urea sites) and electrostatic interactions (pyridinium). Hydrogen bonding promotes long-range, ordered lamellar morphology and shows flow temperature ( $T_f$ ) 80 °C above the hard block  $T_g$ . The introduction of electrostatic interaction disrupts the ordered morphology, leading to a reduction in  $T_f$ . In return, the dissociation of hydrogen bonding is severely depressed by extra electrostatic interactions.

Chapter 8 and 9 focus on understanding ion dynamics in PIL homopolymers and block copolymers. In Chapter 8, novel IL monomers with long alkyl spacers between imidazolium groups and polymer backbones allow the synthesis of four different PIL homopolymers with different counter anions. Counter anions show profound impacts on  $T_g$ , ion conductivity, and radical polymerization kinetics. The promising ion conductivity enables further investigation of this IL monomer in the synthesis of ABA triblock copolymers using styrene as the A blocks in Chapter 9. The triblock copolymers shows decoupling of ion dynamics (ion conductivity) and structural relaxation, allowing tunable viscoelastic properties from composition changes without altering ion conductivity.

Chapter 10 details the synthesis of a new class of polymers: poly(phosphorus ylide). Fast solid-state charge transfer is observed during the synthesis of phosphorus ylide monomers. The resulting monomers and homopolymers synthesized from conventional free radical polymerization exhibited strong visible light absorption and fluorescence, promising their

application as photo-sensitized dye. Finally, Chapter 11 and 12 provide overall conclusions and suggested future work. Some of the future work in Chapter 12 is already in progress, and the rest are suggested continuous work.

# **Chapter 2: Probing Nothing: A Review of Free Volume and its Role in Polymer Structure-Property Relationships**

*(Manuscript in preparation for publication)*

*Mingtao Chen, Maruti Hedge, Timothy E. Long\**

Department of Chemistry, Macromolecules Innovation Institute, Virginia Polytechnic Institute and State University, Blacksburg, Virginia, 24061

\* To whom correspondence should be addressed: [telong@vt.edu](mailto:telong@vt.edu)

## **2.1 Abstract**

Fractional free volume in polymers relates closely to structural relaxation and voids distribution, which proves crucial in understanding and predicting thermomechanical properties and permeation process, respectively. This review focused on the structure-free volume-property relationships in a wide range of polymeric matrices: crosslinked polymers, homopolymers, segmented polymers, block copolymers, polymer blends and additives. The relationships between common environment elements, such as temperature and pressure, and free volume changes are also summarized in this review. Different techniques determined free volume parameters which dictate polymer physical properties, and, in return, contribute to future material design from a molecular level.

## **2.2 Introduction**

Researchers in polymer science and engineering commonly invoke the theory of free volume to rationalize polymer properties and performance, however, these rationalizations are often the result of confounding factors. Thus, this review is intended to present the progression of free volume theory, the common techniques employed in the literature, and diverse examples where free volume was presented to account for structure-property relationships. In simple terms, the polymer free volume primarily refers to the degree of packing, or more specifically, the volume unoccupied by the constituent atoms or molecules in a material.<sup>1</sup> Due to the relationship between free volume and the mobility ( $m$ ) of polymer chains *i.e.* relaxation behavior of materials, theories on free volume are pertinent to the fundamental understanding of polymer physical properties, most notably, thermomechanical properties<sup>2-10</sup> and diffusion properties.<sup>11-24</sup> We will discuss the modification of fractional free volume, free volume size and distribution, through tailoring of polymeric structure,<sup>5, 7, 20, 25-27, 28-30, 15, 31-34</sup> use of additive and blends<sup>16, 19, 37-39</sup> and nanoscale morphologies.<sup>38</sup> We will provide a brief overview on the theoretical concepts of free volume and the experimental techniques used to measure free volume in a polymeric material.

In terms of thermomechanical properties, free volume relates to local mobility and affects segmental motion, thus influencing melt viscosity, glass transition temperature ( $T_g$ ) and Young's modulus.<sup>3, 10, 38-41</sup> For barrier and membrane applications, free volume directly determines the diffusivity and selectivity since free volume typically serves as transportation pathways for small molecules.<sup>12, 21, 24, 37, 42-43</sup> This review on free volume in polymers is geared towards polymer chemists. We will highlight the important progresses in theoretical concepts and techniques used to probe free volume. This review will focus on the inter-relationship of the free volume of a polymer, molecular structure, and physical properties.

### 2.3 Theoretical developments of free volume theory

The first conceptual realization of free volume is credited to van der Waal.<sup>44</sup> In 1873, he postulated that each molecule occupies an intrinsic volume related to its size along with an associated excluded volume to account for its thermal motion. While many researchers intuitively recognized that the properties of a fluid were related to its free volume having a length scale on the order of angstroms, the lack of theoretical models to compute free volume was an obstacle in further developing this prospect. In 1913, Batchinski published his seminal work wherein he recognized that viscosity of simple low molecular weight fluids at constant temperature and pressure scales with density.<sup>45</sup> His work was the first to directly link diffusivity of molecules to free volume. In subsequent years, Hildebrand *et al.* developed on Batchinski's work and showed that the fluid viscosity scales as a function of fractional free volume.<sup>46</sup> Their theories were applicable for simple fluids at elevated temperatures but not strictly suitable at temperatures below the melting point of the fluids.

To account for these shortcomings, in 1951, Doolittle defined free-space as the space arising from the total thermal expansion without a change in phase (Equation 1):

$$\frac{v_f}{v_0} = \frac{(v - v_0)}{v_0} \quad (1)$$

where  $v_f$  represents the volume of free-space per gram of substrate at a given temperature,  $v_0$  is the volume of one gram of substrate extrapolated to absolute zero without a change in phase, and  $v$  represents the volume of one gram of substrate at the given temperature.

Using the relative free volume ( $v_f/v_0$ ) that he defined in Equation 1, Doolittle calculated that the melt viscosity of a fluid correlated well with the observed values over a wide temperature range. Doolittle then successfully correlated melt viscosity ( $\eta$ ) with fractional free volume using Equation 2:

$$\eta = A \exp\left(\frac{B v_0}{v_f}\right) \quad (2)$$

where A and B are empirical constants for a single molecular species. In effect, Doolittle was the first to correlate free-space with the temperature-dependence of melt viscosity. However, the application of Doolittle's theory was restricted by its poor performance at low temperature and complex extrapolation approach. Subsequently, there have been important refinements to this approach.

The relatively successful empirical Doolittle equation resulted in sparse theoretical developments. The Fox-Flory equation was based on the Doolittle expression and dispelled the notion that viscosity peaks at the  $T_g$ . Their expression (Equation 3) implied a direct link between the  $T_g$ , molecular weight, and free volume:

$$T_g = T_{g,\infty} - K/M_n \quad (3)$$

where  $T_{g,\infty}$  is the maximum glass transition temperature at infinite molecular weight,  $M_n$  is the molecular weight, and K is an empirical constant related to free volume.

Although the Doolittle equation has no dependence on temperature, it is suitable only at high temperature where free volume is high. To establish a free volume theory over a wider temperature range, Williams, Landel and Ferry initially simplified the Doolittle equation by

replacing  $v_f/v_0$  with the fractional free volume,  $f$  (where  $f = v_f/(v_0+v_f)$ ) in a supercooled system ( $v_f$  is normally negligible), resulting in Equation 4, now known as the WLF equation:<sup>47</sup>

$$\eta = A \exp\left(\frac{B}{f}\right) \quad (4)$$

Based on the assumption that the fractional free volume scales linearly with temperature, Equation 5 is obtained:

$$f = f_g + \alpha(T - T_g) \quad (5)$$

where  $f$  and  $f_g$  are the free volumes at temperature  $T$  and  $T_g$  ( $T$  is a temperature greater than  $T_g$ ) and  $\alpha$  is the thermal expansion coefficient.

By comparing the viscosities at the  $T_g$  and at temperature  $T$  and substituting for  $f$  in Equation 4, the following expression was derived:

$$\log \frac{\eta}{\eta_g} = -B(1/2.303 f_g)(T - T_g) / [(f_g/\alpha) + T - T_g] \quad (6)$$

Here,  $(B/2.303 f_g)$  and  $(f_g/\alpha)$  are the universal constants  $c_1$  and  $c_2$ :

$$\log \alpha_T = -c_1 (T - T_s) / (c_2 + T - T_s) \quad (7)$$

In most cases, Equation 6 satisfactorily describes the temperature dependence of all mechanical relaxation processes,<sup>47</sup> where  $\alpha_T$  is the ratio of any mechanical relaxation time at temperature  $T$  to its value at a reference temperature. It should be noted that while the reference temperature,  $T_s$ , is arbitrary,  $c_1$  and  $c_2$  are experimentally determined constants. Since  $\alpha_T$  is

approximately the ratio of viscosity  $\eta/\eta_g$  when reduced to  $T_g$ , Combining Equations 4 and 5 combined yield a relationship between  $\alpha_T$  and free volume.<sup>47</sup>

All of the above-mentioned theories center on the link between melt viscosity and free volume of fluids. Important contributions towards explaining the link between mobility and diffusivity of polymer chains and free volume of a material were published in 1957 by Fujita, in 1959 by Cohen and Turnbull, and in 1975 by Vrentas and Duda.

The basis of the Cohen/Turnbull theory is that molecules in a liquid migrate freely due to a greater degree of freedom than in a solid. This feature is attributed to the existence of holes through which the molecules move freely. The space associated with these holes is defined as the free volume. For pure liquids, Cohen and Turnbull derived the link between mobility ( $m$ ) and the number of holes (free volume),

$$\ln m = \ln m_0 - \gamma v_c/v_f \quad (8)$$

Here  $m$  is the molecular mobility,  $m_0$  is a constant with the same dimensions as  $m$ ,  $\gamma$  is a numerical factor between 0.5 and 1,  $v_c$  is the minimum volume of a hole that has to exist in the neighboring molecule, and  $v_f$  is defined as the free volume per molecule. A major drawback of this theory is that  $v_f$  cannot be quantified in known molecular terms. But if free volume is defined as the volume not occupied by the cores of the constituent molecules,  $v_f$  can be equated to  $v_f = v - v_c$ , allowing for the calculation and quantification of  $v_f$ .

The theories of Vrentas/Duda and Cohen/Turnbull essentially separated the free volume into two distinct voids: interstitial free volume and hole free volume. The interstitial free volume is the empty space in polymer crystals. The hole free volume refers to the excess free volume

inherent to the structural disorder in amorphous polymers, which appear as small holes. The energy required for redistribution of interstitial free volume is large whereas the hole free volume is distributed evenly without an energy increase. The theory was distinct from previous theories in the sense that they attributed the hole free volume to be solely responsible for transport properties of an amorphous polymer.<sup>48-56</sup>

During the 1960s, Bondi investigated the relationship of van der Waals volume (i.e., the volume of molecules impenetrable to thermal collision) and radii for various groups using crystallographic analysis.<sup>57</sup> The concept of “occupied volume” derived from Bondi’s interpretation afforded facile calculation over Doolittle’s approach and proved an accurate method of calculating free volume, thereby eventually supplanting Doolittle’s definition.

Later, Paul and colleagues utilized a modified group contribution method to predict transport behavior with significant accuracy.<sup>58</sup> Yet, with the discovery of high free volume glassy polymers (up to 35% for siloxane-containing polymers), the modified Doolittle equation (Equation 3) was no longer appropriate, especially when free volume pores became interconnected or bi-continuous. Additionally, Hill *et al.* showed another modified Doolittle equation with better fitting within a wide range of  $v_f$ .<sup>59</sup> Frisch and Stern published a comprehensive review of diffusion models in polymers, and will not be covered in this review.<sup>60</sup>

## **2.4 Techniques for evaluating free volume in polymers**

The length scales of free volume holes in polymers are on the order of angstroms ( $10^{-10}$  m); therefore, it is not possible to directly measure these voids. The experimental techniques rely on measurement of the surrounding cage enveloping the void and subsequent deduction of the

void characteristics. The most common techniques utilized for these measurements are discussed in the following sections.

### 2.4.1 Melt rheology

Free volume is related to the viscoelastic property of polymers. As described by the Doolittle equation and the WLF equation, as free volume increases, viscosity decreases. A common way to determine free volume is to fit rheological data with the modified WLF equation (Equation 6) in order to determine  $c_1$  and  $c_2$ . The universal constant  $c_1$  can be calculated using the equation below:<sup>61-62</sup>

$$c_1 = B'(1/2.303 f_g) \quad (9)$$

However, the utility of the WLF equation is limited to polymers with relatively low free volume. This method is particularly useful because any mechanical relaxation ratio  $\alpha_T$  (such as conductivity and storage modulus) can be related to free volume, hence providing a convenient pathway for estimating free volume. Most rheology-dependent free volume studies have utilized melt viscosity (or similar mechanical relaxation) to calculate fractional free volume.<sup>43,63,64</sup>

### 2.4.2 Density study and Bondi's group contribution theory

Conducting a density study based on Bondi's theory also represents an effective means for determining fractional free volume ( $V_f$ ). Using this method, the density of the material is determined first, after which the specific volume ( $V_{sp}$ ) at a given temperature is calculated based on a known mass. Equation 10 affords the determination of fractional free volume.<sup>63</sup>

$$V_f = \frac{V_{sp} - V_0}{V_{sp}} \approx \frac{V_{sp} - 1.3V_w}{V_{sp}} \quad (10)$$

where  $V_0$  is the occupied volume of polymer at 0 K, which is estimated as 1.3 times the van der Waals volume ( $V_w$ ), according to Bondi's group contribution theory.<sup>57</sup>

### 2.4.3 Fluorescent Probe

Fluorescent probing is a promising technique to indirectly determine local free volume.<sup>64-68</sup> Fluorescent small molecules with the ability to undergo isomerization upon light stimuli are introduced into polymer matrices. The photoisomerization requires different local volume, and this specific volume enables the indirect detection of local free volume distribution.<sup>69</sup>

Schryver *et al.* demonstrated the application of fluorescent probing to specify local free volume distribution.<sup>70</sup> Small dye molecules underwent photoisomerization in poly(*n*-butyl methacrylate) matrix and the fluorescent intensity of each individual molecule enabled the mapping of free volume distribution (**Figure 2.3-1**). 70 % and 30 % of all fluorescent molecules exhibited steady mean lifetime at 6.2 ns and 3.2 ns, respectively (**Figure 2.3-1a** and **Figure 2.3-1b**), corresponding to two different conformations. Molecules demonstrated a reversible signal as in **Figure 2.3-1c**, which was attributed to the isomerization between the two conformations due to the dynamic structural disorder of the polymer matrix.

This fluorescent approach is highly efficient in determining local free volume and free volume distribution; however, the free volume is only qualitatively compared to the

photoisomerization size without absolute value, making it less useful in comparing multiple systems and predicting properties based on free volume.

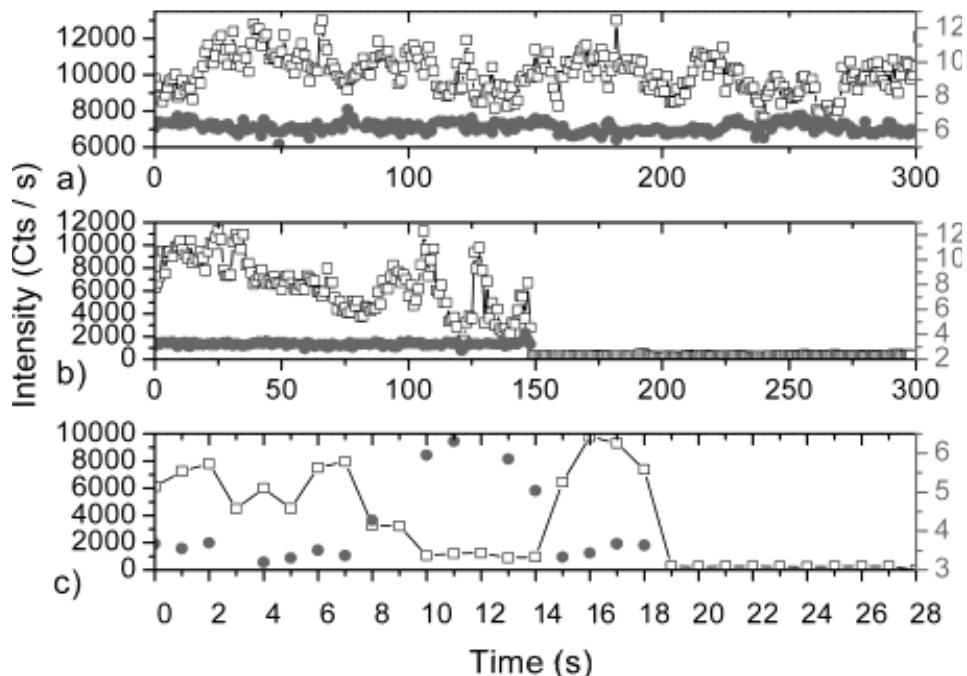


**Figure 2.4.3-1** Fluorescence lifetime (solid circle, right Y axis) and intensity (open square, left Y axis) time traces of tetraphenoxy-perylenetetracarboxy diimide (TPDI) molecules embedded in poly(*n*-butyl methacrylate) matrix (Copyright (2004) American Chemical Society).<sup>70</sup>

#### 2.4.4 Positron Annihilation Lifetime Spectroscopy (PALS)

Positron annihilation lifetime spectroscopy (PALS) is one of the most common techniques for determining polymer free volume.<sup>23, 71-76</sup> PALS works on the principle that positrons ( $e^+$ ), the anti-particle of an electron, are annihilated via interactions with electrons ( $e^-$ ),<sup>77</sup> releasing detectable gamma rays. By measuring the time span between the generation of positrons and release of gamma rays, it is possible to correlate the number of voids or amount of free volume elements in a material. Thus, local electron density, serving as an indicator of local

free volume, affects the positron annihilation significantly. Since the ortho triplet state (o-Ps) annihilation is enhanced by its interactions with other electrons, its lifetime will be reduced significantly (around 0.5 – 5 ns).

A PALS spectrum will typically consist of three lifetimes,  $\tau_1$ ,  $\tau_2$ , and  $\tau_3$ —with corresponding intensities of  $I_1$ ,  $I_2$ , and  $I_3$ . The radius of free volume relates to the o-Ps lifetime  $\tau_3$  (ns), as indicated in Equation 11,<sup>73</sup>

$$\tau_3 = \frac{1}{2} \left[ 1 - \frac{R}{R + \Delta R} + \frac{1}{2\pi} \sin \left( \frac{2\pi R}{R + \Delta R} \right) \right]^{-1} \quad (11)$$

where  $R$  is the free volume and  $\Delta R$  is the empirical electron layer thickness (normally assumed to be 0.166 nm).<sup>78</sup>

The free volume fraction (or fractional free volume,  $V_f$ ) is determined using Equation 12,

$$V_f = AVI_3 \quad (12)$$

where  $A$  is an empirical constant, and  $V = 4\pi R^3/3$ . Shorter  $\tau_3$  lifetime values correspond to decreased free volume due to the enhanced o-Ps annihilation in the presence of other electrons.<sup>77</sup>

The intensity  $I_3$  is an indicator of the number of free volume elements. Typically, PALS is more sensitive to heterogeneities in domain size (in Å) than techniques like DSC and DMA (50 nm),<sup>79</sup> but it only indicates bulk average free volume without revealing position-specific free volume information.

#### 2.4.5 Other approaches

Various indirect approaches to determine free volume, such as DMA<sup>80</sup> and molecular weight analysis<sup>21</sup> will be covered in specific examples, but most are not suitable in a general way for a wide library of materials. Electron spin resonance (ESR) is a commonly used technique to determine local mobility.<sup>81-84</sup> With a spin label (usually a TEMPO group) attached at specific sites of a polymer, local mobility studies afford detailed information at different positions of a single polymer molecule (chain end, middle of chain and chain junction); however, mobility was not directly correlated to free volume in a typical ESR experiment.<sup>81-82</sup> Bartos *et al.* showed qualitative correlation between ESR data (mobility) and PALS data (free volume).<sup>83-84</sup> Nevertheless, employing ESR as a direct technique to determine free volume requires further theoretical development.

## **2.5 Structure-property relationship affected by free volume**

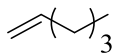
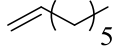
### **2.5.1 Application of free volume: general overview**

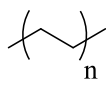
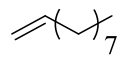
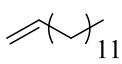
For most macromolecules, free volume is closely related to two important physical properties: segmental mobility and local void distribution. Segmental mobility directly determines the thermomechanical properties of polymeric materials, including the glass transition temperature. As a result, free volume theory provides an excellent approach to predict and control thermomechanical properties for both glassy<sup>2, 8, 31-32, 85-87</sup> and rubbery materials.<sup>7, 10, 35, 88-89</sup> The distribution of local voids, which is crucial for small-molecule diffusion in barrier applications, is dictated by free volume (both free volume size and distribution); thus, free volume theory widely contributes to gas barrier performance.<sup>12-13, 21, 23-24, 37, 43, 90-92</sup> Thus, free volume theory is widely employed in CO<sub>2</sub> gas separation, hydrogen purification, water desalination, etc. This review will focus on parameters related to free volume size and the number of free volume elements. Other free volume parameters, such as free volume element

shape as discussed by Dlubek and coworkers, are beyond the scope of this manuscript.<sup>4, 32</sup> Furthermore, model simulations also extend beyond the scope of this investigation and will not be addressed herein.

Thermomechanical properties of macromolecules relate to either thermal or mechanical relaxation, such as glass transition temperature ( $T_g$ ), melting temperature ( $T_m$ ), elastic storage modulus ( $E'$ ), elastic loss modulus ( $E''$ ) and so on. Therefore, as an indicator of any relaxation process, free volume enables rational explanation of most thermomechanical property changes. As an example of free volume's influence on thermomechanical properties, Dlubek and his coworkers reported that the incorporation of  $\alpha$ -olefin in polyethylene significantly increased free volume size and number of free volume elements, thereby reducing the  $T_g$ ,  $T_m$  and  $X_c$  (**Table 2.5.1-1**).<sup>93</sup> The side chains of  $\alpha$ -olefin served as a defect to interrupt compact polyethylene chain packing, which lead to an increase in free volume (both size and number) and promoted local segmental mobility, which thus lowered  $T_g$  and  $T_m$ .

**Table 2.5.1-1** Thermal properties and free volume parameters of poly(ethylene-co- $\alpha$ -olefin)<sup>93</sup>

Polymer backbone	Branching units	Branching conc. (mol%)	$T_g$ ( $^{\circ}\text{C}$ )	$T_m$ ( $^{\circ}\text{C}$ )	$X_c$ (%)	$v$ ( $\text{\AA}^3$ )	$N_f$ ( $10^{21}/\text{g}$ )
	N/A	0	-3.4	158	41	115.2	0.55
		10	-10	130	26	116.1	0.47
		20	-15	109	20	116.5	0.57
		1.5	-4	141	36	117.0	0.54
		3	-10	131	27	120.6	0.55
		6	-10	108	20	126.3	0.59
		10	-11	100	17	128.0	0.57

		11	-12	88	10	130.3	0.65
		2	-8	135	33	124.3	0.43
		4.5	-12	117	27	129.9	0.53
		8	-16	88	18	143.5	0.58
13		-21	60	9	153.6	0.61	
20		-27	49	3	165.7	0.66	
	6	-19	108	14	146.6	0.51	
	10	-25	83	10	160.0	0.55	
	15	-32	54	8	172.1	0.56	
	6	-24	106	16	155.9	0.49	
	10.5	-32	54, 79	11	165.3	0.51	

$T_g$ ,  $T_m$  and the crystallinity  $X_c$  were determined by DSC. Free volume size  $v$  and the number of free volume  $N_f$  was determined by PALS.

Both size and number of intermolecular voids are critical for permeation membranes, and small molecule diffusion usually correlates with free volume.<sup>94</sup> For a typical permeability study, there are two major factors: solubility and diffusivity. While some studies focus on diffusivity only, the importance of solubility (or sorption) should not be ignored. Fractional free volume dominantly determines permeability by controlling diffusivity, while free volume size and solubility both define the selectivity of polymeric membranes.<sup>28-29, 95-96</sup> Following Nagai *et al.*'s investigation of free volume and its correlation with solubility,<sup>97</sup> this review will focus more on diffusivity. Gas and water separation applications are the most studied topics in this area and will be our major discussion. For a comprehensive discussion on the physics of diffusion in polymeric matrix, see the review from Ramesh *et al.*'s.<sup>98</sup>

Polymeric gas separation membranes have attracted increasing attention, especially for CO<sub>2</sub> separation arising from the high demand to recycle CO<sub>2</sub> as a greenhouse gas.<sup>14</sup> Because of its high affinity for CO<sub>2</sub>, crosslinked poly(ethylene glycol) (PEG) is a common research platform.<sup>99</sup> Lin *et al.* described that higher free volume (lower crosslinking density) induced an increase of permeability for all four tested gas molecules regardless of the polymer backbone structures (**Figure 2.5.1-1**). By varying the crosslink density and copolymer composition, Lin and coworkers achieved different permeability and selectivity.

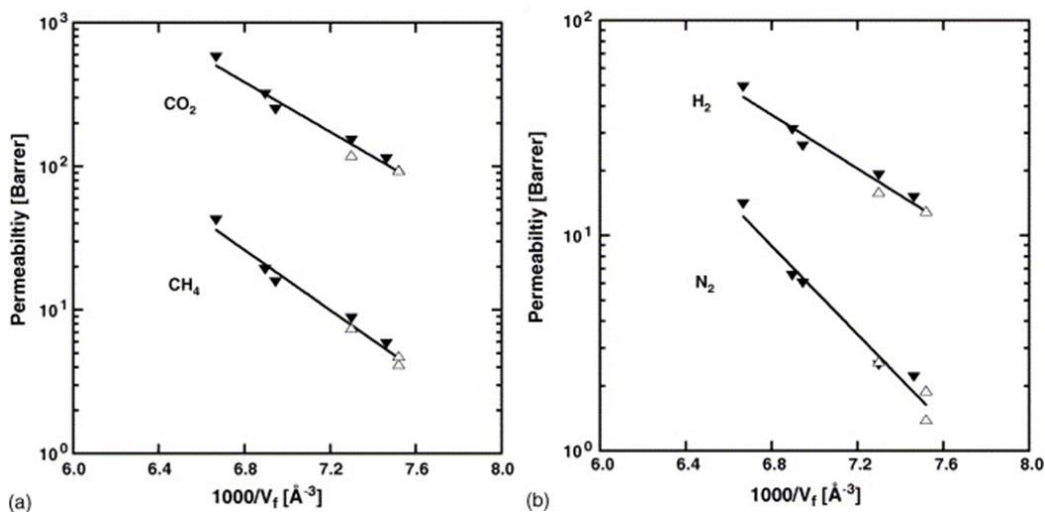


**Figure 2.5.1-1** Correlation between the mean size of free volume elements ( $V_f$ ) from PALS and (a) CO<sub>2</sub> and CH<sub>4</sub> permeability and (b) H<sub>2</sub> and N<sub>2</sub> permeability at infinite dilution and 35 °C in PEGDA/PEGMEA (▼) and PEGDA/PEGA (△) copolymers (Copyright 2006 Elsevier Ltd.).<sup>100</sup>

Water purification, especially desalination, represents a major focus of polymeric membrane applications.<sup>101-105</sup> As mentioned above, both diffusivity and solubility are important in regulating permeation behavior, especially when swelling has a significant influence on solubility during desalination. For example, in a sulfonated poly(arylene ether sulfone) random copolymer system, Xie *et al.* demonstrated that higher sulfonation samples led to lower free volume as a result of promoted intermolecular interaction.<sup>23</sup> Thus, reduced free volume depressed the diffusivity of both water and NaCl (**Figure 2.5.1-2**). As NaCl was the larger

penetrant, the decrease of free volume led to a more prominent decrease of its diffusivity than water, resulting in higher H<sub>2</sub>O/NaCl selectivity.

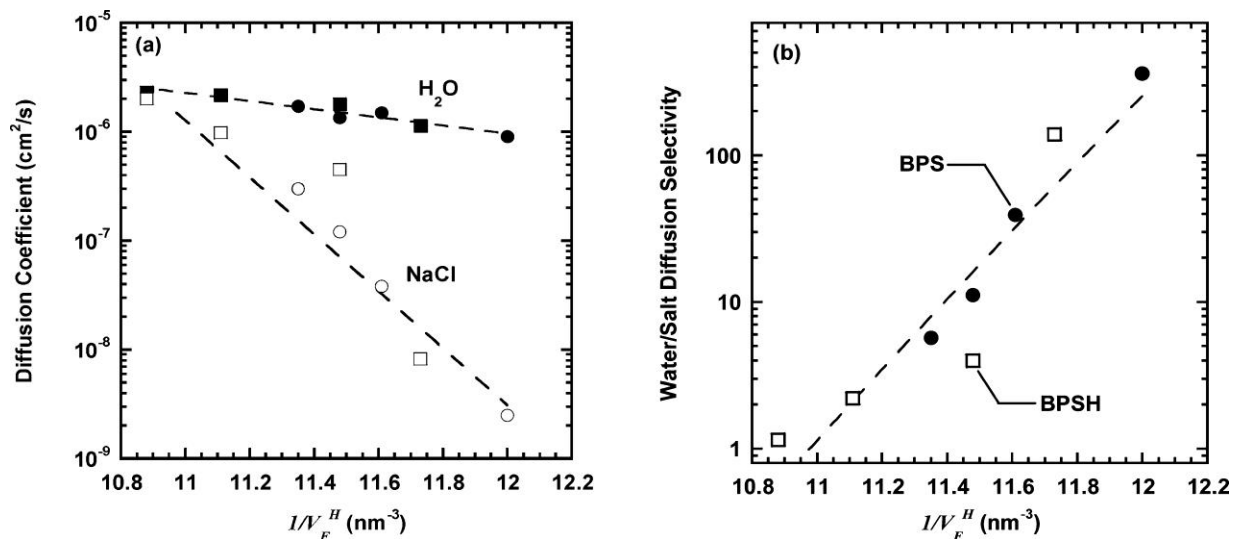


**Figure 2.5.1-2** Influence of free volume size from PALS measurements on: (a) water and NaCl diffusivity and (b) diffusivity selectivity,  $\alpha D$  in BPS (● and ○) and BPSH (■ and □) films. The dashed lines are provided to guide the eye (Copyright (2011) American Chemical Society).<sup>23</sup>

## 2.5.2 The variation in free volume with temperature and pressure

Prior to identifying structure-property relationships using free volume theory, it is critical to understand the inherent nature of free volume—the change of free volume with environmental factors, such as temperature and pressure. As a direct measurement of molecular kinetic energy, temperature steers the segmental mobility of polymers and thus plays a critical role in determining free volume.<sup>32, 106-107</sup> A similar argument applies to pressure.<sup>32, 90, 107-108</sup> Yet, as the variation of temperature is conventional and easier to regulate, pressure-driven free volume change is less studied.

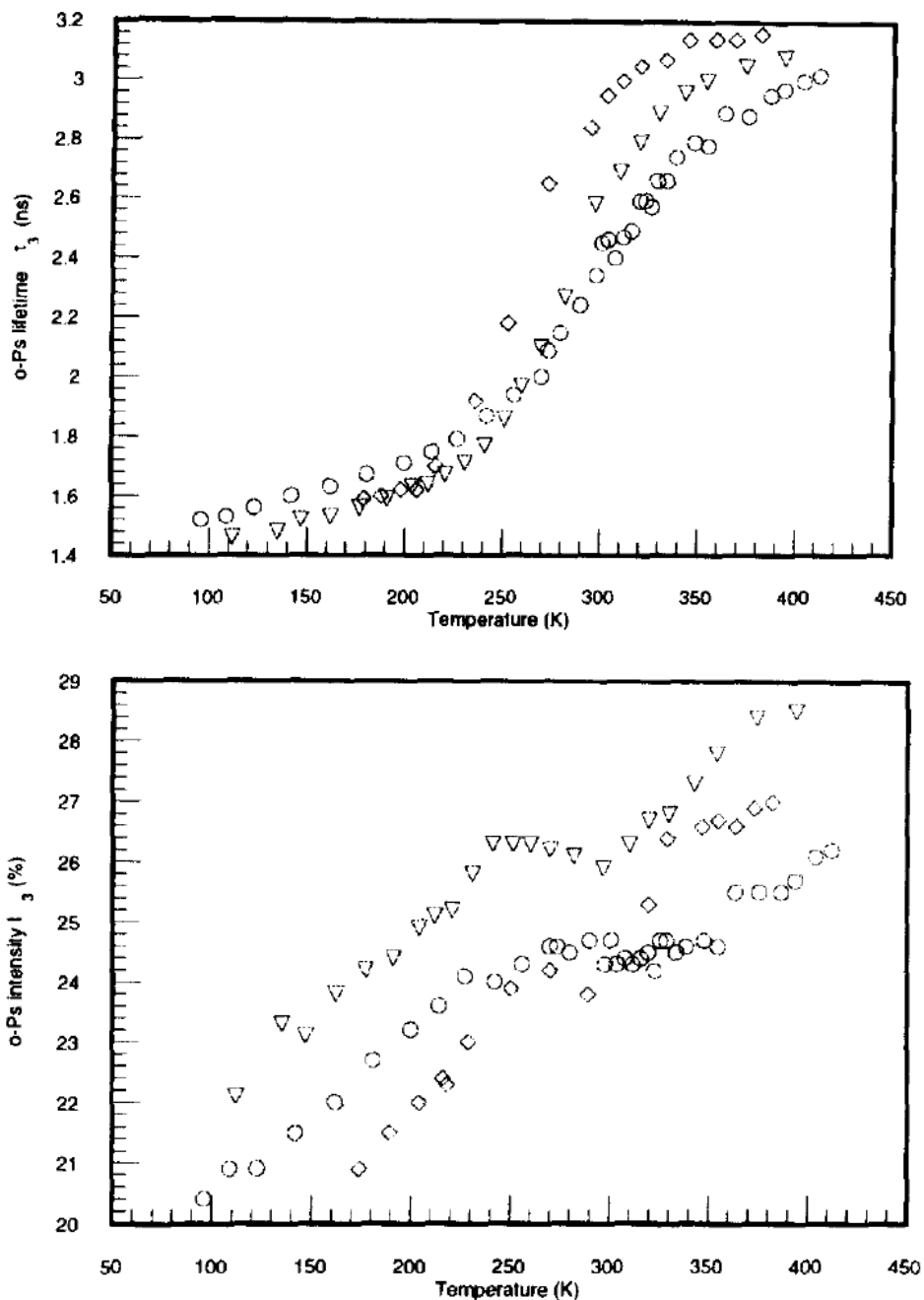


**Figure 2.5.2-1** o-Ps life time (ns) (top) and o-Ps intensity (bottom) for different polyurethanes as a function of temperature. Open circle: 400 kDa molecular weight; open triangle: 1200 kDa molecular weight; open square: 2000 kDa molecular weight (Copyright 1998 Elsevier Ltd.).<sup>106</sup>

Consolati *et al.* probed the impact of temperature on free volume using PALS, and investigated free volume distribution above and below  $T_g$  in different polyurethanes.<sup>106</sup> When the temperature is higher than  $T_g$ , free volume size increased significantly while the number of free

volume sites reached a plateau; below  $T_g$ , both free volume size and the number of free volume sites increased at elevated temperature (**Figure 2.5.2-1**). At high temperature, free volume favored a narrow size distribution, implying that the expansion of smaller free volume voids was the main factor for the increasing free volume.

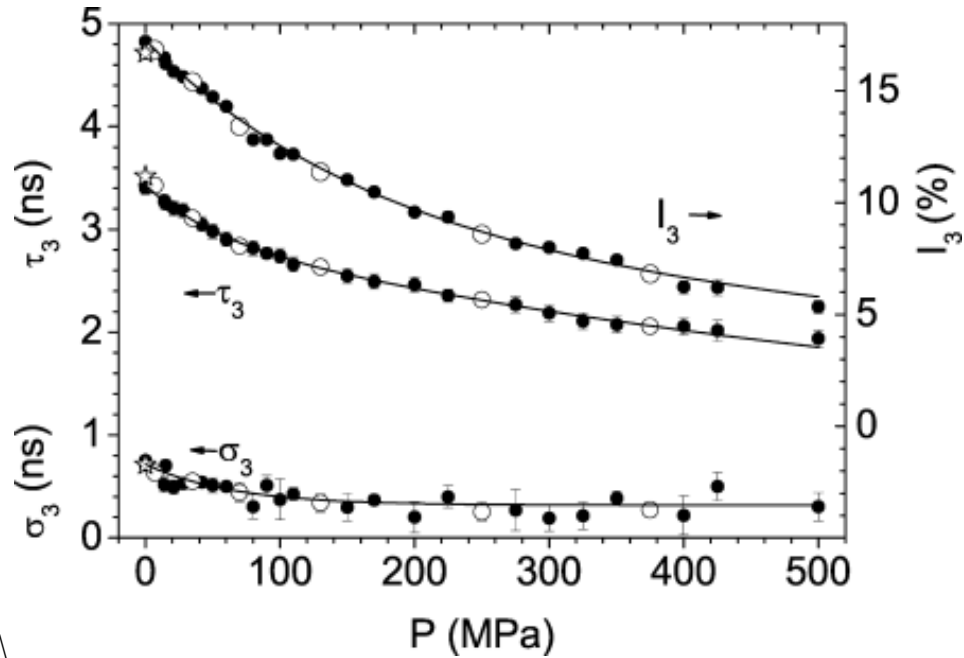


**Figure 2.5.2-2** Lifetime parameters of o-Ps annihilation in CYTOP at 298 K as a function of the pressure P: The mean lifetime  $\tau_3$ , the mean dispersion  $\sigma_3$  (standard deviation of the o-Ps lifetime distribution), and the relative intensity  $I_3$ . The filled symbols: 1.3–2.6 million counts, and the open symbols: 3.8–6.3 million counts. The stars show the lifetime parameters of the last measurement done after finishing the pressure run and decreasing the pressure to the ambient value. The lines are exponential fits of first ( $\sigma_3, I_3$ ) or second order ( $\tau_3$ ) (Copyright (2007) John Wiley and Sons).<sup>107</sup>

Researchers have also studied changes of free volume induced by varying pressure levels. Specifically, Dlubek *et al.* confirmed that in the case of an amorphous perfluorinated polymer,

both free volume size and the number of free volume decreased exponentially with increased pressure at room temperature (**Figure 2.5.2-2**).<sup>107</sup> It is also worth noting that the free volume size distribution decreased at high pressure, which may become beneficial in barrier applications as narrow free volume size distribution normally induces higher selectivity. Kilburn *et al.* reported similar conclusions when examining the pressure-volume-temperature relationships and their impact on free volume and mechanical relaxation.<sup>7, 108</sup>

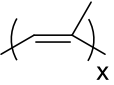
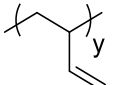
### 2.5.3 Effect of polymer structure on free volume

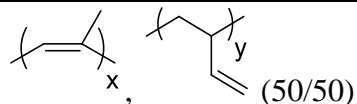
The chemical composition of a polymer backbone dictates polymer physical properties. Unlike other structural aspects discussed later in this review (such as branching and additives), polymer structure defines performance windows for specific properties. While branching, crosslinking, and additives facilitate fine-tuning of polymer physical properties, the initial fundamental property platform is based on polymer structure. This discussion on polymer chemical structure–free volume relationships will primarily focus on the free volume dependence of backbone packing, interaction between polymer chains, and the potential rearrangement of the polymer backbone.

The rigidity and bulkiness of the polymer backbone structure influences the efficiency of polymer chain packing. Inefficient packing generally introduces more free volume as voids residing between chains. Srithawatpong *et al.* compared the fractional free volume ( $V_f$ ) between high-vinyl, polybutadiene (HVBD) and *cis*-polyisoprene (CPI) using PALS (**Table 2.5.3-1**).<sup>89</sup> The authors observed higher fractional free volume (0.041) in HVBD than CPI (0.020), as the high vinyl content disrupted the polymer-chain packing. High fractional free volume of HVBD

also stimulated a significant increase of  $T_g$ . This experimental observation was initially confusing from a free volume point of view: higher free volume promotes local mobility and thus should lead to a reduction in  $T_g$ . An explanation for this phenomenon suggests a common competition mechanism between free volume and steric hindrance in steering  $T_g$ . High free volume from bulky functional groups has the tendency to decrease  $T_g$  through enhanced segmental mobility, while bulky functional groups also induce steric hindrance to local movement. The relationships between free volume and  $T_g$  highly depend on the net result of this competition. If overall mobility increases (free volume dominates) with increasing functional group concentration,  $T_g$  will demonstrate a negative relationship with free volume. However, if the overall mobility decreases (steric hindrance dominates),  $T_g$  will increase at high free volume values. The net result is highly dependent on the nature and concentration of the functional groups, and in the case of Srithawatpong's work, the steric hindrance from the vinyl pendant groups prevailed over free volume change in terms of determining  $T_g$ . More detailed discussion on this competition will be covered in the polymer branching section (3.5).

**Table 2.5.3-1** Glass transition temperature and fractional free volume of high-vinyl polybutadiene and cis-polyisoprene<sup>89</sup>

Polymer structure	$T_g$ (°C)	$V_f$
 (CPI)	-61	0.020
 (HVBD)	-23	0.041



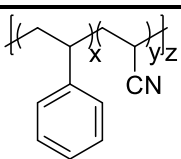
-54

0.024

$T_g$  and fractional free volume ( $V_f$ ) were determined by DSC and PALS, respectively.

Similarly, Dlubek *et al.* investigated the free volume change in poly(styrene-*co*-acrylonitrile) using PALS and concluded that incorporation of acrylonitrile content decreased free volume size while maintaining a constant number of free volume elements (**Table 2.5.3-2**).<sup>32</sup> Acrylonitrile units decreased free volume size as a result of smaller pendant group size compared to styrene units. Meanwhile, the smaller size of acrylonitrile units reduced steric hindrance in comparison to styrene units. In this case, both effects roughly compensated each other, leading to an insignificant  $T_g$  change.

**Table 2.5.3-2** Glass transition temperature and free volume parameters in poly(styrene-*co*-acrylonitrile)<sup>32</sup>

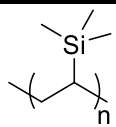
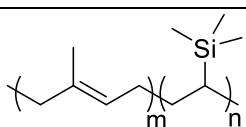
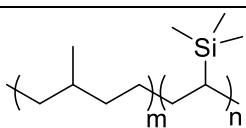
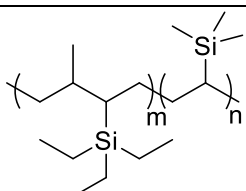
Polymer structure	Acrylonitrile content ( mol%)	$T_g$ (°C)	$v_f$ (Å <sup>3</sup> )	$N_f$ (10 <sup>21</sup> /g)
	0	104	121.0	0.53
	22.1	104	112.7	0.58
	38.4	110	107.7	0.56
	50.6	108	102.1	0.56

$T_g$  was determined by DSC. Free volume size ( $v_f$ ) and number of free volume elements ( $N_f$ ) were calculated through PALS.

Filiz *et al.* observed a similar trend in polyisoprene-*block*-poly(vinyl trimethylsilane) (PI-*b*-PVTMS).<sup>109</sup> Higher polyisoprene content led to a decrease in fractional free volume and thus a reduction in gas permeability (Table 2.5.3-3). Both hydrosilylation and hydrogenation of the polyisoprene block improved gas permeability through introducing more fractional free volume. When comparing hydrosilylation and hydrogenation, hydrosilylated block copolymers achieved

higher fractional free volume due to the bulky triethylsilyl groups. As a result, the hydrosilylated block copolymers exhibited the highest gas permeability. However, the hydrosilylated block copolymers exhibited a reduction in CO<sub>2</sub> gas permeability (155 barrer compared to 164 barrer) relative to PVTMS homopolymer. The authors ascribed the decrease in free volume and gas permeability to the longer ethyl groups in the hydrosilylated block copolymers comparing to the shorter methyl substituents in PVTMS homopolymer.

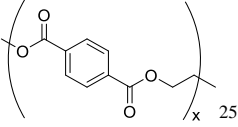
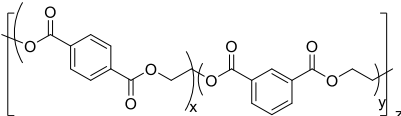
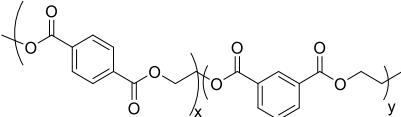
**Table 2.5.3-3** Fractional free volume and CO<sub>2</sub> permeability in poly(isoprene-*b*-vinyl trimethylsilane)<sup>109</sup>

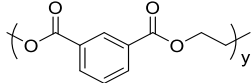
Polymer structure	PI content (%)	V <sub>f</sub> (%)	P (CO <sub>2</sub> ) (Barrer)
	0	21.1	164
	10	20.1	126
	13	19.7	114
	30	18.1	57
	10	20.8	139
	13	20.6	133
	30	19.4	120
	10	21.1	155
	13	21.0	149
	30	19.9	130

Fractional free volume (V<sub>f</sub>) was determined by density study and Bondi's contribution theory.

In more rigid polymers, Liu *et. al* studied the effect of backbone geometry on free volume and its influence on  $T_g$  and permeability behavior.<sup>25</sup> According to PALS, poly(ethylene terephthalate) (PET) exhibited larger free volume size ( $r$  in **Table 2.5.3-4**) than poly(ethylene isophthalate) (PEI). Kinked PEI repeating units served as defect in chain packing to decrease both  $T_m$  and  $T_g$  in PET-*co*-PEI random copolymers. However, in PET-*b*-PEI block copolymers,  $T_g$  decreased with increasing PEI content while  $T_m$  remained unchanged due to their blocky nature. At similar PEI content level, no significant difference in free volume and  $T_g$  appeared between random copolymers and block copolymers. PEI is well known for its better oxygen barrier property than PET. The incorporation of PEI in PET, in both random copolymers and block copolymers, exhibited a decrease in permeability ( $P$ ) as a result of decreased free volume size as expected (**Table 2.5.3-4**). PEI simultaneously depressed  $T_m$  and improved gas barrier properties (as a result of decreased free volume), making it a promising candidate in gas barrier applications. In contrast, most polymeric materials sacrifice flexibility to gain better barrier properties.

**Table 2.5.3-4** Glass transition temperature and free volume parameter between polyethylene terephthalate (PET) and polyethylene isophthalate (PEI)<sup>25</sup>

Polymer structure	PEI content (mol %)	$T_g$ (°C)	$T_m$ (°C)	$r$ (Å)	$P$ (cc cm m <sup>-2</sup> day <sup>-1</sup> atm <sup>-1</sup> )
	0	76	246	2.56	0.424
	10	72	233	2.52	0.371
	20	68	205	2.49	0.294
	30	66	-	2.48	0.249
	10	72	245	2.51	0.328
	20	69	243	2.48	0.278
	30	65	240	2.46	0.239

	100	55	-	2.41	0.090
---	-----	----	---	------	-------

$T_g$  was determined by DSC. The difference in specific volume relative to PET ( $\Delta v$ ) was determined through PALS.

Interaction between polymer chains largely dictates packing through physically varying the distance between neighboring chains. This change in distance proves to have a profound influence on fractional free volume. Xie and coworkers investigated the free volume in disulfonated poly(arylene ether sulfone) random copolymers.<sup>23</sup> The researchers observed competing mechanisms in free volume changes when they varied the degree of sulfonation in their dry film samples (water uptake was negligible). Owing to high polarity of the ions, polymers with a higher degree of sulfonated groups exhibited enhanced intermolecular interaction, resulting in lower fractional free volume. At the same time, bulky sulfonates interrupted efficient chain packing, leading to an increase in free volume. These two factors largely canceled in the salt form (BPS, potassium salt), but the polarity effect prevailed in the acid form (BPSH) (**Table 2.5.3-5**). Hence, with an increasing concentration of disulfonated monomer, free volume size ( $\tau_3$ ) decreased in BPSH but remained relatively unchanged in BPS. BPS exhibited an average larger free volume size than BPSH from PALS because BPS had a bulkier counter ion than its acid analog. Conversely, hydrated polymer films exhibited different properties in comparison to dry films as water uptake participated in determining free volume and became a dominant factor. As a result, free volume size increased at elevated concentrations of disulfonated monomer in both hydrated BPS and BPSH films. The number of free volume elements decreased in the hydrated film, however, the inhibition of o-Ps (the signal that PALS utilized to calculate free volume parameters) might play a significant role.

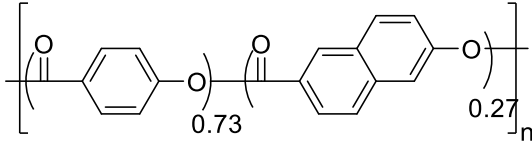
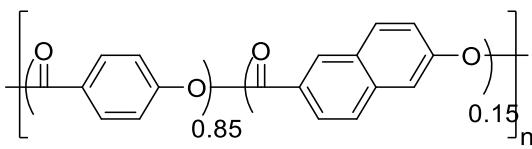
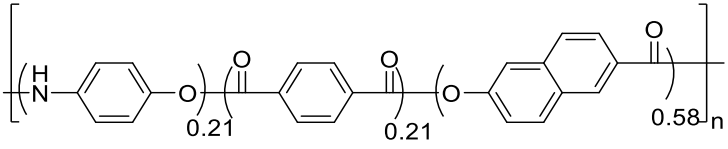
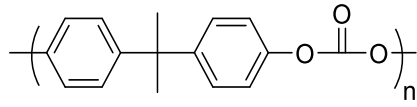
**Table 2.5.3-5** Free volume parameters and water diffusivity of disulfonated poly(arylene ether sulfone) random copolymers<sup>23</sup>

Polymer structure				
Counter ion	Disulfonated monomer (%)	$\tau_3$ (ns)	$I_3$ (%)	Water diffusivity ( $10^{-6}$ cm <sup>2</sup> /s)
M = Na BPS	20	1.853 ± 0.013	19.9 ± 0.4	0.90
	30	1.881 ± 0.016	16.4 ± 0.2	1.4
	35	1.889 ± 0.020	16.3 ± 0.3	1.3
	40	1.899 ± 0.014	15.2 ± 0.2	1.7
M = H BPSH	20	1.871 ± 0.021	19.5 ± 0.3	1.1
	30	1.895 ± 0.014	17.6 ± 0.2	1.8
	35	1.924 ± 0.024	16.8 ± 0.6	2.1
	40	1.939 ± 0.021	16.7 ± 0.3	2.3

Free volume parameters were determined by PALS.

Hsieh and coworkers conducted a thorough study of the structure-free volume-physical properties relationship for thermotropic liquid crystalline polymers (TLCs).<sup>86</sup> Entry 1 in **Table 2.5.3-6** exhibited a larger free volume size compared to Entry 2, suggesting that a kinked structure along the polymer backbone introduced more free volume as a result of packing interference. The amide linkage in Entry 3 demonstrated the potential of hydrogen bonding to reduce free volume due to efficient and ordered packing of polymer chains. All TLCs in this study presented a smaller free volume size than a PC control, indicating the rigid nature of TLCs favored a decline in free volume size. No general trend was observed between  $T_g$  and free volume in this work.

**Table 2.5.3-6** Glass transition temperature and free volume size of thermotropic liquid crystalline polymers<sup>86</sup>

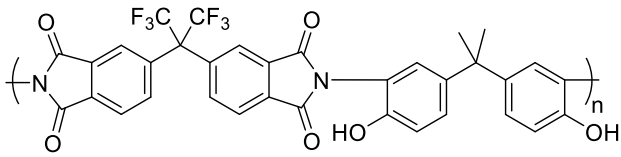
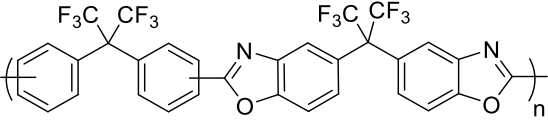
Thermotropic liquid crystalline polymers	T <sub>g</sub> (°C)	v <sub>f</sub> (Å)
 <p>Entry 1</p>	100	37.97 ± 2.14
 <p>Entry 2</p>	99	34.47 ± 4.07
 <p>Entry 3</p>	146	31.01 ± 26.89
 <p>PC</p>	154	99.52 ± 1.7

T<sub>g</sub> and free volume size were determined by DSC and PALS, respectively.

Another interesting approach to alter polymer free volume is thermal rearrangement of the polymer backbone. Park *et al.* employed PALS to determine free volume changes in hydroxyl-containing polyimide (HPI) and its thermally rearranged polybenzoxazoles (TR-PBO).<sup>110</sup> **Table 2.5.3-7** showed that fractional free volume increased from 0.19 to 0.28 after thermal rearrangement based on Bondi's group contribution theory. The increased free volume was presumably due to the disappearance of the hydroxyl group. Without hydroxyl groups in TR-PBO, hydrogen bonding was severely depressed, causing less dense chain packing comparing to HPI. As a result, TR-PBO showed higher permeability than HPI due to its larger

free volume size and/or connected free volume elements. Freeman *et al.* also studied thermally rearranged polymers using PALS and concluded that the higher selectivity of thermally rearranged polymers suggested a favorable free volume distribution.<sup>27</sup>

**Table 2.5.3-7** Fractional free volume and CO<sub>2</sub> permeability before and after thermal rearrangement<sup>110</sup>

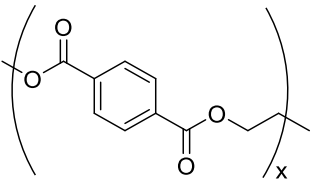
Polymer structure	V <sub>f</sub> (simulated)	V <sub>f</sub> (calculated)	CO <sub>2</sub> Permeability (barrer)
 <p style="text-align: center;">HPI</p>	0.214	0.19	12.2
 <p style="text-align: center;">TR-PBO</p>	0.252	0.28	29.0

Fractional free volume was calculated through simulation and Bondi's group contribution theory.

External forces have the capacity to align polymer backbones. In general, oriented polymer backbones enable efficient packing and thus reduced free volume. Liu *et al.* studied the free volume changes and the consequent oxygen permeability when orienting PET films at various temperature.<sup>25</sup> Comparing to non-oriented films, films oriented at T<sub>g</sub> as well as 15 °C below T<sub>g</sub> exhibited a decrease in free volume, leading to a decrease in oxygen permeability (**Table 2.5.3-8**). The authors ascribed chain orientation below T<sub>g</sub> and amorphous phase orientation at T<sub>g</sub> to the decrease in free volume. In contrast, when orienting PET films at

temperatures higher than  $T_g$  (15 and 30 °C above  $T_g$ ), strain-induced and thermal crystallization occurred and increased free volume. As a result, no oxygen permeability change appeared after orientation at 30 °C above  $T_g$ . Valic *et al.* chose PALS to compare free volume changes with uniaxial deformation of linear low-density polyethylene film (LLDPE) in two different directions.<sup>91</sup> Both parallel and perpendicular deformation appeared to have little influence on free volume size (slightly increased for parallel deformation and almost constant for perpendicular deformation). However, the force-induced close packing from both parallel and perpendicular deformation led to a decrease of the number of free volume. As a result, fractional free volume decreased with deformation, thus, gas permeability decreased. In this case, the direction of deformation seemed to have no effect on free volume behavior.

**Table 2.5.3-8** Free volume and permeability parameters of oriented PET films<sup>25</sup>

Polymer structure	$T_{\text{draw}}$ (°C)	$V_f$ (cm <sup>3</sup> /g)	P (cc cm m <sup>-2</sup> day <sup>-1</sup> atm <sup>-1</sup> )
	-	0.026	0.424
	$T_g - 15$	0.017	0.203
	$T_g$	0.024	0.205
	$T_g + 15$	0.030	0.211
	$T_g + 30$	0.034	0.401

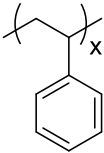
$T_{\text{draw}}$ : orientation temperature

#### 2.5.4 Effect of molecular weight and molecular weight distribution on free volume

Molecular weight is often referred as the “size of a molecule” and used interchangeably with molar mass in polymer synthesis and characterization.<sup>111</sup> Both molecular weight and its distribution dictate polymer physical properties through chain entanglement and chain end concentration. As a rational deduction, higher molecular weight reduces fractional free volume by providing more chain entanglement and reducing chain end concentration. Chain

entanglement leads to compact packing and decreases free volume.<sup>112</sup> Polymer chain ends generally provide more free volume than backbone and are prone to packing imperfection.<sup>112</sup> However, at a high enough molecular weight, fractional free volume becomes an increasing function of molecular weight.

**Table 2.5.4-1** Molecular weight, free volume size and spin-spin relaxation time of polystyrene<sup>113</sup>

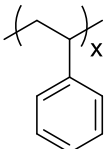
Polymer structure	$M_n$	$M_w$	$\tau_2$
	(kg/mol)	(kg/mol)	(ns)
	0.104	0.104	2.42
	0.545	0.600	2.23
	0.550	0.970	1.96
	1.95	2.1	1.94
	3.27	3.6	1.95
	4.60	5.00	1.86
	9.70	10.3	1.87
	19.6	19.8	1.91
	49.0	51.0	1.90
	96.2	98.2	1.89
	164	173	1.82
	392	411	1.90
	773	867	1.90
	1780	2145	1.94

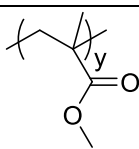
Molecular weight data was determined by SEC as relative molecular weight. Free volume parameter ( $\tau_2$ ) and spin-spin relaxation time ( $T_2$ ) were determined by PALS and NMR, respectively.

West *et al.* studied free volume's dependence on molecular weight over a wide molar mass range.<sup>113</sup> For polystyrene, the free volume size ( $\tau_2$ ) from PALS decreased with increasing molecular weight as expected (**Table 2.5.4-1**). However, the free volume size started to increase again at above 200 kg/mol molecular weight. The authors mentioned the possible influence of fast motion that is normally out of the detection range of PALS.

He and coworkers explored the high molecular weight region of polystyrene (PS) and poly(methyl methacrylate) (PMMA) and observed similar free volume increase with increasing molecular weight.<sup>112</sup> In PS, the free volume size ( $\tau_3$ ) remained relatively constant with molecular weight, while the number of free volume elements ( $I_3$ ) surged from 26.1 % to 30.0 % (**Table 2.5.4-2**). Similarly, in the case of PMMA, the free volume size stayed at a constant value, and the number of free elements increased. Nevertheless, the variation of the number of free volume elements in PMMA was not as significant as in PS. The authors attributed the unorthodox free volume increase to the retardation of fast local motion that was normally undetectable for PALS. At high molecular weight, the chain end concentration was negligible, hence the free volume drop led by the decreasing chain-end concentration was trivial. Meanwhile, high molecular weight slowed down local motions that otherwise were too fast for PALS to detect. Eventually, PALS reveals some of the originally undetectable voids and results in an apparent “increase” of free volume.

**Table 2.5.4-2** Molecular weight and free volume parameter of polystyrene and poly(methyl methacrylate)<sup>112</sup>

Polymer structure	$M_n$ (kg/mol)	$\tau_3$ (ns)	$I_3$ (%)
	140	2.030	26.1
	190	2.039	27.9

	500	2.093	30.0
	980	1.879	20.4
	1470	1.895	20.0
	2020	1.885	21.1

Free volume parameters were determined by PALS.

Suvegh *et al.* specifically addressed the importance of molecular weight distribution in determining free volume.<sup>114</sup> At similar molecular weight, polydisperse poly(methyl methacrylate) (PMMA) always exhibited larger free volume size (o-Ps lifetime) (**Figure 2.5.4-1**). The free volume size in monodisperse PMMA demonstrated little dependence on molecular weight. But in polydisperse PMMA, the free volume size clearly increased before reaching a plateau at high molecular weight.

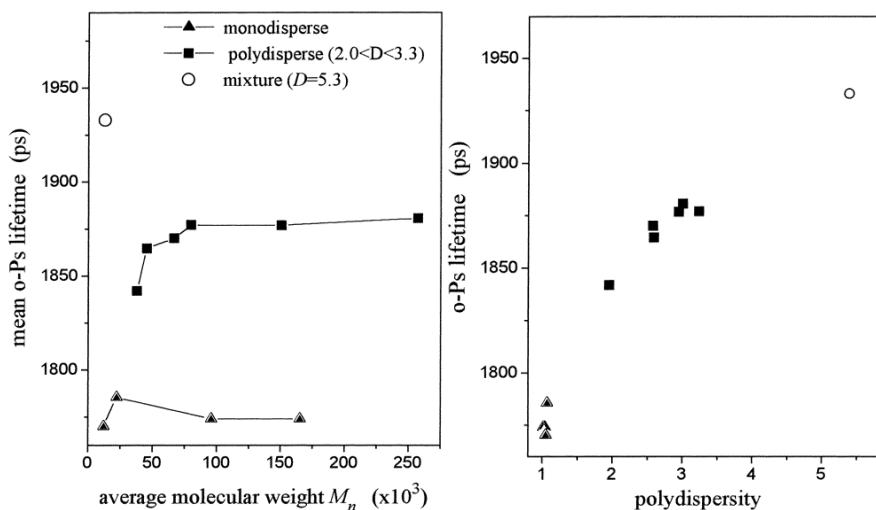


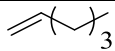
**Figure 2.5.4-1** Free volume size (o-Ps lifetime) as a function of molecular weight (left) and polydispersity (right) in poly(methyl methacrylate) (Copyright (1999) American Chemical Society).<sup>114</sup>

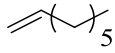
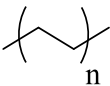
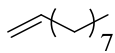
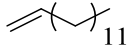
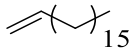
### 2.5.5 Effect of pendant groups and branching on free volume

Branched polymers are often defined as macromolecules with more than two chain ends per chain.<sup>111</sup> Controlled branching is a common strategy to alter polymer physical properties. The branching density, the length of branches, and branching chemical structures determine the physical properties of branched polymers via free volume control. The branching density has a profound influence on free volume, as the addition of extra chain ends from branching, in general, increases the free volume. Longer branch length tends to increase the free volume, thereby greatly influences polymer thermomechanical and barrier properties.<sup>115</sup> Different functional pendant groups provide additional interactions, such as hydrogen bonding, steric hindrance and ionic interactions, which also exhibit various influence on free volume.

Dlubeck *et al.*'s study on polyethylene (PE) represents a typical relationship between free volume and polymer branching (Table 2.5.5-1).<sup>93</sup> The  $\alpha$ -olefin introduced defects to interrupt compact poly(ethylene) chain packing, leading to a decrease in the  $T_g$ ,  $T_m$  and  $X_c$  compared to the linear analog. In conjunction, a subsequent increase in free volume size ( $V_f$ ) and the number of free volume elements ( $N_f$ ) was observed. For example, the introduction of 1-octene increased the free volume size from 124.3 Å<sup>3</sup> (2 mol% branching) to 165.7 Å<sup>3</sup> (20 mol% branching), and the corresponding free volume concentration increased from  $0.43 \times 10^{21}/g$  to  $0.66 \times 10^{21}/g$ .

**Table 2.5.5-1** Thermal properties and free volume results of poly(ethylene-co- $\alpha$ -olefin)<sup>93</sup>

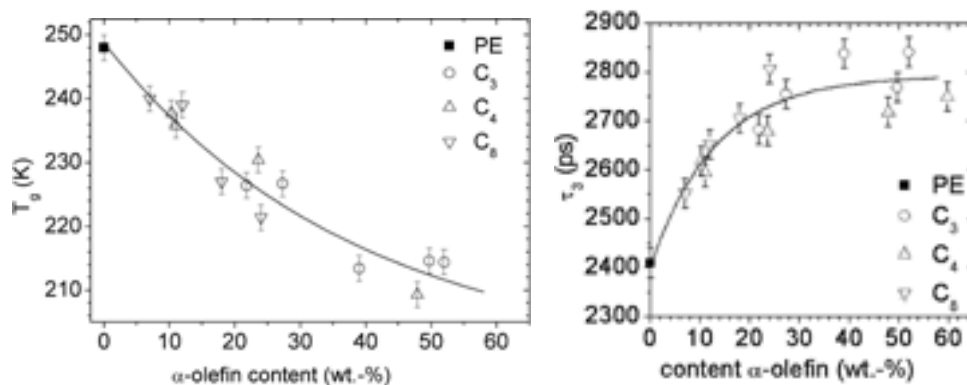
Polymer backbone	Branching units	Branching conc. (mol%)	$T_g$ (°C)	$T_m$ (°C)	$X_c$ (%)	$V_f$ (Å <sup>3</sup> )	$N_f$ (10 <sup>21</sup> /g)
	N/A	0	-3.4	158	41	115.2	0.55
		10	-10	130	26	116.1	0.47

		20	-15	109	20	116.5	0.57
		1.5	-4	141	36	117.0	0.54
		3	-10	131	27	120.6	0.55
		6	-10	108	20	126.3	0.59
		10	-11	100	17	128.0	0.57
		11	-12	88	10	130.3	0.65
		2	-8	135	33	124.3	0.43
		4.5	-12	117	27	129.9	0.53
		8	-16	88	18	143.5	0.58
		13	-21	60	9	153.6	0.61
		20	-27	49	3	165.7	0.66
		6	-19	108	14	146.6	0.51
		10	-25	83	10	160.0	0.55
		15	-32	54	8	172.1	0.56
		6	-24	106	16	155.9	0.49
		10.5	-32	54, 79	11	165.3	0.51

$T_g$ ,  $T_m$  and the crystallinity  $X_c$  were determined by DSC. Free volume size  $V_f$  and the number of free volume  $N_f$  was determined by PALS.

For PE with uniform branch length, the free volume size increased as the branching density increased, resulting in decreased  $T_g$  (**Table 2.5.5-1**). At a similar incorporation levels (10 mol%), longer alkyl pendant groups lowered  $T_g$  further, ranging from -10 °C (1-butene) to -32 °C (1-hexadecene), as a result of increasing free volume. This systematic study represents a

typical structure-free volume-property relationship: at a similar branching level, longer branches tend to lower  $T_g$  more through the introduction of more free volume.

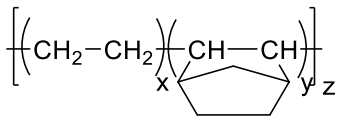


**Figure 2.5.5-1**  $T_g$  (a) determined from DSC and o-Ps lifetime  $\tau_3$  (b) determined from PALS against  $\alpha$ -olefin content (wt%) for ethylene copolymers containing: 1-propene (C3), 1-butene (C4) and 1-octene (C8). Solid lines are least-squares exponential fit (Copyright (2006) John Wiley and Sons).<sup>5</sup>

Dlubeck *et al.* revealed another general relationship between branching density and free volume in *n*-alkyl branched PE using PALS.<sup>5, 85</sup> In the low-branching (< 20%) content materials,  $T_g$  decreased linearly as branching increased, while the change of  $T_g$  diminished at high branching density (**Figure 2.5.5-1a**). The authors attributed the decrease of  $T_g$  to higher segmental mobility through plasticization of branches. Branching led to higher free volume ( $\tau_3$ ) and thus resulted in higher segmental mobility (**Figure 2.5.5-1b**). In the case of high branch content (> 20%),  $T_g$  plateaued due to the appearance of diads (two adjacent *n*-alkyl units), which enabled highly efficient packing and mitigated the increase in segmental mobility and free volume.<sup>85</sup> As a general relationship between branching density and free volume, free volume increases rapidly first as branching density increases; but, when the branching density is high enough (i.e. when diads of the branching repeating units are not negligible any more), the free

volume plateaus. Mader *et al.* confirmed this relationship,<sup>116</sup> proving that with the increasing degree of branching,  $T_g$  decreased rapidly first at low branching level before it plateaued at higher branching density. Furthermore,  $T_g$  even began to increase at very high branching density (80% to 100%).

**Table 2.5.5-2** Thermomechanical properties and fractional free volume of poly(ethylene-*co*-norbornene) copolymers<sup>33</sup>

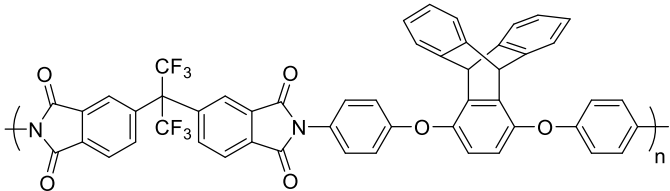
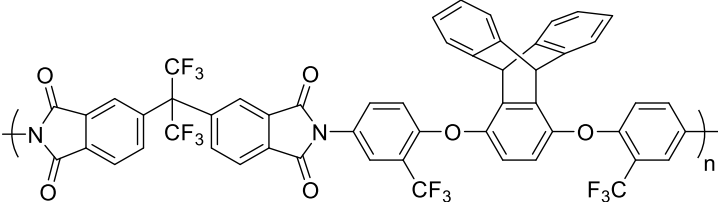
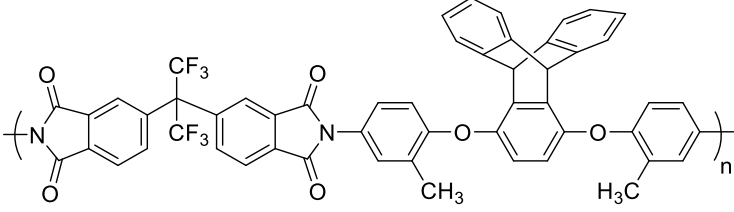
Polymer	Norbornene content (mol%)	$T_g$ (°C)	$V_f$ (%)	Young's modulus (GPa)
	40	81	6.2	1.94
	52	137	11.3	2.06
	54	154	11.9	2.15
	66	173	12.9	2.20

$T_g$ , Young's modulus and fractional free volume ( $V_f$ ) were determined by DSC, Instron 5544 and PALS respectively.

The two general trends discussed above work best for linear branches. However, the introduction of bulky branches introduces a steric hindrance factor that usually competes with free volume. Hu *et al.* studied the influence of cyclic olefin branching on free volume using PALS.<sup>33</sup> The introduction of bulky norbornene groups led to significant free volume ( $V_f$ ) change as expected (**Table 2.5.5-2**). Fractional free volume doubled (from 6.2% to 12.9%) at 66 mol% incorporation of norbornene in comparison to 40 mol% incorporation. However,  $T_g$  also increased with higher branching content due to the interference of bulky pendant groups on segmental motion. In this case, the hindrance of segmental motion from bulky cyclic pendant groups surpassed the effect of free volume increase, thus higher fractional free volume failed to

lower the  $T_g$ . This behavior is interesting, as high permeation behavior (high free volume) with a good thermal property (high  $T_g$ ) coexist in the same matrices. Such properties are critical and ideal for barrier applications. As shown by the authors, polymers with higher norbornene content exhibited a higher permeability coefficient with improved mechanical properties.

**Table 2.5.5-3** Fractional free volume and gas permeability of triptycene-based polyimides<sup>26</sup>

Polymer	$V_f$ (%)	CO <sub>2</sub> permeability (Barrer)
	15.6	14.4
	18.3	19.7
	15.1	9.0

Fractional free volume ( $V_f$ ) was determined by density study. CO<sub>2</sub> permeability was measured at 35 °C and 130 psig.

Similarly, aromatic branches and pendant groups have a more significant influence on free volume due to their inherent rigidity. Wiegand *et al.* characterized triptycene-based polyimides to elucidate the free volume effect on gas separation.<sup>26</sup> Using density studies coupled with Bondi's theory, the calculated fractional free volume ( $V_f$ ) increased with the introduction of

bulky triptycene in the backbones (**Table 2.5.5-3**). The addition of bulky  $-\text{CF}_3$  substituents further increased the free volume from 15.6 % to 18.3 % by disrupting chain packing. In contrast, smaller  $-\text{CH}_3$  groups reduced the free volume to 15.1 %. The authors postulated that the small methyl groups resided partially in the free volume void provided by the bulky triptycene groups and thus led to a decrease in free volume. As expected, gas permeability increased with increasing fractional free volume. The  $T_g$ s of these polyimides (ranging from 280 to 300 °C) demonstrated no general correlation with free volume in this case, as both the molecular weight and molecular weight distribution were not controlled.

Despite the two general relationships between free volume and polymer branches or pendant groups, the direct relationship between glass transition temperature and free volume is a case-by-case study. Branches, in general, act as plasticizers to introduce more free volume and thus lower  $T_g$ .<sup>5, 8, 10, 86</sup> However, researchers have argued that pendant groups with secondary interactions lead to a decrease in free volume and result in a higher  $T_g$ .<sup>86</sup> Also, for bulky branches, both free volume and  $T_g$  increase with increased branching content.<sup>33</sup> In this case, branches and pendant groups increase free volume, but the additional entanglement from the bulky pendant groups overcome the free volume effect, leading to a decrease in segmental mobility. This competition between free volume and local steric hindrance is the key to understanding and designing polymers. If the disruption of close chain-packing dominates over the effect of constraint on segmental motion (e.g., linear alkyl pendant group),  $T_g$  will decrease as a result of increasing free volume. In a reversed situation, local mobility will decrease and result in higher  $T_g$  despite increasing free volume. In special cases when the branching density is too high<sup>5</sup> or the pendant groups promote inter-molecular interactions<sup>86</sup>, the free volume tends to plateau or even decrease with increasing branching contents. In conclusion, careful consideration

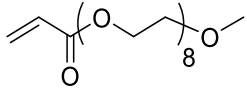
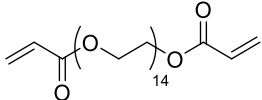
must be given to the competition between increased free volume and elevated entanglement from branching when interpreting and designing polymers.

### 2.5.6 Effect of crosslinking on free volume

Covalently crosslinked polymers refer to materials where covalent bonds connect multiple chains, and a functionality of a crosslinking agent exceeds 2.0.<sup>111</sup> Crosslinking is a common strategy to improve mechanical and chemical stability of polymers through covalently or non-covalently linking individual polymer chains.<sup>10, 15, 35, 117-118</sup> As a trade-off for the improved stability, the polymer chain mobility is often restricted, making free volume especially critical in determining polymer physical properties. While increasing crosslinking density facilitates mechanical integrity, it significantly reduces free volume as a result. During transport process, this inherent paradox between mechanical integrity and high free volume (for permeation) is detrimental. However, variation on the crosslinking agent or pendant groups elucidate potential resolution for this problem. Pendant group effects include steric hindrance effect, inherent free volume increase by bulky groups, intra- and inter-chain secondary interactions, and polymer backbone rigidity. As a result, even though a few general trends of free volume change in crosslinking matrix stand, the rational design and interpretation of crosslinking materials based on free volume becomes complicated.

**Table 2.5.6-1** Thermal properties and free volume parameter for PEG based crosslinking system<sup>100</sup>

Monomer structure	Crosslinker	Crosslinker density (wt%)	T <sub>g</sub> (°C)	τ <sub>3</sub> (ns)	I <sub>3</sub> (%)
		1.3	-65	2.54	22.0
		30	-57	2.59	21.6

 (PEGMEA)	50	-52	2.48	21.6
	80	-44	2.41	21.0
	100	-40	2.38	22.2
 (PEGA)	0	-45	2.41	20.6
	30	-44	2.37	20.6
	50	-42	2.37	21.3
	100	-40	2.38	22.2

$T_g$  and  $\tau_3$  were determined by DSC and PALS, respectively.

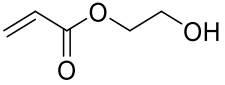
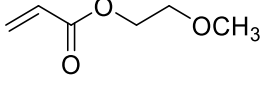
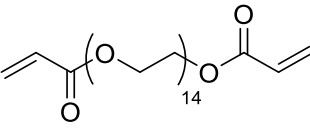
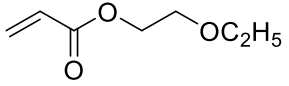
In general, higher crosslinking density leads to lower free volume. But free volume size and the number of free volume have different dependence on crosslinking density. Lin *et al.* conducted a series of gas permeability studies based on free volume theory in poly(ethylene glycol diacrylate) based crosslinked matrices (**Table 2.5.6-1**).<sup>100</sup> Different copolymers PEGDA/PEGMEA and PEGDA/PEGA shows different free volume changes as a function of crosslinking density and pendant groups. In PEGDA/PEGMEA, free volume size ( $\tau_3$ ) increased with increasing PEGMEA (-OCH<sub>3</sub> terminated) component, while in PEGDA/PEGA, variation in the PEGA (-OH terminated) component had little effect on free volume radius. This indicated that -OCH<sub>3</sub> terminated pendant groups (from PEDMEA) increased free volume size more prominently than -OH terminated pendant groups. While both PEGMEA and PEGA introduce more free volume to the materials, the -OH terminated PEGA has the extra potential of hydrogen bonding. As a result, the hydrogen bonding in PEGA bridged polymer chains closer to each other and mitigated the increase in free volume. Accordingly,  $T_g$  increased with decreasing free volume size in PEGDA/PEGMEA crosslinking matrices and remained relatively unchanged in PEGDA/PEGA due to constant free volume size. The permeability of the investigated gases (CO<sub>2</sub>, CH<sub>4</sub>, H<sub>2</sub> and N<sub>2</sub>) demonstrated strong linear relationship with  $1/V_f$  (fractional free

volume), as expected. Free volume also affected selectivity: CO<sub>2</sub>/N<sub>2</sub> and CO<sub>2</sub>/CH<sub>4</sub> selectivity deteriorated with increasing fractional free volume while CO<sub>2</sub>/H<sub>2</sub> selectivity improved with increasing fractional free volume. Since CO<sub>2</sub> has a smaller diameter than N<sub>2</sub> and CH<sub>4</sub>, but a larger diameter than H<sub>2</sub>, the experimental selectivity results corresponded well with theory.

Kusuma *et al.* investigated the influence of crosslinking density on free volume and gas permeability in similar crosslinked matrices (**Table 2.5.6-2**).<sup>15</sup> Three different monomers, 2-hydroxyethyl acrylate (2-HEA), ethylene glycol methyl ether acrylate (EGMEA), and 2-ethoxyl acrylate (2-EEA) with different pendant groups (hydroxyl, methoxy, and ethoxy group, respectively) exhibited different thermal and barrier properties in PEGDA crosslinked matrix.<sup>15</sup> With increasing crosslink density, PEGDA/EGMEA and PEGDA/2-EEA exhibited a decrease in fractional free volume ( $V_f$ ) while PEGDA/2-HEA demonstrated an opposite trend. The methoxy (EGMEA) and ethoxy groups (2-EEA) weakened internal interactions between ether oxygens in PEGDA and resulted in more fractional free volume. Meanwhile hydroxyl groups (2-HEA) had the potential to reduce fractional free volume by promoting intra-chain interactions through hydrogen bonding. For example, at similar crosslinking density (~80 %), 2-HEA resulted in lower free volume (0.118) than EGMEA (0.126) and 2-EEA (0.132). The corresponding  $T_g$  in PEGDA/2-HEA (-28 °C) is 10 °C higher than both PEGDA/EGMEA (-35 °C) and PEGDA/EEA (-38 °C).

**Table 2.5.6-2** Thermal properties and free volume parameters in PEG based crosslink system<sup>15</sup>

Monomer structure	Crosslinker	Crosslink density (wt%)	$T_g$ (°C)	$V_f$
		40.3	-9	0.110
		59.9	-18	0.113

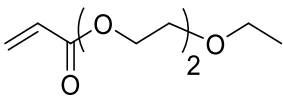
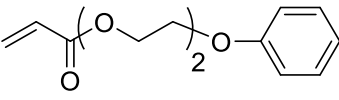
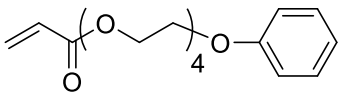
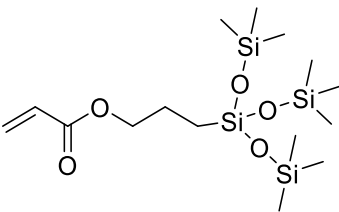
 2-HEA		79.9	-28	0.118
		89.9	-33	0.117
		96	-35	0.119
		100	-37	0.120
<hr/>				
 EGMEA		37.7	-34	0.137
		57.4	-35	0.133
		78.8	-35	0.126
		88.8	-36	0.121
		95.5	-36	0.123
		100	-37	0.120
<hr/>				
 2-EEA		35.5	-39	0.150
		54.8	-38	0.140
		76.5	-38	0.132
		88.0	-37	0.125
		94.7	-37	0.121
	100	-37	0.120	

$T_g$  was determined by DSC and  $V_f$  was determined by Bondi group contribution theory with density study.

Gas permeability improved with decreasing PEGDA crosslinker concentration in PEGDA/EGMEA and PEGDA/2-EEA while lower crosslinking density deteriorated gas permeability in PEGDA/2-HEA. Increase of the free volume in PEGDA/2-HEA resulted in a significant  $T_g$  drop. However, decrease of the free volume in PEGDA/EGMEA and PEGDA/2-EEA has little influence on  $T_g$ .

**Table 2.5.6-3** Thermal properties and free volume parameters in PEG based crosslink system<sup>117-118</sup>

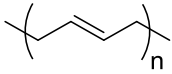
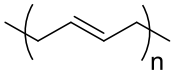
Monomer structure	Crosslinker	Crosslink wt%	$T_g$ (°C)	$V_f$
		29	-46	0.146

 <p>DEGEEA</p>	48	-44	0.139
	71	-41	0.131
	85	-39	0.126
	94	-38	0.123
	100	-37	0.120
 <p>DEGPEA</p>	0	-12	0.135
	25	-17	0.133
	43	-23	0.129
	66	-29	0.126
	82	-32	0.122
 <p>PEGPEA</p>	92	-35	0.123
	100	-37	0.120
	0	-28	0.135
	35	-31	0.128
	59	-33	0.126
 <p>TRIS-A</p>	77	-35	0.125
	90	-37	0.124
	100	-37	0.120
	0	-7	0.158
	10	-22	0.156
	20	-42	0.150
	40	-43	0.142
	50	-40	0.141
	60	-40	0.138
	70	-39	0.134
80	-38	0.132	
90	-38	0.129	
100	-39	0.128	

$T_g$  was determined by DSC and  $V_f$  was determined by Bondi group contribution theory with density study

Similar to the situation in branched polymers, bulky groups introduce more free volume but promote chain entanglement through steric hindrance in crosslinked polymers. Kusuma *et al.* studied the influence of phenoxy pendant groups on free volume and their influence on thermal properties in crosslinked PEGDA.<sup>118</sup> Increasing crosslink density led to smaller fractional free volume ( $V_f$ ) as expected (**Table 2.5.6-3**). But larger fractional free volume failed to affect the  $T_g$  in PEGDA/DEGPEA and PEGDA/PEGPEA. The bulky phenoxy groups introduced more free volume and lowered the  $T_g$ , but they encountered more steric hindrance against local segmental motion. In this case, steric hindrance effect dominated over free volume effect, simultaneously achieving high  $T_g$  and high free volume. Kusuma *et al.* later investigated bulkier but softer pendant groups 3-[tris-(trimethylsiloxy)sily] propyl acrylate monomers (TRIS-A) in the same PEGDA crosslinking matrices (**Table 2.5.6-3**).<sup>117</sup> TRIS-A significantly increased fractional free volume ( $V_f$ ) by interrupting chain packing. In comparison to phenoxy pendant groups, TRIS-A is bulkier and leads to even higher free volume. At 0 % crosslinking density, TRIS-A possessed significant higher free volume (0.158) than DEGPEA and PEGPEA (0.135). Yet, in a similar fashion to the phenoxy example, the bulky TRIS-A group encountered a competition between higher free volume and the steric hindrance of segmental motion. In this case,  $T_g$  remained relatively unchanged because these two effects roughly balanced each other. Gas permeability increased sharply with increasing TRIS-A content as a result of more free volume.

**Table 2.5.6-4** Thermal properties and free volume parameters for crosslinked polybutadiene<sup>10</sup>

Polymer structure	<i>cis</i> 1,4 content (%)	<i>trans</i> 1,4 content (%)	1,2 content (%)	T <sub>g</sub> (°C)	v <sub>f</sub> (Å <sup>3</sup> )
	97	2	1	-106	149.4
(cured)	38	51	11	-93	159.3
	97	2	1	-105	139.5
(uncured)	38	51	11	-92	115.8

T<sub>g</sub> and v<sub>f</sub> (free volume size) were determined by DSC and PALS, respectively.

Another interesting aspect of free volume changes in crosslinking matrix is the isomerization of repeating units. Mansilla *et al.* reported that the influence of crosslinking density on free volume depended on the microstructures in crosslinked polybutadiene.<sup>10</sup> For polybutadiene with high *cis* (97%) stereochemistry, free volume size (v<sub>f</sub>) remained relatively unchanged under various crosslinking density (**Table 2.5.6-4**). While for polybutadiene with moderate *cis* (38%) content, free volume size increased sharply initially, then decreased with higher crosslink density. The authors attributed this phenomena to the interference among crosslinking, isomerization, and crosslink reversion. Crosslinking-induced isomerization may account for this unorthodox relationship between free volume and crosslinking density.

**Table 2.5.6-5** Thermal properties and free volume parameters in crosslinked polyisoprene/polybutadiene blend initiated by dicumylperoxide.<sup>89</sup>

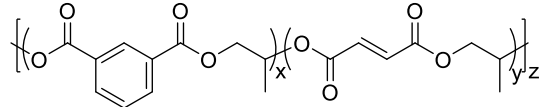
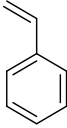
Polymer structure	Crosslinker concentration (1g / 100g)	T <sub>g</sub> (°C)	<V <sub>f</sub> > <sub>g</sub> (10 <sup>3</sup> nm <sup>3</sup> )
	0	-54	67.8

	1	-54	67.1
	3	-46	68.9
(50/50)	5	-40	69.0

$T_g$  was determined by DSC and  $V_f$  was determined by PALS.

Srithawatpong and coworkers studied free volume changes at different temperatures in crosslinked polyisoprene/polybutadiene blends (**Table 2.5.6-5**).<sup>89</sup> Free volume size decreased in the rubbery state, but remained constant in the glassy state with increased crosslinking density. The authors attributed this finding to the fact that crosslinking restricted the thermal expansion significantly when polymer chains are above  $T_g$  but had less influence in the glassy state. Increasing crosslinking density introduced more free volume ( $\langle V_f \rangle_g$ , free volume at  $T_g$ ) and led to a higher  $T_g$ . The authors suggested a kinetic explanation that high- $T_g$  polymers require larger free volume to pass into a liquid-like state (above  $T_g$ ) from a solid-like state (below  $T_g$ ).

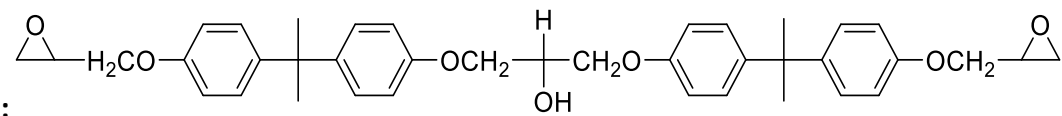
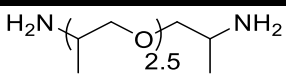
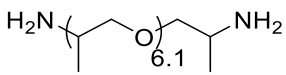
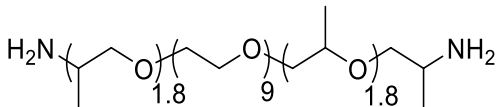
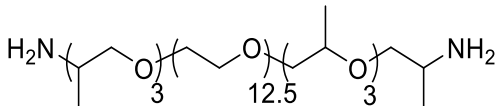
**Table 2.5.6-6** Thermal properties and free volume parameters in crosslinked unsaturated polymer ester<sup>119</sup>

Polymer structure	Crosslinker	Crosslink density (%)	$T_g$ (°C)	$V_f$
		0.00	-20.8	0.0828
		3.17	0.1	0.0704
		9.95	48.4	0.0466
		12.25	68.3	0.0382
		15.52	103.7	0.0269

$T_g$  was determined by TMA and  $V_f$  was determined by Simha-Boyer's equation. Crosslink density was characterized by FTIR.

The effects of crosslinking on free volume are even more substantial in a rigid matrix where mobility is further restricted compared to aliphatic matrices. An early study by Ma *et al.* revealed that lower crosslinking density increased the free volume ( $V_f$ ) and caused a decrease of the  $T_g$  (Table 2.5.6-6).<sup>119</sup> At 15% crosslink density, free volume drastically decreased from 0.0828 (non-crosslinked) to 0.0269, causing an increase in  $T_g$  from -21 °C to 104 °C.

**Table 2.5.6-7** Thermal properties and free volume parameter in epoxy-polyether amine networks<sup>41</sup>

Epoxy resin					
					
Amine component	$T/T_g$	$l$ (nm)	$\tau_3$ (ns)	$I_3$ (%)	$v$
	0.82	1.09	1.61	19.45	2.18
	0.93	1.25	1.69	20.25	2.53
	1.02	1.28	1.81	18.79	2.69
	1.12	1.35	1.95	21.00	3.51

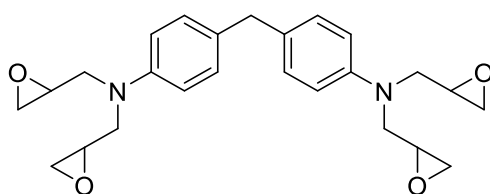
$T_g$  was determined by DSC. Free volume parameters and the distance between crosslink ( $l$ ) were determined using PALS.

Patil *et al.* studied the relationship between the degree of crosslinking and free volume in both glassy and rubbery epoxy-amine networks (Table 2.5.6-7).<sup>41</sup> Within the same networks, both free volume size and the number of free volume increased when crosslinking density decreased, which was consistent with previous studies. A comparison between the glassy and

rubbery networks suggested a decrease of free volume size and an increase of the number of free volume when changing from the glassy state to the rubbery state. Overall, larger free volume leads to lower  $T_g$ , and glassy networks feature smaller free volume size but more free volume elements than rubbery matrices.

**Table 2.5.6-8** Thermomechanical properties and fractional free volume in epoxy-amine crosslinking matrices<sup>120</sup>

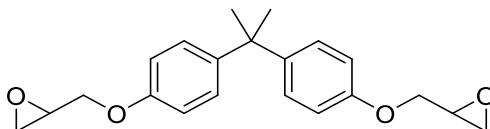
**Epoxy resin:**



(TGDDM)

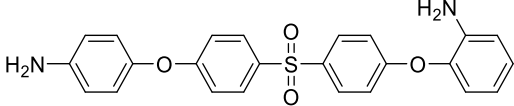
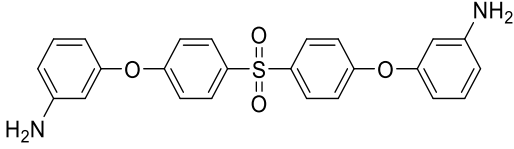
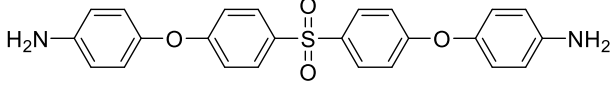
Amine component	$T_g$ (°C)	$G'$ ( $10^{10}$ dyn/cm <sup>2</sup> )	$V_f$ (%)
 (33' DDS)	231	2.1	1.74
 (44' DDS)	260	1.8	2.11

**Epoxy resin:**



(DGEBA)

Amine component	$T_g$ (°C)	$G'$ ( $10^{10}$ dyn/cm <sup>2</sup> )	$V_f$ (%)
 (43' DDS)	170	1.4	2.67

 (42'DDS)	140	1.5	1.82
 (33'DDS)	213	1.5	1.51
 (44'DDS)	230	2.1	1.91

$T_g$  and fractional free volume were determined by DSC and PALS, respectively. Shear modulus (stiffness),  $G'$ , was determined by Instron at room temperature.

In other rigid epoxy crosslinking network examples, Jean *et al.* demonstrated that configurational isomers had significant impact on free volume and the corresponding thermomechanical properties (**Table 2.5.6-8**).<sup>120</sup> With identical amine component, TGDDM exhibited smaller fractional free volume ( $V_f$ ) in comparison to DGEBA, presumably due to higher crosslinking density of TGDDM (from higher functionality). When using the same epoxy resin, different configurational isomers of amines showed significant influence on free volume. 44'DDS allowed more extended chain configuration and afforded more free volume compared to 33'DDS. Asymmetric amines demonstrated complicated effects on free volume: 43'DDS introduced more free volume than 44'DDS, but 42'DDS reduced free volume in comparison to 44'DDS. Glass transition temperatures increased with increasing free volume when using symmetric amines, but no clear trend existed between  $T_g$  and free volume in asymmetric amine networks. However, shear modulus ( $G'$ ) always decreased when free volume increased regardless of the amine structures.

In crosslinking networks, free volume normally decreases with increasing crosslinking density due to restricted segmental motion. However, in the case of crosslinking materials with isomerization, such as crosslinked polybutadiene or polyisoprene, high free volume and high crosslinking density are achievable at the same time, likely due to the crosslinking-induced isomerization. At similar crosslinking level, pendant groups steer the free volume change, and the common argument of its influence on free volume (section 2.5.5) is valid in crosslinked materials as well.

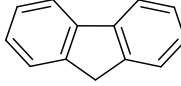
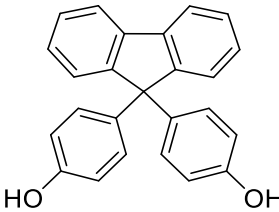
### **2.5.7 Effect of polymer blends and additives on free volume**

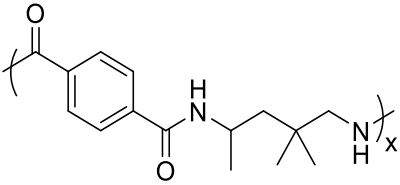
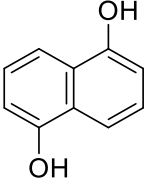
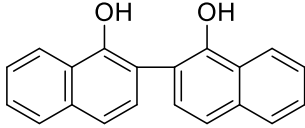
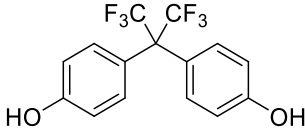
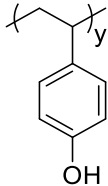
Additives in polymers and polymer blends are mixtures of polymers with other small molecules or macromolecules, respectively. They provide facile approaches to alter polymers' thermomechanical,<sup>2, 80, 121</sup> biological,<sup>122</sup> electrical<sup>123-124</sup> and permeation properties<sup>125-127</sup> without redesigning polymer chemical structures. Additives and blends involve free molecules in comparison to branching and crosslinked networks, making them generally more efficient to modify free volume and eventually polymer physical properties.

As mobile small molecules, additives normally tend to introduce more free volume to polymer networks through plasticization and thus decrease  $T_g$ . However, bulky additives also promote chain entanglement that tends to elevate  $T_g$ . Additives with strong interaction to polymer chains (hydrogen bonding, electrostatic interactions, etc.) reduce free volume by bridging polymer chains as intermolecular linkers. Naturally, there is a competition between inter-chain and intra-chain interactions, which has the potential to increase or reduce free volume. A similar argument applies to polymer blends except that polymer blends are naturally bulkier and their diffusion is highly restricted in comparison to small-molecule additives.

Garcia *et al.* studied the plasticization and anti-plasticization effect of aromatic additives in a polyamide matrix (Trogamid) and their effect on free volume (**Table 2.5.7-1**).<sup>2</sup> All small-molecule additives decreased the  $T_g$  (plasticization) in comparison to the pure polymer matrix Trogamid. However, the free volume size ( $v_f$ ) exhibited different trends depending on different additive structures. Additives with hydroxyl groups (FDPh, Ndiol, and Binaphthol) tended to decrease free volume size by promoting inter-molecular interactions through hydrogen bonding. Instead of increasing  $T_g$ , smaller free volume size led to a decrease in  $T_g$ , presumably due to increasing number of free volume elements, which the authors did not convey. But for HFBA, due to the kinked structures between the two aromatic rings and the trifluoromethyl groups, the free volume size increased despite the presence of hydroxyl groups. PVPh polymers demonstrated antiplasticization due to decreased free volume. Further studies on additive effect at different loading level revealed that the Trogamid/HFBA blends gained more free volume with increasing additive content due to plasticization, and  $T_g$  decreased accordingly. In contrast, the Trogamid/PVPh blends showed a decrease in fractional free volume with increasing levels of polymer blends (PVPh) and resulted in  $T_g$  increase.

**Table 2.5.7-1** Thermal properties and free volume parameters of a polyimide matrix with various additives.<sup>2</sup>

Polymer structure	Additives	$T_g$ (°C)	$v_f$ (Å <sup>3</sup> )
	N/A	146	81.4
		136	81.2
	Fluorene		
		144	78.0
	FDPh		

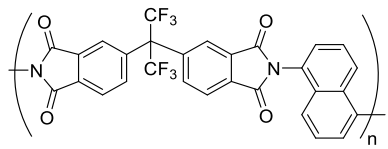
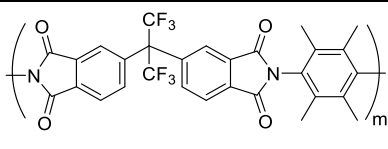
 <p>Trogamid</p>	 <p>Ndiol</p>	122	73.9
	 <p>Binaphthol</p>	133	77.6
	 <p>HFBA</p>	133	84.7
	 <p>PVPh</p>	157	79.3

All additives were blended in to Trogamid at the concentration of 15 wt%.  $T_g$  and free volume parameter were determined by DSC and PALS, respectively.

In a more rigid network, Low *et al.* employed PALS to study the influence of additives on free volume and the corresponding gas permeability properties (**Table 2.5.7-2**).<sup>128</sup> By adding azide to linear polyimides, both free volume size and number of free volume elements decreased in all the polyimide systems due to the formation of poly(azide) networks within a polyimide framework. In this rigid polyimide matrix, the number of free volume elements changed more significantly than free volume size. The overall reduction of free volume resulted in lower  $T_g$ . Between the two different polyimide systems studied, the one with higher free volume showed lower permeability. The authors attributed these uncommon observations to the fact that when applying free volume theory to predict gas permeability, only free volume elements with comparable or larger dimension than the gas molecules are responsible for gas permeation. As

PALS reliably detects free volume with size as small as 1.6 Å, the cavities with sizes smaller than gas molecules are meaningless for gas permeation. For an accurate quantitative prediction of gas permeability from free volume theory, it is necessary to quantitatively determine free volume size distribution before any quantitative conclusion.<sup>128</sup>

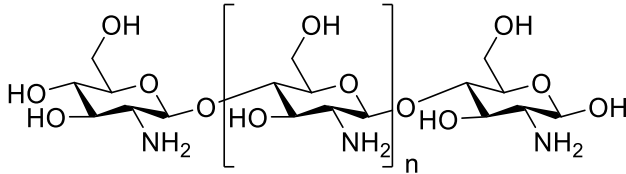
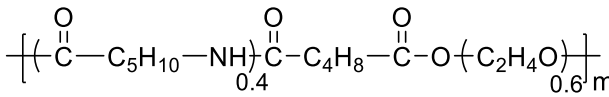
**Table 2.5.7-2** Thermal properties and free volume parameters of polyimide with azide as additives.<sup>128</sup>

Polymer structure	Azide additives	Azide wt%	T <sub>g</sub> (°C)	I <sub>3</sub> (%)	τ <sub>3</sub> (ns)
Polyazide		100	283	N/A	N/A
<hr/>		0	395	5.36	2.94
	10	371	2.66	2.57	
	30	331	1.97	2.59	
	50	312	1.55	2.58	
	0	419	6.13	2.70	
	10	411	4.43	2.60	
	30	406	3.87	2.47	

T<sub>g</sub> and free volume parameter were determined by DSC and PALS, respectively.

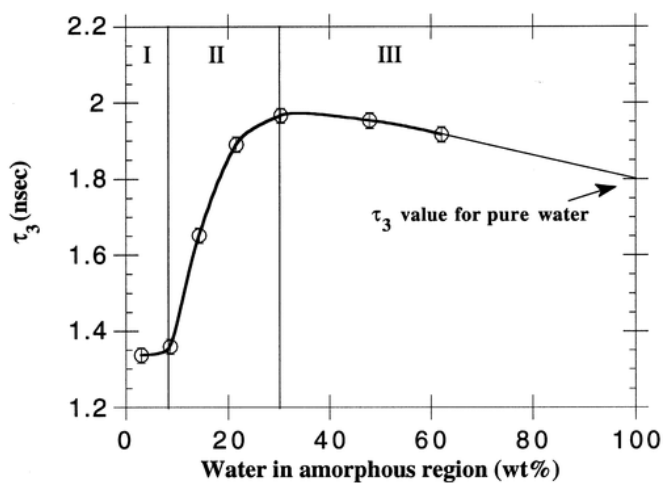
Liu *et al.* investigated CO<sub>2</sub> permeability in chitosan (CS)/poly(ether-*b*-amide) (Pebax<sup>®</sup>) blends (Table 2.5.7-3).<sup>37</sup> Compared to uncrosslinked CS, all crosslinked matrices showed decreased free volume size. Within crosslinked samples, Pebax<sup>®</sup> efficiently increased free volume size (τ<sub>3</sub>) and overall fractional free volume by its hard, glassy polyimide segments. This increase in free volume from Pebax<sup>®</sup> significantly improved CO<sub>2</sub> permeability.

**Table 2.5.7-3** Free volume parameters of CS/Pebax® polymer blends.<sup>37</sup>

Polymer structures	Pebax® wt%	I <sub>3</sub> (%)	τ <sub>3</sub> (ns)
 (uncrosslinked CS)	0	14.02	1.87
 crosslinked CS	0	10.61	1.34
+	25	9.83	1.60
 Pebax	33	10.84	1.72
	50	11.65	1.79

All parameters were determined by PALS.

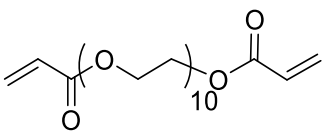
Water is a frequently encountered additive and poses the potential of both intra- and inter-molecular interactions. Along with a swelling effect, free volume changes become complex and highly dependent on specific polymer chemical structures. For example, free volume size increased in poly(vinyl alcohol) but decreased in poly(ethylene oxide) with increasing water content. The change in free volume is complicated, as discussed below.

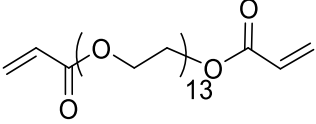
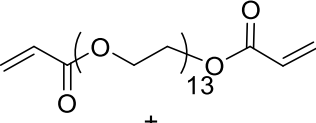
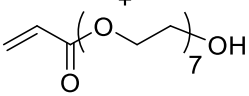


**Figure 2.5.7-1** Measured oPs pickoff lifetimes for the PVOH/water system as a function of water content (Copyright (1996) American Chemical Society).<sup>29</sup>

An early study from Hodge *et al.* employed PALS to study the plasticization of water in poly(vinyl alcohol) films.<sup>29</sup> By varying the water content, the authors observed three distinct regions of the free volume size change: a constant initial region, an increase of  $\tau_3$  (free volume size) with increasing water content, and a slow decay of  $\tau_3$  with increasing water content (**Figure 2.5.7-1**). Consequently,  $T_g$  decreased with increasing water content and reached a plateau at high water content. Hodge *et al.* attributed the constant initial region to either the detection limit of  $\tau_3$  in PALS (0.03 ns) or the absence of o-Ps near the hydroxyl groups. In the second region, water molecules interrupted inter-molecular hydrogen bonding between the polymer hydroxyl groups, leading to an increase in free volume and a decrease in  $T_g$  determined by DSC. The upper limit of this region indicated the presence of 30 wt% bound water, which agreed with the theoretical maximum. Above 30 wt% water incorporation, freezing water (compared to bound non-freezing water) accumulated and gradually reduced free volume. Only the bound non-freezing water contributed to the observed plasticizing effects. In contrast, Trotzic's research on poly(ethylene oxide) showed different results.<sup>28</sup> Without strong inter-molecular hydrogen bonding as in PVA, the authors reported that the incorporation of water lowered  $T_g$  and decreased both free volume size and number of free volume elements.

**Table 2.5.7-4** Free volume parameters of hydrated crosslinked PEG films with water as additives<sup>129</sup>

Polymer structure	Prepolymerization water content (wt%)	$\tau_3$ (ns)	I <sub>3</sub> (%)	$v_f$ (Å <sup>3</sup> )
	0	2.15	18.7	112
	20	2.12	19.5	109

Crosslinked	40	2.10	20.1	106
	60	2.03	21.9	100
	80	1.95	22.8	92
	0	2.10	19.8	107
	20	2.07	20.6	104
Crosslinked	40	2.05	20.9	102
	60	2.03	21.5	100
	80	1.97	22.7	95
	0	2.06	20.6	103
	20	2.06	20.8	103
	40	2.04	21.5	101
	60	2.01	22.5	98
Crosslinked (50/50 wt/wt)	80	1.96	23.0	93

Free volume parameters were determined by PALS.

Ju *et al.* characterized sodium chloride and water transport behavior of three different PEGDA-based hydrogels with varying water content in prepolymerization mixtures (**Table 2.5.7-4**).<sup>129</sup> As the water content of the prepolymerization mixture (wet film) increased, the permeability of water, NaCl and MgSO<sub>4</sub> all increased. PALS results confirmed a linear decrease of free volume size ( $v_f$  and  $\tau_3$ ) and a linear increase of the number of free volume elements ( $I_3$ ) with increasing water contents. As a net result, overall fractional free volume proportionally increased with equilibrium water content up to 80%. The hydrogen bonding between water molecules and two ether oxygen molecules from PEO segments promoted denser packing and reduced free volume size.<sup>130</sup>

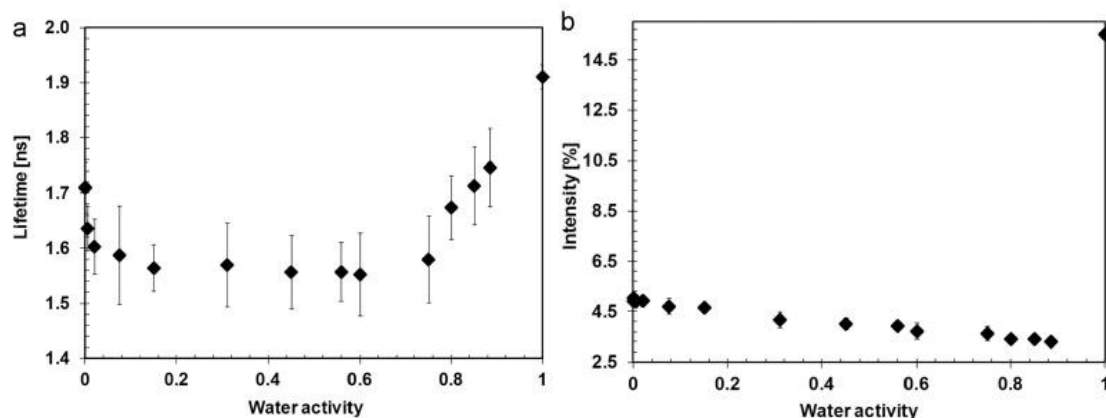


**Figure 2.5.7-2** o-Ps lifetime (a) and o-Ps intensity (b) plotted as a function of relative humidity for the aromatic polyamide isolated from SW30 (Copyright (2013) Elsevier Ltd.).<sup>131</sup>

In a more rigid matrix, Lee *et al.* investigated the free volume of aromatic polyamide reverse osmosis membranes under water vapor.<sup>131</sup> Free volume size (o-Ps lifetime) initially decreased rapidly to a plateau then increased continuously when the relative humidity is sufficiently high (~60%) (**Figure 2.5.7-2a**). Additionally, the intensity of o-Ps (the number of free volume elements) gradually dropped with increasing relative humidity (**Figure 2.5.7-2b**). An earlier study provides some insight to understand this observation.<sup>132</sup> Robertson *et al.* investigated hole-filling and pore-swelling mechanisms. Initially, small water molecules filled up free volume sites, therefore reduced free volume. Once free volume sites became saturated, a plateau appeared. At high water content, the swelling effect started dominating the free volume change and led to higher free volume. The increase in free volume led to higher flux of salt solution and lower salt rejection.

**Table 2.5.7-5** Thermal properties and free volume of epoxy resin/polyurethane network and organophilic montmorillonite (oM) polymer nanocomposites<sup>8</sup>

Polymer structure	oM content (wt%)	$v_f$ ( $\text{\AA}^3$ )	$V_f$	$T_{g1}$ ( $^{\circ}\text{C}$ )	$T_{g2}$ ( $^{\circ}\text{C}$ )
Epoxy resin	0	0.282	0.0300	33.9	48.9

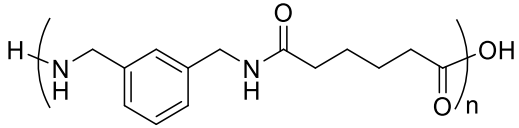
+	1	0.270	0.0277	35.6	49.0
Polyurethane	3	0.274	0.0291	37.3	49.8
	5	0.276	0.0294	40.6	50.6

T<sub>g</sub> and free volume parameters were determined by DSC and PALS, respectively.

Clay is a commonly used material in polymer nanocomposites in fundamental research and industrial studies. Jia *et al.* employed PALS to investigate the structure-free volume-properties relationships for organophilic Montmorillonite (oM) in epoxy resin/polyurethane (EP/PU) networks (Table 2.5.7-5).<sup>8</sup> The addition of oM reduced free volume size ( $v_f$ ) and overall free volume ( $V_f$ ). The authors attributed the decrease in free volume to the potential compatibilization effect of Montmorillonite which improved the miscibility between PU and EP. Additionally, the hydrogen bonding among PU, EP and oM also decreased free volume. Although the free volume size decreased with increasing oM content, the number of free volume elements actually increased with higher oM concentration. As a net result, free volume reached a minimal value at 1 wt% loading of oM. T<sub>g</sub> demonstrated an inverse relationship with free volume, but the corresponding drop in T<sub>g</sub> with free volume changes only appeared at polyurethane rich region (T<sub>g1</sub>), indicating more prominent influence of free volume in polyurethane-rich region than epoxy-rich region.

**Table 2.5.7-6** Thermal properties and free volume of poly(m-xylene adipamide)/montmorillonite nanocomposites<sup>71</sup>

Polymer structure	Additives	OTR (cc/m <sup>2</sup> d)	I <sub>3</sub> (%)	τ <sub>3</sub> (ns)
	N/A	5.6	22.07	1.47

	$\begin{array}{c} \text{CH}_2\text{CH}_2\text{OH} \\   \\ \text{H}_3\text{C}-\text{N}^{\oplus}-\text{T} \\   \\ \text{CH}_2\text{CH}_2\text{OH} \end{array}$	4.0	21.65	1.49
	(Cloisite 30B)			
	$\begin{array}{c} \text{CH}_3 \\   \\ \text{H}_3\text{C}-\text{N}^{\oplus}-\text{CH}_2-\text{C}_6\text{H}_5 \\   \\ \text{HT} \end{array}$	1.9	20.71	1.51
	(Cloisite 10A)			
	$\begin{array}{c} \text{H} \\   \\ \text{H}_3\text{C}-\text{N}^{\oplus}-\text{HT} \\   \\ \text{HT} \end{array}$	5.8	22.00	1.49
	(Cloisite 93A)			

T is tallow, 65% C18; HT is hydrogenated tallow, 65% C18. OTR: Oxygen transmission rate, 23 °C, 0% RH. Free volume parameters was determined by PALS.

Ammala *et al.*'s research on poly(*m*-xylylene adipamide)/montmorillonite nanocomposites shed light on free volume changes upon the introduction of secondary interactions to nanocomposites (**Table 2.5.7-6**).<sup>71</sup> The free volume size remained relatively the same ( $\tau_3$ ) for all three additives, but the number of free volume elements ( $I_3$ ) differed. Hydrogen bonding (Cloisite 30B) and  $\pi$ - $\pi$  stacking (Cloisite 10A) promoted the inter-chain interaction and, as a result, decreased the free volume.  $T_g$ s exhibited similar inverse relationships with free volume and the oxygen transmission rate (OTR) reduced significantly with decreasing free volume.

**Table 2.5.7-7** Free volume of phenol-formaldehyde resin using multi-wall carbon nanotubes (MWCNTs) as nanocomposites<sup>133</sup>

Polymer structure	MWCNTs content (w/w %)	$\tau_3$	$I_3$
-------------------	------------------------	----------	-------

		(ns)	(%)
	0	1.38	18.3
	2	1.52	16.4
	5	1.52	14.5
	10	1.60	14.3
	20	1.70	16.0
phenol-formaldehyde resin			

Free volume parameters were determined by PALS.

Carbon nanotubes are also widely studied as mechanical reinforcing additives in polymers. Sharma *et al.* studied the free volume change in phenol-formaldehyde (PF) resin using multi-wall carbon nanotubes (MWCNTs) as additives (**Table 2.5.7-7**).<sup>133</sup> The free volume size ( $\tau_3$ ) increased with increasing MWCNTs content, while the number of free volume elements decreased. As a result, the overall free volume increased at higher loading of MWCNTs. Montazeri *et al.* used dynamic mechanical thermal analysis (DMTA) to calculate free volume in MWNT/epoxy nanocomposites.<sup>39</sup> The fractional free volume decreased with increased nanotube content and resulted in an increase in  $T_g$ . In this instance, the nanotubes functioned as fillers to reduce free volume, thereby enhancing thermomechanical properties.

Polymer blends and additives also serve as a qualitative way to compare free volume when applying additives as filling materials to probe free volume size. When used as a polymer blends, poly(ethylene oxide)-*b*-poly(propylene oxide)-*b*-poly(ethylene oxide) (PEO-PPO-PEO) block copolymers improved flexural modulus (bending deformation) of epoxy-resin and diamine (DGEBA/DDM) networks. PEO-PPO-PEO block copolymers with shorter PEO chains exhibited

greater modulus improvement than PEO-PPE-PEO block copolymers with longer PEO chains.<sup>80</sup> While incorporating only PEO enhanced flexural modulus, the addition of PPO had the opposite effect. Larranaga *et al.* hypothesized that PEO segments migrated into the free volume of DGEBA/DDM to improve mechanical performance. Above a certain length, however, the PEO segments become too bulky to fill into the free volume voids and demonstrated no improvement in flexural modulus.

Car *et al.* also applied an indirect approach to study fractional free volume for a polymer blend of Pebax<sup>®</sup>MH 1657 and PEG.<sup>14</sup> Pebax<sup>®</sup>MH consisted of an aliphatic polyamide “hard” block and a PEO polyether block to provide gas transport properties. The authors used the additive model to calculate the theoretical density of the polymer blends with various PEO contents. Since the additive model doesn’t take the free volume change into account, the difference between experimental and theoretical density represents the change of free volume.<sup>134</sup> Density of the blended membranes was lower than the predicted value when PEG component exceeded 30 vol%, suggesting an increase in fractional free volume with increasing PEG content.

As polymer additives and blends are free-moving molecules, free volume has more profound influence on polymer physical properties than in crosslinking polymers. The intra- and inter-molecular interactions are the key to understanding and predicting free volume change in polymer additives and blends. The diffusion of additives and blends makes free volume change more complicated when they have a comparable size with free volume voids. The swelling effect from additives is also critical and sometimes dominates the free volume change.

## 2.6 Conclusions

Free volume theory provides insight into understanding structural relaxation (such as  $T_g$ ) and small molecule mass transfer (such as permeation process). Current techniques allow the

determination of global free volume size and the number of free volume elements. Yet, no technique is capable of pinpointing local free volume information, which is a promising direction for future development of free volume determination techniques. Local free volume information is of great importance in understanding materials with hierarchical structures, such as microphase separated morphologies or 3D printed complex objects.

When considering the change of fractional free volume, several common conclusions are valid in most polymeric materials: (1) free volume increases with increasing size of pendant groups, branches and backbone repeating units; (2) inter-molecular interaction decreases free volume while intra-molecular interaction increases free volume; (3) additives and blends have the potential to either increase or decrease free volume depending their sizes compared to individual free volume size. However, when applying free volume theory to predict polymer physical properties, competing mechanisms should not be ignored. For example, the steric hindrance effect in bulky pendant groups are able to cancel or even overcome free volume increase and led to an increase of  $T_g$  despite free volume increase. Nevertheless, free volume theory is an efficient means to bridge sub-nano scale structural variation and macroscopic polymer physical properties.

## 2.7 References

1. Doolittle, K., Studies in Newtonian Flow. II. The Dependence of the Viscosity of Liquids on Free-Space *J. Appl. Phys.* **1951**, *22*, 1471.
2. Garcia, A.; Iriarte, M.; Uriarte, C.; Iruin, J. J.; Etxeberria, A.; del Rio, J., Antiplasticization of a polyamide: a positron annihilation lifetime spectroscopy study *Polymer* **2004**, *45*, 2949-2957.
3. Liu, H. W.; Wilen, C. E., Extension of the chain-end, free-volume theory for predicting glass temperature as a function of conversion in hyperbranched polymers obtained through one-pot approaches *J. Polym. Sci., Part B: Polym. Phys* **2004**, *42*, 1235-1242.
4. Dlubek, G.; Sen Gupta, A.; Pionteck, J.; Hassler, R.; Krause-Rehberg, R.; Kaspar, H.; Lochhaas, K. H., Glass transition and free volume in the mobile (MAF) and rigid (RAF)

- amorphous fractions of semicrystalline PTFE: a positron lifetime and PVT study *Polymer* **2005**, *46*, 6075-6089.
5. Bamford, D.; Dlubek, G.; Lupke, T.; Kilburn, D.; Stejny, J.; Menke, T. J.; Alam, M. A., Free volume, glass transition and degree of branching in ethylene/alpha-olefin copolymers: Positron lifetime, differential scanning calorimetry, wide-angle X-ray scattering, and density studies *Macromol. Chem. Phys.* **2006**, *207*, 492-502.
  6. Di Maio, E.; Iannace, S.; Mensitieri, G.; Nicolais, L., A predictive approach based on the Simha-Somcynsky free-volume theory for the effect of dissolved gas on viscosity and glass transition temperature of polymeric mixtures *J. Polym. Sci., Part B: Polym. Phys* **2006**, *44*, 1863-1873.
  7. Kilburn, D.; Dlubek, G.; Pionteck, J.; Alam, M. A., Free volume in poly(n-alkyl methacrylate)s from positron lifetime and PVT experiments and its relation to the structural relaxation *Polymer* **2006**, *47*, 7774-7785.
  8. Jia, Q. M.; Zheng, M.; Zhu, Y. C.; Li, J. B.; Xu, C. Z., Effects of organophilic montmorillonite on hydrogen bonding, free volume and glass transition temperature of epoxy resin/polyurethane interpenetrating polymer networks *Eur. Polym. J.* **2007**, *43*, 35-42.
  9. Kim, S. H.; Chung, J. W.; Kang, T. J.; Kwak, S. Y.; Suzuki, T., Determination of the glass transition temperature of polymer/layered silicate nanocomposites from positron annihilation lifetime measurements *Polymer* **2007**, *48*, 4271-4277.
  10. Mansilla, M. A.; Garraza, A. L. R.; Silva, L.; Salgueiro, W.; Macchi, C.; Marzocca, A. J.; Somoza, A., Evolution of the free volume and glass transition temperature with the degree of cure of polybutadiene rubbers *Polym. Test.* **2013**, *32*, 686-690.
  11. Arnold, M. E.; Nagai, K.; Freeman, B. D.; Spontak, R. J.; Betts, D. E.; DeSimone, J. M.; Pinnau, I., Gas permeation properties of poly(1,1'-dihydroperfluorooctyl acrylate), poly(1,1'-dihydroperfluorooethyl methacrylate), and poly(styrene)-b-poly(1,1'-dihydroperfluorooethyl acrylate) block copolymers *Macromolecules* **2001**, *34*, 5611-5619.
  12. Lin, H. Q.; Kai, T.; Freeman, B. D.; Kalakkunnath, S.; Kalika, D. S., The effect of cross-linking on gas permeability in cross-linked poly(ethylene glycol diacrylate) *Macromolecules* **2005**, *38*, 8381-8393.
  13. Lin, H.; Freeman, B. D.; Kalakkunnath, S.; Kalika, D. S., Effect of copolymer composition, temperature, and carbon dioxide fugacity on pure- and mixed-gas permeability in poly(ethylene glycol)-based materials: Free volume interpretation *J. Membr. Sci.* **2007**, *291*, 131-139.
  14. Car, A.; Stropnik, C.; Yave, W.; Peinemann, K.-V., PEG modified poly(amide-b-ethylene oxide) membranes for CO<sub>2</sub> separation *J. Membr. Sci.* **2008**, *307*, 88-95.
  15. Kusuma, V. A.; Freeman, B. D.; Borns, M. A.; Kalika, D. S., Influence of chemical structure of short chain pendant groups on gas transport properties of cross-linked poly(ethylene oxide) copolymers *J. Membr. Sci.* **2009**, *327*, 195-207.
  16. Yave, W.; Car, A.; Peinemann, K.-V.; Shaikh, M. Q.; Raetzke, K.; Faupel, F., Gas permeability and free volume in poly(amide-b-ethylene oxide)/polyethylene glycol blend membranes *J. Membr. Sci.* **2009**, *339*, 177-183.
  17. Yave, W.; Car, A.; Funari, S. S.; Nunes, S. P.; Peinemann, K.-V., CO<sub>2</sub>-Philic Polymer Membrane with Extremely High Separation Performance *Macromolecules* **2010**, *43*, 326-333.
  18. Fan, Y.; Zhang, M.; Moore, R. B.; Lee, H.-S.; McGrath, J. E.; Cornelius, C. J., Viscoelastic and gas transport properties of a series of multiblock copolymer ionomers *Polymer* **2011**, *52*, 3963-3969.

19. Li, H.; Freeman, B. D.; Ekiner, O. M., Gas permeation properties of poly(urethane-urea)s containing different polyethers *J. Membr. Sci.* **2011**, *369*, 49-58.
20. Loria-Bastarrachea, M. I.; Aguilar-Vega, M., Membranes from rigid block hexafluoro copolyaramides: Effect of block lengths on gas permeation and ideal separation factors *J. Membr. Sci.* **2013**, *443*, 36-44.
21. Kwisnek, L.; Goetz, J.; Meyers, K. P.; Heinz, S. R.; Wiggins, J. S.; Nazarenko, S., PEG Containing Thiol-Ene Network Membranes for CO<sub>2</sub> Separation: Effect of Cross-Linking on Thermal, Mechanical, and Gas Transport Properties *Macromolecules* **2014**, *47*, 3243-3253.
22. Tung, K. L.; Jean, Y. C.; Nanda, D.; Lee, K. R.; Hung, W. S.; Lo, C. H.; Lai, J. Y., Characterization of multilayer nanofiltration membranes using positron annihilation spectroscopy *J. Membr. Sci.* **2009**, *343*, 147-156.
23. Xie, W.; Ju, H.; Geise, G. M.; Freeman, B. D.; Mardel, J. I.; Hill, A. J.; McGrath, J. E., Effect of Free Volume on Water and Salt Transport Properties in Directly Copolymerized Disulfonated Poly(arylene ether sulfone) Random Copolymers *Macromolecules* **2011**, *44*, 4428-4438.
24. Geise, G. M.; Freeman, B. D.; Paul, D. R., Sodium chloride diffusion in sulfonated polymers for membrane applications *J. Membr. Sci.* **2013**, *427*, 186-196.
25. Liu, R. Y. F.; Hu, Y. S.; Hibbs, M. R.; Collard, D. M.; Schiraldi, D. A.; Hiltner, A.; Baer, E., Improving oxygen barrier properties of poly(ethylene terephthalate) by incorporating isophthalate. I. Effect of orientation *J. Appl. Poly. Soc* **2005**, *98*, 1615-1628.
26. Wiegand, J. R.; Smith, Z. P.; Liu, Q.; Patterson, C. T.; Freeman, B. D.; Guo, R. L., Synthesis and characterization of triptycene-based polyimides with tunable high fractional free volume for gas separation membranes *J. Mater. Chem. A* **2014**, *2*, 13309-13320.
27. Sanders, D. F.; Smith, Z. P.; Ribeiro, C. P.; Guo, R. L.; McGrath, J. E.; Paul, D. R.; Freeman, B. D., Gas permeability, diffusivity, and free volume of thermally rearranged polymers based on 3,3'-dihydroxy-4,4'-diamino-biphenyl (HAB) and 2,2'-bis-(3,4-dicarboxyphenyl) hexafluoropropane dianhydride (6FDA) *J. Membr. Sci.* **2012**, *409*, 232-241.
28. Trotzig, C.; Abrahmsen-Alami, S.; Maurer, F. H. J., Structure and mobility in water plasticized poly(ethylene oxide) *Polymer* **2007**, *48*, 3294-3305.
29. Hodge, R. M.; Bastow, T. J.; Edward, G. H.; Simon, G. P.; Hill, A. J., Free volume and the mechanism of plasticization in water-swollen poly(vinyl alcohol) *Macromolecules* **1996**, *29*, 8137-8143.
30. Ribeiro, C.; Zimeri, J. E.; Yildiz, E.; Kokini, J. L., Estimation of effective diffusivities and glass transition temperature of polydextrose as a function of moisture content *Carbohydr. Polym.* **2003**, *51*, 273-280.
31. Kilburn, D.; Bamford, D.; Lupke, T.; Dlubek, G.; Menke, T. J.; Alam, M. A., Free volume and glass transition in ethylene/1-octene copolymers: positron lifetime studies and dynamic mechanical analysis *Polymer* **2002**, *43*, 6973-6983.
32. Dlubek, G.; Bondarenko, V.; Al-Qaradawi, I. Y.; Kilburn, D.; Krause-Rehberg, R., The structure of the free volume in poly(styrene-co-acrylonitrile) from positron lifetime and pressure volume temperature (PVT) experiments - II. Local free volume from positron annihilation lifetime spectroscopy (PALS) *Macromol. Chem. Phys.* **2004**, *205*, 512-522.
33. Hu, C. C.; Lee, K. R.; Ruaan, R. C.; Jean, Y. C.; Lai, J. Y., Gas separation properties in cyclic olefin copolymer membrane studied by positron annihilation, sorption, and gas permeation *J. Membr. Sci.* **2006**, *274*, 192-199.

34. Yave, W.; Szymczyk, A.; Yave, N.; Roslaniec, Z., Design, synthesis, characterization and optimization of PTT-b-PEO copolymers: A new membrane material for CO<sub>2</sub> separation *J. Membr. Sci.* **2010**, *362*, 407-416.
35. Peng, Z. L.; Olson, B. G.; Srithawatpong, R.; McGervey, J. D.; Jamieson, A. M.; Ishida, H.; Meier, T. M.; Halasa, A. F., Study of free volume in high-vinyl polybutadiene/cis-polyisoprene blends using positron annihilation spectroscopy *J. Polym. Sci., Part B: Polym. Phys* **1998**, *36*, 861-871.
36. Ye, Y. S.; Elabd, Y. A., Anion exchanged polymerized ionic liquids: High free volume single ion conductors *Polymer* **2011**, *52*, 1309-1317.
37. Liu, Y.; Yu, S.; Wu, H.; Li, Y.; Wang, S.; Tian, Z.; Jiang, Z., High permeability hydrogel membranes of chitosan/poly ether-block-amide blends for CO<sub>2</sub> separation *J. Membr. Sci.* **2014**, *469*, 198-208.
38. Zhang, H.; Wang, S.; Weber, S. G., Morphology and free volume of nanocomposite Teflon AF 2400 films and their relationship to transport behavior *J. Membr. Sci.* **2013**, *443*, 115-123.
39. Montazeri, A.; Pourshamsian, K.; Riazian, M., Viscoelastic properties and determination of free volume fraction of multi-walled carbon nanotube/epoxy composite using dynamic mechanical thermal analysis *Mater. Des.* **2012**, *36*, 408-414.
40. Chieng, N.; Cicerone, M. T.; Zhong, Q.; Liu, M.; Pikal, M. J., Characterization of dynamics in complex lyophilized formulations: II. Analysis of density variations in terms of glass dynamics and comparisons with global mobility, fast dynamics, and Positron Annihilation Lifetime Spectroscopy (PALS) *Eur. J. Pharm. Biopharm.* **2013**, *85*, 197-206.
41. Patil, P. N.; Rath, S. K.; Sharma, S. K.; Sudarshan, K.; Maheshwari, P.; Patri, M.; Praveen, S.; Khandelwal, P.; Pujari, P. K., Free volumes and structural relaxations in diglycidyl ether of bisphenol-A based epoxy-polyether amine networks *Soft Matter* **2013**, *9*, 3589-3599.
42. Ryzhikh, V. E.; Alent'ev, A. Y.; Yampol'skii, Y. P., Relation of gas-transport parameters of amorphous glassy polymers to their free volume: Positron annihilation study *Polym. Sci. Ser. A* **2013**, *55*, 244-252.
43. Ong, R. C.; Chung, T. S.; Helmer, B. J.; de Wit, J. S., Characteristics of water and salt transport, free volume and their relationship with the functional groups of novel cellulose esters *Polymer* **2013**, *54*, 4560-4569.
44. van der Waals, J. D. Over de Continuïteit van den Gas- en Vloeistoftoestand (on the continuity of the gas and liquid state). University of Leiden, 1873.
45. Batschinski, A. J., *Z. physik Chem.* **1913**, *84*, 644.
46. Hildebrand, J. H., FREE VOLUMES IN LIQUIDS *Journal of Chemical Physics* **1959**, *31*, 1423-1425.
47. Ferry, M. L. W. R. F. L. J. D., The Temperature Dependence of Relaxation Mechanisms in Amorphous Polymers and Other Glass-forming Liquids *J. Am. Chem. Soc.* **1955**, *77*, 3701.
48. Vrentas, J. S.; Jarzelski, C. M.; Duda, J. L., DEBORAH NUMBER FOR DIFFUSION IN POLYMER-SOLVENT SYSTEMS *AIChE J.* **1975**, *21*, 894-901.
49. Vrentas, J. S.; Duda, J. L., DIFFUSION IN POLYMER-SOLVENT SYSTEMS .3. CONSTRUCTION OF DEBORAH NUMBER DIAGRAMS *J. Polym. Sci., Part B: Polym. Phys* **1977**, *15*, 441-453.
50. Vrentas, J. S.; Duda, J. L., DIFFUSION IN POLYMER-SOLVENT SYSTEMS .2. PREDICTIVE THEORY FOR DEPENDENCE OF DIFFUSION-COEFFICIENTS ON

TEMPERATURE, CONCENTRATION, AND MOLECULAR-WEIGHT *J. Polym. Sci., Part B: Polym. Phys* **1977**, *15*, 417-439.

51. Vrentas, J. S.; Duda, J. L., DIFFUSION IN POLYMER - SOLVENT SYSTEMS .1. RE-EXAMINATION OF FREE-VOLUME THEORY *J. Polym. Sci., Part B: Polym. Phys* **1977**, *15*, 403-416.

52. Vrentas, J. S.; Duda, J. L., SOLVENT AND TEMPERATURE EFFECTS ON DIFFUSION IN POLYMER-SOLVENT SYSTEMS *J. Appl. Poly. Soc* **1977**, *21*, 1715-1728.

53. Vrentas, J. S.; Duda, J. L., DIFFUSION OF SMALL MOLECULES IN AMORPHOUS POLYMERS *Macromolecules* **1976**, *9*, 785-790.

54. Vrentas, J. S.; Duda, J. L., DIFFUSION IN DILUTE POLYSTYRENE SOLUTIONS *J. Polym. Sci., Part B: Polym. Phys* **1976**, *14*, 101-109.

55. Vrentas, J. S.; Duda, J. L., RELATIONSHIPS BETWEEN DIFFUSION AND FRICTION COEFFICIENTS *J. Appl. Poly. Soc* **1976**, *20*, 2569-2574.

56. Vrentas, J. S.; Duda, J. L., DIFFUSION IN INFINITELY DILUTE POLYSTYRENE SOLUTIONS *J. Appl. Poly. Soc* **1976**, *20*, 1125-1131.

57. Bondi, A., *J. Phys. Chem.* **1964**, *68*, 441.

58. Park, J. Y.; Paul, D. R., *J. Membr. Sci.* **1997**, *125*, 23.

59. Thornton, A. W.; Nairn, K. M.; Hill, A. J.; Hill, J. M., New relation between diffusion and free volume: I. Predicting gas diffusion *J. Membr. Sci.* **2009**, *338*, 29-37.

60. Frisch, H. L. S., S. A., *Crit. Rev. Solid State Mater. Sci.* **1983**, *11*, 123.

61. Choi, U. H.; Ye, Y. S.; de la Cruz, D. S.; Liu, W. J.; Winey, K. I.; Elabd, Y. A.; Runt, J.; Colby, R. H., Dielectric and Viscoelastic Responses of Imidazolium-Based Ionomers with Different Counterions and Side Chain Lengths *Macromolecules* **2014**, *47*, 777-790.

62. Rosedale, J. H. B., F. S., *Macromolecules* **1990**, *23*, 2329.

63. Pixton, M. R.; Paul, D. R., *Relationship between structure and transport properties for polymers with aromatic backbones*. CRC Press: 1994.

64. Royal, J. S.; Victor, J. G.; Torkelson, J. M., PHOTOCROMIC AND FLUORESCENT-PROBE STUDIES IN GLASSY POLYMER MATRICES .4. EFFECTS OF PHYSICAL AGING ON POLY(METHYL METHACRYLATE) AS SENSED BY A SIZE DISTRIBUTION OF PHOTOCROMIC PROBES *Macromolecules* **1992**, *25*, 729-734.

65. Royal, J. S.; Torkelson, J. M., PHYSICAL AGING EFFECTS ON MOLECULAR-SCALE POLYMER RELAXATIONS MONITORED WITH MOBILITY-SENSITIVE FLUORESCENT MOLECULES *Macromolecules* **1993**, *26*, 5331-5335.

66. Miller, K. E.; Krueger, R. H.; Torkelson, J. M., MOBILITY-SENSITIVE FLUORESCENCE PROBES FOR QUANTITATIVE MONITORING OF WATER SORPTION AND DIFFUSION IN POLYMER-COATINGS *J. Polym. Sci., Part B: Polym. Phys* **1995**, *33*, 2343-2349.

67. Ellison, C. J.; Torkelson, J. M., Sensing the glass transition in thin and ultrathin polymer films via fluorescence probes and labels *J. Polym. Sci., Part B: Polym. Phys* **2002**, *40*, 2745-2758.

68. Siekierzycka, J. R. H., C.; Wuerthner, F.; Williams, R. M.; Brouwer, A. M., *Cent. Eur. J. Chem* **2014**, *12*, 937-952.

69. Victor, J. G.; Torkelson, J. M., PHOTOCROMIC AND FLUORESCENT-PROBE STUDIES IN GLASSY POLYMER MATRICES .3. EFFECTS OF PHYSICAL AGING AND MOLAR WEIGHT ON THE SIZE DISTRIBUTION OF LOCAL FREE VOLUME IN POLYSTYRENE *Macromolecules* **1988**, *21*, 3490-3497.

70. Vallee, R. A. L.; Cotlett, M.; Van der Auweraer, M.; Hofkens, J.; Mullen, K.; De Schryver, F. C., Single-molecule conformations probe free volume in polymers *Journal of the American Chemical Society* **2004**, *126*, 2296-2297.
71. Ammala, A.; Pas, S. J.; Lawrence, K. A.; Stark, R.; Webb, R. I.; Hill, A. J., Poly(m-xylene adipamide)-montmorillonite nanocomposites: effect of organo-modifier structure on free volume and oxygen barrier properties *J. Mater. Chem.* **2008**, *18*, 911-916.
72. Geise, G. M.; Doherty, C. M.; Hill, A. J.; Freeman, B. D.; Paul, D. R., Free volume characterization of sulfonated styrenic pentablock copolymers using positron annihilation lifetime spectroscopy *J. Membr. Sci.* **2014**, *453*, 425-434.
73. Meng, X. Y.; Liu, X.; Li, Z. X.; Zhou, Q., Positron Annihilation Lifetime Spectroscopy for Miscibility Investigations of Styrene-Butadiene-Styrene Copolymer/Polystyrene Blends *Polym. Eng. Sci.* **2014**, *54*, 785-793.
74. Rowe, B. W.; Pas, S. J.; Hill, A. J.; Suzuki, R.; Freeman, B. D.; Paul, D. R., A variable energy positron annihilation lifetime spectroscopy study of physical aging in thin glassy polymer films *Polymer* **2009**, *50*, 6149-6156.
75. Thornton, A. W.; Nairn, K. M.; Hill, A. J.; Hill, J. M.; Huang, Y., New relation between diffusion and free volume: II. Predicting vacancy diffusion *J. Membr. Sci.* **2009**, *338*, 38-42.
76. Zamfirova, G.; Misheva, M.; Perez, E.; Benavente, R.; Cerrada, M. L.; Djourelou, N.; Kresteva, M.; Perena, J. M., Norbornene-ethylene copolymers studied by non-destructive methods *Polym. J.* **2002**, *34*, 779-785.
77. Pethrick, R. A., POSITRON ANNIHILATION-A PROBE FOR NANOSCALE VOIDS AND FREE VOLUME? *Prog. Polym. Sci.* **1997**, *22*, 1.
78. Tao, S. J., *J. Chem. Phys.* **1972**, *56*, 5499.
79. Kammer, H. W.; Kressler, J.; Kummerloewe, C., PHASE-BEHAVIOR OF POLYMER BLENDS - EFFECTS OF THERMODYNAMICS AND RHEOLOGY *Adv. Polym. Sci.* **1993**, *106*, 31-85.
80. Larranaga, M.; Serrano, E.; Martin, M. D.; Tercjak, A.; Kortaberria, G.; de la Caba, K.; Riccardi, C. C.; Mondragon, I., Mechanical properties-morphology relationships in nano-/microstructured epoxy matrices modified with PEO-PPO-PEO block copolymers *Polym. Int.* **2007**, *56*, 1392-1403.
81. Miwa, Y.; Tanase, T.; Yamamoto, K.; Sakaguchi, M.; Sakai, M.; Shimada, S., Influence of chain end and molecular weight on molecular motion of polystyrene, revealed by the ESR selective spin-label method *Macromolecules* **2003**, *36*, 3235-3239.
82. Miwa, Y.; Yamamoto, K.; Sakaguchi, M.; Sakai, M.; Tanida, K.; Hara, S.; Okamoto, S.; Shimada, S., A site-specific ESR spin-labeling study of molecular motion in microphase-separated polystyrene-block-poly(methyl acrylate) with lamellar morphology *Macromolecules* **2004**, *37*, 831-839.
83. Svajdlenkova, H.; Bartos, J., Spin Probe Mobility in Relation to Free Volume and Relaxation Dynamics of Glass-Formers: A Series of Spin Probes in Poly(isobutylene) *J. Polym. Sci., Part B: Polym. Phys.* **2009**, *47*, 1058-1068.
84. Svajdlenkova, H.; Iskrova, M.; Sausa, O.; Dlubek, G.; Kristiak, J.; Bartos, J., The Spin Probe Dynamics and the Free Volume in a Series of Amorphous Polymer Glass-Formers *Polym. Spectros.* **2011**, *305*.
85. Dlubek, G.; Bamford, D.; Rodriguez-Gonzalez, A.; Petters, K.; Hubner, C.; Bornemann, S.; Lupke, T.; Henschke, O.; Stejny, J.; Alam, M. A.; Arnold, M., Local free volume and glass transition in propylene/alpha-olefin copolymers with a defined length and number of branches.

In *Positron Annihilation - Icpa-12*, Triftshauser, W.; Kogel, G.; Sperr, P., Eds. 2001; Vol. 363-3, pp 303-305.

86. Hsieh, T. T.; Tiu, C.; Simon, G. P., Correlation between molecular structure, free volume, and physical properties of a wide range of main chain thermotropic liquid crystalline polymers *J. Appl. Polym. Soc* **2001**, *82*, 2252-2267.

87. Kannappan, V.; Mahendran, S.; Sathyamoorthy, P.; Roopsingh, D., Ultrasonic method of determination of glass transition temperatures of certain thermotropic liquid crystalline copolyesters *J. Polym. Mater.* **2001**, *18*, 409-416.

88. Li, H. L.; Ujihira, Y.; Nanasawa, A., Evaluation of free volume in styrene-butadiene block copolymers probed by positron annihilation lifetime technique *Kobunshi Ronbunshu* **1998**, *55*, 456-464.

89. Srithawatpong, R.; Peng, Z. L.; Olson, B. G.; Jamieson, A. M.; Simha, R.; McGervey, J. D.; Maier, T. R.; Halasa, A. F.; Ishida, H., Positron annihilation lifetime studies of changes in free volume on cross-linking cis-polyisoprene, high-vinyl polybutadiene, and their miscible blends *J. Polym. Sci., Part B: Polym. Phys* **1999**, *37*, 2754-2770.

90. Kim, H. J.; Moon, H. C.; Kim, H.; Kim, K.; Kim, J. K.; Cho, J., Pressure Effect of Various Inert Gases on the phase Behavior of Polystyrene-block-Poly(n-pentyl methacrylate) Copolymer *Macromolecules* **2013**, *46*, 493-499.

91. Klepac, D.; Scetar, M.; Kurek, M.; Mallon, P. E.; Luyt, A. S.; Galic, K.; Valic, S., Oxygen permeability, electron spin resonance, differential scanning calorimetry and positron annihilation lifetime spectroscopy studies of uniaxially deformed linear low-density polyethylene film *Polym. Int.* **2013**, *62*, 474-481.

92. Lau, C. H.; Li, P.; Li, F.; Chung, T.-S.; Paul, D. R., Reverse-selective polymeric membranes for gas separations *Prog. Polym. Sci.* **2013**, *38*, 740-766.

93. Dlubek, G.; Bamford, D.; Rodriguez-Gonzalez, A.; Bornemann, S.; Stejny, J.; Schade, B.; Alam, M. A.; Arnold, M., Free volume, glass transition, and degree of branching in metallocene-based propylene/alpha-olefin copolymers: Positron lifetime, density, and differential scanning calorimetric studies *J. Polym. Sci., Part B: Polym. Phys* **2002**, *40*, 434-453.

94. Budd, P. M.; McKeown, N. B.; Fritsch, D., Free volume and intrinsic microporosity in polymers *J. Mater. Chem.* **2005**, *15*, 1977-1986.

95. Sodaye, H. S.; Pujari, P. K.; Goswami, A.; Manohar, S. B., Probing the microstructure of Nafion-117 using positron annihilation spectroscopy *J. Polym. Sci., Part B: Polym. Phys* **1997**, *35*, 771-776.

96. Trotzig, C.; Abrahmsen-Alami, S.; Maurer, F. H. J., Transport properties of water in hydroxypropyl methylcellulose *Eur. Polym. J.* **2009**, *45*, 2812-2820.

97. Kanehashi, S.; Koyama, Y.; Ando, S.; Konishi, S.; Shindo, R.; Miyata, S.; Sato, S.; Miyakoshi, T.; Nagai, K., Characterization and water vapor sorption property of ABA-type triblock copolymers derived from polyimide and poly(methyl methacrylate) *Polym. Int.* **2014**, *63*, 435-444.

98. Ramesh, N.; Davis, P. K.; Zielinski, J. M.; Danner, R. P.; Duda, J. L., Application of Free-Volume Theory to Self Diffusion of Solvents in Polymers Below the Glass Transition Temperature: A Review *J. Polym. Sci., Part B: Polym. Phys* **2011**, *49*, 1629-1644.

99. Lin, H.; Freeman, B. D., *J. Membr. Sci.* **2004**, *239*, 105-117.

100. Lin, H. Q.; Van Wagner, E.; Swinnea, J. S.; Freeman, B. D.; Pas, S. J.; Hill, A. J.; Kalakkunnath, S.; Kalika, D. S., Transport and structural characteristics of crosslinked poly(ethylene oxide) rubbers *J. Membr. Sci.* **2006**, *276*, 145-161.

101. Blok, A. J.; Chhasatia, R.; Dilag, J.; Ellis, A. V., Surface initiated polydopamine grafted poly(2-(methacryloyloxy)ethyl trimethylammonium chloride) coatings to produce reverse osmosis desalination membranes with anti-biofouling properties *J. Membr. Sci.* **2014**, *468*, 216-223.
102. Devi, S.; Ray, P.; Singh, K.; Singh, P. S., Preparation and characterization of highly microporous PVDF membranes for desalination of saline water through vacuum membrane distillation *Desalination* **2014**, *346*, 9-18.
103. Lei, Y. L.; Luo, Y. J.; Chen, F.; Mei, L. H., Sulfonation Process and Desalination Effect of Polystyrene/PVDF Semi-Interpenetrating Polymer Network Cation Exchange Membrane *Polymer* **2014**, *6*, 1914-1928.
104. Venugopal, K.; Dharmalingam, S., Evaluation of synthetic salt water desalination by using a functionalized polysulfone based bipolar membrane electro dialysis cell *Desalination* **2014**, *344*, 189-197.
105. Zhao, D. L.; Wang, P.; Zhao, Q. P.; Chen, N. P.; Lu, X. M., Thermoresponsive copolymer-based draw solution for seawater desalination in a combined process of forward osmosis and membrane distillation *Desalination* **2014**, *348*, 26-32.
106. Consolati, G.; Kansy, J.; Pegoraro, M.; Quasso, F.; Zanderighi, L., Positron annihilation study of free volume in cross-linked amorphous polyurethanes through the glass transition temperature *Polymer* **1998**, *39*, 3491-3498.
107. Dlubek, G.; Pionteck, J.; Sniegocka, M.; Hassan, E. M.; Krause-Rehberg, R., Temperature and pressure dependence of the free volume in the perfluorinated polymer glass CYTOP: A positron lifetime and pressure-volume-temperature study *J. Polym. Sci., Part B: Polym. Phys* **2007**, *45*, 2519-2534.
108. Kilburn, D.; Wawryszczuk, J.; Dlubek, G.; Pionteck, J.; Hassler, R.; Alam, M. A., Temperature and pressure dependence of the free volume in polyisobutylene from positron lifetime and pressure-volume-temperature experiments *Macromol. Chem. Phys.* **2006**, *207*, 721-734.
109. Gacal, B. N.; Filiz, V.; Shishatskiy, S.; Rangou, S.; Neumann, S.; Abetz, V., Modification of polyisoprene-block-poly(vinyl trimethylsilane) block copolymers via hydrosilylation and hydrogenation, and their gas transport properties *J. Polym. Sci., Part B: Polym. Phys* **2013**, *51*, 1252-1261.
110. Park, C. H.; Tocci, E.; Kim, S.; Kumar, A.; Lee, Y. M.; Drioli, E., A Simulation Study on OH-Containing Polyimide (HPI) and Thermally Rearranged Polybenzoxazoles (TR-PBO): Relationship between Gas Transport Properties and Free Volume Morphology *J. Phys. Chem. B* **2014**, *118*, 2746-2757.
111. Odian, G., *Principles of Polymerization, Fourth Edition*. 2004.
112. He, C. Q.; Dai, Y. Q.; Wang, B.; Wang, S. J., Molecular weight effect on the microstructure and local motion in high molecular weight polymer observed by positrons. In *Positron Annihilation - Icpa-12*, Triftshauer, W.; Kogel, G.; Sperr, P., Eds. Trans Tech Publications Ltd: Zurich-Uetikon, 2001; Vol. 363-3, pp 309-312.
113. West, D. H. D.; McBrierty, V. J.; Delaney, C. F. G., POSITRON DECAY IN POLYMERS - MOLECULAR-WEIGHT DEPENDENCE IN POLYSTYRENE *Applied Physics* **1975**, *7*, 171-174.
114. Suvegh, K.; Klapper, M.; Domjan, A.; Mullins, S.; Wunderlich, W.; Vertes, A., Free volume distribution in monodisperse and polydisperse poly(methyl methacrylate) samples *Macromolecules* **1999**, *32*, 1147-1151.

115. McKee, M. G.; Unal, S.; Wilkes, G. L.; Long, T. E., Branched polyesters: recent advances in synthesis and performance *Prog. Polym. Sci.* **2005**, *30*, 507-539.
116. Mader, D. H., J.; Walter, P.; Mulhaupt, R., *Macromolecules* **2000**, *33*, 1254.
117. Kusuma, V. A.; Freeman, B. D.; Smith, S. L.; Heilman, A. L.; Kalika, D. S., Influence of TRIS-based co-monomer on structure and gas transport properties of cross-linked poly(ethylene oxide) *J. Membr. Sci.* **2010**, *359*, 25-36.
118. Kusuma, V. A.; Matteucci, S.; Freeman, B. D.; Danquah, M. K.; Kalika, D. S., Influence of phenoxy-terminated short-chain pendant groups on gas transport properties of cross-linked poly(ethylene oxide) copolymers *J. Membr. Sci.* **2009**, *341*, 84-95.
119. Ma, S. C.; Lin, H. L.; Yu, T. L., GLASS-TRANSITION TEMPERATURE, FREE-VOLUME, AND CURING KINETICS OF UNSATURATED POLYESTER *Polym. J.* **1993**, *25*, 897-907.
120. Jean, Y. C.; Deng, Q.; Nguyen, T. T., Free-volume hole properties in thermosetting plastics probed by positron annihilation spectroscopy: Chain extension chemistry *Macromolecules* **1995**, *28*, 8840-8844.
121. Wang, W. J.; Li, C. H.; Cao, Y. X.; Chen, J. Z.; Wang, J. W., Rheological Characteristics and Morphologies of Styrene-Butadiene-Maleic Anhydride Block Copolymers *J. Appl. Poly. Soc* **2012**, *123*, 3234-3241.
122. Hasegawa, T.; Iwasaki, Y.; Ishihara, K., Preparation and performance of protein-adsorption-resistant asymmetric porous membrane composed of polysulfone/phospholipid polymer blend *Biomaterials* **2001**, *22*, 243-251.
123. Jangu, C.; Savage, A. M.; Zhang, Z. Y.; Schultz, A. R.; Madsen, L. A.; Beyer, F. L.; Long, T. E., Sulfonimide-Containing Triblock Copolymers for Improved Conductivity and Mechanical Performance *Macromolecules* **2015**, *48*, 4520-4528.
124. Jangu, C.; Wang, J. H. H.; Wang, D.; Sharick, S.; Heflin, J. R.; Winey, K. I.; Colby, R. H.; Long, T. E., Well-Defined Imidazolium ABA Triblock Copolymers as Ionic-Liquid-Containing Electroactive Membranes *Macromol. Chem. Phys.* **2014**, *215*, 1319-1331.
125. Cui, X. G.; Wang, X. D., Preparation, morphology, and properties of multilamellar barrier materials based on blends of high-density polyethylene and copolyester *J. Appl. Poly. Soc* **2006**, *101*, 3791-3799.
126. Donadi, S.; Modesti, M.; Lorenzetti, A.; Besco, S., PET/PA Nanocomposite Blends with Improved Gas Barrier Properties: Effect of Processing Conditions *J. Appl. Poly. Soc* **2011**, *122*, 3290-3297.
127. Ophir, A.; Dotan, A.; Belinsky, I.; Kenig, S., Barrier and Mechanical Properties of Nanocomposites Based on Polymer Blends and Organoclays *J. Appl. Poly. Soc* **2010**, *116*, 72-83.
128. Low, B. T.; Chung, T. S.; Chen, H.; Jean, Y.-C.; Pramoda, K. P., Tuning the Free Volume Cavities of Polyimide Membranes via the Construction of Pseudo-Interpenetrating Networks for Enhanced Gas Separation Performance *Macromolecules* **2009**, *42*, 7042-7054.
129. Ju, H.; Sagle, A. C.; Freeman, B. D.; Mardel, J. I.; Hill, A. J., Characterization of sodium chloride and water transport in crosslinked poly(ethylene oxide) hydrogels *J. Membr. Sci.* **2010**, *358*, 131-141.
130. Trotzig, C. A.-A., S.; Maurer, F. H. J., Structure and mobility in water plasticized poly(ethylene oxide) *Polymer* **2007**, *48*, 3294.
131. Lee, J.; Doherty, C. M.; Hill, A. J.; Kentish, S. E., Water vapor sorption and free volume in the aromatic polyamide layer of reverse osmosis membranes *J. Membr. Sci.* **2013**, *425*, 217-226.
132. Robertson, J. E.; Ward, T. C.; Hill, A. J., *Polymer* **2000**, *41*, 6251-6262.

133. Sharma, S. K.; Prakash, J.; Sudarshan, K.; Maheshwari, P.; Sathiyamoorthy, D.; Pujari, P. K., Effect of interfacial interaction on free volumes in phenol-formaldehyde resin-carbon nanotube composites: positron annihilation lifetime and age momentum correlation studies *Physical Chemistry Chemical Physics* **2012**, *14*, 10972-10978.
134. Rezac, M. E.; Tilo, J., *Polymer* **1998**, *39*, 599.

# Chapter 3: Advances in Electrolytes: Phosponium-based Ionic Liquids and Poly(Ionic Liquid)s

*(Manuscript in preparation for publication)*

*Mingtao Chen, B. Tyler White, Christopher R. Kasprzak, and Timothy E. Long\**

Macromolecules Innovation Institute, Virginia Tech, Blacksburg, 24061, USA  
Department of Chemistry, Virginia Tech, Blacksburg, 24061, USA

\*To whom correspondence should be addressed: [telong@vt.edu](mailto:telong@vt.edu)

## 3.1 Abstract

Ionic liquids (ILs) and poly(ionic liquid)s (PILs) are attracting increasing research interest as safe and efficient electrolytes. Most research efforts focus on nitrogen based ILs and PILs (ammonium, imidazolium, pyridinium, *etc.*), while phosphorus based ILs and PILs have received less attention despite exhibiting higher ion conductivity over their nitrogen-based counterparts. In this review, we provide an overview of the structural elements in phosphorus based ILs and PILs that alter ion conductivity, such as size of ions, polarizability of ions, counterion identity, and backbone flexibility. We also highlight dominant physical parameters dictating ion conductivity including viscosity and glass transition temperature. A fundamental understanding of this structure-ion conductivity relationship will benefit the future rational design of phosphorus based ILs and PILs as electrolytes.

## 3.2 Introduction

Ionic liquids (ILs) and poly(ionic liquid)s (PILs) are standing on the verge of a great breakthrough in battery design as neoteric electrolytes. An obvious question to ask is: Why study ILs and PILs as electrolytes when commonly used solvent-based electrolytes

seem to work fine? The answer is that solvent-based electrolytes are no longer safe as industry pursues batteries with low volume and higher power density. Two urgent safety concerns for today's battery fabrication are dendrite formation from electrodes (in lithium batteries) and flammability of organic solvent in electrolytes. ILs and PILs promise great potential to resolve both safety concerns and pave the way towards next generation electrolytes.

Historically, ILs are defined as molten salts with a melting temperature below the boiling point of water.<sup>1</sup> Typical attributes of ILs include high stability (thermally, chemically, and electrochemically), negligible volatility, and high concentration of ions.<sup>1-2</sup> The combination of high stability and negligible volatility grant ILs two important advantages over solvent-based electrolytes: safety towards fire hazards and wide liquid-phase windows. High density of ions impart high ion conductivities, which is also important when employing ILs as electrolytes.

However, ILs still encounter safety concerns stemming from uncontrolled dendritic lithium formation, which results in continuous electrolyte decomposition. A simple solution is to introduce mechanical integrity to the electrolytes to avoid electric short caused by dendrite penetration.<sup>3</sup> Hence, PILs (macromolecular forms of polymerizable ILs) have continually drawn more attention, as PILs and crosslinked ILs normally show greater mechanical integrity than their ILs analogs. However, the tradeoff is lower ion conductivities. As shown in **Figure 3.1**, various PILs architectures are under investigation in the current literature, such as singly-charged polymers, zwitterionic polymers, polyelectrolyte blends, and ion-containing block copolymers. While PILs give tunable mechanical integrity as well as superb morphology control, the decreased ion

mobility in polymeric matrices is detrimental to ion conductivity. During the endeavor to solve this paradox between mechanical integrity and ion conductivities, researchers have chosen two quite different, but equally effective approaches: 1) Increase the mechanical integrity of ILs; 2) Increase the ion conductivities of PILs.

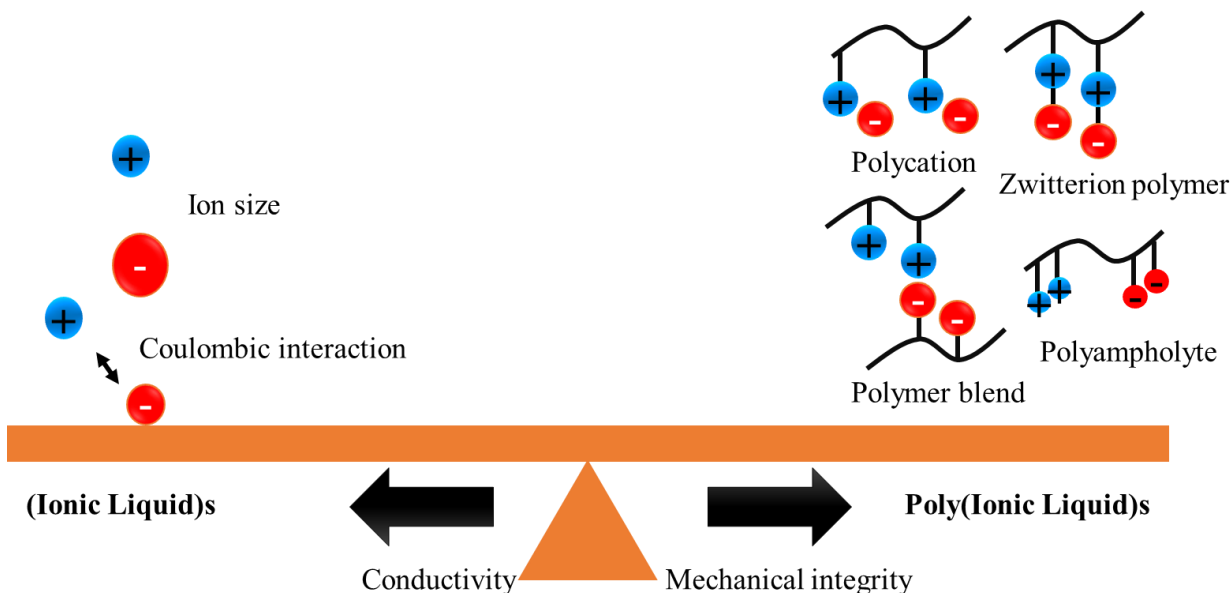


**Figure 3.1** Comparison between ILs and PILs in mechanical integrity and ion conductivity.

Lodge *et al.* have pioneered the work on enhancing the mechanical integrity of ILs, and promised the potential of ion gels as solid electrolytes with excellent ion conductivities.<sup>2, 4-6</sup> Ion gels consist of block copolymers swollen in ILs, which serve as solvents for block copolymer. Block copolymers provide physical crosslinks as one of the blocks is insoluble in the ILs chosen and self-assembles into aggregates. The resulting soft ion gels showed good elasticity (up to 350% strain and  $10^3$  to  $10^5$  Pa elastic storage modulus) as well as high ion conductivities. Another attempt focuses on increasing ion mobility in PILs.<sup>2, 5</sup> To improve ion conductivity of polymeric matrices, Drockenmuller and coworkers synthesized 1,2,3-triazolium-based PILs with siloxane backbones.<sup>7</sup> The

siloxane backbone decreased glass transition temperature ( $T_g$ ) to as low as  $-100\text{ }^\circ\text{C}$ , and led to promising ion conductivity even at room temperature ( $0.63\text{ mS/cm}$ ). Long *et al.* studied a series of imidazolium-based PILs, and achieved more than an order of magnitude increase in ion conductivities when switching counter ions from trifluoromethane sulfonate ( $\text{TfO}^-$ ) to bis(trifluoromethane sulfonyl)imide ( $\text{Tf}_2\text{N}^-$ ).<sup>8</sup>

Current research of novel ILs and PILs electrolytes have primarily involved nitrogen-based (N-based) salts, such as imidazolium,<sup>5, 8-11</sup> pyridinium,<sup>12</sup> 1,2,3-triazolium,<sup>7, 13</sup> ammonium,<sup>14</sup> *etc.* In contrast, quaternary phosphonium-based (P-based) ILs and PILs received much less research attention despite their advantages compared to N-based counterparts. P-based ILs and PILs show improved thermal stability,<sup>15-17</sup> base stability,<sup>18</sup> and ion conductivities<sup>15-16</sup> compared to their N-based analogs. For instance, Long *et al.* compared poly(4-vinylbenzyl ammonium) and poly(4-vinylbenzyl phosphonium) homopolymers with various alkyl substitutes, and P-based PILs showed an over  $100\text{ }^\circ\text{C}$  increase of thermal degradation temperatures.<sup>15</sup> Ammonium salts undergo Hoffman elimination and/or reverse Menshutkin degradation (for benzylic protons). In contrast, phosphonium salts are less vulnerable to both degradation pathways, leading to higher thermal stability.<sup>19</sup> Phosphonium PILs also exhibited higher ion conductivities (normalized with  $T_g$ ) compared to their ammonium counterparts. Coates and coworkers reported the synthesis of polyethylene functionalized with phosphonium pendant groups as alkaline anion exchange membranes.<sup>18</sup> When comparing the base stability of N-based and P-based ILs, P-based ILs showed no backbone degradation in  $1\text{ M NaOD/CD}_3\text{OD}$  at  $80\text{ }^\circ\text{C}$  after 20 d while N-based ILs reported a 66% degradation.

In summary, P-based ILs and PILs exhibits great potential as novel electrolytes materials, but remain underexploited compared to their ammonium analogs. Although ILs and PILs have found various application in gas separation,<sup>20-26</sup> antimicrobial coating,<sup>27-29</sup> and gene delivery,<sup>30-31</sup> this review intends to address the structure-property relationship of P-based ILs and PILs as electrolytes and conductive materials only. For this purpose, we will not address the synthesis methods of P-based ILs<sup>32</sup> and the study of ionic liquid solutions.<sup>33</sup>

### **3.3 Phosphonium-based ionic liquids**

Ionic liquids (ILs) are superior electrolytes materials compared to solvent-based electrolytes in most aspects, such as volatility, thermal stability, and ion concentration. However, one critical drawback of ILs is their high viscosity, normally 1 ~ 3 orders of magnitude higher than organic solvent-based electrolytes.<sup>34</sup> High viscosity restricts mass transfer and significantly decreases ion conductivities. Hence, research has focused on altering the viscosity of ILs through rational design of cations and anions to eventually achieve tunable ion conductivities.

Inter- and intra-molecular interactions are the key factors to lower viscosity and increased ion conductivities. The size, shape and symmetry of ions dominate the characteristic physical properties of ILs. For instance, hexafluorophosphate anions ( $\text{PF}_6$ ) exhibited high viscosity, while bulkier and less symmetric bis(trifluoromethane sulfonyl)imide anions ( $\text{Tf}_2\text{N}$ ) showed much lower viscosity.<sup>35</sup> A similar argument can be applied to cations. Longer alkyl substituents lead to an increase in viscosity due to increased van der Waals interactions between cations.<sup>36-37</sup> Branching of alkyl substituents, on the other hand, reduces viscosity as a result of decreased van der Waals interactions.<sup>38</sup> P-based ILs

almost always showed lower viscosity compared to their N-based counterparts, granting them higher ion conductivity.

Tsunashima *et al.* synthesized a series of P-based ILs, PRR'<sub>3</sub>, with various R groups (R' was fixed), and studied their viscosity-conductivity relationship (structure shown in **Figure 3.2a**).<sup>16, 39-40</sup> **Figure 3.2a** described the change of ion conductivities and viscosity of P-based IL when varying substituents. For *n*-alkyl substituents, P-based ILs with longer alkyl substituents showed significantly higher viscosity than those with shorter alkyl substituents, ascribed to increased van der Waals interactions as a result of increased molecular weight. Ion conductivities of ILs follow an inverse relationship with viscosity. Hence, P-based ILs with shortest alkyl substituents demonstrated the highest ion conductivities (1.73 mS/cm). This trend has been confirmed by various P-based ILs with various counter anions.<sup>17, 41-43</sup> Aromatic substituents introduced more van der Waals interaction, which lead to high viscosity (248 mPa•S) and low ion conductivities (0.74 mS/cm).<sup>16</sup> The introduction of carbon-carbon double bonds lowered the viscosity from 88 mPa•S (pentyl) to 71 mPa•S (pentenyl), leading to an increase of ion conductivity from 1.73 mS/cm to 2.10 mS/cm (**Figure 3.2a**).<sup>39</sup> The authors attributed the decreased viscosity to the weakening of hydrogen bonding. Further enhancement of ion conductivities was achieved when introducing methoxy end groups. A possible explanation involved electron donation from the methoxy groups to the cationic centers which reduces the positive charge on the cation. As a result, the weakened electrostatic interaction between ions leads to a decrease of viscosity, and consequently an increase of ion conductivities.<sup>44</sup>

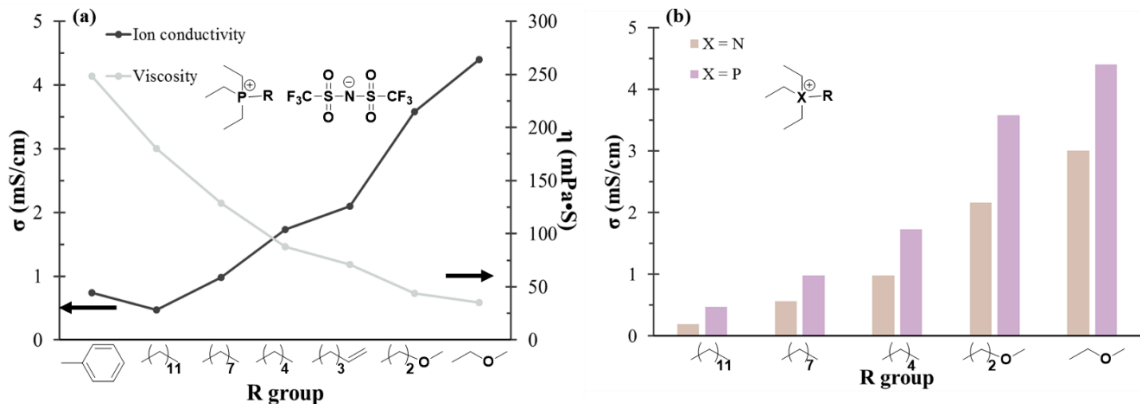


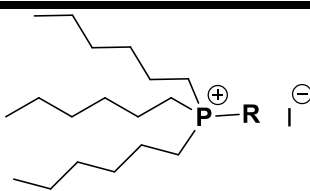
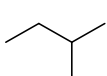
**Figure 3.2** Ion conductivities and viscosity of phosphonium-based and ammonium based ILs with different substituents.  $T = 25\text{ }^{\circ}\text{C}$ , counter ions =  $\text{Tf}_2\text{N}^-$ .<sup>39-40</sup>

Comparing the ion conductivities of P-based ILs and their N-based ILs counter parts, P-based ILs improved ion conductivity regardless of the substituents (**Figure 3.2b**).<sup>40</sup> P-based ILs showed a larger deviation from the ideal Walden line (the ion conductivity of 0.01 M KCl aqueous solution as a function of viscosity to represent full ionization) than N-based ILs in the non-ionic region, indicating weaker electrostatic interactions due to a decrease in viscosity and enhances ion conductivity. P-based ILs with methoxy end groups showed even further deviation from the ideal Walden line, further supporting above argument on methoxy groups weakening electrostatic interactions. Similarly, when varying R' group in  $\text{PRR}'_3$  type ILs, P-based ILs showed higher ion conductivity (0.42 mS/cm) than its N-based analogs (0.31 mS/cm) due to lower viscosity.<sup>45</sup> Interestingly, even P-based ILs with aromatic substituents exhibited much lower viscosity than N-based ILs with alkyl substituents at any given temperature.<sup>46</sup> Colby and coworkers provided a rationale for the supreme ion conductivity of P-based PILs based on electron negativity argument, which will be covered in a later section.<sup>47-48</sup>

Branching of substituents efficiently decreases viscosity and increases ion conductivities. Tri(methyl) *n*-propylphosphonium  $\text{Tf}_2\text{N}$  is a crystalline solid at room temperature,<sup>49</sup>

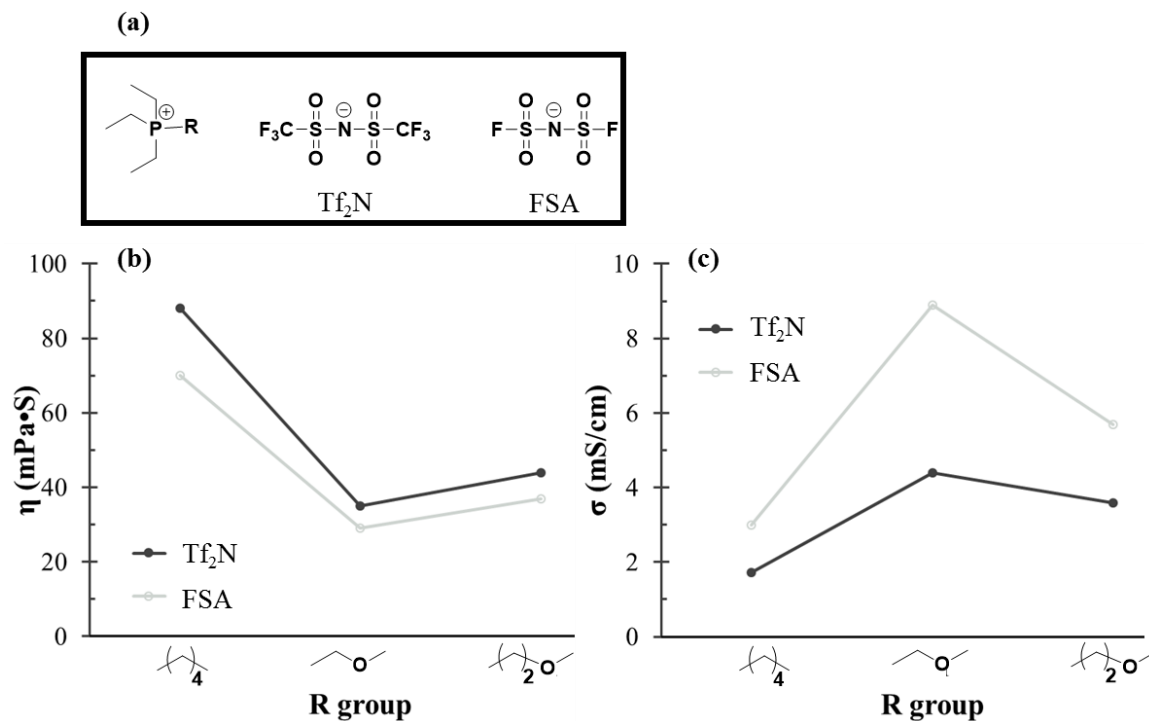
while tri(methyl) *i*-butylphosphonium Tf<sub>2</sub>N is a room temperature ionic liquid (RTIL) with 7.3 mS/cm ion conductivity.<sup>50</sup> Sanchez *et al.* studied the electrical and physical properties of quaternary P-based ILs with iodide (I) as counter anions.<sup>51-53</sup> As depicted in **Table 3.1**, P-based IL with *i*-butyl substituents ( $0.38 \times 10^{-3}$  mS/cm) nearly doubled the ion conductivities of that with *n*-butyl substituents ( $0.21 \times 10^{-3}$  mS/cm) at 25 °C. The authors attributed the increase of ion conductivities to reduced van der Waals interaction.

**Table 3.1** Ion conductivity of P-based ILs with various alkyl substituents (T = 25 °C)<sup>51</sup>

	$\sigma$ (mS/cm)
	
R = 	$0.21 \times 10^{-3}$
R = 	$0.38 \times 10^{-3}$

Instead of designing and synthesizing novel ILs, counter ion exchange of already existing ILs provides a facile approach to alter IL viscosity and its consequent ion conductivity. Tsunashima evaluated two series of quaternary P-based ILs with two different counter anions: Tf<sub>2</sub>N and bis(fluorosulfonyl)amide (FSA) as potential electrolytes (structures shown in **Figure 3.3a**).<sup>40, 54</sup> ILs with Tf<sub>2</sub>N counter anions exhibited excellent ion conductivities (within mS/cm range) at 25 °C, as Tf<sub>2</sub>N only provides weak electrostatic interactions due to its bulkiness and delocalized charge. Ion exchange from Tf<sub>2</sub>N to FSA further decreased the viscosity of ILs (**Figure 3.3b**). As a result, ILs with FSA counter anions showed even higher ion conductivities at various test temperatures. Furthermore, the methoxy groups increased ion conductivities as a result of lower viscosity. However,

the increase of ion conductivities from FSA counter anions came at a cost of thermal stability. ILs with FSA anions were thermally stable up to approximately 300 °C while those with Tf<sub>2</sub>N anions showed no degradation until 380 °C. Tsunashima *et al.* also demonstrated, in another study, that tri(methyl) methoxyphosphonium Tf<sub>2</sub>N (4.1 mS/cm) showed half the conductivity of tri(methyl) methoxyphosphonium FSA (8.9 mS/cm).<sup>49</sup>

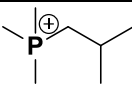
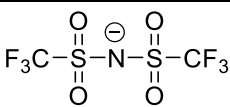
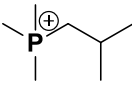
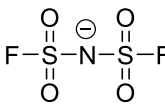
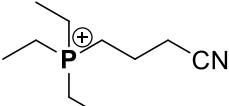
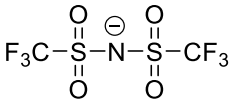
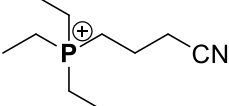
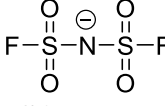


**Figure 3.3** Comparison of P-based ILs with different counter anions (T = 25 °C).<sup>40, 54</sup>

Howlett *et al.* observed similar enhancement of ion conductivities when replacing Tf<sub>2</sub>N counter anions with FSA anions.<sup>55</sup> As depicted in **Table 3.2**, both quaternary P-based ILs with FSA counter anions showed significantly higher ion conductivities than their counterparts with Tf<sub>2</sub>N anions. Viscosity of ILs exhibited an inverse relationship with ion conductivities as expected. When comparing different cations, molecular weight controlled both viscosity and ion conductivities. Lower molecular weight P<sub>111i4</sub> exhibited lower viscosity and higher ion conductivity compared to P<sub>CN</sub>. Other researchers have also

shown the influence of a wide variety of counter ions on ion conductivities through viscosity control.<sup>56-57</sup>

**Table 3.2** Ion conductivities of P-based ILs with different counter ions (T = 50 °C)<sup>55</sup>

Cations	Anions	$\sigma$ (mS/cm)
 <b>P111i4</b>	 <b>Tf<sub>2</sub>N</b>	5.1
 <b>P111i4</b>	 <b>FSA</b>	13.8
 <b>PCN</b>	 <b>Tf<sub>2</sub>N</b>	1.9
 <b>PCN</b>	 <b>FSA</b>	5.0

Battez *et al.* probed the possibility of employing phosphate counter anions, and studied the influence of counter ions on the conductivities of P-based ILs.<sup>58</sup> Phosphate anions demonstrated significantly higher viscosity than Tf<sub>2</sub>N counter anions, resulting in a drastic decrease of ion conductivities from 0.14 mS/cm to  $0.97 \times 10^{-3}$  mS/cm as shown in **Table 3.3**. Although the ion conductivities of phosphate anions are not promising compared to traditional counter ions, this study promises a potential application of P-based ILs in bio-related fields, where phosphates are widely employed. Zhang *et al.* also showed an interesting approach of utilizing amino acid-based phosphonium ILs in biological applications.<sup>20</sup>

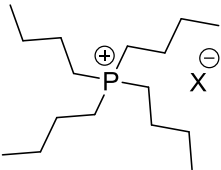
**Table 3.3** Viscosity and ion conductivities of P-based ILs with different counter ions (T = 25 °C)<sup>58</sup>

	$\eta$ (mPa·S)	$\sigma$ (mS/cm)
X =	1064	$0.97 \times 10^{-3}$
X =	1050	$0.19 \times 10^{-3}$ (27 °C)
X =	296	0.14

The effect of counter ions on ion conductivities is more profound and complicated when strong electrostatic interaction are present. **Table 3.4** showed that the ion conductivities of symmetric quaternary P-based ILs with halide counter anions followed the order of (FH)<sub>2.3</sub>F (3.7 mS/cm) > Cl ( $2.4 \times 10^{-6}$  mS/cm) > Br (not detectable).<sup>41, 59</sup> Unlike ILs with relatively weak electrostatic interactions, smaller halide counter anions are advantageous for ion conductivities. The distribution of charge (or polarizability) is not a significant factor for halide counter anions. Instead, smaller ion size affords higher mobility, leading to higher ion conductivities. Another important phenomena of P-based ILs with halide counter ions is the effective shielding of electrostatic interactions.<sup>59</sup> As halide-containing ILs have strong electrostatic interactions, the alkyl substituents of the phosphonium cation requires a specific length to achieve effective shielding of electrostatic interactions. Otherwise, extra electrostatic interactions from incomplete shielding will cause an increase of viscosity and thus an increase of ion conductivities. For instance,

PR<sub>4</sub>Br ILs exhibited a decrease in ion conductivity from  $2.0 \times 10^{-7}$  mS/cm (hexyl substituents) to  $1.9 \times 10^{-8}$  mS/cm (octyl substituents) and  $6.2 \times 10^{-10}$  mS/cm (decanyl substituents) as expected.<sup>59</sup> However, PR<sub>4</sub>Br with butyl substituents showed significantly lower ion conductivities, which is comparable to PR<sub>4</sub>Br with dodecyl substituents.

**Table 3.4** Ion conductivities of P-based ILs with halide counter anions (T = 25 °C)<sup>41, 59</sup>

	$\sigma$ (mS/cm)
X = (FH) <sub>2,3</sub> F	3.7
X = Cl	$2.4 \times 10^{-6}$
X = Br	N/A

Addition of salts is normally detrimental to ion conductivities. The increase of ion concentration from salt addition is insignificant in ILs as ILs already have high ion concentration. Instead, the addition of salts causes an increase of viscosity due to ion aggregates, resulting in lower ion conductivity.<sup>50</sup> Howlett *et al.* studied the effect of lithium Tf<sub>2</sub>N salts (LiTf<sub>2</sub>N) on the viscosity and ion conductivities of P-based ILs (structure shown in **Figure 3.4a**).<sup>50</sup> The addition of lithium salt lowered both melting temperatures (T<sub>m</sub>) and crystallization temperatures (T<sub>c</sub>) while increasing T<sub>g</sub> indicative of less mobility. **Figure 3.4a** demonstrated the changes of viscosity and ion conductivity as a function of salt concentration. Neat ILs showed the highest ion conductivities of 7.3 mS/cm at 50 °C, and increasing salt concentration led to a decrease in ion conductivity. Ion conductivity exhibited an inverse relationship with viscosity, suggesting viscosity is the dominant factor of conductivity changes. Howlett and coworkers further extended their investigation to three different quaternary P-based ILs with FSA as counter anions,

and observed a similar increase of  $T_g$  due to salt addition (structure shown in **Figure 3.4b**).<sup>55</sup> Higher  $T_g$  imparted restricted mobility and higher viscosity causing ion conductivity to decrease at higher salt concentrations (**Figure 3.4b**). The Walden plots of both neat ILs and ILs with salts are similar, indicating salt addition has limited impact on ion association, and the decrease of ion conductivity through salt addition is predominantly due to increased viscosity.

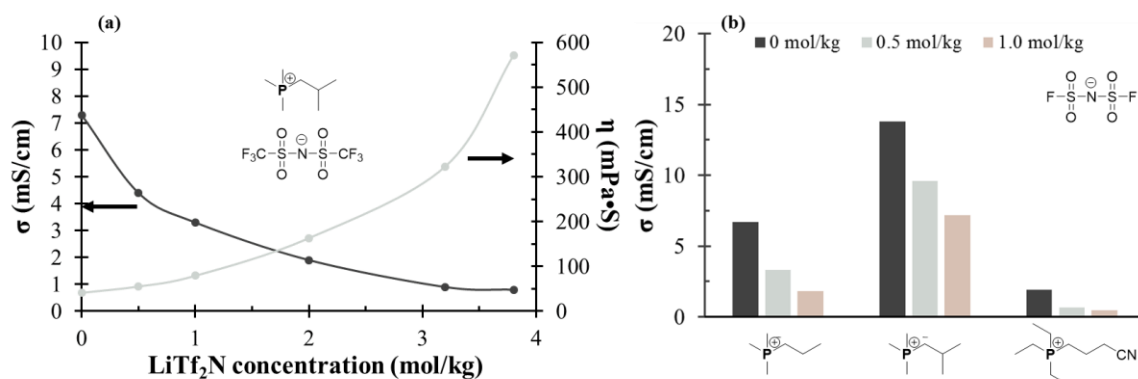


**Figure 3.4** Influence of lithium salt concentration on (a) viscosity and ion conductivities of P-based ILs;<sup>50</sup> (b) ion conductivities of various P-based ILs ( $T = 50\text{ }^{\circ}\text{C}$ ).<sup>55</sup>

Torresi *et al.* synthesized methoxy substituted P-based ILs, and studied the influence of LiTf<sub>2</sub>N salt addition on viscosity and ion conductivity.<sup>60</sup> Similar to alkyl substituted ILs, salt addition increased viscosity and decreased the diffusion of both cations and anions significantly at low temperature while the viscosity change diminished at high temperature (**Figure 3.5a**). Correspondently, ion conductivities were significantly different between neat ILs and ILs with salt at elevated temperature, but the difference diminished at low temperature (**Figure 3.5b**). Amine and coworkers observed the same reverse relationship between salt concentration and ion conductivities for siloxane functionalized P-based ILs.<sup>61</sup>

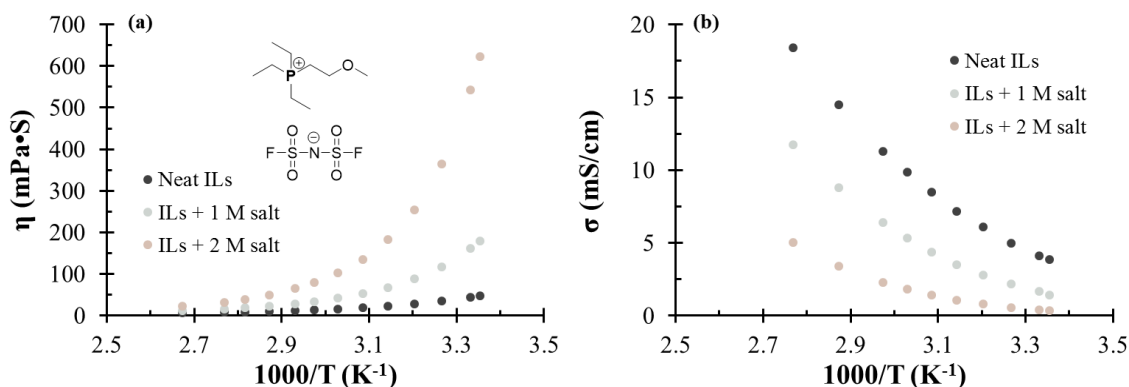


**Figure 3.5** Temperature dependence of (a) viscosity and (b) ion conductivities in P-based ILs with different salt concentration.<sup>60</sup>

Another attempt to further increase charge density in ILs is multi-charged systems, such as divalent anions<sup>62</sup> and zwitterions.<sup>63</sup> Similar to the discussion on salt addition, multi-charged ILs intensify electrostatic interactions significantly, which dictates viscosity changes. Grinstaff *et al.* compared P-based ILs with mono- and di-phosphonium cations, and observed a five orders of magnitude increase in viscosity and approximately five times decrease in ion conductivities when replacing monophosphonium cations with diphosphonium cations.<sup>64</sup> Runde and coworkers showed that tetra-alkyl P-based IL with oxalate (divalent anion) was a semi-solid at room temperature while its counterpart with carboxyformate (monovalent anion) was a RTIL.<sup>62</sup> Ohno synthesized zwitterion ILs with phosphonium cations and sulfonate anions, and studied their potential as electrolytes with high transfer number of selective ions.<sup>63</sup> The ion conductivity of ILs with equimolar addition of HTf<sub>2</sub>N showed strong dependence on humidity and morphology. 20 wt% water increased ion conductivity to 2.0 mS/cm at 25 °C, approximately 50 times higher than dry ILs mixture. The authors ascribed the enhancement of ion conductivities to the formation of hydrogen bonding networks through water molecules, which leads to improved proton transfer. Transformation from polydomain to monodomain liquid-

crystalline state further increased the ion conductivity to 79 mS/cm at 25 °C. On heating, ion conductivities showed minimal variation until the isotropic temperatures, which led to a significant reduction of ion conductivities. Seki *et al.* reported a similar counterintuitive conductivity dependence on temperatures as a result of phase transitions.<sup>65</sup>

A few studies also addressed the possibility of P-based ILs in an organic-inorganic hybrid system. Phosphonium cations coupled with polyoxometalate (POM) afforded ILs with high viscosity at low temperature.<sup>66</sup> However, the viscosity of POM-IL hybrid decreased faster than its analog with bromide anions, suggesting its use as high temperature electrolytes or semiconductors. Other counter anions under investigation in P-based ILs includes borate anions,<sup>67</sup> pyrazolide,<sup>42</sup> and indazolide.<sup>42</sup>

### **3.4 Phosphonium-based poly(ionic liquid)s**

Poly(ionic liquid)s (PILs) are macromolecular forms of polymerizable ionic liquids. PILs provide great mechanical integrity in addition to ion conductivities, paving the way towards more compact and safer solid electrolytes. Rational design of the chemical structures and architectures of PILs affords a variety of additional features, such as tunable mechanical properties, morphologies, and multi-responsive behaviors.<sup>5-6, 15, 48</sup> However, PILs generally suffer from low ion conductivities compared to ILs due to restricted segmental mobility.

One important thing to clarify in PILs is that the contribution of bounded ions to ion conductivity is normally negligible, and “free” counter ions determine ion conductivity to a large degree. In PILs, glass transition temperature ( $T_g$ ) normally has an inverse

relationship with ion conductivities, similar to viscosity in ILs.<sup>15, 48</sup> Lower  $T_g$  corresponds to more mobile matrices for counter ions, leading to higher ion conductivities. Two major mechanisms contribute to the reduction of  $T_g$ . From a free volume point of view, bulkier ions introduce more free volume to decrease  $T_g$ . In this case, ions function as pendant groups, and various studies have showed larger pendant groups tend to decrease  $T_g$  via introduction of more free volume.<sup>68-70</sup> Another consideration focuses on electrostatic interactions, which act as physical crosslinks in polymer matrices to restrict mass transfer. Hence, weak electrostatic interactions lead to weak physical crosslinks and low  $T_g$ .<sup>48</sup>

However, low  $T_g$  is not the only condition required for higher conductivities. Subtle structural variation can improve ion conductivity through reducing electrostatic interaction but cause minimal  $T_g$  change. In this regard, P-based PILs promised great potential in improving ion conductivity compared to their N-based analogs without compromising mechanical properties (decreased  $T_g$ ).<sup>15</sup> In this section, we will compare N-based PILs and P-based PILs and highlight chemical designs to further improve ion conductivity for P-based PILs, such as substituent size, counterion identity, ion concentration and swelling.

As discussed in the ILs section, P-based PILs showed improved thermal stability over their N-based counterparts as a result of negligible degradation from Hoffman elimination and reverse Menschutkin degradation. As depicted in **Figure 3.6a**, Long *et al.* synthesized two series of styrenic PILs with either quaternary ammonium or phosphonium cations and reported significantly higher thermal degradation temperatures of P-based PILs.<sup>15</sup> P-based PILs exhibited similar  $T_g$ s (**Figure 3.6b**) but much higher ion

conductivities (**Figure 3.6c**) compared to their N-based analogs, promising P-based PILs as ideal electrolytes or ion exchange membranes with good mechanical integrity and high ion conductivities. The size difference between nitrogen and phosphorus is not substantial enough to cause prominent  $T_g$  change; however, P-based PILs have weaker electrostatic interactions than N-based PILs resulting in increased ion conductivities. The difference of electrostatic interactions between N-based PILs and P-based PILs originates from the electronegativities of nitrogen, phosphorus and carbon.<sup>48</sup> In ammonium cations, nitrogen has a partial negative charge as its electronegativity is higher than the  $\alpha$ -carbon. In contrast, phosphorus has a partial positive charge in phosphonium cations as a result of its lower electronegativity than carbon, which leads to slightly negatively charged  $\alpha$ -carbon. This negatively charged  $\alpha$ -carbon effectively shields the positive charge on phosphorus and weakened the electrostatic interactions. Other researchers have reported a similar increase in ion conductivities when replacing nitrogen with phosphorus.<sup>48</sup>

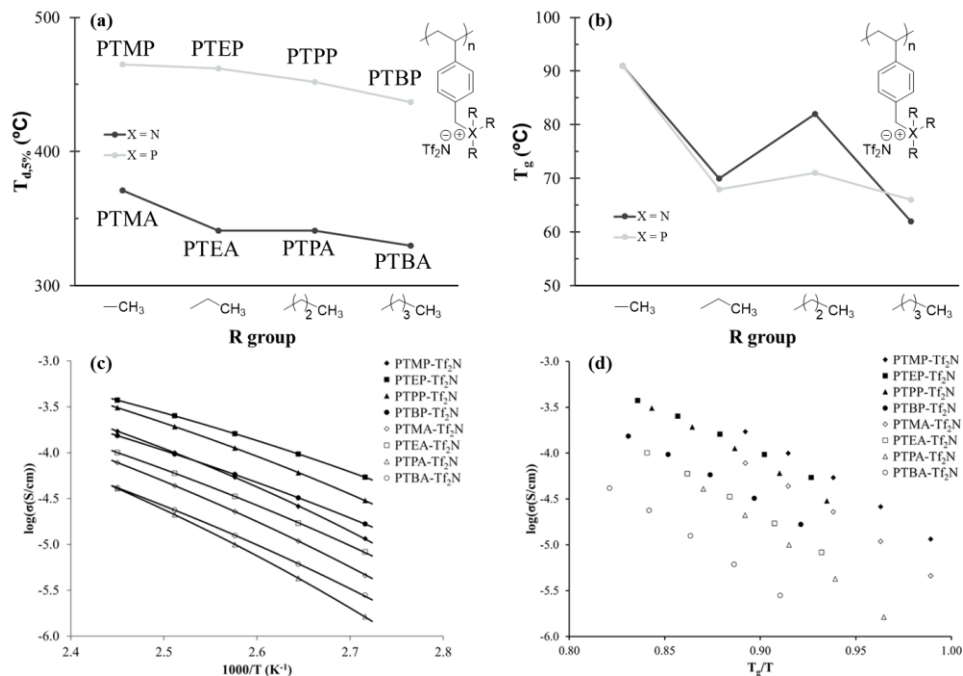


**Figure 3.6** Comparison of (a) thermal stability, (b)  $T_g$ , (c) temperature dependent ion conductivities and (d) ion conductivities normalized with  $T_g$  of P-based PILs and N-based PILs (Copyright (2013) John Wiley and Sons).<sup>15</sup>

Unlike replacing nitrogen with phosphorus, varying alkyl substituent length cause substantial change in  $T_g$ . **Figure 3.6b** demonstrated a decrease of  $T_g$  from 91 °C to 68 °C when replacing methyl R groups (PTMP) with ethyl R groups (PTEP). Further elongation of alkyl substituents only results in limited decrease of  $T_g$ . At the same temperature, shorter alkyl substituents showed higher ion conductivities (**Figure 3.6c**) with the exception of methyl substituents, which has 20 °C higher  $T_g$  than other PILs. The ion conductivities after normalizing with  $T_g$  showed the expected trend without exception: methyl > ethyl > propyl > butyl (**Figure 3.6d**). This trend corresponds well with ILs, ascribing to higher mobility and ion content from smaller size and less non-ionic content, respectively. Gin, Noble and coworkers studied the same P-based PILs with even longer alkyl substituents (hexyl and octyl), and observed a continuous decrease of  $T_g$  with longer

alkyl substituents.<sup>71</sup> Between hexyl and octyl substituents, their ion conductivities followed the same trend at high temperature: short substituents exhibited higher conductivity. However, the change in ion conductivity was less prominent between long alkyl substituents. The fact that P-based PILs exhibited higher ion conductivities than N-based counterparts even after  $T_g$  normalization further showing the superiority of P-based PILs in conductivity.

Counter ion exchange is an efficient way to alter PIL ion conductivity through both plasticization effect and electrostatic interaction control. Bulky counter ions introduce more free volume (to plasticize polymer networks) and achieved lower  $T_g$  to facilitate mass transfer (ion conductivity). Meanwhile, counter ions with more delocalized charged density show high ion conductivities due to weakened electrostatic interaction. The influence of  $T_g$  and electrostatic interaction can either be constructive or destructive. Colby *et al.* studied the influence of counter cations on  $T_g$  and ion conductivity in polyurethane-carboxylate ionomers (structures shown in **Figure 3.7a**).<sup>48</sup> **Figure 3.7a** revealed a 30 °C  $T_g$  reduction from  $\text{Na}^+$  (strong electrostatic interaction) to quaternary cations, which led to significant improvement of ion conductivities shown in **Figure 3.7b**. Comparing quaternary ammonium cation ( $\text{Bu}_4\text{N}^+$  in **Figure 3.7a**) and phosphonium cation ( $\text{Bu}_4\text{P}^+$  in **Figure 3.7a**) with similar size and chemical structure, P-based PIL demonstrated a substantial reduction of  $T_g$  from 16 °C to 0 °C. Weaker electrostatic interaction in P-based PILs allows higher mobility (lower  $T_g$ ) as a result of reduced physical crosslinking strength. As discussed above, Long *et al* reported no  $T_g$  change between N-based PILs and P-based PILs, which seems to contradict Colby and coworkers' finding. The molar volume of pendant groups sheds light on this

“contradictory” phenomena.<sup>47, 72</sup> Colby, Winey and coworkers have demonstrated that increased side group volume (including counter ions) leads to lower  $T_g$  until the larger molar volume limit.<sup>47</sup> After that,  $T_g$  becomes insensitive to the molar volume of side groups. In Long *et al.*'s study,<sup>15</sup>  $Tf_2N$  counter anions were bulky enough to reach the larger molar volume limit, making polymers insensitive to any further size change. While in Coby *et al.*' study,<sup>48</sup> both quaternary cations and carboxylate anions are not as bulky as  $Tf_2N$  counter anions. Hence, variation in ion size causes more substantial  $T_g$  changes. Long *et al.* showed over 100 °C  $T_g$  reduction of phosphonium containing copolymers after ion exchange from Cl to  $Tf_2N$  counter anions.<sup>73</sup>

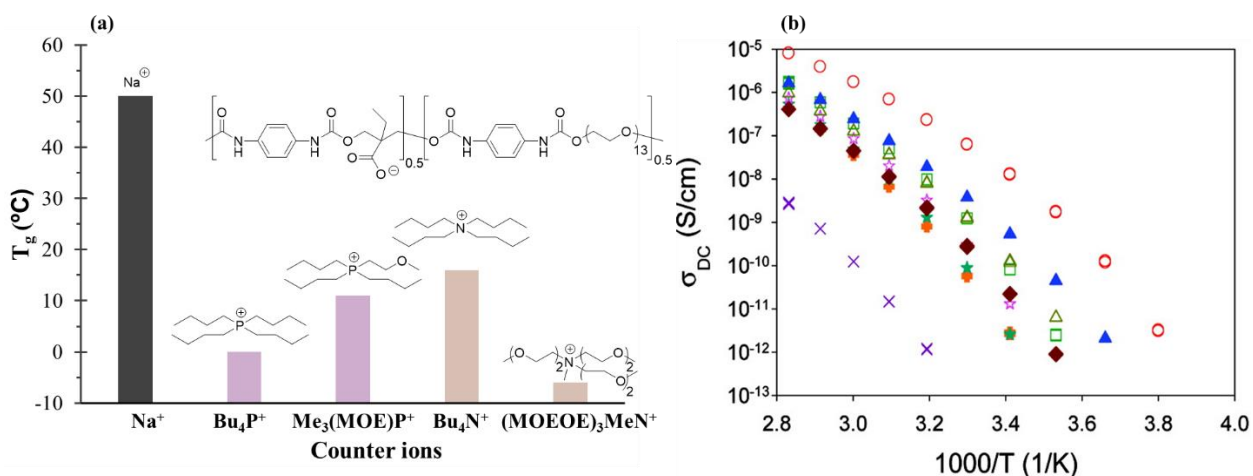


**Figure 3.7** The influence of different counter cations on (a)  $T_g$  and (b) ion conductivity (purple x is  $Na^+$ , dark red solid diamond is  $Bu_4N^+$ , blue solid triangle is  $Bu_4P^+$ , olive green triangle is  $Me_3(MOE)P^+$ , red open circle is  $(MOEOE)_3MeN^+$ ) (Copyright (2011) American Chemical Society).<sup>48</sup>

Ether substituents have an opposite influence on the  $T_g$  and ion conductivity of N-based PILs compared to P-based PILs.<sup>48</sup> As illustrated in **Figure 3.7a**, ether substituents increased the  $T_g$  of P-based PILs, but decreased the  $T_g$  of N-based PILs. In P-based PILs, carbon atoms bear a partial negative charge. Ether oxygens reduce their partial negative charge through electron withdrawing effect. As a result, the negatively charged

“shielding” of positively charged phosphonium weakens, and  $T_g$  increased due to stronger electrostatic interaction. In N-based PILs, where carbon atoms are already positively charged, ether oxygens provide shielding from anions and decrease  $T_g$ . Ion conductivities followed opposite trend of  $T_g$  as expected. Ether containing P-based PILs ( $\text{Me}_4(\text{MOE})\text{P}^+$  (olive green triangle in **Figure 3.7b**) exhibited lower ion conductivities than alkyl substituted P-based PILs ( $\text{Bu}_4\text{P}^+$ , blue solid triangle in **Figure 3.7b**).  $(\text{MOE})_3\text{MeN}^+$  (red open circle in **Figure 3.7b**), on the other hand, demonstrated improved ion conductivity compared to  $\text{Bu}_4\text{P}^+$  (dark red solid diamond in **Figure 3.7b**).

In more mobile polymeric matrices, such as polysiloxane,  $T_g$  becomes insensitive to ion exchange.<sup>47</sup> As depicted in **Figure 3.8a**, ion exchange from Br and F counter ions to  $\text{Tf}_2\text{N}$  counter anions exhibited no statistical change of  $T_g$ , which contradicts other studies where the  $T_g$  of the polymer backbones are higher than polysiloxane.<sup>15, 73</sup> Nevertheless,  $\text{Tf}_2\text{N}$  counter anions reduced electrostatic interaction, and increased ion conductivity substantially as shown in **Figure 3.8b**. When discussing ion concentration (or ion content), two competing mechanisms determine its net result on  $T_g$  and ion conductivities. Ion conductivity benefits from high ion concentration and potential plasticization effect from bulky ions. However, high physical crosslink density due to high ion concentration tends to elevate  $T_g$  which is detrimental to ion conductivity. In this particular case, the polysiloxane backbone provides enough mobility that the influence of ion concentration on  $T_g$  and ion conductivity becomes less effective.<sup>47</sup> Long *et al.* demonstrated that high ion concentrations resulted in high ion conductivity in crosslinked PEG matrices, where the segmental motion of the polymer backbone has been severely restricted.<sup>74-75</sup> The plasticization effect from bulky  $\text{Tf}_2\text{N}$  counter ions and tri(octyl)phenyl

phosphonium cations dominantly determined  $T_g$ , and higher ion concentration actually caused a reduction of  $T_g$ . As a result, the ion conductivity increased with higher ion concentration.

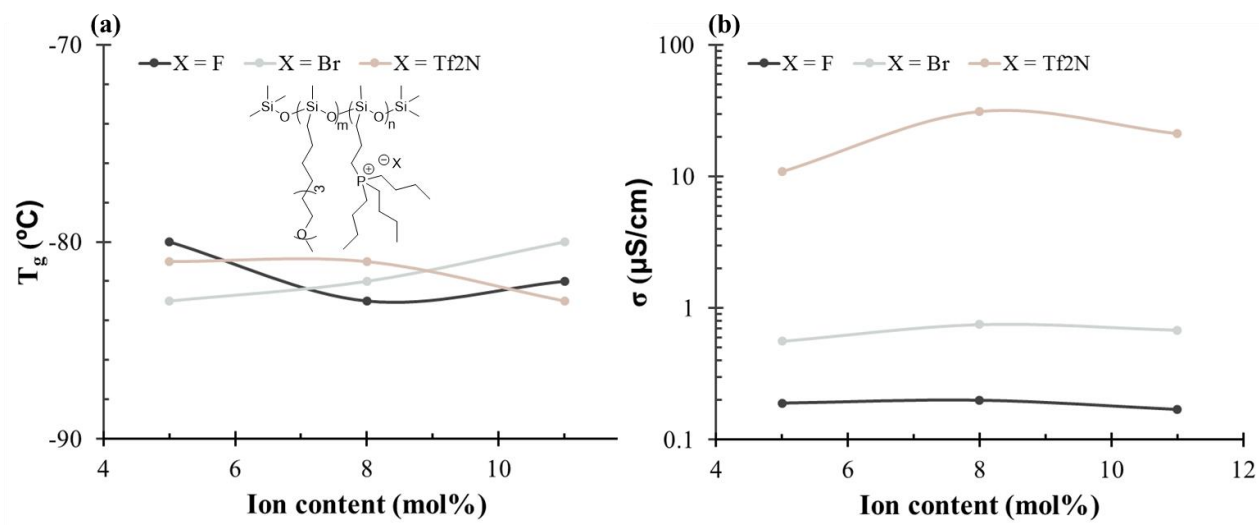


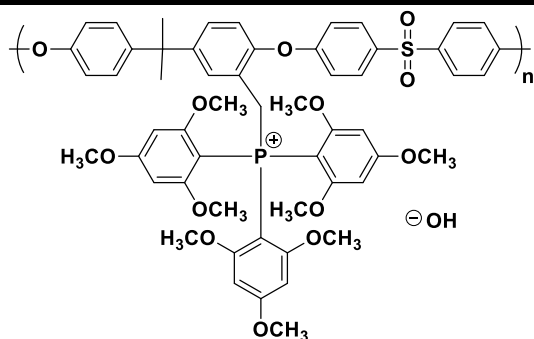
**Figure 3.8** The influence of counter ions and ion concentration on (a)  $T_g$  and (b) ion conductivity (at 30 °C).<sup>47</sup>

Swelling of PILs represents another common approach to increase ion conductivity.<sup>76-80</sup>

Yan and coworkers investigated the hydroxide conductivity of tris(2,4,6-trimethoxyphenyl) phosphonium functionalized polysulfone films after swelling in water.<sup>78-80</sup> As shown in **Table 3.4**, at water uptake levels under 137%, hydroxide conductivity increased with increasing water uptake due to increased mobility of both polymer matrices and hydroxide counter anions. However, excessive water uptake (798%) caused a reduction of hydroxide conductivity. Phosphonium polymers exhibited high ion conductivity (45 mS/cm) at low ion exchange capacity (1.17 mmol/g), indicative of achieving high conductivity and good mechanical properties simultaneously.<sup>79</sup> To further improve the dimensional stability and solvent resistance, Yan *et al.* studied the crosslinked phosphonium containing polysulfone (Structure shown in **Table 3.5**).<sup>80</sup>

Through Friedel-Crafts electrophilic substitution between the chloromethyl group and electron-rich aromatic ring, phosphonium-containing polysulfone self-crosslinked and showed a significant reduction of swelling ratio (15 %) compared to uncrosslinked counterparts (157 %). In addition to improved solvent resistance and thermal stability, crosslinked polysulfone retained high ion conductivity (38 S/cm). Other studies have investigated the usage of tris(2,4,6-trimethoxyphenyl) phosphonium pendant groups in poly(2,6-dimethyl-1,4-phenylene oxide),<sup>81</sup> poly(ether ether ketone),<sup>82</sup> and block copolymers of isoprene and chloromethyl styrene.<sup>83</sup> Xu, Wu and coworkers studied a similar polysulfone with bromomethyl substituents on the aromatic groups in phosphonium cations instead of methoxy substituents.<sup>84</sup> The water uptake increased with higher degree of bromomethyl substitution as expected, and a similar conductivity (above 30 mS/cm) plateau appeared when water uptake reached a threshold (circa 65%).

**Table 3.5** Hydroxide conductivity and water uptake of swelled phosphonium polymer films at different chloromethylation level. T = 20 °C<sup>78-80</sup>



Chloromethylation (%)	Water uptake (%)	Hydroxide conductivity (mS/cm)
99	41	11
124	70	27

152	137	45
178	798	38
Crosslinked	N/A	38

### 3.5 Future perspectives

To date, most efforts in novel electrolytes, either ILs or PILs, still focus on N-based materials,<sup>7, 9, 13-14, 85</sup> and the application of P-based ILs and PILs as conductive materials are under developed. However, the above examples have showed their superior stability (both thermally and chemically) and conductivity compared to their N-based analogs. These findings have raised a significant impetus to employ P-based ILs as alternatives of N-based ILs for conductive and safe electrolyte materials. In addition, previous limited commercial supply of P-based ILs has been alleviated recently.<sup>86</sup> Meanwhile, most P-based PILs have served as ion exchange membranes instead of electrolytes until now.<sup>87-88</sup> Nevertheless, P-based PILs exhibit great potential as solid/gel state electrolytes, such as ion gels.<sup>2, 4-6, 89-93</sup> Microphase separated morphologies, tunable and responsive mechanical properties, and continual improvement of ion conductivity distinguishes P-based PILs as strong competitors in novel electrolyte applications. However, the synthesis of various P-based PILs and their structure-property relationship are still underexploited. Further endeavors to access new phosphonium containing polymers<sup>94</sup> and in depth understanding of their structure-property relationship at both meso- and macro-scale are the keys for their success in energy-related topics.

### 3.6 Reference

1. Wilkes, J. S., A short history of ionic liquids-from molten salts to neoteric solvents *Green Chemistry* **2002**, *4*, 73-80.
2. Lodge, T. P., Materials science - A unique platform for materials design *Science* **2008**, *321*, 50-51.
3. Li, W. Y.; Yao, H. B.; Yan, K.; Zheng, G. Y.; Liang, Z.; Chiang, Y. M.; Cui, Y., The synergetic effect of lithium polysulfide and lithium nitrate to prevent lithium dendrite growth *Nature Communications* **2015**, *6*.
4. Hall, C. C.; Zhou, C.; Danielsen, S. P. O.; Lodge, T. P., Formation of Multicompartment Ion Gels by Stepwise Self-Assembly of a Thermoresponsive ABC Triblock Terpolymer in an Ionic Liquid *Macromolecules* **2016**, *49*, 2298-2306.
5. Lodge, T. P.; Ueki, T., Mechanically Tunable, Readily Processable Ion Gels by Self-Assembly of Block Copolymers in Ionic Liquids *Acc. Chem. Res* **2016**, *49*, 2107-2114.
6. Moon, H. C.; Kim, C. H.; Lodge, T. P.; Frisbie, C. D., Multicolored, Low-Power, Flexible Electrochromic Devices Based on Ion Gels *ACS Appl. Mater. Interfaces* **2016**, *8*, 6252-6260.
7. Obadia, M. M.; Jourdain, A.; Serghei, A.; Ikeda, T.; Drockenmuller, E., Cationic and dicationic 1,2,3-triazolium-based poly(ethylene glycol ionic liquid)s *Polym. Chem.* **2017**, *8*, 910-917.
8. Green, M. D.; Salas-de la Cruz, D.; Ye, Y. S.; Layman, J. M.; Elabd, Y. A.; Winey, K. I.; Long, T. E., Alkyl-Substituted N-Vinylimidazolium Polymerized Ionic Liquids: Thermal Properties and Ionic Conductivities *Macromol. Chem. Phys.* **2011**, *212*, 2522-2528.
9. Wang, A. L.; Xu, H.; Liu, X.; Gao, R.; Wang, S.; Zhou, Q.; Chen, J.; Liu, X. F.; Zhang, L. Y., The synthesis of a hyperbranched star polymeric ionic liquid and its application in a polymer electrolyte *Polym. Chem.* **2017**, *8*, 3177-3185.
10. Allen, M. H.; Wang, S.; Hemp, S. T.; Chen, Y.; Madsen, L. A.; Winey, K. I.; Long, T. E., Hydroxyalkyl-Containing Imidazolium Homopolymers: Correlation of Structure with Conductivity *Macromolecules* **2013**, *46*, 3037-3045.
11. Green, M. D.; Long, T. E., Designing Imidazole-Based Ionic Liquids and Ionic Liquid Monomers for Emerging Technologies *Polymer Reviews* **2009**, *49*, 291-314.
12. Mousavi, M. P. S.; Wilson, B. E.; Kashefolgheta, S.; Anderson, E. L.; He, S. Y.; Buhmann, P.; Stein, A., Ionic Liquids as Electrolytes for Electrochemical Double-Layer Capacitors: Structures that Optimize Specific Energy *ACS Applied Materials & Interfaces* **2016**, *8*, 3396-3406.
13. Jourdain, A.; Serghei, A.; Drockenmuller, E., Enhanced Ionic Conductivity of a 1,2,3-Triazolium-Based Poly(siloxane ionic liquid) Homopolymer *ACS Macro Lett.* **2016**, *5*, 1283-1286.
14. Shaplov, A. S.; Lozinskaya, E. I.; Losada, R.; Wandrey, C.; Zdvizhkov, A. T.; Korlyukov, A. A.; Lyssenko, K. A.; Malyshkina, I. A.; Vygodskii, Y. S., Polymerization of the new double-charged monomer bis-1,3(N,N,N-trimethylammonium dicyanamide)-2-propylmethacrylate and ionic conductivity of the novel polyelectrolytes *Polym. Adv. Technol.* **2011**, *22*, 448-457.

15. Hemp, S. T.; Zhang, M. Q.; Allen, M. H.; Cheng, S. J.; Moore, R. B.; Long, T. E., Comparing Ammonium and Phosphonium Polymerized Ionic Liquids: Thermal Analysis, Conductivity, and Morphology *Macromol. Chem. Phys.* **2013**, *214*, 2099-2107.
16. Tsunashima, K.; Niwa, E.; Kodama, S.; Sugiya, M.; Ono, Y., Thermal and Transport Properties of Ionic Liquids Based on Benzyl-Substituted Phosphonium Cations *J. Phys. Chem. B* **2009**, *113*, 15870-15874.
17. Janikowski, J.; Razali, M. R.; Forsyth, C. M.; Nairn, K. M.; Batten, S. R.; MacFarlane, D. R.; Pringle, J. M., Physical Properties and Structural Characterization of Ionic Liquids and Solid Electrolytes Utilizing the Carbamoylcyano(nitroso)methanide Anion *ChemPlusChem* **2013**, *78*, 486-497.
18. Noonan, K. J. T.; Hugar, K. M.; Kostalik, H. A.; Lobkovsky, E. B.; Abruna, H. D.; Coates, G. W., Phosphonium-Functionalized Polyethylene: A New Class of Base-Stable Alkaline Anion Exchange Membranes *J. Am. Chem. Soc.* **2012**, *134*, 18161-18164.
19. Li, Y. Y.; Wu, X. F.; Wu, Q. Y.; Ding, H.; Yan, W. F., Ammonium- and phosphonium-based temperature control-type polyoxometalate ionic liquids *Dalton Trans.* **2014**, *43*, 13591-13595.
20. Zhang, Y. Q.; Zhang, S. J.; Lu, X. M.; Zhou, Q.; Fan, W.; Zhang, X. P., Dual Amino-Functionalised Phosphonium Ionic Liquids for CO<sub>2</sub> Capture *Chem.-Eur. J.* **2009**, *15*, 3003-3011.
21. Bara, J. E.; Hatakeyama, E. S.; Gin, D. L.; Noble, R. D., Improving CO<sub>2</sub> permeability in polymerized room-temperature ionic liquid gas separation membranes through the formation of a solid composite with a room-temperature ionic liquid *Polym. Adv. Technol.* **2008**, *19*, 1415-1420.
22. Cheng, J.; Hu, L. Q.; Li, Y. N.; Liu, J. Z.; Zhou, J. H.; Cen, K. F., Improving CO<sub>2</sub> permeation and separation performance of CO<sub>2</sub>-philic polymer membrane by blending CO<sub>2</sub> absorbents *Appl. Surf. Sci.* **2017**, *410*, 206-214.
23. Estahbanati, E. G.; Omidkhah, M.; Arnooghini, A. E., Interfacial Design of Ternary Mixed Matrix Membranes Containing Pebax 1657/Silver-Nanopowder/ BMIM BF<sub>4</sub> for Improved CO<sub>2</sub> Separation Performance *ACS Appl. Mater. Interfaces* **2017**, *9*, 10094-10105.
24. Fam, W.; Mansouri, J.; Li, H. Y.; Chen, V., Improving CO<sub>2</sub> separation performance of thin film composite hollow fiber with Pebax (R) 1657/ionic liquid gel membranes *J. Membr. Sci.* **2017**, *537*, 54-68.
25. Moghadam, F.; Kamio, E.; Yoshioka, T.; Matsuyama, H., New approach for the fabrication of double-network ion-gel membranes with high CO<sub>2</sub>/N<sub>2</sub> separation performance based on facilitated transport *J. Membr. Sci.* **2017**, *530*, 166-175.
26. Nguyen, P. T.; Voss, B. A.; Wiesenauer, E. F.; Gin, D. L.; Noble, R. D., Physically Gelled Room-Temperature Ionic Liquid-Based Composite Membranes for CO<sub>2</sub>/N<sub>2</sub> Separation: Effect of Composition and Thickness on Membrane Properties and Performance *Ind. Eng. Chem. Res.* **2013**, *52*, 8812-8821.
27. Lukac, M.; Devinsky, F.; Pisarcik, M.; Papapetropoulou, A.; Bukovsky, M.; Horvath, B., Novel Phosphonium-Type Cationic Surfactants: Synthesis, Aggregation Properties and Antimicrobial Activity *J. Surfactants Deterg.* **2017**, *20*, 159-171.
28. Xue, Y.; Xiao, H. N.; Zhang, Y., Antimicrobial Polymeric Materials with Quaternary Ammonium and Phosphonium Salts *International Journal of Molecular Sciences* **2015**, *16*, 3626-3655.

29. Qin, J.; Guo, J. N.; Xu, Q. M.; Zheng, Z. Q.; Mao, H. L.; Yan, F., Synthesis of Pyrrolidinium-Type Poly(ionic liquid) Membranes for Antibacterial Applications *ACS Appl. Mater. Interfaces* **2017**, *9*, 10504-10511.
30. Rose, V. L.; Mastrotto, F.; Mantovani, G., Phosphonium polymers for gene delivery *Polymer Chemistry* **2017**, *8*, 353-360.
31. Jung, S.; Lodge, T. P.; Reineke, T. M., Complexation between DNA and Hydrophilic-Cationic Diblock Copolymers *J. Phys. Chem. B* **2017**, *121*, 2230-2243.
32. Bradaric, C. J.; Downard, A.; Kennedy, C.; Robertson, A. J.; Zhou, Y., Industrial preparation of phosphonium ionic liquids *Green Chemistry* **2003**, *5*, 143-152.
33. Bejan, D.; Ignat'ev, N.; Willner, H., New ionic liquids with the bis bis(pentafluoroethyl)phosphinyl imide anion, (C<sub>2</sub>F<sub>5</sub>)<sub>2</sub>P(O) (2)N<sup>-</sup> Synthesis and characterization *J. Fluor. Chem.* **2010**, *131*, 325-332.
34. Hapiot, P.; Lagrost, C., Electrochemical Reactivity in Room-Temperature Ionic Liquids *Chemical Reviews* **2008**, *108*, 2238-2264.
35. Dzyuba, S. V.; Bartsch, R. A., Influence of Structural Variations in 1-Alkyl(aralkyl)-3-Methylimidazolium Hexafluorophosphates and Bis(trifluoromethylsulfonyl)imides on Physical Properties of the Ionic Liquids *ChemPhysChem* **2002**, *3*, 161-166.
36. Tokuda, H.; Hayamizu, K.; Ishii, K.; Susan, M. A. B. H.; Watanabe, M., Physicochemical Properties and Structures of Room Temperature Ionic Liquids. 2. Variation of Alkyl Chain Length in Imidazolium Cation *The Journal of Physical Chemistry B* **2005**, *109*, 6103-6110.
37. Huddleston, J. G.; Visser, A. E.; Reichert, W. M.; Willauer, H. D.; Broker, G. A.; Rogers, R. D., Characterization and comparison of hydrophilic and hydrophobic room temperature ionic liquids incorporating the imidazolium cation *Green Chemistry* **2001**, *3*, 156-164.
38. Papaiconomou, N.; Salminen, J.; Lee, J.-M.; Prausnitz, J. M., Physicochemical Properties of Hydrophobic Ionic Liquids Containing 1-Octylpyridinium, 1-Octyl-2-methylpyridinium, or 1-Octyl-4-methylpyridinium Cations *Journal of Chemical & Engineering Data* **2007**, *52*, 833-840.
39. Tsunashima, K.; Ono, Y.; Sugiya, M., Physical and electrochemical characterization of ionic liquids based on quaternary phosphonium cations containing a carbon-carbon double bond *Electrochimica Acta* **2011**, *56*, 4351-4355.
40. Tsunashima, K.; Sugiya, M., Physical and electrochemical properties of low-viscosity phosphonium ionic liquids as potential electrolytes *Electrochemistry Communications* **2007**, *9*, 2353-2358.
41. Kanematsu, S.; Matsumoto, K.; Hagiwara, R., Electrochemically stable fluorohydrogenate ionic liquids based on quaternary phosphonium cations *Electrochemistry Communications* **2009**, *11*, 1312-1315.
42. Sun, L. Y.; Morales-Collazo, O.; Xia, H.; Brennecke, J. F., Effect of Structure on Transport Properties (Viscosity, Ionic Conductivity, and Self-Diffusion Coefficient) of Aprotic Heterocyclic Anion (AHA) Room Temperature Ionic Liquids. 2. Variation of Alkyl Chain Length in the Phosphonium Cation *J. Phys. Chem. B* **2016**, *120*, 5767-5776.
43. Vega, J. A.; Zhou, J. F.; Kohl, P. A., Electrochemical Comparison and Deposition of Lithium and Potassium from Phosphonium- and Ammonium-TFSI Ionic Liquids *J. Electrochem. Soc.* **2009**, *156*, A253-A259.

44. Sato, T.; Masuda, G.; Takagi, K., Electrochemical properties of novel ionic liquids for electric double layer capacitor applications *Electrochimica Acta* **2004**, *49*, 3603-3611.
45. Tsunashima, K.; Yonekawa, F.; Kikuchi, M.; Sugiya, M., Tributylmethylphosphonium Bis(trifluoromethylsulfonyl)amide as an Effective Electrolyte Additive for Lithium Secondary Batteries *J. Electrochem. Soc.* **2010**, *157*, A1274-A1278.
46. AlOmar, M. K.; Hayyan, M.; Alsaadi, M. A.; Akib, S.; Hayyan, A.; Hashim, M. A., Glycerol-based deep eutectic solvents: Physical properties *J. Mol. Liq.* **2016**, *215*, 98-103.
47. Liang, S. W.; O'Reilly, M. V.; Choi, U. H.; Shiau, H. S.; Bartels, J.; Chen, Q.; Runt, J.; Winey, K. I.; Colby, R. H., High Ion Content Siloxane Phosphonium Ionomers with Very Low T-g *Macromolecules* **2014**, *47*, 4428-4437.
48. Wang, S. W.; Liu, W. J.; Colby, R. H., Counterion Dynamics in Polyurethane-Carboxylate Ionomers with Ionic Liquid Counterions *Chem. Mat.* **2011**, *23*, 1862-1873.
49. Tsunashima, K.; Sakai, Y.; Matsumiya, M., Physical and electrochemical properties of phosphonium ionic liquids derived from trimethylphosphine *Electrochemistry Communications* **2014**, *39*, 30-33.
50. Girard, G. M. A.; Hilder, M.; Zhu, H.; Nucciarone, D.; Whitbread, K.; Zavorine, S.; Moser, M.; Forsyth, M.; MacFarlane, D. R.; Howlett, P. C., Electrochemical and physicochemical properties of small phosphonium cation ionic liquid electrolytes with high lithium salt content *Phys. Chem. Chem. Phys.* **2015**, *17*, 8706-8713.
51. Ramirez, R. E.; Sanchez, E. M., Molten phosphonium iodides as electrolytes in dye-sensitized nanocrystalline solar cells *Sol. Energy Mater. Sol. Cells* **2006**, *90*, 2384-2390.
52. Ramirez, R. E.; Torres-Gonzalez, L. C.; Hernandez, A.; Garcia, A.; Sanchez, E. M., Conductivity and Viscosity Behavior of Asymmetric Phosphonium Iodides *J. Phys. Chem. B* **2010**, *114*, 4271-4275.
53. Ramirez, R. E.; Torres-Gonzalez, L. C.; Sanchez, E. M., Electrochemical aspects of asymmetric phosphonium ionic liquids *J. Electrochem. Soc.* **2007**, *154*, B229-B233.
54. Tsunashima, K.; Kawabata, A.; Matsumiya, M.; Kodama, S.; Enomoto, R.; Sugiya, M.; Kunugi, Y., Low viscous and highly conductive phosphonium ionic liquids based on bis(fluorosulfonyl)amide anion as potential electrolytes *Electrochemistry Communications* **2011**, *13*, 178-181.
55. Hilder, M.; Girard, G. M. A.; Whitbread, K.; Zavorine, S.; Moser, M.; Nucciarone, D.; Forsyth, M.; MacFarlane, D. R.; Howlett, P. C., Physicochemical characterization of a new family of small alkyl phosphonium imide ionic liquids *Electrochimica Acta* **2016**, *202*, 100-109.
56. Green, M. D.; Schreiner, C.; Long, T. E., Thermal, Rheological, and Ion-Transport Properties of Phosphonium-Based Ionic Liquids *J. Phys. Chem. A* **2011**, *115*, 13829-13835.
57. Yoshii, K.; Yamaji, K.; Tsuda, T.; Tsunashima, K.; Yoshida, H.; Ozaki, M.; Kuwabata, S., Physicochemical Properties of Tri-n-butylalkylphosphonium Cation-Based Room-Temperature Ionic Liquids *J. Phys. Chem. B* **2013**, *117*, 15051-15059.
58. Battez, A. H.; Bartolome, M.; Blanco, D.; Viesca, J. L.; Fernandez-Gonzalez, A.; Gonzalez, R., Phosphonium cation-based ionic liquids as neat lubricants: Physicochemical and tribological performance *Tribol. Int.* **2016**, *95*, 118-131.

59. Imamura, K.; Nogami, T.; Mikawa, H., BROMIDE ANION CONDUCTIVITIES OF QUATERNARY PHOSPHONIUM BROMIDES POSSESSING LONG ALKYL CHAINS *Solid State Ion.* **1985**, *17*, 77-80.
60. Martins, V. L.; Sanchez-Ramirez, N.; Ribeiro, M. C. C.; Torresi, R. M., Two phosphonium ionic liquids with high Li<sup>+</sup> transport number *Phys. Chem. Chem. Phys.* **2015**, *17*, 23041-23051.
61. Weng, W.; Zhang, Z. C.; Lu, J.; Amine, K., A disiloxane-functionalized phosphonium-based ionic liquid as electrolyte for lithium-ion batteries *Chem. Commun.* **2011**, *47*, 11969-11971.
62. Quiroz-Guzman, M.; Fagnant, D. P.; Chen, X. Y.; Shi, C. J.; Brennecke, J. F.; Goff, G. S.; Runde, W., Synthesis and characterization of the thermodynamic and electrochemical properties of tetra-alkyl phosphonium oxalate ionic liquids *RSC Adv.* **2014**, *4*, 14840-14846.
63. Ueda, S.; Kagimoto, J.; Ichikawa, T.; Kato, T.; Ohno, H., Anisotropic Proton-Conductive Materials Formed by the Self-Organization of Phosphonium-Type Zwitterions *Advanced Materials* **2011**, *23*, 3071-3074.
64. Yonekura, R.; Grinstaff, M. W., The effects of counterion composition on the rheological and conductive properties of mono- and diphosphonium ionic liquids *Phys. Chem. Chem. Phys.* **2014**, *16*, 20608-20617.
65. Seki, S.; Umabayashi, Y.; Tsuzuki, S.; Hayamizu, K.; Kobayashi, Y.; Ohno, Y.; Kobayashi, T.; Mita, Y.; Miyashiro, H.; Terada, N.; Ishiguro, S. I., Phase transition and conductive acceleration of phosphonium-cation-based room-temperature ionic liquid *Chem. Commun.* **2008**, 5541-5543.
66. Rickert, P. G.; Antonio, M. R.; Firestone, M. A.; Kubatko, K. A.; Szreder, T.; Wishart, J. F.; Dietz, M. L., Tetraalkylphosphonium polyoxometalate ionic liquids: Novel, organic-inorganic hybrid materials *J. Phys. Chem. B* **2007**, *111*, 4685-4692.
67. Shah, F. U.; Glavatskih, S.; MacFarlane, D. R.; Somers, A.; Forsyth, M.; Antzutkin, O. N., Novel halogen-free chelated orthoborate-phosphonium ionic liquids: synthesis and tribophysical properties *Phys. Chem. Chem. Phys.* **2011**, *13*, 12865-12873.
68. Bamford, D.; Dlubek, G.; Lupke, T.; Kilburn, D.; Stejny, J.; Menke, T. J.; Alam, M. A., Free volume, glass transition and degree of branching in ethylene/alpha-olefin copolymers: Positron lifetime, differential scanning calorimetry, wide-angle X-ray scattering, and density studies *Macromol. Chem. Phys.* **2006**, *207*, 492-502.
69. Kusuma, V. A.; Freeman, B. D.; Borns, M. A.; Kalika, D. S., Influence of chemical structure of short chain pendant groups on gas transport properties of cross-linked poly(ethylene oxide) copolymers *J. Membr. Sci.* **2009**, *327*, 195-207.
70. Kusuma, V. A.; Freeman, B. D.; Smith, S. L.; Heilman, A. L.; Kalika, D. S., Influence of TRIS-based co-monomer on structure and gas transport properties of cross-linked poly(ethylene oxide) *J. Membr. Sci.* **2010**, *359*, 25-36.
71. Cowan, M. G.; Masuda, M.; McDanel, W. M.; Kohno, Y.; Gin, D. L.; Noble, R. D., Phosphonium-based poly(Ionic liquid) membranes: The effect of cation alkyl chain length on light gas separation properties and Ionic conductivity *Journal of Membrane Science* **2016**, *498*, 408-413.
72. Choi, U. H.; Mittal, A.; Price, T. L.; Gibson, H. W.; Runt, J.; Colby, R. H., Polymerized Ionic Liquids with Enhanced Static Dielectric Constants *Macromolecules* **2013**, *46*, 1175-1186.

73. Cheng, S.; Zhang, M.; Wu, T.; Hemp, S. T.; Mather, B. D.; Moore, R. B.; Long, T. E., Ionic aggregation in random copolymers containing phosphonium ionic liquid monomers *Journal of Polymer Science Part A: Polymer Chemistry* **2012**, *50*, 166-173.
74. Schultz, A. R.; Lambert, P. M.; Chartrain, N. A.; Ruohoniemi, D. M.; Zhang, Z. Y.; Jangu, C.; Zhang, M.; Williams, C. B.; Long, T. E., 3D Printing Phosphonium Ionic Liquid Networks with Mask Projection Microstereolithography *ACS Macro Lett.* **2014**, *3*, 1205-1209.
75. Schultz, A. R.; Fahs, G. B.; Jangu, C.; Chen, M. T.; Moore, R. B.; Long, T. E., Phosphonium-containing diblock copolymers from living anionic polymerization of 4-diphenylphosphino styrene *Chem. Commun.* **2016**, *52*, 950-953.
76. Soares, B. G.; Pontes, K.; Marins, J. A.; Calheiros, L. F.; Livi, S.; Barra, G. M. O., Poly(vinylidene fluoride-co-hexafluoropropylene)/polyaniline blends assisted by phosphonium – Based ionic liquid: Dielectric properties and  $\beta$ -phase formation *Eur. Polym. J.* **2015**, *73*, 65-74.
77. Ge, C.; Ling, Y.; Yan, S.; Luan, S.; Zhang, H.; Tang, H., Preparation and Mechanical Properties of Strong and Tough Poly (vinyl alcohol)-Polypeptide Double-Network Hydrogels *Eur. Polym. J.* **2018**.
78. Gu, S.; Cai, R.; Luo, T.; Chen, Z.; Sun, M.; Liu, Y.; He, G.; Yan, Y., A Soluble and Highly Conductive Ionomer for High-Performance Hydroxide Exchange Membrane Fuel Cells *Angewandte Chemie International Edition* **2009**, *48*, 6499-6502.
79. Gu, S.; Cai, R.; Luo, T.; Jensen, K.; Contreras, C.; Yan, Y. S., Quaternary Phosphonium-Based Polymers as Hydroxide Exchange Membranes *ChemSusChem* **2010**, *3*, 555-558.
80. Gu, S.; Cai, R.; Yan, Y. S., Self-crosslinking for dimensionally stable and solvent-resistant quaternary phosphonium based hydroxide exchange membranes *Chem. Commun.* **2011**, *47*, 2856-2858.
81. Liu, Y.; Zhang, B. Z.; Kinsinger, C. L.; Yang, Y.; Seifert, S.; Yan, Y. S.; Maupin, C. M.; Liberatore, M. W.; Herring, A. M., Anion exchange membranes composed of a poly(2,6-dimethyl-1, 4-phenylene oxide) random copolymer functionalized with a bulky phosphonium cation *Journal of Membrane Science* **2016**, *506*, 50-59.
82. Yan, X. M.; Gu, S.; He, G. H.; Wu, X. M.; Zheng, W. J.; Ruan, X. H., Quaternary phosphonium-functionalized poly(ether ether ketone) as highly conductive and alkali-stable hydroxide exchange membrane for fuel cells *Journal of Membrane Science* **2014**, *466*, 220-228.
83. Zhang, W.; Liu, Y.; Jackson, A. C.; Savage, A. M.; Ertem, S. P.; Tsai, T. H.; Seifert, S.; Beyer, F. L.; Liberatore, M. W.; Herring, A. M.; Coughlin, E. B., Achieving Continuous Anion Transport Domains Using Block Copolymers Containing Phosphonium Cations *Macromolecules* **2016**, *49*, 4714-4722.
84. Jiang, L. H.; Lin, X. C.; Ran, J.; Li, C. R.; Wu, L.; Xu, T. W., Synthesis and Properties of Quaternary Phosphonium-based Anion Exchange Membrane for Fuel Cells *Chin. J. Chem.* **2012**, *30*, 2241-2246.
85. Shaplov, A. S.; Lozinskaya, E. I.; Ponkratov, D. O.; Malyshkina, I. A.; Vidal, F.; Aubert, P.-H.; Okatova, O. g. V.; Pavlov, G. M.; Komarova, L. I.; Wandrey, C.; Vygodskii, Y. S., Bis(trifluoromethylsulfonyl)amide based “polymeric ionic liquids”: Synthesis, purification and peculiarities of structure–properties relationships *Electrochimica Acta* **2011**, *57*, 74-90.

86. Fraser, K. J.; MacFarlane, D. R., Phosphonium-Based Ionic Liquids: An Overview *Australian Journal of Chemistry* **2009**, *62*, 309-321.
87. Cotanda, P.; Sudre, G.; Modestino, M. A.; Chen, X. C.; Balsara, N. P., High Anion Conductivity and Low Water Uptake of Phosphonium Containing Diblock Copolymer Membranes *Macromolecules* **2014**, *47*, 7540-7547.
88. Ye, Y.; Stokes, K. K.; Beyer, F. L.; Elabd, Y. A., Development of phosphonium-based bicarbonate anion exchange polymer membranes *Journal of Membrane Science* **2013**, *443*, 93-99.
89. Arafune, H.; Honma, S.; Morinaga, T.; Kamijo, T.; Miura, M.; Furukawa, H.; Sato, T., Highly Robust and Low Frictional Double-Network Ion Gel *Advanced Materials Interfaces* **2017**, *4*, 5.
90. Bara, J. E.; Lessmann, S.; Gabriel, C. J.; Hatakeyama, E. S.; Noble, R. D.; Gin, D. L., Synthesis and Performance of Polymerizable Room-Temperature Ionic Liquids as Gas Separation Membranes *Ind. Eng. Chem. Res.* **2007**, *46*, 5397-5404.
91. del Agua, I.; Mantione, D.; Casado, N.; Sanchez-Sanchez, A.; Malliaras, G. G.; Mecerreyes, D., Conducting Polymer longels Based on PEDOT and Guar Gum *ACS Macro Lett.* **2017**, *6*, 473-478.
92. Kitazawa, Y.; Ueki, T.; McIntosh, L. D.; Tamura, S.; Niitsuma, K.; Imaizumi, S.; Lodge, T. P.; Watanabe, M., Hierarchical Sol-Gel Transition Induced by Thermosensitive Self-Assembly of an ABC Triblock Polymer in an Ionic Liquid *Macromolecules* **2016**, *49*, 1414-1423.
93. Lee, J. H.; Lee, A. S.; Hong, S. M.; Hwang, S. S.; Koo, C. M., Hybrid ionogels derived from polycationic polysilsesquioxanes for lithium ion batteries *Polymer* **2017**, *117*, 160-166.
94. Womble, C. T.; Coates, G. W.; Matyjaszewski, K.; Noonan, K. J. T., Tetrakis(dialkylamino)phosphonium Polyelectrolytes Prepared by Reversible Addition-Fragmentation Chain Transfer Polymerization *ACS Macro Lett.* **2016**, *5*, 253-257.

## Chapter 4: Room temperature Michael addition reactions for structural adhesives

(Manuscript in preparation for publication)

Mingtao Chen,<sup>1,2</sup> Alison R. Schultz,<sup>1,2</sup> Michael J. Scanish,<sup>3</sup> S. Richard Turner,<sup>1,2</sup> Timothy E. Long<sup>1,2,\*</sup>

<sup>1</sup> Macromolecules Innovation Institute, Virginia Tech, Blacksburg, VA 24061

<sup>2</sup> Department of Chemistry, Virginia Tech, Blacksburg, VA 24061

<sup>3</sup> Carlisle Construction Materials, Carlisle, PA 17013

\*To whom the correspondence should be addressed: [telong@vt.edu](mailto:telong@vt.edu)

### 4.1 Abstract

This manuscript presents a novel adhesive network based on Michael addition click chemistry using diacrylates as Michael donors, and bisacetoacetate as Michael acceptors. Two one-pot, one-step nucleophilic reactions of hydrogenated polybutadiene diol (hPB) enabled facile preparation of the Michael donors and acceptors. The described Michael networks crosslinked over a wide temperature range (-10 °C to 50 °C) and showed fast and tunable gel time. Rheology revealed that catalyst concentrations, molecular weight, and additives readily dictated crosslinking kinetics. *In situ* FTIR confirmed the kinetic differences depended on the molecular weights of diacrylates. In both 90° and 180° peel tests, Michael networks demonstrated comparable adhesion strength on various commercial substrates compared to adhesive controls. The introduction of tackifiers further improved adhesive properties and doubled the maximum load between substrates in comparison to commercial adhesive controls. Additional pre-cure time before adhering also benefited adhesive performance on certain substrates.

### 4.2 Introduction

Chemically crosslinked polymeric networks offer a myriad of opportunities for emerging technologies. Extensive research has investigated the synthetic design and physical characteristics of various crosslinked networks including adhesives, sealants, and synthetic rubbers.<sup>1-3</sup> Recent impetus on improving efficiency and environmental impact provides a strong demand for novel crosslinking chemistries under ambient conditions. Next generation crosslinkers must eliminate the use of volatile organic compounds (VOCs) and provide successful adhesion at different temperatures with a special emphasis on room temperature crosslinking. Next generation crosslinked networks should also offer versatility, provide good adhesion properties on various substrates, and act as universal adhesives for various applications over a range of temperatures.

The elimination of VOCs is a resonating trend and long-desired goal throughout the history of adhesive productions because VOCs are not environmentally friendly and are harmful to human health.<sup>4-6</sup> Typical adhesive application requires efficient wetting on a substrate area, hardening, and active load transmission between interfaces, which VOCs readily facilitate.<sup>7</sup> Although solvents help to wet surface substrates, additional time is required during the hardening process for solvent evaporation, which is detrimental during fast curing applications. Recent EPA regulations restrict the solvent choice to a narrow supply of approved low VOC solvents. For example, solvents such as toluene, heptane, and xylene enabled high performance bonding adhesives for several decades but no longer suit EPA low VOC standards. Substitution with approved low VOCs including acetone, *tert*-butyl acetate, parachlorobenzotrifluoride, and methyl ethyl ketone achieves compatibility with EPA regulations yet fails to provide comparable adhesive performance

to conventional formulations. Therefore, high demand exists for solvent-free adhesives with comparable adhesive properties to traditional solvent-based adhesives.

Previous studies have addressed solvent-free adhesives from various approaches, such as melt adhesives and suspension adhesives.<sup>4, 6</sup> However, melt adhesives suffer from a narrow pool of available chemistries due to thermal stability constraints and suspension-type formulations introduce complexity in manufacture and application of adhesives. Bulk crosslinked networks based on oligomers or polymers provide an ideal alternative approach towards solvent-free adhesives while maintaining reasonable mobility (for surface wettability) and fast hardening.

Common room-temperature, bulk crosslinking systems include epoxy/diamine,<sup>8-10</sup> carbodiimides,<sup>11</sup> peroxide chemistry,<sup>12-15</sup> and Michael addition reactions.<sup>2</sup> Our research group has conducted extensive studies on oligomer-based Michael addition reactions between bisacetoacetate (bisAcAc) and diacrylate (DA) at room temperature and highlighted their unique advantages stemmed from readily tunable physical properties.<sup>1, 16-18</sup> We have demonstrated that PEG-based bisAcAc and DA crosslinked within minutes at room-temperature.<sup>1</sup> The crosslinking kinetics were tunable through the molecular weights of PEG precursors, where 1000 g/mol and 8000 g/mol PEG showed 2 min and 7 min gel time, respectively. Further, within the same bisAcAc-DA Michael addition network scope, different synthetic strategies are available for specific applications. For example, our group realized bio-degradable, room-temperature crosslinked networks based on poly( $\epsilon$ -caprolactone) bisAcAc and neopentyl glycol diacrylate.<sup>17</sup> The utilization of acid-cleavable diacrylate in bisAcAc-DA networks generated crosslinked materials that degraded in less than 1 min under acidic conditions.

Herein, we propose the synthesis of hydrogenated polybutadiene diacrylate (hPBDA) and bisAcAc (hPBbisAcAc) as Michael acceptor and donor, respectively, through one-step nucleophilic reaction.  $^1\text{H}$  NMR spectroscopy confirmed the successful synthesis of Michael acceptor and donor after minimal purification. Michael acceptor and donor crosslinked readily after the introduction of catalytic amount of base. The resulting Michael networks highlighted tunable crosslinking kinetics with gel time varied from minutes to hours via molecular weight and chemical structures control. Michael networks showed consistent performance over a wide temperature range. Peel tests revealed comparable adhesive properties of Michael networks compared to commercial adhesive products. The introduction of tackifiers further improved the adhesive properties, promising Michael networks as solvent-free adhesive for the replacement of traditional solvent-based adhesives.

### **4.3 Experimental**

#### **4.3.1 Materials**

Hydrogenated polybutadiene diol (hPB, 2000 g/mol), commercial adhesive control, ethylene propylene diene monomer rubber (EPDM), polyvinyl chloride rubber (PVC), thermoplastic olefin (TPO), and plywood samples were provided by Carlisle Construction Materials. Acryloyl chloride, *t*-butyl acetoacetate (tBuAcAc), dichloromethane (DCM), toluene, 1,8-diazabicyclo[5.4.0]undec-7-ene (DBU), potassium carbonate, and aluminum oxide (neutral) were purchased from Sigma-Aldrich and used without further purification.

#### **4.3.2 Synthesis of hydrogenated polybutadiene diacrylate (hPBDA)**

A two-necked, 500-mL round-bottomed flask equipped with a 50-mL addition funnel containing acryloyl chloride (5.2 g, 0.055 mol) in anhydrous DCM (20 mL), was charged

with 2,000 g/mol hPB (50 g, 0.025 mol) and anhydrous  $K_2CO_3$  (10.4 g, 0.075 mol) and was sealed with a rubber septum. Anhydrous DCM (110 mL) was cannulated into the reaction flask and an ice bath was assembled to cool the reaction contents to 0 °C. Acryloyl chloride was added dropwise overnight and the reaction was allowed to warm to 23 °C. Reaction mixture was stirred with  $Al_2O_3$  overnight. DCM was removed under reduced pressure after filtration and the product was isolated as a viscous, clear liquid and dried in vacuum at 23 °C (48.23 g, 96 % yield).  $^1H$  NMR (400 MHz,  $CDCl_3$ ): 6.47 (d, 2H), 6.22 (dd, 2H), 5.77 (d, 2H), 4.13 (m, 4H), 0.75-1.5 (polymer back-bone).

#### **4.3.3 Synthesis of hydrogenated polybutadiene bisacetoacetate (hPBbisAcAc)**

In a typical procedure, 2,000 g/mol hPB (10.0 g, 10 mmol), tBuAcAc (6.3 g, 40 mmol, 4 equiv.), and toluene (50 mL) were charged to a two-necked, 100-ml flask equipped with a short-path distillation head, receiving flask, and magnetic stirrer. The mixture was kept at 110 °C for 4 h and vacuum (0.1 mmHg) was applied to remove the *t*-butanol by-product and excess tBuAcAc. An additional 6.3 g tBuAcAc was added and heating continued for 3 h at 130 °C in order to ensure quantitative functionalization. Vacuum (0.1 mmHg) at 130 °C was applied to remove volatile starting reagents and reaction by-products.  $^1H$  NMR (400MHz,  $CDCl_3$ ): 0.75-1.5 (polymer backbone), 1.24 ppm (dd, 6H), 2.26 ppm (s, 6H), 5.08 ppm (m, 4H), 5.29 ppm (s, 1H).

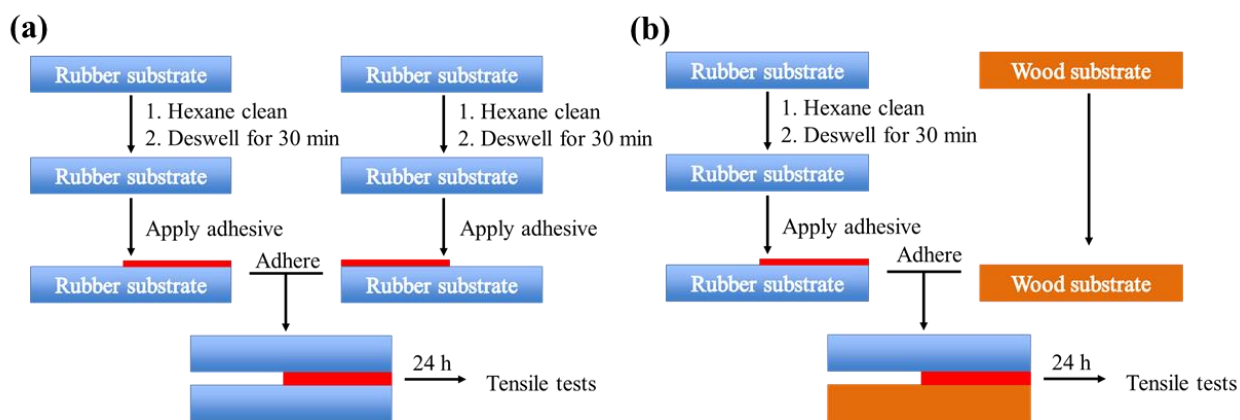
#### **4.3.4 Preparation of adhesive samples**

Equal weight of hPB and hPBbisAcAc (5 g) was mixed in a 50-ml beaker. A specific amount of DBU catalysts (50 mg, 1 wt% to DA) was added all at once, and mixed thoroughly using brushes. The mixture was quickly transfer to either rheometer plates or peel test substrates without further stirring.

### 4.3.5 Sample preparation for peel tests

The preparation of peel test substrates followed the description in **Scheme 4.1**. In 180° peel tests, both rubber membranes were cleaned with hexane to remove dust (**Scheme 4.1a**). After deswelling (30 min), freshly made adhesives were applied on both surfaces using brushes. Two surfaces were adhered immediately, and a 10-pound roller was employed to ensure good contact between adhesives and substrates. Then the samples were given 24 h at ambient condition to allow complete crosslinking before the test. The test samples were cut into 6 inches × 1 inches pieces, and adhesives were only applied in a 3 inches × 1 inches area (**Figure S4.1a**). As depicted in **Scheme 4.1b**, the sample preparation of 90° peel tests was similar to 180° peel tests except the wood substrates were directly utilized without any pretreatment. The rubber substrates were 10 inches × 3 inches and adhesives were applied in a 5 inches × 3 inches area (**Figure S4.1b**).

To prepare the Michael adhesives, equal weight of hPB and hPBbisAcAc (5 g) mixed in a 50-ml flask. A specific amount of DBU catalyst (50 mg, 1 wt% to DA) was added all at once, and mixed thoroughly. The mixture was immediately transfer to 10 tested substrates without further stirring.



**Scheme 4.1** Sample preparation for peel tests: (a) 180° peel tests between two identical rubber substrates; (b) 90° peel tests at the interfaces between rubber substrates and wood.

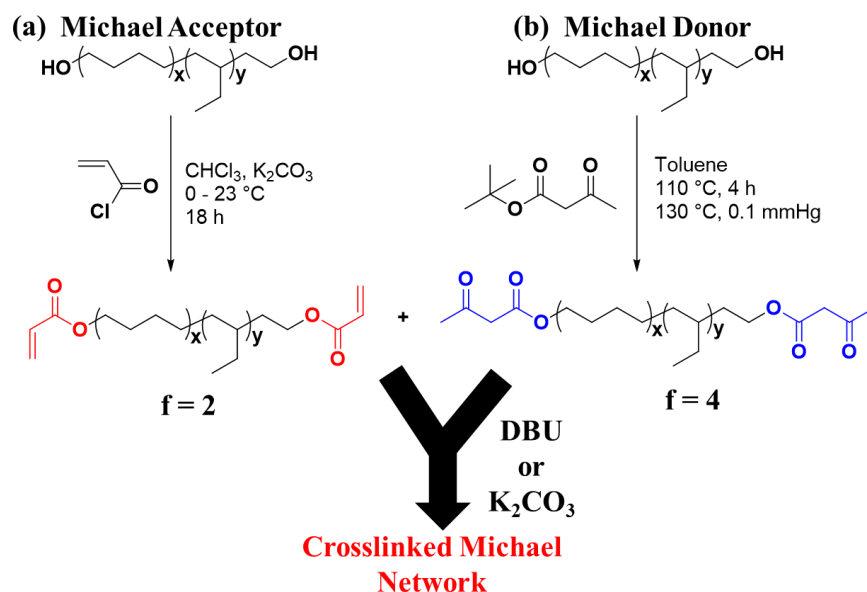
### 4.3.6 Analytic methods

<sup>1</sup>H nuclear magnetic resonance (<sup>1</sup>H NMR) spectroscopy was performed on a Varian Unit 400 MHz with CDCl<sub>3</sub> as solvent (23 °C). The crosslinking kinetic study was conducted using a TA AR-G2 rheometer where a time sweep was performed at 0 °C, 25 °C, and 50 °C, respectively (25 mm disposable parallel plates, 1 Hz, 1.25 % strain, and 1000 μm gap). Adhesive properties were investigated through a Instron 5500 at 50 mm/min rates for both 90 ° and 180 ° tests. The 90 ° peeling tests employed a special geometry that was provided by Carlisle Construction Materials (Figure S1b). All reported values were average of 5 samples. *In situ* FTIR was performed on a Mettlor Toledo ReactIR 45M with DiComp Probe, and the C=C vinyl peaks at 890 cm<sup>-1</sup> were employed to monitor the disappearance of diacrylates. Each FTIR spectrum was an average of 64 scans within 50 sec, and the area under peak determined chemical concentrations.

### 4.4 Results and Discussion

**Scheme 4.2** depicts the base-catalyzed synthesis of hydrogenated poly-butadiene diacrylate (hPBDA) and bisAcAc (hPBbisAcAc) and their crosslinking reaction. Telechelic hydrogenated polybutadiene diol (hPB) reacted with acryloyl chloride and *t*-butyl acetoacetate respectively to produce Michael acceptor hPBDA and Michael donor hPBbisAcAc, respectively. **Scheme 4.2a** shows the formation of hPBDA through nucleophilic attack of acryloyl chloride where **Scheme 4.2b** similarly shows the formation of hPBbisAcAc through nucleophilic attack of *t*-butyl acetoacetate. Both reactions completed in 24 h, and afforded quantitative yield with minimum purification. Hydrogenated polybutadiene was chosen for this study because it exhibits excellent thermal stability, good weatherability, hydrophobicity, low color, high clarity, and low glass transition temperatures (T<sub>g</sub> = -55 °C), affording their compatibility for applications

involving acid and base resistance, adhesion, asphalt miscibility, electrical insulation, and low temperature flexibility. Each bisAcAc molecule had four acid protons accessible for deprotonation, allowing chemical crosslinking with two acrylate groups per AcAc moiety. The synthesis is applicable for different telechelic oligomer backbones, affording tunable thermomechanical properties and hydrophobicity.



**Scheme 4.2** The synthesis of hPBDA (Michael acceptor) and hPBbisAcAc (Michael donor).

**Figure 4.1** illustrated the change of gel time as a function of catalyst concentrations and temperature. Gel time represents the crossover point of storage modulus ( $G'$ ) and loss modulus ( $G''$ ), symbolizing a transformation from viscous liquids towards solids. Figure 1a described the modulus change over time in a typical time sweep experiment of hPBDA and hPBbisAcAc Michael networks. At the initial state of the Michael addition reactions,  $G''$  was higher than  $G'$ , indicating primarily viscous liquid-like behavior. As the crosslinking proceeded, chemically crosslinked sites restricted the segmental motion of oligomer chains, causing a more solid-like behavior as evidenced by the evolution of

$G'$  over time. Eventually,  $G'$  surpassed  $G''$  to form a gel. As shown in Figure 1b, catalyst concentrations altered crosslinking kinetics significantly at 25 °C. Higher catalyst concentrations accelerated crosslinking kinetics, causing a decrease of gel time from 80 min (1 wt%) to 16 min (3 wt%). Hence, catalyst concentrations provided a facile approach to control crosslinking kinetics. Figure 1c and 1d demonstrated fast gel time at 25 °C (16 min) and 50 °C (10 min). At lower temperature (-10 °C), the mobility of both DA and bisAcAc decreased significantly, resulting in a much longer gel time (300 min).

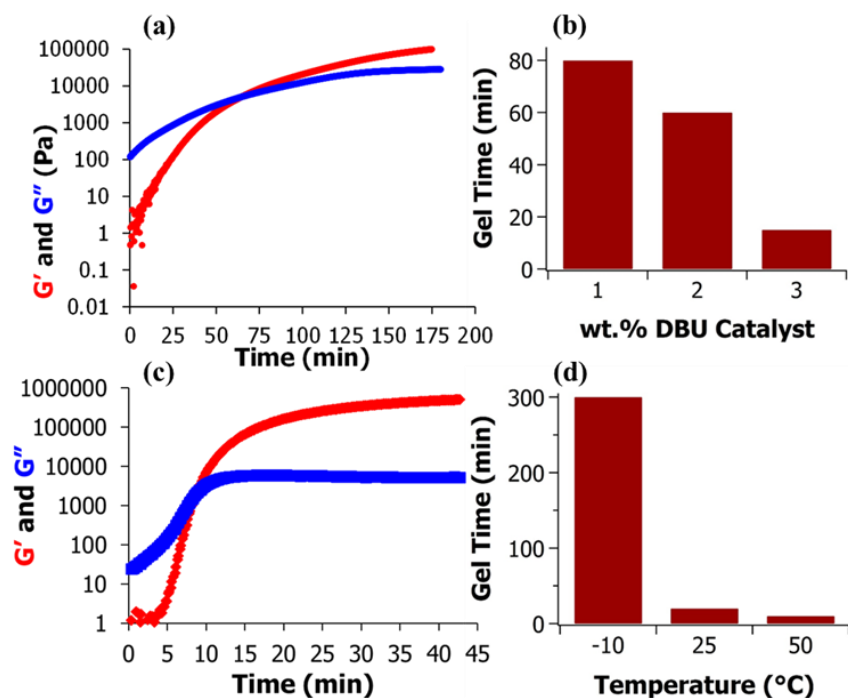


**Figure 4.1** Influence of catalyst concentrations (a & b) and temperatures (c & d) on crosslinking kinetics through rheology at 25 °C for a and b while catalyst concentration was set to 3 wt% (to bisAcAc) in c & d.

Molecular weights represent another commonly utilized parameter to control crosslinking kinetics. To investigate the influence of molecular weight on crosslinking kinetics, we employed three different DAs with a constant molecular weight hPBbisAcAc species. Three DAs covered a wide molecular weight range while maintaining low enough

viscosity as adhesive precursors: 2000 g/mol (hPBDA), 296 g/mol (trimethylolpropane triacrylate, TMPATA), and 198 g/mol (1,4-butanediol diacrylate, 1,4-BDA) (chemical structures shown as inset in **Figure 4.2c**). **Figure 4.2a** represents the typical Michael addition crosslinking behavior between DA and bisAcAc. Parallel plate rheology measured both  $G'$  and  $G''$ , which followed a similar pattern as described in the catalyst concentration study (**Figure 4.1a**). The temperature and catalyst concentration were set to 25 °C and 1 wt% for all rheological measurements. Michael networks with hPBDA exhibited the longest gel time (80 min), and lower molecular weight DAs demonstrated much faster crosslinking kinetics with circa 10 min gel time (**Figure 4.2b**). The molar ratios between acrylate and bisAcAc groups were constant to exclude functional group concentration differences. Hence we attributed the longer gel time from high molecular weight hPBDA to its higher viscosity and lower endgroup mobility.

*In situ* Fourier-transform infrared spectroscopy (FTIR) showed faster crosslinking kinetics with decreasing molecular weight of DAs, further supporting the conclusions from above rheology study (**Figure 4.2c**). The area under C=C vinyl peaks at 890  $\text{cm}^{-1}$  represents diacrylate concentration. Both TMPTA and 1,4-BDA revealed a complete consumption of acrylate groups within 10 min. However, the Michael addition between hPBDA and hPBbisAcAc extended to 90 min before 100% conversion. The time at 100% conversion correlated well with the gel times from rheological study, indicative of a complete consumption of acrylate groups before gel points. After gel points, both  $G'$  and  $G''$  started to plateau.

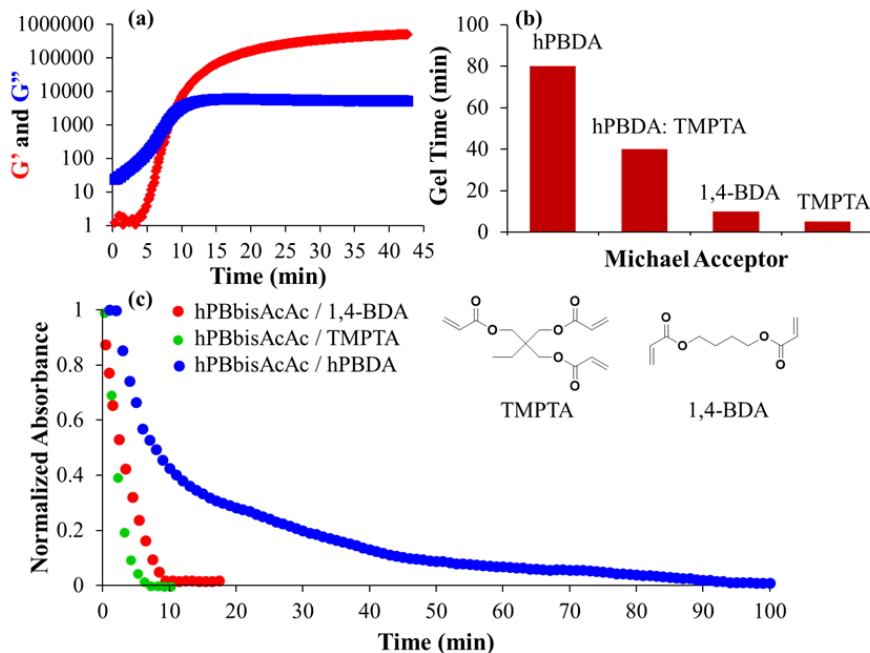


**Figure 4.2** Influence of diacrylate molecular weight on crosslinking kinetics using rheology (a & b) and *in situ* FTIR (c). Rheology:  $T = 25\text{ }^{\circ}\text{C}$ ; catalyst concentration = 3 wt% (to the weight of bisAcAc).

Another common strategy to fine tune the viscosity of adhesives, improve surface wetting, and enhance load transition between substrates is the addition of additives. For example, the addition of tackifiers improves adhesive properties, but also alters viscosity leading to variations in crosslinking kinetics. Hence, it is important to study the influence of tackifiers on crosslinking kinetics as well as adhesive properties. We conducted similar rheological studies in hPBDA/hPBbisAcAc matrices with 10 wt% of two commercial tackifiers: Indopole H-100 and Wingtack 10 (chemical structures shown in **Figure 4.3a**). **Figure 4.3b** showed the evolution of  $G'$  and  $G''$  as a function of reaction time after adding 10 wt% Indopole H-100. As illustrated in **Figure 4.3c**, we ascribed the increase of gel time (from 80 min to 120 min) to both diluted function group concentrations and increased viscosity compared to neat Michael networks. The gel time increased with the addition of 10 wt% Wingtack 10 as well due to the same reasons.

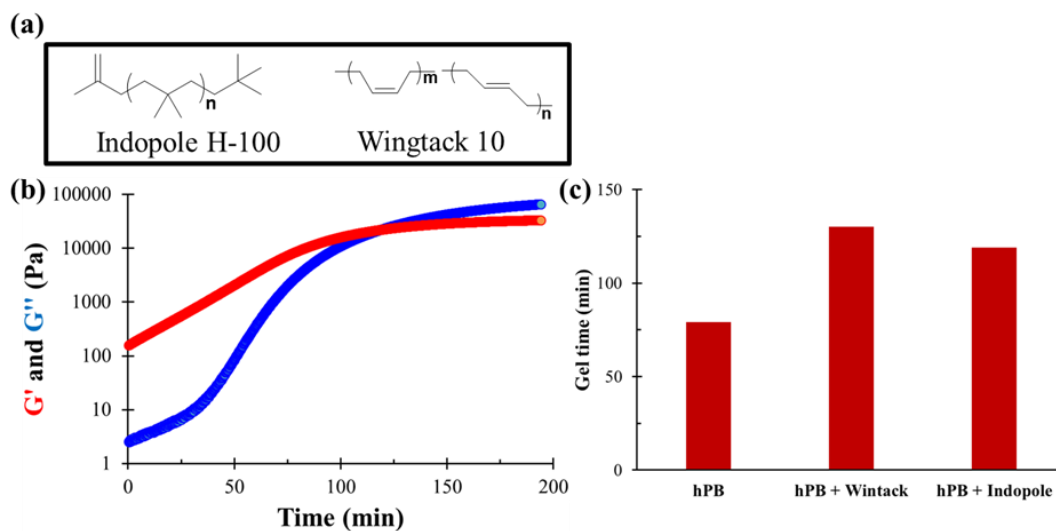


**Figure 4.3** Michael network crosslinking kinetics with the addition of tackifiers. Rheology:  $T = 25\text{ }^{\circ}\text{C}$ ; catalyst concentration = 1 wt%.

To evaluate the adhesive properties of Michael network over a wide range of substrates, we conducted  $180^{\circ}$  peel tests on three different rubber substrates for roofing applications: EPDM (ethylene propylene diene monomer), PVC (polyvinyl chloride), and TPO (thermoplastic polyolefin). Water contact angle study in **Figure S4.2** showed that EPDM was hydrophobic, while TPO and PVC were more hydrophilic. **Figure 4.4a** showed the load between two EPDM membranes as a function of peel time. Michael network with hPBDA/hPBbisAcAc demonstrated improved adhesive properties ( $\text{Load}_{\text{max}} = 3.6\text{ N}$  in Table 1) compared to commercial adhesive control ( $\text{Load}_{\text{max}} = 1.5\text{ N}$  in Table 1). Replacing hPBDA with 1,4-BDA yielded similar adhesive properties ( $\text{Load}_{\text{max}} = 3.6\text{ N}$  and  $3.1\text{ N}$ ) although their gel time was drastically different (80 min to 10 min), promising a facile approach to significantly alter crosslinking kinetics while maintaining similar adhesive properties (**Figure 4.4a** and **Table 4.1**). However, on PVC substrates, hPBDA and 1,4-BDA demonstrated different adhesion performance (**Figure 4.4b** and **Table 4.1**) where hPBDA showed lower maximum load (1.3 N) compared to adhesive control (3.5

N), presumably due to wettability differences. Interestingly, at TPO interfaces, the maximum load of Michael network decreased with decreasing molecular weight of DAs (10.0 N for hPBDA, and 4.6 N for 1,4-BDA) and both DAs showed improved adhesive properties than adhesive control. In summary, most Michael networks exhibited comparable or improved adhesive properties in comparison to low VOC adhesive controls, suggesting Michael networks as promising solvent-free adhesives.

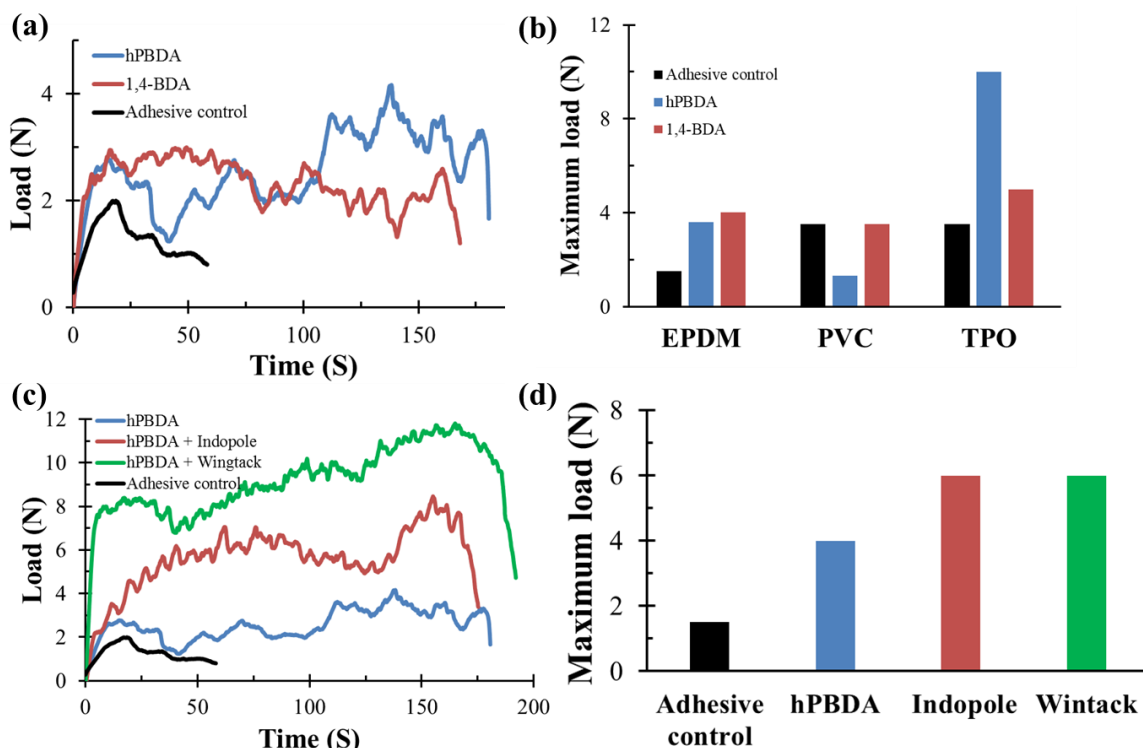


**Figure 4.4** 180° Peel test results: influence of diacrylate molecular weight (a & b) and tackifier addition (c & d) on adhesive properties. Rheology: T = 25 °C; catalyst concentration = 1 wt%.

**Table 4.1** Tensile results of 180° peel tests on EPDM, PVC, and TPO membranes.

Adhesive/substrates	Failure mode	Load <sub>max</sub> (N)
hPBDA/EPDM	Cohesive	3.6 ± 1.0
1,4-BDA/EPDM	Cohesive	3.1 ± 0.9
Control/EPDM	Cohesive	1.5 ± 0.6
hPBDA/PVC	Cohesive	1.3 ± 0.6

1,4-BDA/PVC	Cohesive	$3.7 \pm 0.4$
Control/PVC	Cohesive	$3.5 \pm 0.7$
hPBDA/TPO	Cohesive	$10.0 \pm 2.1$
1,4-BDA/TPO	Cohesive	$4.6 \pm 1.3$
Control/TPO	Cohesive	$3.5 \pm 1.8$

To further improve the adhesive properties, we introduced two different tackifiers (10 wt%) into the formula: Indopole H-100 and Wingtack 10. As **Figure 4.4c** and **Figure 4.4d** demonstrated, the adhesive properties further improved. Both Indopole H-100 and Wingtack 10 increased the maximum load from 3.6 N to 6.0 N at the EPDM interfaces. According to previous rheology study, the introduction of tackifiers slowed down the crosslinking kinetics but still reached the gel point within 2 h. Hence tackifiers successfully improved the adhesive performance of Michael networks at the minimal expense of slower crosslinking kinetics.

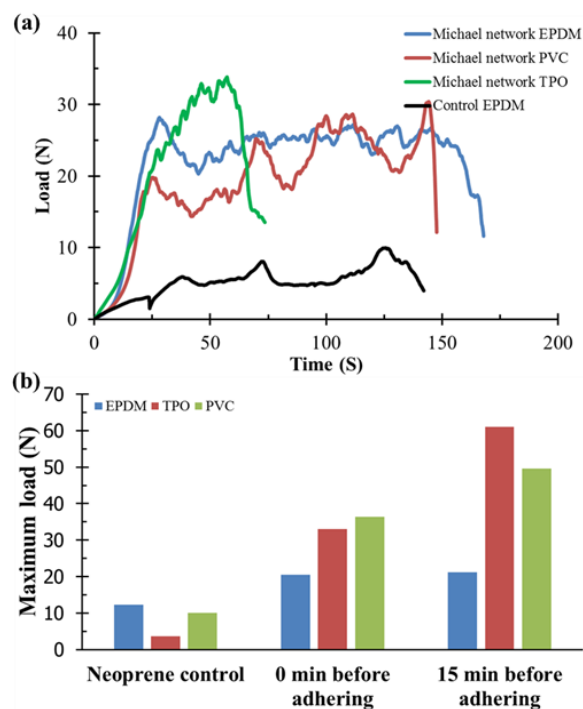


**Figure 4.5** 90° Peel test results on three different substrates (a) with different pre-cure time (b).

We further explore the potential of Michael networks as adhesives on other substrates, such as plywood. With the aid of tackifiers, Michael networks at least doubled the performance of adhesive control on all three rubber substrates as illustrated in **Figure 4.5a**. The fact that Michael networks generated excellent and similar adhesive properties across three different membranes demonstrated great potential for their use as universal adhesives. The adhesive properties of Michael networks between rubber membranes and plywood substrates further improved when allowing extra curing time before adhering two substrates together. **Figure 4.5b** featured the maximum loads from 90° peel tests on all three membranes (EPDM, PVC, and TPO). For EPDM/wood surfaces, 15 min extra curing time before adhering EPDM and plywood resulted in no improvement on the adhesive properties. However, at the PVC/wood and TPO/wood interfaces, 15 min additional curing time before adhering induced a significant enhancement of the maximum loads.

#### **4.5 Conclusion**

We successfully synthesized a novel pair of Michael donors and acceptor based on hydrogenated polybutadiene diol. The resulting Michael network exhibited tunable and facile crosslinking kinetics over a wide temperature range. Catalyst concentrations, molecular weight variation, and additives provided facile approaches to alter crosslinking kinetics. The peel tests revealed the Michael network afforded comparable adhesive properties at rubber/rubber interfaces and improved adhesive properties at rubber/wood interfaces compared to a commercial adhesive control. The fact that Michael networks yielded comparable or better adhesive properties at various interfaces compared to

commercial adhesive controls, promising their great potential as next-generation, solvent-free universal adhesives.

#### 4.6 Acknowledgment

The authors would like to thank Carlisle Construction Materials for funding this study and providing necessary materials and instruments. The authors would also like to thank Dr. E. Bruce Orler for discussion and input on this project.

#### 4.7 References

1. Mather, B. D.; Miller, K. M.; Long, T. E., Novel Michael addition networks containing poly(propylene glycol) telechelic oligomers *Macromol Chem. Phys.* **2006**, *207*, 1324-1333.
2. Tillet, G.; Boutevin, B.; Ameduri, B., Chemical reactions of polymer crosslinking and post-crosslinking at room and medium temperature *Prog. Polym. Sci.* **2011**, *36*, 191-217.
3. Zhu, J.; Peng, H. Q.; Rodriguez-Macias, F.; Margrave, J. L.; Khabashesku, V. N.; Imam, A. M.; Lozano, K.; Barrera, E. V., Reinforcing epoxy polymer composites through covalent integration of functionalized nanotubes *Adv. Funct. Mater.* **2004**, *14*, 643-648.
4. Czech, Z., Development of solvent-free pressure-sensitive adhesive acrylics *Int. J. Adhes. Adhes.* **2004**, *24*, 119-125.
5. Czech, Z.; Milker, R., Solvent-free radiation-curable polyacrylate pressure-sensitive adhesive systems *J. Appl. Polym. Sci.* **2003**, *87*, 182-191.
6. Czech, Z.; Wesolowska, M., Development of solvent-free acrylic pressure-sensitive adhesives *Eur. Polym. J.* **2007**, *43*, 3604-3612.
7. Gordon, J. E., *The New Science of Strong Materials*. Penguin Books: 1991.
8. Dodiuk, H.; Kenig, S., Low temperature curing epoxies for structural repair *Prog. Polym. Sci.* **1994**, *19*, 439-467.
9. Laurichesse, S.; Averous, L., Chemical modification of lignins: Towards biobased polymers *Prog. Polym. Sci.* **2014**, *39*, 1266-1290.
10. Geurts, J. M.; vanEs, J.; German, A. L., Latexes with intrinsic crosslink activity *Prog. Org. Coat.* **1996**, *29*, 107-115.
11. Pham, H. H.; Winnik, M. A., Polymer Interdiffusion vs Cross-Linking in Carboxylic Acid-Carbodiimide Latex Films *Macromolecules* **1999**, *32*, 7692-7695.
12. Chen, F.-B.; Bufkin, B. G., Crosslinkable emulsion polymers by autoxidation. II *J. Appl. Polym. Sci.* **1985**, *30*, 4551-4570.
13. Chung, T. C.; Lu, H. L.; Li, C. L., Synthesis and Functionalization of Unsaturated Polyethylene: Poly(ethylene-co-1,4-hexadiene) *Macromolecules* **1994**, *27*, 7533-7537.
14. Marshall, G. L.; Cudby, M. E. A.; Smith, K.; Stevenson, T. H.; Packer, K. J.; Harris, R. K., <sup>13</sup>C solid-state nuclear magnetic resonance spectra of some air-cured alkyd polyester paints *Polymer* **1987**, *28*, 1093-1097.
15. Sianesi, D.; Caporiccio, G., Polymerization and copolymerization studies on vinyl fluoride *J. Polym. Sci. Pol. Chem.* **1968**, *6*, 335-352.

16. Mather, B. D.; Viswanathan, K.; Miller, K. M.; Long, T. E., Michael addition reactions in macromolecular design for emerging technologies *Prog. Polym. Sci.* **2006**, *31*, 487-531.
17. Ozturk, G.; Long, T. E., Michael Addition for Crosslinking of Poly(caprolactone)s *J. Polym. Sci. Pol. Chem.* **2009**, *47*, 5437-5447.
18. Mather, B. D.; Williams, S. R.; Long, T. E., Synthesis of an acid-labile diacrylate crosslinker for cleavable Michael addition networks *Macromol Chem. Phys.* **2007**, *208*, 1949-1955.

#### 4.8 Supporting Information

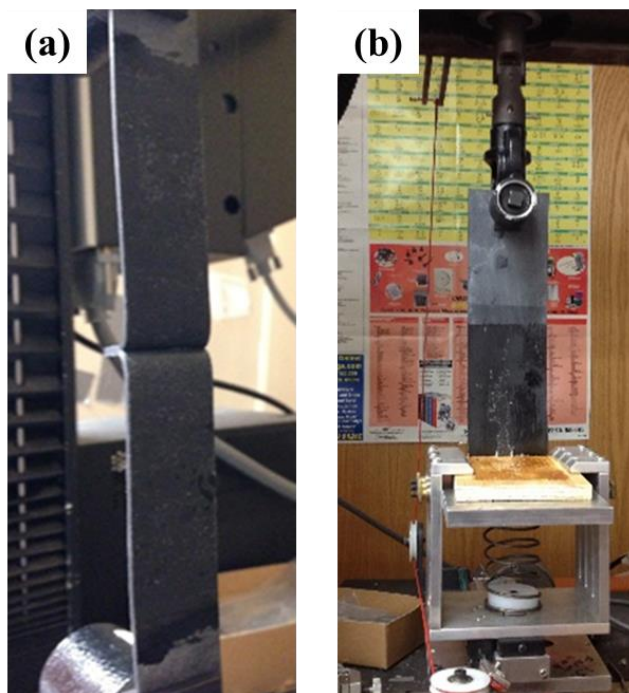


**Figure S4.1** Graphic illustration of 180° (a) and 90° (b) peel tests using Instron 5500.

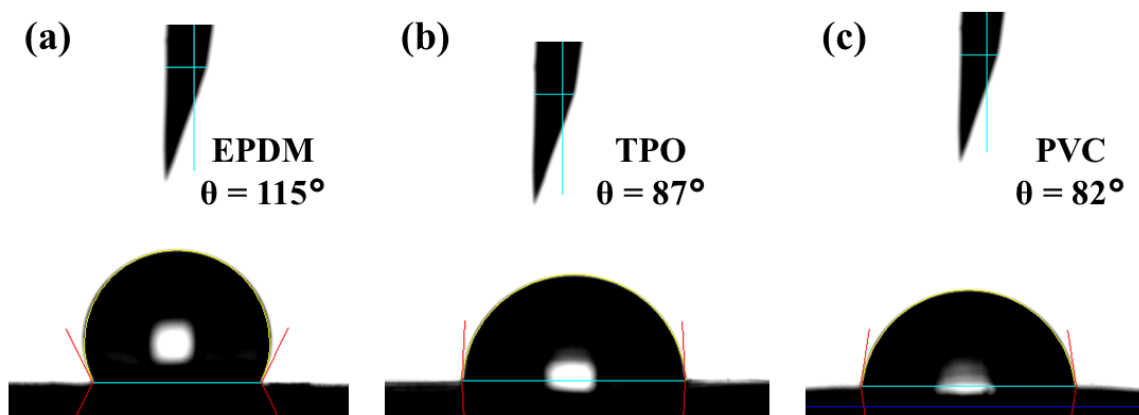


**Figure S4.2** Water contact angles on EPDM (a), TPO (b), and PVC (c).

# **Chapter 5: Polyisoprene-Microstructure Control through Anionic Polymerization: Synthesis of 4-Vinylbenzyl Piperidine-Containing ABC Triblock Copolymers**

*(manuscript in preparation for publication)*

*Mingtao Chen, Alison R. Schultz, Sachin Bobade, Timothy E. Long\**

Department of Chemistry, Virginia Tech., Blacksburg, VA 24061, USA.

Macromolecules Innovation Institute (MII), Virginia Tech., Blacksburg, VA 24061, USA

\*To whom correspondence should be addressed: [telong@vt.edu](mailto:telong@vt.edu)

## **5.1 Abstract**

Anionic polymerization of 4-vinylbenzyl piperidine, isoprene, and styrene in nonpolar solvent produced ABC triblock copolymers containing polystyrene and poly(4-vinylbenzyl piperidine) (poly4VBP) outer blocks separated by a polyisoprene central block. The microstructure of the polyisoprene repeat units was controllable through the order of monomer addition. For synthesis beginning with the 4VBP monomer, the presence of the polar poly4VBP segment led to high 3,4-addition polyisoprene (38 ~ 49%). However the addition of monomers in the sequence of styrene, isoprene, then 4VBP yielded poly(styrene-*b*-isoprene-*b*-4-vinylbenzyl piperidine), poly(S-I-4VBP), triblock copolymers with polyisoprene blocks containing significantly lower 3,4 addition

content (8%) and *trans/cis*-1,4 addition ratio. To the best of our knowledge, this is the first report of high 3,4-addition polyisoprene block synthesis without polar additives in nonpolar solvent. *In situ* Fourier transfer infrared spectroscopy (FTIR) monitored the anionic polymerization process and confirmed the quantitative polymerization within 2 hours. Dynamic mechanical analysis (DMA) and differential scanning calorimetry (DSC) demonstrated either microphase mixing or separation depending on the polymer molecular weights and 3,4 addition content of isoprene. Facile alkylation of 4VBP in 4VB-I-S provided a charged polymer mimic of SIS rubber for future study.

## 5.2 Introduction

Block copolymers have been the subject of sustained research focus for decades due to their ability to synergize different properties of its constituent blocks. Block copolymers widely serve as thermoplastic elastomers,<sup>1-5</sup> barrier membranes,<sup>6-10</sup> sensing agents,<sup>11-14</sup> electroactive devices<sup>15-19</sup> and lithographic patterning materials.<sup>20-23</sup> To further fine tune block copolymer properties, synthetic design focuses on either new monomer structures<sup>24-27</sup> or control of repeat unit microstructures. Microstructure such as tacticity,<sup>28-29</sup> chirality<sup>30-32</sup>, 1,4/1,2/3,4 addition ratio<sup>33-35</sup> and *cis/trans* ratio<sup>33-42</sup> provides significant tunability in polymer properties.

Tenhu *et al.* demonstrated that ABA triblock copolymers composed of inner atactic and outer isotactic poly(N-isopropylacrylamide) (PNIPAM) blocks exhibited two distinct glass transition temperatures ( $T_g$ ).<sup>29</sup> Chen *et al.* studied the solubility of glycosylated antibiotic nocathiacin I in methoxyl-poly(ethylene glycol)-*b*-polylactate micelles (MPEG-PLA).<sup>30</sup> The authors demonstrated that both L- and D- block copolymers enhanced the aqueous solubility of nocathiacin I, but the degree of

enhancement was dependent on the chirality of the PLA block. D-poly lactate-based micelles promoted the solubility of D-sugar-containing nocathiacin I more than L-sugar-containing nocathiacin I.

Similar to tacticity and chirality, *1,4/1,2/3,4* addition ratio in polydienes affords drastic changes in polymer properties. Hadjichristidis and Thomas *et al.* showed significant  $T_g$  shift from high *1,4* addition polyisoprene (-80 °C) to high *3,4* addition polyisoprene (-30 °C).<sup>39</sup> Cui *et al.* studied polyisoprene with remarkably high *3,4* addition (> 95 %) using a rare earth metal carbene complex.<sup>33</sup> High *3,4* addition polyisoprene exhibited  $T_g$ s between 40-50 °C.

The strong influence of *1,4/1,2* addition ratio on polymer physical properties stimulates ongoing investigation into the synthesis of stereo-specific diene polymers. The majority of successful stereo-controls in diene polymers involve metal complex catalysts.<sup>35-38, 43-45</sup> However polar additives, such as tetrahydrofuran (THF), are also used to increase polymerization rate and thus favor the formation of kinetic products, namely *1,2* or *3,4* addition.<sup>39, 46</sup> Interestingly, Bini *et al.* also probed the possibility of controlling *3,4*-polyisoprene content through pressure.<sup>47</sup>

Herein we proposed the synthesis of diblock (AB) and triblock (ABC) copolymers with high *3,4* addition polyisoprene blocks through anionic polymerization in nonpolar solvent and without any polar additives. Formed first in the polymerization, a polar hard block served as internal polar additives to promote *3,4* addition in the subsequent polyisoprene block. Long *et al.* demonstrated 4-vinylbenzyl piperidine (4VBP) was suitable for anionic polymerization, and readily alkylated to afford a charged segment.<sup>48</sup> This study investigates the incorporation of this polymer into block

copolymers and the effects of the polar repeat units on the polymerization conditions. *In situ* FTIR monitored the synthesis of poly(4-vinylbenzyl piperidine-*b*-isoprene-*b*-styrene), poly(4VBP-I-S), and elucidated the rapid conversion of both 4VBP and styrene monomers in cyclohexane. <sup>1</sup>H NMR spectroscopy revealed that both poly(4VBP-I) and poly(4VBP-I-S) block copolymers contained high 3,4 addition content in the polyisoprene segments (38 ~ 49%). Moreover, quantitative <sup>13</sup>C NMR spectroscopy showed significant reduction of *cis*-1,4 addition for polyisoprene blocks polymerized in the presence of the polar poly4VBP segment. Conversely, when introducing polystyrene as the first block in poly(S-I-4VBP), the polyisoprene blocks exhibited low 3,4 addition values in nonpolar environment and preferred *cis*-1,4 addition (72%). In most AB and ABC block copolymers, dynamic mechanical analysis (DMA) and differential scanning calorimetry (DSC) suggested the presence of microphase separation. However, low molecular-weight polyisoprene with high 3,4 addition exhibited microphase mixing with poly4VBP segments. We attribute the phase mixing to a combined effect of increased polarity from high 3,4 addition content and decreased molecular weight.

## 5.3 Experimental

### 5.3.1 Materials

Piperidine (> 99.5 %, purified by redistillation), 4-vinylbenzyl chloride ( $\geq 90$  %), calcium hydride (95 %), di-*n*-butylmagnesium solution (DBM, 1.0 M in heptane), and *sec*-butyllithium solution (1.4 M in cyclohexane) were purchased from Sigma Aldrich and used as received. N-methyl piperidine was purchased from Sigma Aldrich and freshly distilled from CaH<sub>2</sub> prior to use. Cyclohexane was purchased from Sigma Aldrich and passed through an activated alumina column to remove moisture and oxygen. Styrene

(stabilized by 4-*tert*-butylcatechol,  $\geq 99$  %) and isoprene (99 %) were purchased from Sigma Aldrich and distilled twice from calcium hydride and DBM and degassed via freeze-pump-thaw prior to use. 4-vinylbenzyl piperidine (4VBP) was synthesized based on previous literature, and distilled twice from calcium hydride and DBM and degassed through freeze-pump-thaw prior to use.<sup>49</sup>

### 5.3.2 Instrumentation

<sup>1</sup>H nuclear magnetic resonance (NMR) spectroscopy was performed on an Agilent Technologies 400 MR (400 MHz) NMR spectrometer in deuterated chloroform (256 scans). <sup>13</sup>C NMR was conducted on a Varian 400-MR (400 MHz) NMR spectrometer with 5 s relaxation delay and 3400 scans in decouple – NOS mode. Thermal stability under nitrogen atmosphere was determined using TA Instruments thermogravimetric analysis (TGA) Q500 with 10 °C/min heating rate. Differential scanning calorimetry (DSC) was performed through a TA instruments Q2000. T<sub>g</sub> values were reported from the middle point of second heat in a heat/cool/heat cycle (10 °C/min heating rate and quench cool under nitrogen). A TA Instruments Q800 dynamic mechanical analysis (DMA) was applied in film tension mode at a heating rate of 3 °C/min (1 Hz). *In situ* FTIR analysis was conducted using a Mettler Toledo ReactIR 45M attenuated total reflectance reaction apparatus connected with a light conduit and DiComp 9diamond composite insertion probe.

### 5.3.3 Monitoring of poly(4VBP-I-S) anionic polymerization through *in situ* FTIR

Synthesis of poly(4VBP-I-S) through anionic polymerization was monitored using *in situ* FTIR. A typical procedure of poly(4VBP-I-S) (10-10-10 kg/mol) synthesis was performed as follows: the IR reference signals of 4-vinylbenzyl piperidine, styrene,

isoprene and cyclohexane were collected prior to the reaction. A two-neck, 25-mL round-bottomed flask with a magnetic stir bar was flame-dried with nitrogen purge and sealed with rubber septum and copper wire. Cyclohexane (10 mL) was added via gas-tight syringe to the reaction flask under nitrogen. With continued nitrogen purge, a DiComp probe was inserted and sealed tightly via a Teflon adapter. The probe tip was submerged below the solvent surface, and the experiment was set to collect one spectrum per minute for 12 h. 4VBP (1.0 g, 1.01 mL) was added to the reaction flask via gas-tight syringe under nitrogen with strong stirring. The initiator, *sec*-butyllithium (0.07 mL), was added to the reaction via gas-tight syringe under nitrogen and the data collection started at the same time. Red color appeared in the solution immediately upon initiator addition corresponding to the living 4VBP anions. The vinyl peak at 907  $\text{cm}^{-1}$  was monitored to determine the monomer conversion over time. After the vinyl peak stabilized at the baseline, isoprene (1g, 1.47 mL) was added via gas-tight syringe under nitrogen. The red color faded gradually due to crossover and propagation of the polyisoprene segments. Then styrene (1g, 1.1 mL) was injected to the reaction flask under nitrogen after the second baseline was reached, and an orange color appeared from styrenic anions. Degassed methanol was added via gas-tight syringe to terminate the polymerization after full depletion of the styrene vinyl peak.

#### **5.3.4 Anionic polymerization of 4VBP containing block copolymers**

Anionic polymerization was conducted under dry nitrogen in round-bottomed flask and the monomers were introduced to the system sequentially as designed. A typical synthesis of poly(4VBP-I-S) 10-10-10 kg/mol was demonstrated as follows: A flame-dried, one-neck, 100 mL round-bottomed flask was sealed tightly with rubber septum and

copper wire, then the reaction flask was charged with ~35 mL cyclohexane and 3 g 4-vinylbenzyl piperidine (3.03 mL) via gas-tight syringe. The round-bottomed flask was further sealed with Teflon<sup>®</sup> tape and parafilm<sup>®</sup>. Under strong stirring, *sec*-butyllithium (0.21 mL) was injected rapidly to the reaction flask via gas-tight syringe. Instant red color indicated the successful initiation of 4-vinylbenzyl piperidine. After 1 h, isoprene (3 g, 4.4 mL) was added to the reaction flask. The red color gradually faded and became pale yellow. After 2 h, styrene (3 g, 3.1 mL) was injected to the reaction flask and allowed to propagate for 1 h. The reemergence of light red color indicated the successful crossover from isoprene to styrene. Finally, the polymerization was terminated using degassed methanol (1 mL) and polymers were recovered by precipitating into excess methanol twice. Obtained polymers were dried at 23 °C under reduced pressure for 48 h to yield a white powder (~ 90 % isolation yield). All block copolymers were stored in dry desiccator under vacuum. Composition of block copolymers and polymer structures were further confirmed by <sup>1</sup>H NMR spectroscopy (**Figure 1**). All the control homopolymers were synthesized and purified in the same fashion.

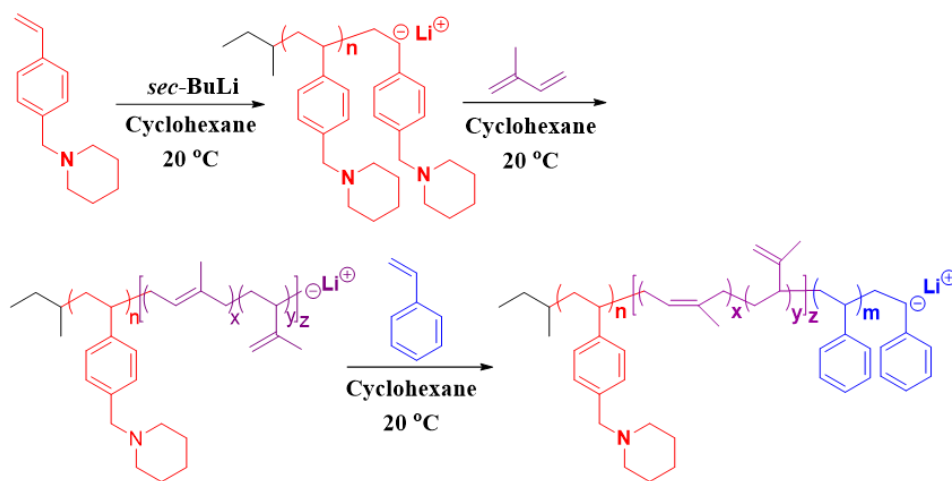
### 5.3.5 Film casting

All block copolymers were casted from 25 wt% solution in THF. The films were allowed to dry under ambient conditions for 24 then in active fume hood for 24 h. The films were then further dried *in vacuo* for 12 h. The films were annealed at 120 °C for 6 h and cooled down to 23 °C slowly *in vacuo* to avoid isoprene oxidation. <sup>1</sup>H NMR spectroscopy of the annealed film showed negligible oxidation.

## 5.4 Results and discussion

### 5.4.1 Anionic polymerization of 4VBP-containing block copolymers

Owing to the thermal autopolymerization of 4VBP, typical controlled radical polymerizations (CRP) which employ thermal initiator at elevated reaction temperature are not suitable for the synthesis of 4VBP-containing block copolymers.<sup>48</sup> Instead, anionic polymerization of 4VBP allows fast synthesis of 4VBP-containing block copolymers at room temperature. In order to prepare well-defined block copolymers, rapid and quantitative consumption of all monomers added in sequence is necessary. *In situ* FTIR provides a facile approach to monitor the reaction rate and helps determine the reaction time for each block.



**Scheme 5.1** The synthesis of poly(4VBP-b-I-b-S) block copolymers using living anionic polymerization.

Therefore we applied *in situ* FTIR to probe the kinetics of anionic polymerization for the synthesis of poly(4VBP-I-S) triblock copolymers (**Scheme 5.1**) with a target number average molecular weight  $M_n$  of 10-10-10 kg/mol. Recorded FTIR waterfall plots showed the decrease of monomer concentration with time, as monitored by the disappearance of the peak intensity at  $907\text{ cm}^{-1}$  corresponding to the vinyl vibration of the monomers (**Figure 5.1**). As shown in **Figure 5.1**, the completion of 4VBP occurred

within 5 min after the initiation. After 10 min equilibration, the intensity of the vinyl peak spiked as a result of the introduction of isoprene monomers, and the propagation of isoprene block proceeded much slower compared to 4VBP. The intensity of the vinyl peak reached the baseline after 60 min. The new baseline was higher than the baseline after 4VBP injection as a result of residual double bonds in isoprene repeating units. After the addition of styrene monomers, the double bond intensity increased rapidly again and then decreased to baseline within 10 min. The successful, sequential addition of isoprene and styrene further supported the “living” nature of this polymerization.

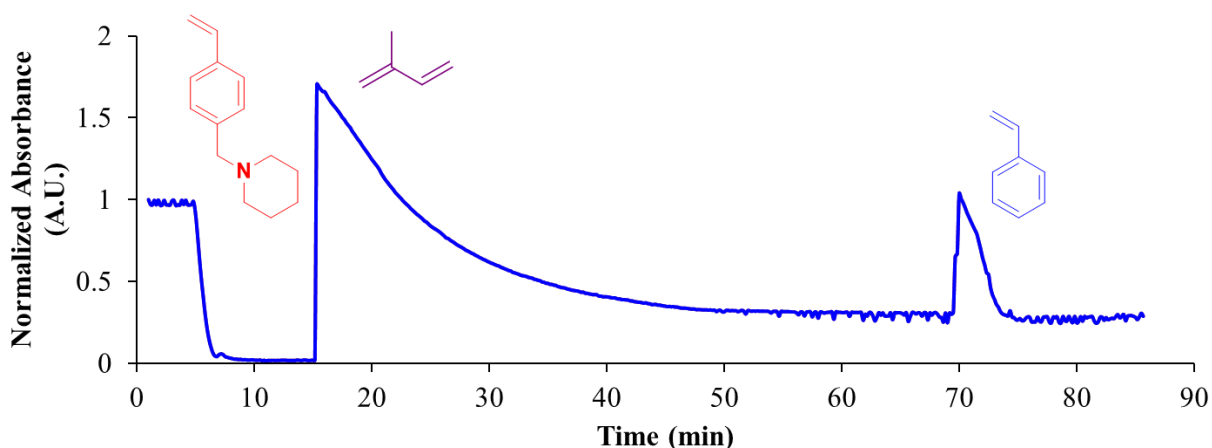


**Figure 5.1.** *In situ* Fourier transform infrared spectroscopy of poly(4VBP-*b*-I-*b*-S) block copolymers synthesized through living anionic polymerization.

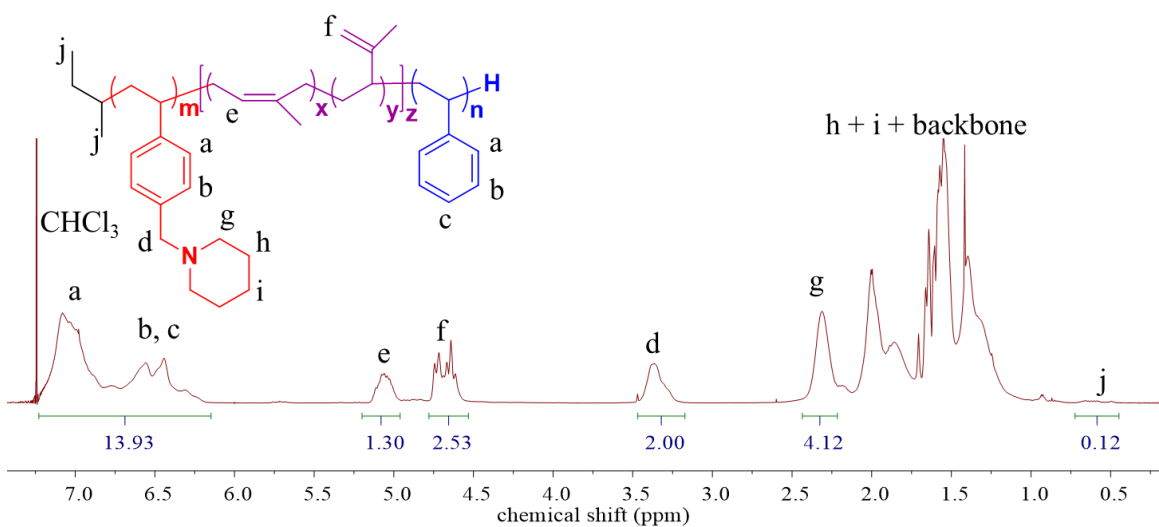


**Figure 5.2.**  $^1\text{H}$  NMR spectroscopy allowed the calculation of the  $M_n$  of poly(4VBP-I-S) (10-10-9 kg/mol shown). The existence of 4VBP segment led to higher 3, 4 addition percent in the isoprene block.

Previous work from our lab employed SEC with THF mobile phase to determine the molecular weight of 4VBP-containing styrenic based block copolymers.<sup>48</sup> However, with the introduction of polyisoprene, the block copolymers potentially interact with the SEC columns and fail to yield meaningful data. Therefore,  $^1\text{H}$  NMR spectroscopy served as the sole method for molecular weight determination, through comparison of the repeat unit peak integrations (**Figure 5.2** peak d) to that of the methyl groups on the initiator (**Figure 5.2** peak j). The calculated molecular weight of a series of 4-VBP containing diblock and triblock copolymers agreed well with the target molecular weights (**Table S5.1**). Due to lack of SEC characterization, the target molecular weights remained between 10 to 25 kg/mol to avoid significant calculation errors from  $^1\text{H}$  NMR spectroscopy.

#### **5.4.2 Polyisoprene microstructure study**

The polyisoprene homopolymer prepared in nonpolar solvent showed only 5 % 3,4 addition in  $^1\text{H}$  NMR spectroscopy (**Table 5.1**). However, diblock and triblock copolymers beginning with the poly4VBP block showed significantly higher 3,4 addition 38 ~ 49 %. In contrast, the poly(S-I-4VBP) triblock copolymer, where the polymerization of isoprene occurred prior to the introduction of poly4VBP, exhibited significantly lower 3,4 content (8 %), similar to that of the polyisoprene homopolymer (**Figure S5.1**). To further confirm the influence of poly4VBP segments on polyisoprene microstructure, poly4VBP homopolymer (21 kg/mol) and N-methylpiperidine were used as free additives in the synthesis of polyisoprene homopolymer. **Table 5.1** shows that

both polar additives (poly4VBP and N-methylpiperidine) resulted in polyisoprene homopolymers with high 3,4 addition (21% and 37%) as expected. Meanwhile, poly(I-4VBP-I) (9-10-9 kg/mol) triblock copolymers demonstrated 30 % 3,4 addition, suggesting an isoprene block with low 3,4 addition content prior to poly4VBP block and final isoprene block with high 3,4 addition. When comparing the two poly(4VBP-I-S) triblock copolymers or the two poly(4VBP-I) diblock copolymers, the 3,4 addition increased with higher 4VBP/I ratio, further supporting 4VBP's polarity effect on the polyisoprene microstructures (**Table 5.1**). Whereas, for poly(S-I-4VBP) triblock copolymers, such effect was absent and resulted in the polyisoprene blocks with lower 3,4 addition repeating units. Thus, the microstructures of polyisoprene blocks were controlled through a polar segment (poly4VBP) either prior or after the polymerization of isoprene monomers.

**Table 5.1** Isoprene microstructure study using  $^1\text{H}$  NMR spectroscopy.  $M_n$  and isoprene 3,4 addition percent calculated from  $^1\text{H}$  NMR: a. isoprene (3g) + poly4VBP homopolymers (1g); b. isoprene (3g) + N-methylpiperidine (3g)

Polymers	$M_n$ (kg/mol) $^1\text{H}$ NMR	3,4 addition in isoprene block (%)
Polyisoprene	14	5
Poly4VBP	21	N/A
Polyisoprene + poly4VBP <sup>a</sup>	25 + 21	21
Polyisoprene + N-methylpiperidine <sup>b</sup>	20	37
Poly(4VBP- <i>b</i> -I)	25-13	43
Poly(4VBP- <i>b</i> -I)	25-23	38
Poly(4VBP- <i>b</i> -I- <i>b</i> -S)	25-10-10	39
Poly(4VBP- <i>b</i> -I- <i>b</i> -S)	10-10-9	49

Poly(S- <i>b</i> -I- <i>b</i> -4VBP)	25-28-11	8
Poly(S- <i>b</i> -I- <i>b</i> -4VBP)	10-10-10	8
Poly(I- <i>b</i> -4VBP- <i>b</i> -I)	9-10-9	30

Due to peak overlap in the 4VBP-containing block copolymers,  $^1\text{H}$  NMR spectroscopy was not suitable to study the *trans/cis* ratio. Instead, quantitative  $^{13}\text{C}$  NMR enabled a detailed study on the *trans/cis* ratio (**Figure S5.2**). Due to the interference of other carbon peaks in poly4VBP and polystyrene blocks, only the methyl groups in isoprene repeating units allowed for calculation of both 3,4 addition content and the *trans/cis* ratio in 1,4 addition through quantitative  $^{13}\text{C}$  NMR spectroscopy.<sup>50</sup> As shown in **Table 5.2**, the 3,4 addition value from  $^{13}\text{C}$  NMR spectroscopy closely aligned with  $^1\text{H}$  NMR spectroscopy. While the *trans*-1,4 addition content remained relatively constant for all the samples, the *cis*-1,4 addition decreased when 4VBP was polymerized before isoprene. Poly(4VBP-I-S) 10-10-9 kg/mol and poly(S-I-4VBP) 10-10-10 kg/mol showed similar *trans*-1,4 addition content (18% and 23%). However, poly(4VBP-I-S) triblock copolymers demonstrated significantly lower *cis*-1,4 addition content (30%) than poly(S-I-4VBP) (68%). Within two poly(4VBP-I-S) samples, increased 4VBP content (10-10-9 kg/mol) further increased 3,4 addition and decreased *cis*-1,4 addition. The rationale behind these phenomena was the polar poly4VBP blocks promoted 3,4 addition by depressing the formation of the other kinetic product *cis*-1,4 addition. However, as a thermodynamically favored product, *trans*-1,4 addition content remained relatively constant since the reaction temperatures were similar.

**Table 5.2** The results of quantitative  $^{13}\text{C}$  NMR spectroscopy of 4VBP-containing triblock copolymers

Polymers	$M_n$	3,4 addition	1,4 addition (%)
----------	-------	--------------	------------------

	(kg/mol)	(%)	<i>cis</i>	<i>trans</i>
Polyisoprene + poly4VBP	25 + 21	22	53	25
poly(4VBP-I-S)	25-10-10	33	49	18
poly(4VBP-I-S)	10-10-9	46	30	24
poly(S-I-4VBP)	25-28-11	9	72	19
poly(S-I-4VBP)	10-10-10	9	68	23

### 5.4.3 Thermal and thermomechanical analysis

TGA of 4VBP-containing block copolymers showed similar thermal stability and exhibited 5 wt% loss degradation temperature ( $T_{d,5\%}$ ) above 340 °C. The homopolymers of 4VBP and styrene had a  $T_g$  at 70 °C and 100 °C from DSC, respectively. Whereas, the  $T_g$  of polyisoprene homopolymer depends on 3,4 addition percent. Polyisoprene with 3,4 addition values of 5 %, 21 % and 37 % had a  $T_g$  of -60, -52 and -46 °C, respectively (Figure 5.3 & Table 5.3).

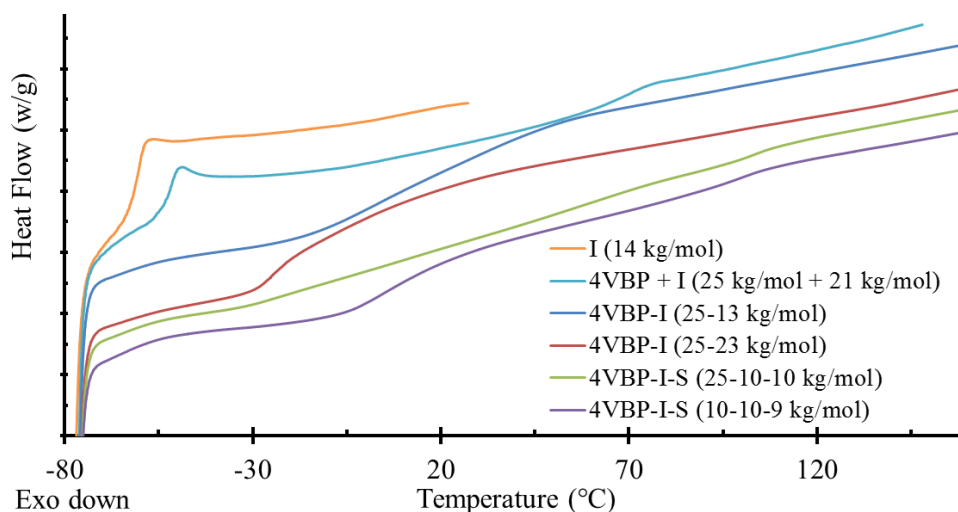


**Figure 5.3.** DSC suggested micro-phase mixing of isoprene block with low molecular weight 4VBP block and micro-phase separation of isoprene block with high molecular weight 4VBP.

Blends of low and high 3,4 addition polyisoprene homopolymers (5 % and 21 %) with poly4VBP (21 kg/mol) exhibited two distinct  $T_g$ s indicating the immiscible nature of

the two blocks. However, for both poly(4VBP-I) and poly(4VBP-I-S) block copolymers, samples with low molecular weight polyisoprene (25-13 and 10-10-9 kg/mol) yielded a  $T_g$  at 0 °C suggesting microphase mixing between poly4VBP and polyisoprene segments (**Figure 5.3 & Table 5.3**). For block copolymers with higher molecular weight of polyisoprene and poly4VBP, the  $T_g$  decreased to -21 °C and -30 °C, indicating a better microphase separation. According to Flory-Huggins theory, high molecular weight facilitates microphase separation.<sup>51-53</sup> The  $T_g$ s of polyisoprene with different 3,4 addition levels correspond with previous reports.<sup>54</sup> In general, polyisoprene tends to undergo microphase separation from poly4VBP segments. However, low-molecular weight, high 3,4 addition polyisoprene block demonstrated microphase mixing with poly4VBP, suggested by DSC. We ascribe this phenomena to both high polarity from 3,4 addition content and low molecular weight. The lower  $T_g$ s in microphase separated block copolymers were still higher than the  $T_g$  (-46 °C) of the polyisoprene homopolymer with similar 3,4 addition content as expected. Similar to most block copolymers, the  $T_g$ 's of the soft segments tend to increase due to the restricted mobility of hard segments.<sup>55</sup>

In contrast, poly(S-I-4VBP) block copolymers with low molecular weight (10-10-10 kg/mol) exhibited similar low  $T_g$  as high molecular weight analogs (25-28-11 kg/mol) suggested microphase separation between polyisoprene and poly4VBP blocks was independent of the molecular weights. In this case, the polyisoprene segment with only 8 % 3,4 repeating units was less polar than those in poly(4VBP-I-S) making them immiscible with poly4VBP even at low molecular weight. As a result of controllable polyisoprene microstructures, the microphase morphology and corresponding

thermomechanical properties were tunable depending on the monomer sequence and the molecular weights of each block.

**Table 5.3** Thermomechanical study of 4VBP containing block copolymers and control polymers.  $M_n$ , number average molecule weight, calculated from  $^1\text{H}$  NMR.  $T_g$ , glass transition temperature, obtained from DSC middle point and DMA  $\tan \delta$ .

Polymers	$M_n$ (kg/mol) $^1\text{H}$ NMR	$T_g$ ( $^{\circ}\text{C}$ ) DSC	3,4 addition% in isoprene block
Polyisoprene	14	-60	5 %
Poly4VBP	21	70	N/A
Polyisoprene + poly4VBP	14 + 21	-56, 68	5 %
Polyisoprene + poly4VBP	25 + 21	-52, 69	21 %
Polyisoprene + N-methylpiperidine	20	-46	37 %
Poly(4VBP- <i>b</i> -I)	25-13	6 (broad)	43 %
Poly(4VBP- <i>b</i> -I)	25-23	-21	38 %
Poly(4VBP- <i>b</i> -I- <i>b</i> -S)	25-10-10	-30, 103	39 %
Poly(4VBP- <i>b</i> -I- <i>b</i> -S)	10-10-9	0, 98	49 %
Poly(S- <i>b</i> -I- <i>b</i> -4VBP)	25-28-11	-54, 88	8 %
Poly(S- <i>b</i> -I- <i>b</i> -4VBP)	10-10-10	-51, 62	8 %
Poly(I- <i>b</i> -4VBP- <i>b</i> -I)	9-10-9	-44	30 %

The absence of the poly4VBP  $T_g$  in the highly microphase-separated 4VBP-containing block copolymers were presumably due to the low sensitivity of DSC. In order to further study microphase separation, we employed DMA to probe the thermomechanical properties of these block copolymers (**Figure 5.4**). All block copolymers showed comparable glassy modulus at low temperature, and reached a plateau prior to yield. All three microphase-separated samples exhibited a low  $T_g$  (-21 ~ -36  $^{\circ}\text{C}$ ) consistent with DSC (**Table 5.4** entry a, c, d). The shoulder peak at around 70  $^{\circ}\text{C}$  proved the existence of microphase separated poly4VBP block. However, for the

microphase mixed poly(4VBP-I-S) 10-10-9 kg/mol block copolymer (**Table 5.4** entry b), only two  $T_g$ 's appeared. The lower  $T_g$  agreed with the value from DSC and increased by more than 20 °C comparing the lower  $T_g$  of the other compositions, further supporting the micro-phase mixing conclusion from DSC.

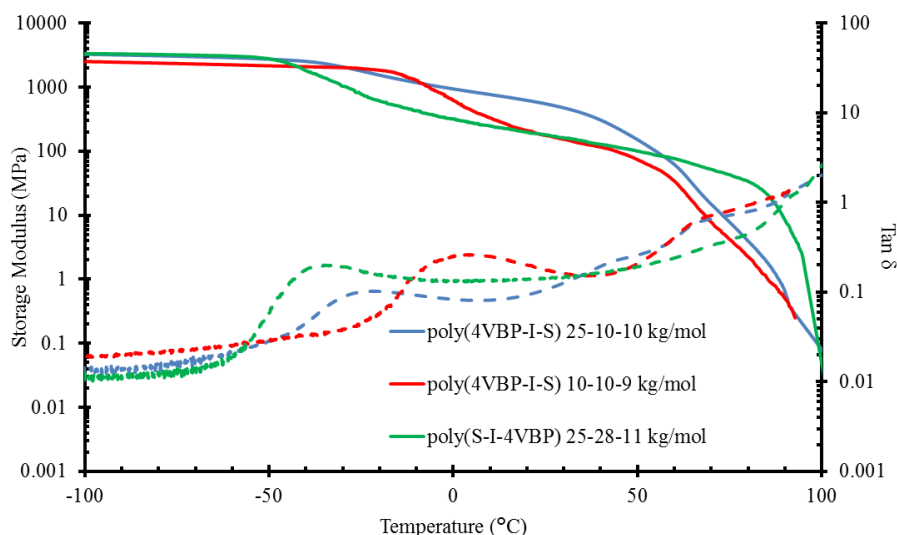


**Figure 5.4** Dynamic mechanical analysis demonstrated similar  $T_g$ s to DSC from 4VBP containing block copolymers: solid line, storage modulus; dash line,  $\tan \delta$ .

Owing to the stability of polyisoprene block, polymer thin films underwent no thermal annealing prior to the DMA tests. However, a short (6 h) thermal annealing at 120 °C under vacuum were applied to a few samples to probe the possible influence of annealing, especially for the microphase mixed samples.  $^1\text{H}$  NMR spectroscopy after short annealing exhibited no obvious oxidation of the polyisoprene blocks. The resolution of microphase-separated block copolymer films improved upon 6 h annealing (**Figure S5.3**), but poly(4VBP-I-S) 10-10-9 kg/mol remained microphase mixed without any shift in  $T_g$ .

**Table 5.4** DMA exhibited one extra  $T_g$  corresponding to 4VBP block compared to DSC, and further supported micro-phase behavior concluded from DSC data.

Polymers	Mn (kg/mol)	$T_g$ ( $^{\circ}$ C) DSC	$T_g$ ( $^{\circ}$ C) DMA	3,4 addition%
a. Poly(4VBP-I-S)	25-10-10	-30, 103	-21, 72, 103	37 %
b. Poly(4VBP-I-S)	10-10-9	0, 98	0, 67	49 %
c. Poly(S-I-4VBP)	25-28-11	-54, 88	-36, 68, 93	8 %
d. Poly(S-I-4VBP)	10-10-10	-51,62	-35,55	8%

## 5.5 Conclusions

We successfully synthesized a novel series of 4VBP-containing diblock and triblock copolymers through anionic polymerization. *In situ* FTIR spectroscopy demonstrated the successful sequential addition 4VBP monomer with isoprene and styrene.  $^1\text{H}$  NMR spectroscopy revealed that the presence of the poly4VBP block increased the polarity of the reaction solution and thus promoted increased 3,4 addition in the polyisoprene block providing a facile strategy to synthesize high 3,4-polyisoprene containing block copolymers without polar additives in non-polar solvent. While most 4VBP-containing diblock and triblock copolymers demonstrated microphase separation in polymer films, low-molecular weight, high-3,4 addition block copolymers exhibited microphase mixing instead. This difference in morphological behavior through microstructural control provides a unique approach to direct polymer physical properties.

## 5.6 References

1. Juhari, A.; Mosnacek, J.; Yoon, J. A.; Nese, A.; Koynov, K.; Kowalewski, T.; Matyjaszewski, K., Star-like poly(n-butyl acrylate)-b-poly(alpha-methylene-gamma-butyrolactone) block copolymers for high temperature thermoplastic elastomers applications *Polymer* **2010**, *51*, 4806-4813.

2. Pu, Z.; Mark, J. E.; Li, Z.; Zhu, J., Some block copolymers illustrating the effects of siloxane and silane units on the properties of terephthalate-glycol thermoplastics *Polymer* **1999**, *40*, 4695-4701.
3. Puskas, J. E.; Foreman-Orlowski, E. A.; Lim, G. T.; Porosky, S. E.; Evancho-Chapman, M. M.; Schmidt, S. P.; El Fray, M.; Piatek, M.; Prowans, P.; Lovejoy, K., A nanostructured carbon-reinforced polyisobutylene-based thermoplastic elastomer *Biomaterials* **2010**, *31*, 2477-2488.
4. Schmalz, H.; Abetz, V.; Lange, R., Thermoplastic elastomers based on semicrystalline block copolymers *Compos. Sci. Technol.* **2003**, *63*, 1179-1186.
5. Zhou, W. D.; Zhang, Y. J.; Xu, Y.; Wang, P. L.; Gao, L.; Zhang, W.; Ji, J. H., Synthesis and characterization of bio-based poly(butylene furandicarboxylate)-b-poly(tetramethylene glycol) copolymers *Polym. Degrad. Stab.* **2014**, *109*, 21-26.
6. Jangu, C.; Savage, A. M.; Zhang, Z. Y.; Schultz, A. R.; Madsen, L. A.; Beyer, F. L.; Long, T. E., Sulfonimide-Containing Triblock Copolymers for Improved Conductivity and Mechanical Performance *Macromolecules* **2015**, *48*, 4520-4528.
7. Yave, W.; Szymczyk, A.; Yave, N.; Roslaniec, Z., Design, synthesis, characterization and optimization of PTT-b-PEO copolymers: A new membrane material for CO<sub>2</sub> separation *J. Membr. Sci.* **2010**, *362*, 407-416.
8. Yave, W.; Car, A.; Peinemann, K.-V.; Shaikh, M. Q.; Raetzke, K.; Faupel, F., Gas permeability and free volume in poly(amide-b-ethylene oxide)/polyethylene glycol blend membranes *J. Membr. Sci.* **2009**, *339*, 177-183.
9. Kim, H. J.; Moon, H. C.; Kim, H.; Kim, K.; Kim, J. K.; Cho, J., Pressure Effect of Various Inert Gases on the phase Behavior of Polystyrene-block-Poly(n-pentyl methacrylate) Copolymer *Macromolecules* **2013**, *46*, 493-499.
10. Gacal, B. N.; Filiz, V.; Shishatskiy, S.; Rangou, S.; Neumann, S.; Abetz, V., Modification of polyisoprene-block-poly(vinyl trimethylsilane) block copolymers via hydrosilylation and hydrogenation, and their gas transport properties *J. Polym. Sci., Part B: Polym. Phys* **2013**, *51*, 1252-1261.
11. Hemp, S. T.; Allen, M. H.; Smith, A. E.; Long, T. E., Synthesis and Properties of Sulfonium Polyelectrolytes for Biological Applications *ACS Macro Lett.* **2013**, *2*, 731-735.
12. Oupicky, D.; Konak, C.; Ulbrich, K., DNA complexes with block and graft copolymers of N-(2-hydroxypropyl) methacrylamide and 2-(trimethylammonio)ethyl methacrylate *J. Biomater. Sci., Polym. Ed.* **1999**, *10*, 573-590.
13. Huang, K. K.; Fang, Y. K.; Hsu, J. C.; Kuo, C. C.; Chang, W. H.; Chen, W. C., Synthesis, Micellar Structures, and Multifunctional Sensory Properties of Poly(3-hexylthiophene)-block-poly(2-(dimethylamino)ethyl methacrylate) Rod-Coil Diblock Copolymers *J. Polym. Sci., Part A: Polym. Chem.* **2011**, *49*, 147-155.
14. Kuila, B. K.; Stamm, M., Transparent, Versatile Chemical Vapor Sensor Using Supramolecular Assembly of Block Copolymer and Carbon Nanotubes *Macromol. Rapid Commun.* **2010**, *31*, 1881-1885.
15. Jangu, C.; Wang, J. H. H.; Wang, D.; Sharick, S.; Heflin, J. R.; Winey, K. I.; Colby, R. H.; Long, T. E., Well-Defined Imidazolium ABA Triblock Copolymers as Ionic-Liquid-Containing Electroactive Membranes *Macromol. Chem. Phys.* **2014**, *215*, 1319-1331.

16. Green, M. D.; Wang, D.; Hemp, S. T.; Choi, J. H.; Winey, K. I.; Heflin, J. R.; Long, T. E., Synthesis of imidazolium ABA triblock copolymers for electromechanical transducers *Polymer* **2012**, *53*, 3677-3686.
17. Kim, O.; Kim, S. Y.; Park, B.; Hwang, W.; Park, M. J., Factors Affecting Electromechanical Properties of Ionic Polymer Actuators Based on Ionic Liquid-Containing Sulfonated Block Copolymers *Macromolecules* **2014**, *47*, 4357-4368.
18. Gao, R. L.; Wang, D.; Heflin, J. R.; Long, T. E., Imidazolium sulfonate-containing pentablock copolymer-ionic liquid membranes for electroactive actuators *J. Mater. Chem.* **2012**, *22*, 13473-13476.
19. Zhang, C. H.; Wang, D. R.; He, J.; Liu, M. J.; Hu, G. H.; Dang, Z. M., Synthesis, nanostructures and dielectric properties of novel liquid crystalline block copolymers *Polym. Chem.* **2014**, *5*, 2513-2520.
20. Horechyy, A.; Nandan, B.; Zafeiropoulos, N. E.; Formanek, P.; Oertel, U.; Bigall, N. C.; Eychmuller, A.; Stamm, M., A Step-Wise Approach for Dual Nanoparticle Patterning via Block Copolymer Self-Assembly *Adv. Funct. Mater* **2013**, *23*, 483-490.
21. Huda, M.; Liu, J.; Bin Mohamad, Z.; Yin, Y.; Hosaka, S., Attempts to form the 10-nm-order pitch of self-assembled nanodots using PS-PDMS block copolymer *Int. J. Nanotechnol.* **2014**, *11*, 425-433.
22. Suzuki, H.; Kometani, R.; Ishihara, S.; Warisawa, S., Selectively patterned metal nanodots fabrication by combining block copolymer self-assembly and electron beam lithography. In *Nanoengineering: Fabrication, Properties, Optics, and Devices IX*, Dobisz, E. A.; Eldada, L. A., Eds. 2012; Vol. 8463.
23. Hayakawa, T.; Kouketsu, T.; Kakimoto, M.; Yokoyama, H.; Horiuchi, S., Patterned surfaces in self-organized block copolymer films with hexagonally ordered microporous structures *Macromol. Res.* **2006**, *14*, 52-58.
24. Zhang, Q. L.; Hou, Z. Y.; Louage, B.; Zhou, D. Y.; Vanparijs, N.; De Geest, B. G.; Hoogenboom, R., Acid-Labile Thermoresponsive Copolymers That Combine Fast pH-Triggered Hydrolysis and High Stability under Neutral Conditions *Angew. Chem. Int. Edit.* **2015**, *54*, 10879-10883.
25. Murugaboopathy, S.; Matsuoka, H., Salt-dependent surface activity and micellization behaviour of zwitterionic amphiphilic diblock copolymers having carboxybetaine *Colloid Polym. Sci.* **2015**, *293*, 1317-1328.
26. Liu, Y. J.; Liu, B.; Nie, Z. H., Concurrent self-assembly of amphiphiles into nanoarchitectures with increasing complexity *Nano Today* **2015**, *10*, 278-300.
27. Kotsuchibashi, Y.; Ebara, M.; Hoffman, A. S.; Narain, R.; Aoyagi, T., Temperature-responsive mixed core nanoparticle properties determined by the composition of statistical and block copolymers in the core *Polym. Chem.* **2015**, *6*, 1693-1697.
28. Agatemor, C.; Shaver, M. P., Tacticity-Induced Changes in the Micellization and Degradation Properties of Poly(lactic acid)-block-poly(ethylene glycol) Copolymers *Biomacromolecules* **2013**, *14*, 699-708.
29. Nuopponen, M.; Kalliomaki, K.; Laukkanen, A.; Hietala, S.; Tenhu, H., A-B-A stereoblock copolymers of N-isopropylacrylamide *J. Polym. Sci., Part A: Polym. Chem.* **2008**, *46*, 38-46.
30. Feng, K.; Wang, S. Z.; Ma, H. R.; Chen, Y. J., Chirality plays critical roles in enhancing the aqueous solubility of nocathiacin I by block copolymer micelles *J. Pharm. Pharmacol.* **2013**, *65*, 64-71.

31. Kumazawa, S.; Castanon, J. R.; Shiotsuki, M.; Sato, T.; Sanda, F., Chirality amplification in helical block copolymers. Synthesis and chiroptical properties of block copolymers of chiral/achiral acetylene monomers *Polym. Chem.* **2015**, *6*, 5931-5939.
32. Suarez-Suarez, S.; Carriedo, G. A.; Soto, A. P., Tuning the Chirality of Block Copolymers: From Twisted Morphologies to Nanospheres by Self-Assembly *Chem. Eur. J.* **2015**, *21*, 14129-14139.
33. Wang, B. L.; Cui, D. M.; Lv, K., Highly 3,4-selective living polymerization of isoprene with rare earth metal fluorenyl N-heterocyclic carbene precursors *Macromolecules* **2008**, *41*, 1983-1988.
34. Yao, C. G.; Liu, D. T.; Li, P.; Wu, C. J.; Li, S. H.; Liu, B.; Cui, D. M., Highly 3,4-Selective Living Polymerization of Isoprene and Copolymerization with epsilon-Caprolactone by an Amidino N-Heterocyclic Carbene Ligated Lutetium Bis(alkyl) Complex *Organometallics* **2014**, *33*, 684-691.
35. Wang, Z. H.; Qian, Y. Q.; Zhang, W. J.; Wang, J. Y.; He, L. X.; Lin, Q. J.; Sun, W. H., Highly cis-1,4-selective polymerization of isoprene achieved using neodymium chloride 8-hydroxyquinolines *Polym. Int.* **2015**, *64*, 1030-1036.
36. Du, G. X.; Xue, J. P.; Peng, D. Q.; Yu, C.; Wang, H. H.; Zhou, Y. N.; Bi, J. J.; Zhang, S. W.; Dong, Y. P.; Li, X. F., Copolymerization of isoprene with ethylene catalyzed by cationic half-sandwich fluorenyl scandium catalysts *J. Polym. Sci., Part A: Polym. Chem.* **2015**, *53*, 2898-2907.
37. Guo, F.; Meng, R.; Li, Y.; Hou, Z. M., Highly cis-1,4-selective terpolymerization of 1,3-butadiene and isoprene with styrene by a C5H5-ligated scandium catalyst *Polymer* **2015**, *76*, 159-167.
38. Meng, R.; Guo, F.; Shi, Z. H.; Li, Y., Highly Cis-1,4-selective Copolymerization of Isoprene with Styrene Catalyzed by Half-sandwich Scandium Complexes *Acta Polym. Sin.* **2015**, 1189-1195.
39. Avgeropoulos, A.; Paraskeva, S.; Hadjichristidis, N.; Thomas, E. L., Synthesis and microphase separation of linear triblock terpolymers of polystyrene, high 1,4-polybutadiene, and high 3,4-polyisoprene *Macromolecules* **2002**, *35*, 4030-4035.
40. Bertini, F.; Canetti, M.; De Chirico, A.; Ricci, G., Thermal characterization of butadiene-isoprene copolymers with a 1,2/3,4 structure *J. Appl. Polym. Sci.* **2003**, *88*, 2737-2743.
41. Li, S. H.; Miao, W.; Tang, T.; Dong, W. M.; Zhang, X. Q.; Cui, D. M., New rare earth metal bis(alkyl)s bearing an iminophosphonamido ligand. Synthesis and catalysis toward highly 3,4-selective polymerization of isoprene *Organometallics* **2008**, *27*, 718-725.
42. Niu, H.; Dong, J. Y., Regio-chemistry control in propylene/isoprene copolymerization by metallocene catalysts *Polym. Int.* **2015**, *64*, 1023-1029.
43. Vlieg, J.; Kingma, J.; van den Wijngaard, A. J.; Janssen, D. B., A glutathione S-transferase with activity towards cis-1,2-dichloroepoxyethane is involved in isoprene utilization by *Rhodococcus* sp. strain AD45 *Appl. Environ. Microbiol.* **1998**, *64*, 2800-2805.
44. Nath, D. C. D.; Shiono, T.; Ikeda, T., Copolymerization of 1,3-butadiene and isoprene with cobalt dichloride/methylaluminumoxane in the presence of triphenylphosphine *J. Polym. Sci., Part A: Polym. Chem.* **2002**, *40*, 3086-3092.

45. Liu, B.; Wang, X. B.; Pan, Y. P.; Lin, F.; Wu, C. J.; Qu, J. P.; Luo, Y.; Cui, D. M., Unprecedented 3,4-Isoprene and cis-1,4-Butadiene Copolymers with Controlled Sequence Distribution by Single Yttrium Cationic Species *Macromolecules* **2014**, *47*, 8524-8530.
46. Rangou, S.; Theodorakis, P. E.; Gergidis, L. N.; Avgeropoulos, A.; Efthymiopoulos, P.; Smyrniotis, D.; Kosmas, M.; Vlahos, C.; Giannopoulos, T., Synthesis, molecular characterization and theoretical study of first generation dendritic homopolymers of butadiene and isoprene with different microstructures *Polymer* **2007**, *48*, 652-663.
47. Citroni, M.; Ceppatelli, M.; Bini, R.; Schettino, V., Dimerization and polymerization of isoprene at high pressures *J. Phys. Chem. B* **2007**, *111*, 3910-3917.
48. Schultz, A. R.; Jangu, C.; Long, T. E., Thermal and living anionic polymerization of 4-vinylbenzyl piperidine *Polym. Chem.* **2014**, *5*, 6003-6011.
49. Miyamura, H.; Morita, M.; Inasaki, T.; Kobayashi, S., Aerobic Oxidation of Amines Catalyzed by Polymer-Incarcerated Au Nanoclusters: Effect of Cluster Size and Cooperative Functional Groups in the Polymer *Bull. Chem. Soc. Jpn.* **2011**, *84*, 588-599.
50. Dai, L. M., Thermal cis-trans isomerization and temperature-dependent phase behaviour of polyisoprene-polyacetylene solutions *Macromolecular Chemistry and Physics* **1997**, *198*, 1723-1738.
51. Bates, F. S.; Fredrickson, G. H., Block Copolymer Thermodynamics: Theory and Experiment *Annu. Rev. Phys. Chem.* **1990**, *41*, 525-557.
52. Leibler, L., Theory of Microphase Separation in Block Copolymers *Macromolecules* **1980**, *13*, 1602-1617.
53. Sinturel, C.; Bates, F. S.; Hillmyer, M. A., High  $\chi$ -Low N Block Polymers: How Far Can We Go? *ACS Macro Lett.* **2015**, *4*, 1044-1050.
54. Widmaier, J. M.; Meyer, G. C., GLASS-TRANSITION TEMPERATURE OF ANIONIC POLYISOPRENE *Macromolecules* **1981**, *14*, 450-452.
55. Wunderlich, B., Reversible crystallization and the rigid-amorphous phase in semicrystalline macromolecules *Prog. Polym. Sci.* **2003**, *28*, 383-450.

## 5.7 Supporting information

**Table S5.1** Polymers synthesized through anionic polymerization. Molecular weights were confirmed by  $^1\text{H}$  NMR spectroscopy

Polymers	Target $M_n$ (kg/mol)	$^1\text{H}$ NMR $M_n$ (kg/mol)
Polyisoprene	15	14
Poly4VBP	20	21
Polyisoprene + poly4VBP	20 + 21	25 + 21
Polyisoprene + N-methylpiperidine	20	20

Poly(4VBP- <i>b</i> -I)	25-12	25-13
Poly(4VBP- <i>b</i> -I)	25-25	25-23
Poly(4VBP- <i>b</i> -I- <i>b</i> -S)	25-12-12	25-10-10
Poly(4VBP- <i>b</i> -I- <i>b</i> -S)	10-10-10	10-10-9
Poly(S- <i>b</i> -I- <i>b</i> -4VBP)	25-25-10	25-28-11
Poly(S- <i>b</i> -I- <i>b</i> -4VBP)	10-10-10	10-10-10
Poly(I- <i>b</i> -4VBP- <i>b</i> -I)	10-10-10	9-10-9

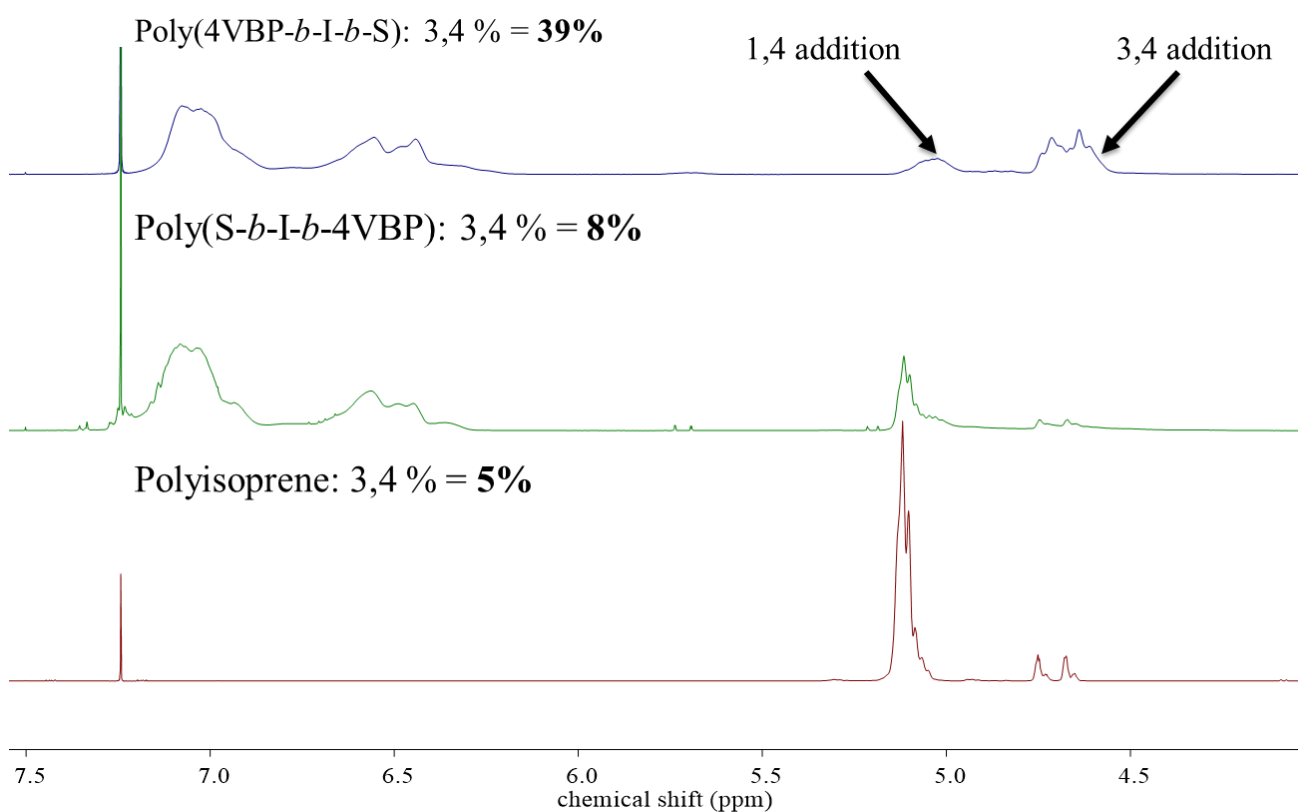


**Figure S5.1**  $^1\text{H}$  NMR spectroscopy demonstrated high 3, 4 addition isoprene blocks in poly(4VBP-*b*-I-*b*-S) triblock copolymers in comparison to control polymers.

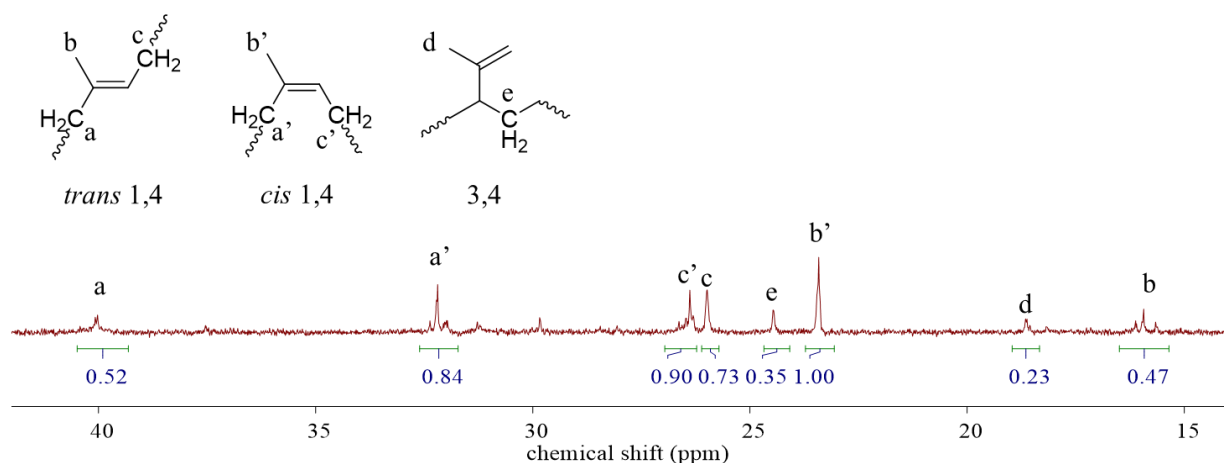


**Figure S5.2** Quantitative  $^{13}\text{C}$  NMR for the polymer blends of polyisoprene (25 kg/mol) and poly4VBP (21 kg/mol).

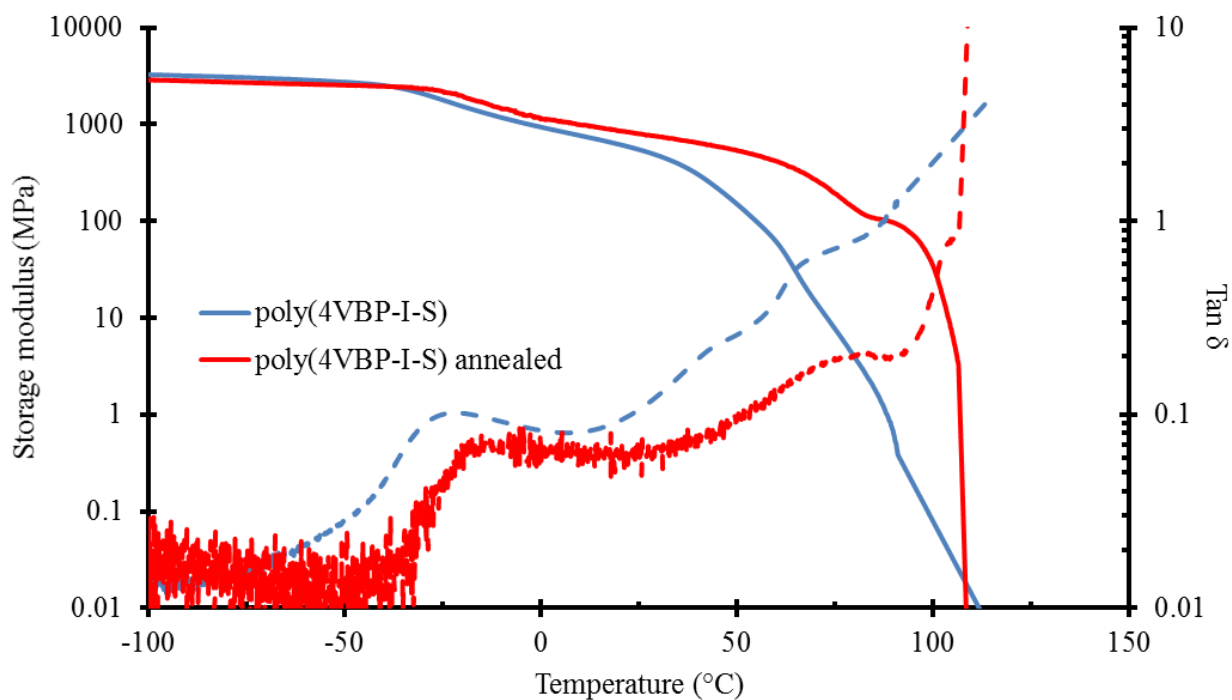


**Figure S5.3** Thermal annealing further promoted phase separation. Polymers shown: poly(4VBP-*b*-I-*b*-S) 25-10-10 kg/mol. Solid line: Storage modulus; Dash line: tan  $\delta$ .

# **Chapter 6: Synthesis of Urea-Containing ABA Triblock Copolymers: Influence of Pendant Hydrogen Bonding on Morphology and Thermomechanical Properties**

*(Published in Journal of Polymer Science, Part A: Polymer Chemistry, ASAP)*

*Mingtao Chen, David L. Inglefield Jr., Keren Zhang, Amanda G. Hudson, Samantha J. Talley, Robert B. Moore, Timothy E Long\**

Department of Chemistry and Macromolecules Innovation Institute (MII), Virginia Tech, Blacksburg, VA 24061

\*To whom the correspondence should be addressed: [telong@vt.edu](mailto:telong@vt.edu)

## **6.1 Abstract**

Reversible addition-fragmentation chain transfer (RAFT) polymerization produced novel ABA triblock copolymers with associative urea sites within pendant groups in the external hard blocks. The ABA triblock copolymers served as models to study the influence of pendant hydrogen bonding on polymer physical properties and morphology. The triblock copolymers consisted of a soft central block of poly(di(ethylene glycol) methyl ether methacrylate) (polyDEGMEMA, 58 kg/mol) and hard copolymer external blocks of poly(2-(3-hexylureido)ethyl methacrylate-*co*-2-(3-phenylureido)ethyl methacrylate) (polyUrMA, 18 to 116 kg/mol). Copolymerization of 2-(3-hexylureido)ethyl methacrylate (HUrMA) and 2-(3-phenylureido)ethyl methacrylate

(PhUrMA) imparted tunable hard block  $T_{gs}$  from 69 °C to 134 °C. Dynamic mechanical analysis (DMA) of the triblock copolymers exhibited high modulus plateau regions (~100 MPa) over a wide temperature range (-10 - 90 °C), which was indicative of microphase separation. Atomic force microscopy (AFM) and small angle x-ray scattering (SAXS) further confirmed short-range microphase separation with various morphologies. Variable temperature FTIR (VT-FTIR) revealed the presence of both monodentate and bidentate hydrogen bonding, and pendant hydrogen bonding remained as an ordered structure to higher than expected temperatures. This study presents a fundamental understanding of the influence of hydrogen bonding on polymer physical properties and reveals the response of pendant urea hydrogen bonding as a function of temperature as compared to main chain polyureas.

## **6.2 Introduction**

Researchers continue to address the potential synergy between non-covalent interactions and macromolecular architecture. Non-covalent interactions offer significant impact on the physical properties of polymers, such as thermomechanical properties,<sup>1-5</sup> morphology,<sup>6-10</sup> and electromagnetic performance.<sup>11-14</sup> A commonly utilized non-covalent interaction is hydrogen bonding due to its potential for specificity, directionality, and reversibility. Thus, researchers invoke thermo-reversible hydrogen bonding as a means to improve mechanical properties,<sup>1-2</sup> induce microphase separation,<sup>6, 10</sup> impart self-healing performance,<sup>15-18</sup> and facilitate liquid crystal formation.<sup>19-22</sup>

Hydrogen bonding within the polymer main chain leads to compact intermolecular packing and provides significant improvement to thermomechanical properties.<sup>1</sup> In contrast, pendant hydrogen bonding sites retain higher mobility, suggesting less ordered

hydrogen bonding networks. Previous work in our laboratories demonstrated the ability of quadruple pendant hydrogen bonding moieties to promote long range, ordered microphase morphology despite increased mobility.<sup>10</sup> However, for more weakly associated hydrogen bonds, the enhanced mobility of pendant sites may result in less ordered microstructures, imparting a different influence on polymer physical properties compared to main chain hydrogen bonding. The lack of cooperativity in the organization of pendant hydrogen bonding is a potential obstacle for the “unzipping” of hydrogen bonding at elevated temperature, thus providing a desirable, broader temperature range for the retention of ordered, hydrogen bonded structures.

Urea sites associate through relatively weak hydrogen bonding compared to multiple hydrogen bonding containing nucleobases, serving as an ideal hydrogen bonding site to study pendant hydrogen bonding.<sup>10</sup> Earlier literature widely describes urea sites within the polymer backbone, which generally demonstrates obvious shifts from ordered structures to disordered structures with increasing temperatures.<sup>1-2</sup> Kuo and coworkers studied hydrogen bonding dissociation of poly(urethane urea)s using Fourier transform infrared spectroscopy (FTIR) at various temperatures.<sup>23</sup> The intensity of hydrogen bonded carbonyl stretching peaks decreased as temperature increased, leading to a simultaneous increase of free carbonyl intensity. Similarly, Painter *et al.* showed a complete transition from ordered hydrogen bonding to disordered and dissociated hydrogen bonding in polyureas when temperatures exceeded 160 °C.<sup>24</sup> Long *et al.* used step-growth polymerizations to study the influence of main chain urea sites on the physical properties of polymers<sup>2</sup> where they showed the ordered and compact hydrogen bonding extended the modulus plateau above 120 °C. In addition, study of poly(dimethyl

siloxane) containing oxamide units demonstrated a complete transition from ordered hydrogen bonding to disordered hydrogen bonding at 170 °C, according to variable temperature FTIR (VT-FTIR).<sup>1</sup> However, to our best knowledge, the earlier literature has not described the temperature response of pendant urea sites, which will influence thermomechanical properties and morphologies.

Controlled radical polymerization (CRP) allows for the precise synthesis of well-defined block polymers with various pendant functionalities.<sup>25-28</sup> Frequently used CRP techniques include nitroxide-mediated polymerization (NMP), atom transfer radical polymerization (ATRP), and reversible addition-fragmentation chain transfer (RAFT) polymerization. NMP is suitable for a relatively narrow monomer selection and less control of the molecular weight distribution, and ATRP is limited in this current study due to potential interactions of urea groups with metallic catalysts. Thus, RAFT polymerization remains a popular CRP method to synthesize various well-defined, functional block copolymers.<sup>25, 29-30</sup> However, only a few studies address the synthesis and characterization of polymers with pendant urea sites using RAFT, and only Long *et al.* successfully synthesized block copolymers with pendant urea sites through RAFT polymerization.<sup>7</sup>

Molecular weight distribution strongly influences polymer physical properties and morphologies. Narrow molecular weight distribution (low polydispersity) facilitates well-defined morphologies and associated mechanical properties.<sup>31</sup> In RAFT polymerization, the synthesis of block copolymers typically involves isolation and re-initiation of each block. The molecular weight distribution tends to increase during the re-initiation process, which becomes significant in multi-block copolymer synthesis.<sup>32</sup> For symmetric

ABA block copolymers, a difunctional chain transfer agent (CTA) is a common strategy to reduce re-initiation and thus lower polydispersity index (PDI).<sup>6</sup>

In this manuscript, we demonstrate the synthesis of well-defined pendant urea-containing ABA triblock copolymers through RAFT polymerization, and we report the influence of hydrogen bond association on polymer physical properties and morphologies. A difunctional RAFT CTA facilitated the synthesis of symmetric ABA type block copolymers, poly(UrMA-*b*-DEGMEMMA-*b*-UrMA), through a divergent mechanism.<sup>6</sup> Different compositions of random copolymers, poly(UrMA), allowed the variation of the  $T_g$  for the external blocks. Dynamic mechanical analysis (DMA) and differential scanning calorimetry (DSC) of the triblock copolymers collectively displayed two distinct  $T_g$ s attributed to soft and hard blocks. Poly(UrMA-*b*-DEGMEMMA-*b*-UrMA) exhibited a high plateau modulus (~100 MPa) over a wide temperature range. Atomic force microscopy (AFM) and small angle x-ray scattering (SAXS) demonstrated microphase-separated morphologies, which agreed with thermomechanical analysis. VT-FTIR revealed the retention of ordered hydrogen bonding at 160 °C, suggesting a retardation of hydrogen bond dissociation due to less cooperativity relative to main chain hydrogen bonding. This work describes the role of pendant hydrogen bonding on polymer physical properties and morphologies, and we propose the use of pendant hydrogen bonding to delay dissociation temperatures while maintaining microphase separated morphologies.

## **6.3 Experimental**

### **6.3.1 Materials**

N,N-dimethylformamide (DMF, anhydrous, 99.8%), dichloromethane (DCM, anhydrous,  $\geq 99.8\%$ ), dimethyl sulfoxide (DMSO, anhydrous,  $\geq 99.9\%$ ), hexane, ethyl acetate, unstabilized tetrahydrofuran (THF), methanol, hexamethylenediamine (98%), N,N'-dicyclohexylcarbodiimide (DCC, 99%), 4-(dimethylamino)pyridine (DMAP,  $\geq 99.0\%$ ), and lithium bromide were purchased from Sigma-Aldrich and used without further purification. 2-Isocyanatoethyl methacrylate (2-ICMA,  $> 98\%$ ) was purchased from TCI America and used as received. Hexylamine (99%) and aniline (99%) were purchased from Sigma-Aldrich and distilled before use. Di(ethylene glycol) methyl ether methacrylate (DEGMEMA) was purchased from Sigma-Aldrich and passed through neutral aluminum oxide (activated) immediately prior to use. 4,4'-Azobis(4-cyanovaleric acid) (V-501) and 4-cyano-4-[(dodecylsulfanylthiocarbonyl)sulfanyl]pentanoic acid (CDP) were purchased from Sigma-Aldrich and recrystallized from methanol prior to use.

### **6.3.2 Analytical methods**

$^1\text{H}$  and  $^{13}\text{C}$  nuclear magnetic resonance (NMR) spectroscopies were performed on a Varian Unity 400 MHz NMR spectrometer (128 scans). NMR samples were dissolved in deuterated chloroform or DMSO. Mass spectrometry was conducted on an Agilent 6220 Accurate Mass TOF LC-MS system. Size exclusion chromatography determined molecular weight distributions using a Waters 515 HPLC pump equipped with a Waters 717 plus autosampler. Absolute molecular weight was determined through a Wyatt Technology miniDawn MALLS detector operating at 690 nm and a Waters 2414 refractive index detector operating at 880 nm with a flow rate of 0.8 mL/min in either DMF with 0.05 M LiBr or aqueous solution (54/23/23 v/v/v% water/methanol/acetic acid

with 0.1 M sodium acetate). Specific refractive index value ( $dn/dc$ ) was determined offline using an Optilab T-rEX refractometer ( $\lambda = 658$  nm) and was used to calculate weight-average molecular weight ( $M_w$ ) from SEC. Thermal stability was determined using thermogravimetric analysis (TGA) on a TA Instruments Q500 under nitrogen purge with a heating rate of 10 °C/min. TA Instruments Q2000 differential scanning calorimetry (DSC) determined glass transition temperatures and reported as the midpoint of the transition (heat flow vs. temperature plot). The second heat of a heat/cool/heat procedure determined reported values with 10 °C/min heating rate and quench cool under nitrogen. Dynamic mechanical analysis (DMA) was conducted using a TA Instruments Q800 in film tension mode (3 °C/min heating ramp and 1 Hz frequency). Variable temperature Fourier transform infrared spectroscopy (VT-FTIR) was used to evaluate the effect of temperatures on hydrogen bonding. The instrument consists of a Varian 670-IR with a PIKE GladiATR attachment with a scan range 4000-400  $\text{cm}^{-1}$  and resolution of 4  $\text{cm}^{-1}$ . Spectra were collected every 5 °C as an average of 32 scans during a temperature ramp from 25 °C to 165 °C (1 °C/min). Surface morphology was determined with atomic force microscopy (AFM) on a Veeco Multimode AFM in the tapping mode using a set point ratio of 0.7 and 42 N/m high spin constant cantilevers. Bulk morphology was characterized with Rigaku S-Max 3000 3 pinhole two-dimensional small angle x-ray scattering (SAXS). Wavelength was 1.54 Å. 2D multiwire gas-filled detector determined scattering intensity with an exposure time of 2 h. SAXSGUI software package analyzed all SAXS data to obtain intensity versus scattering vector  $q$  plot ( $q = 4\pi\sin(\theta)/\lambda$ ,  $2\theta$  is the scattering angle).

### 6.3.3 Synthesis of urea methacrylate monomers

2-Isocyanatoethyl methacrylate (2-ICMA) readily reacts with primary amines to give urea methacrylate monomers in quantitative yield. A modified procedure for the synthesis of urea methacrylate monomers is as follows:<sup>7</sup> 1 equiv. of aniline 10 g (20 wt% in chloroform) was added to a 100-mL, two-necked, round-bottomed flask equipped with a magnetic stir bar, and an addition funnel under nitrogen. The addition funnel was charged with 1 equiv. of 2-ICMA (15.15 mL). After purging with nitrogen for 15 min, the reaction flask was cooled to 0 °C in an ice bath and 2-ICMA was added dropwise. After stirring for 4 h, the ice bath was removed, and the flask was slowly warmed to room temperature and stirred for 20 h. The solution was diluted to 10 wt% with chloroform. The diluted solution was passed through aluminum oxide column to remove inhibitors, and solvent was removed under reduced pressure to yield a white solid product, which was further dried *in vacuo* at 25 °C for 24 h (yield  $\geq$  98 %). <sup>1</sup>H and <sup>13</sup>C NMR spectroscopy confirmed the purity and structure of monomer. <sup>1</sup>H NMR (DMSO-*d*<sub>6</sub>, 25 °C,  $\delta$ ): 1.8 (-CH<sub>3</sub>, vinyl methyl protons), 3.3 (-CH<sub>2</sub>-N, methylene protons), 4.1 (-CH<sub>2</sub>-O, methylene protons), 5.7 (-CH<sub>2</sub>-NH-, amine protons), 6.0 (=CH<sub>2</sub>, vinyl proton), 6.2 (=CH<sub>2</sub>, vinyl proton), 6.9-7.3 (aromatic protons), 8.5 (-NH-Ar, amine proton). The synthesis of HUrMA followed the same procedure with quantitative yield (> 98%). <sup>1</sup>H NMR (DMSO-*d*<sub>6</sub>, 25 °C,  $\delta$ ): 0.8 (-CH<sub>3</sub>, methyl protons), 1.3 (-CH<sub>2</sub>-, methylene protons), 1.8 (-CH<sub>3</sub>, vinyl methyl protons), 3.1 (-CH<sub>2</sub>-N, methylene protons), 3.5 (-CH<sub>2</sub>-N, methylene protons), 4.2 (-CH<sub>2</sub>-O, methylene protons), 4.4 (-CH<sub>2</sub>-NH-, amine protons), 4.6 (-CH<sub>2</sub>-NH-, amine protons), 5.6 (=CH<sub>2</sub>, vinyl proton), 6.1 (=CH<sub>2</sub>, vinyl proton).

#### **6.3.4 Free radical polymerization for poly(HUrMA-*co*-PhUrMA)**

Free radical copolymerization of HUrMA and PhUrMA with different feed ratios yielded poly(HUrMA-*co*-PhUrMA). As an example, 80/20 (wt/wt%) HUrMA/PhUrMA was synthesized as follows: A 50-mL, one necked, round-bottomed flask was charged with 0.4 g of HUrMA, 0.1 g of PhUrMA and 0.33 mg AIBN (0.1 mol% to monomers) in 10 mL anhydrous DMF. The solution was sparged with nitrogen for 25 min before polymerization. The polymerization was performed at 65 °C for 24 h with vigorous stirring. The solution was precipitated into 4/1 (v/v) methanol/water and the resulting white solid was dried *in vacuo* at 65 °C for 12 h. The compositions of copolymers matched closely to the feed ratio according to <sup>1</sup>H NMR spectroscopy. <sup>1</sup>H NMR (DMSO-*d*<sub>6</sub>, 25 °C, δ): 8.52 (-NH-Ar, amine proton in PhUrMA), 7.32, 7.17, 6.85 (aromatic protons), 6.25 (-NH-C=O, amine proton in PhUrMA), 5.98 (-NH-C=O, amine protons in HUrMA), 3.82 (-CH<sub>2</sub>-O-C=O, methylene protons), 3.22 (-CH<sub>2</sub>-NH-, methylene protons), 2.92 (-CH<sub>2</sub>-NH-, methylene protons), 1.85 (backbone methylene protons), 1.32 (-CH<sub>2</sub>-, methylene protons in HUrMA), 0.81 (-CH<sub>3</sub>, methyl protons).

### 6.3.5 Difunctional CTA synthesis

The synthesis of a difunctional CTA was adapted from a previously reported procedure.<sup>6</sup> A 25-mL, one-necked, round-bottomed, flask was charged with 3 equiv. of CDP (1g) in 11 mL anhydrous dichloromethane in an ice bath. Catalytic amount of DMAP (40 mg) and 1 equiv. of hexamethylenediamine (96 mg) were dissolved in 4 mL anhydrous dichloromethane in a second round-bottomed flask. Both flasks were cooled to 0 °C and purged for 5 min with nitrogen. The DMAP and hexamethylenediamine solution were added at once, followed immediately by 3.3 equiv. of DCC (0.57 g). After stirring under inert atmosphere at 0 °C for 4 h, the solution was slowly warmed to room temperature

and allowed to react for 20 h. After the filtration of solid dicyclohexylurea byproducts, the filtrate was washed with saturated sodium bicarbonate solution three times and then dried over magnesium sulfate. Removal of solvent concentrated the washed filtrate. The concentrated solution was further purified using silica column chromatography. The impurity was first removed using 80/20 (v/v%) hexane/ethyl acetate as eluent, then the desired product was eluted with 50/50 (v/v%) ethyl acetate/methanol. Removal of solvent yielded a yellow solid product which was further dried at 23 °C *in vacuo* for 12 h (~60% yield). <sup>1</sup>H NMR (DMSO-*d*<sub>6</sub>, 25 °C, δ): 0.81 (-CH<sub>3</sub>, methyl protons), 1.20 (-CH<sub>2</sub>-, methylene protons), 1.32 (-CH<sub>2</sub>-, methylene protons), 1.60 (-CH<sub>2</sub>-, methylene protons), 1.81 (-CH<sub>3</sub>, methyl protons), 2.30 (O=C-CH<sub>2</sub>-, CN-C-CH<sub>2</sub>-, methylene protons), 2.99 (NH-CH<sub>2</sub>-, methylene protons), 3.24 (S-CH<sub>2</sub>-, methylene protons), 7.93 (-NH-, amine protons). <sup>13</sup>C NMR (DMSO-*d*<sub>6</sub>, 25 °C, δ): 218.8 (S-C=S, trithiocarbonate carbon), 170.0 (NH-C=O, amide carbonyl), 119.6 (-CN), 47.5 (-C-NH-), 38.9 – 22.6 (alkyl carbon), 14.4 (-CH<sub>3</sub>, methyl carbon). MS-TOF: *m/z* calculated for [M + H<sup>+</sup>] 888.502 g/mol; found 888.455 g/mol.

### 6.3.6 Kinetic analysis of poly(DEGMEMA) macroCTA synthesis

A master solution of CTA, monomers and initiator was prepared as described above, then it was separated equally into six 25 mL round-bottomed flasks equipped with magnetic stir bars. After sparging with nitrogen for 25 min, all six flasks were stirred at 65 °C. At different time intervals, one 25 mL round-bottomed flask was quenched and labelled. After purification by dialysis against unstabilized THF, the solvent was removed and then the polymers were dried *in vacuo* at 25 °C for 24 h.

### 6.3.7 Synthesis of polyDEGMEMA macroCTA using RAFT polymerization

A 100-mL, one-necked, round-bottomed flask was equipped with a magnetic stir bar and charged with 7 g of monomer (DEGMEMA), 94.1 mg CTA (dCDP) and 14.9 mg initiator (V-501) in DMSO (74.4 mL) at 0.5 M monomer concentration. The [dCDP]/[V-501] ratio of 2:1 ([CTA]/[I] ratio of 4:1) was used and the degree of polymerization at 100% monomer conversion was set to 350. The solution was sparged with nitrogen for 30 min and stirred at 65 °C for a given time to obtain macroCTA with desired molecular weights. Exposure to air quenched and quenching to 0 °C quenched the reaction. Polymers were dialyzed against unstabilized THF three times for 24 h. The dialysis solvent was replaced every 8 h. After removal of solvent under reduced pressure and drying *in vacuo* at 25 °C for 12 h and 50 °C for 12 h, sticky yellow products were obtained. The reaction time for macroCTA synthesis was determined through a kinetic study of PDEGMEMA macroCTA in a similar fashion (S.I.). Aqueous SEC and DMF SEC light scattering with  $dn/dc$  values 0.1267 mL/g and 0.0515 mL/g, respectively, determined absolute weight-average molecular weight.

### **6.3.8 Synthesis of poly(UrMA-*b*-DEGMEMA-*b*-UrMA) using RAFT polymerization**

The synthesis of poly(UrMA-*b*-DEGMEMA-*b*-UrMA) was similar to the synthesis of polyDEGMEMA macroCTA. For a typical ABA triblock synthesis: a 100-mL, one-necked, round-bottomed flask was charged with 3.6 g of HUrMA, 0.9 g of PhUrMA, 1.62 g of poly(DEGMEMA) macroCTA (58 kg/mol), and 3.12 mg of V-501 in 36.3 mL anhydrous DMSO at 0.5 M monomer concentration. The feed weight ratio (w/w) of HUrMA/PhUrMA was set to 4:1 as an arbitrary composition, and [dCDP]/[V-501] ratio was set to 2.5 to retain control of molecular weight distribution. The solution was sparged with nitrogen for 40 min. Then the solution was stirred at 65 °C for a given time interval.

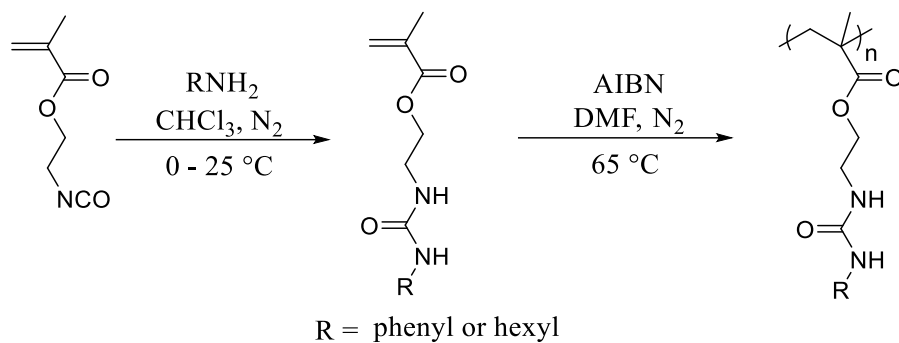
The reaction was quenched by exposure to air and cooling to 0 °C. The resulting polymers were purified through dialysis against THF three times for 24 h (solvent replaced every 8 h). Removal of dialysis solvent resulted in a pale yellow solid, which was further dried *in vacuo* at 25 °C for 24 h and 50 °C for 12 h. A kinetic study of triblock copolymer formation was conducted using a similar procedure to poly(DEGMEMMA). Absolute molecular weight was determined by DMF SEC light scattering signal with  $dn/dc$  values of 0.0705 mL/g.

### 6.3.9 Film casting

All triblock copolymers were cast from 25 wt% solution in THF onto Mylar<sup>®</sup>. Polymer films were slowly dried under ambient conditions for 2 d. The films were further dried *in vacuo* for 12 h and annealed *in vacuo* at 100 °C for 24 h prior to analysis.

## 6.4 Results and Discussion

The reaction between a primary amine and an isocyanate of 2-ICMA afforded urea-containing methacrylate monomers (hexyl urea methacrylate, HUrMA, and phenyl urea methacrylate, PhUrMA) in quantitative yield (**Scheme 6.1**). Free radically polymerized poly(HUrMA) and poly(PhUrMA) homopolymers yielded  $T_g$ s of 69 °C and 134 °C, respectively. Copolymerization of HUrMA and PhUrMA provided a facile approach to tailor the  $T_g$  of the hard segment, affording tunable physical properties. <sup>1</sup>H NMR spectroscopy confirmed copolymer compositions, and final compositions agreed well with the feed ratios.



**Scheme 6.1** Urea-containing methacrylate monomer synthesis and free radical polymerization.

**Figure 6.1a** shows the thermal properties of poly(HUrMA-*co*-PhUrMA) copolymers using differential scanning calorimetry (DSC). Copolymers with higher weight fractions of PhUrMA led to an increase in  $T_g$  due to the presence of a rigid phenyl substituent in PhUrMA. **Figure 6.1b** demonstrated good agreement of the measured  $T_g$  and predicted value from the Fox equation, suggesting poly(HUrMA-*co*-PhUrMA) was a statistical copolymer. Yet, direct validation of the random copolymerization of HUrMA and PhUrMA will require *in situ* FTIR measurement to investigate the reactive ratios in the future. The  $T_g$  of poly(HUrMA) homopolymer was too low to produce free-standing films in the triblock copolymer synthesis, and a high content of PhUrMA led to brittle films. Therefore, the copolymer with a low amount of PhUrMA (20 wt%) as the external hard block was chosen. Due to the brittle nature of poly(HUrMA-*co*-PhUrMA), a soft segment was necessary. PolyDEGMEMA has a low  $T_g$  of  $-40\text{ }^\circ\text{C}$  and serves as a soft, central segment to provide flexibility and improve overall solubility.

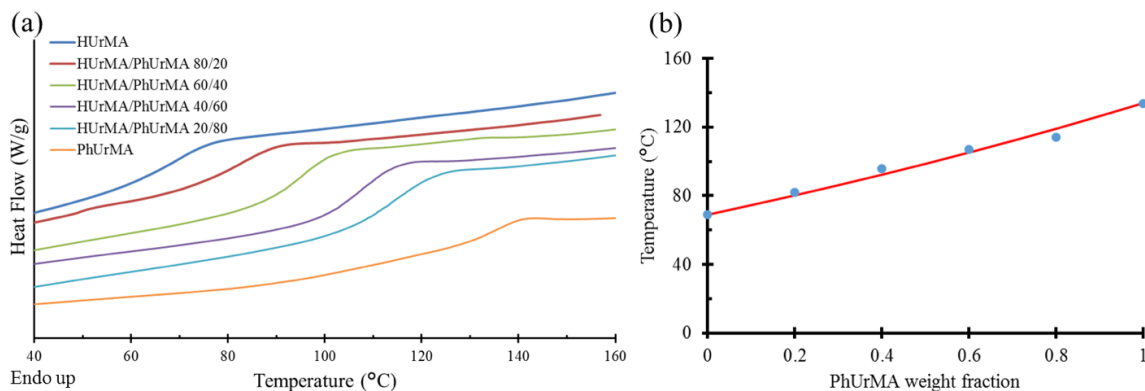
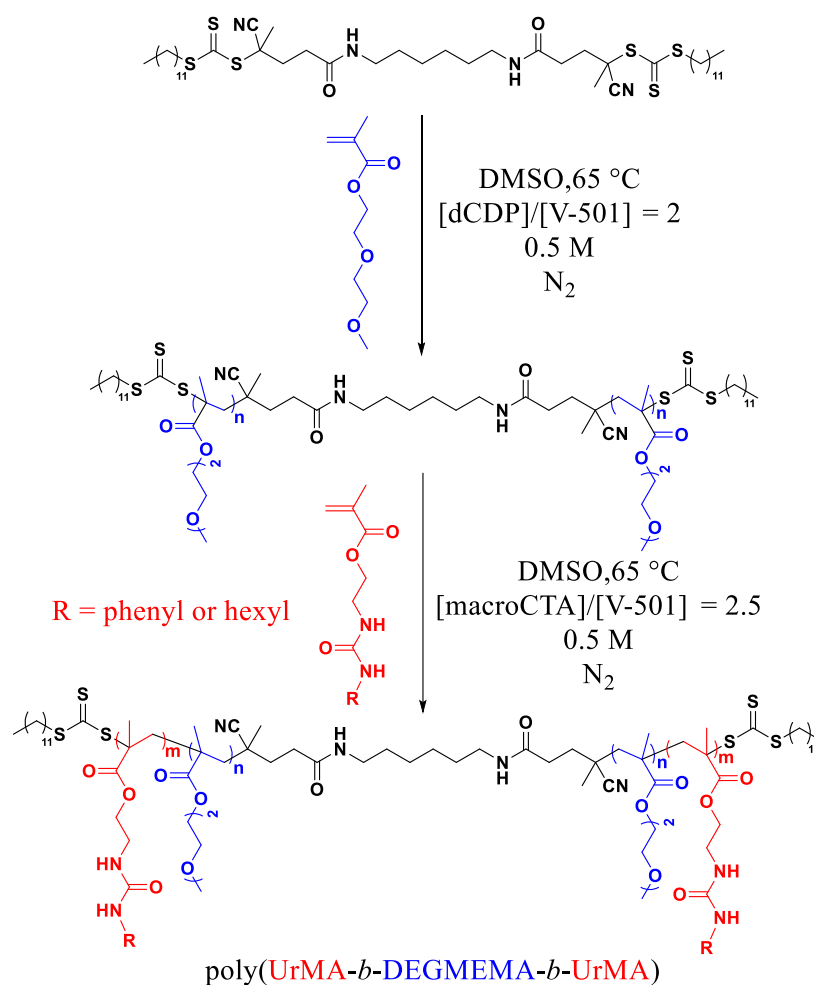


**Figure 6.1. a)** Thermal transitions of poly(HUrMA-*co*-PhUrMA) statistical copolymers. **b)**  $T_g$  of poly(HUrMA-*co*-PhUrMA) agreed with the Fox Equation: measured data (blue dots) and theoretical values from Fox Equation (red line).  $T_g$  values determined at the midpoint of the transition on the second heat at 10 °C/min.

In this study, a difunctional chain transfer agent (CTA) enabled the preparation of ABA triblock copolymers in a two-step synthesis (**Scheme 6.2**). In the first step, a polyDEGMEMA soft central block was synthesized using V-501/dCDP as an initiator/CTA pair. Both V-501 and dCDP fragmented into identical reactive radicals during initiation. As a result, the kinetic difference between initiator and CTA was negligible, which attributed to improved control over molecular weight distribution.<sup>32</sup> Aqueous size exclusion chromatography (SEC) with a light scattering detector yielded absolute molecular weights with well-controlled PDI (< 1.10) and a linear relationship between weight-average molecular weight and time. PolyDEGMEMA macroCTAs (58 kg/mol) allowed for further chain growth with UrMA monomers to produce well-defined ABA triblock copolymers with hard block composition varying from 25 wt% to 67 wt%.



**Scheme 6.2.** Synthesis of poly(UrMA-*b*-DEGMEMA-*b*-UrMA) triblock in a divergent fashion using RAFT polymerization.

**Figure 6.2** demonstrates shifts of SEC retention times from polyDEGMEMA macroCTA to poly(UrMA-*b*-DEGMEMA-*b*-UrMA) triblock copolymers. The shifts of peak positions toward shorter retention time indicated the successful chain growth of the external blocks. Higher content of polyUrMA led to better signal-to-noise ratio due to low  $dn/dc$  values of polyDEGMEMA macroCTAs in DMF + 0.05 M LiBr mobile phase. Monomodal peaks in **Figure 6.2** and low polydisperse index (PDI) in **Table 6.1** prove the RAFT polymerization was well-controlled. The nomenclature, poly(UrMA<sub>x</sub>-*b*-

DEGMEMA $y$ - $b$ -UrMA $x$ ), represented the molecular weights ( $x$  and  $y$ ) of each block. Initially, poly(UrMA- $b$ -DEGMEMA- $b$ -UrMA) showed a linear increase of molecular weight with increasing polymerization time. After 6 h, the molecular weight plateaued at  $M_n$  of 174 kg/mol due to the high viscosity and low monomer concentration (85 % monomer conversion).

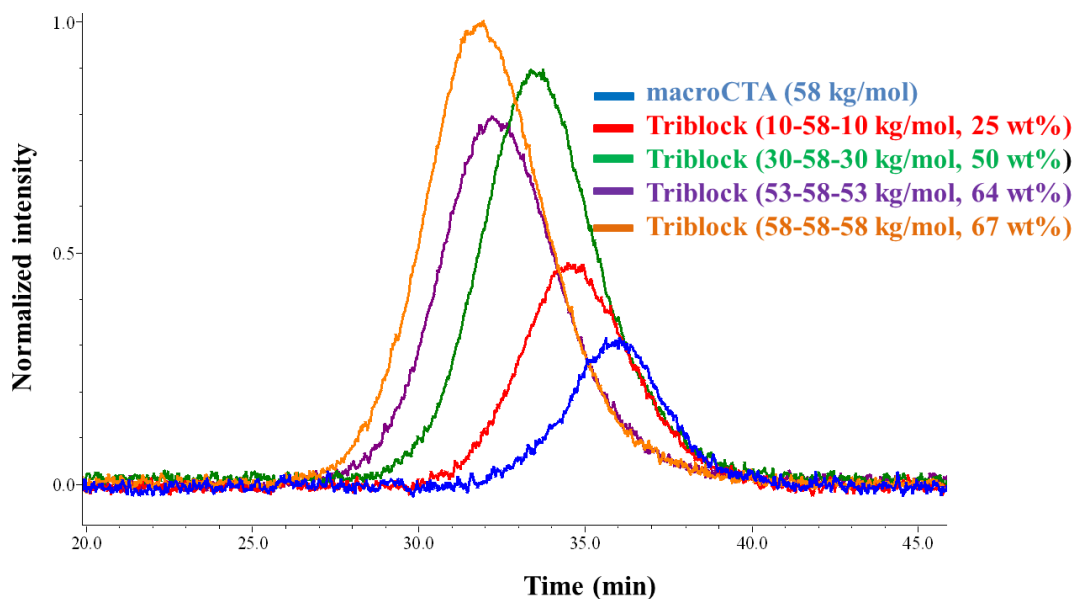


**Figure 6.2.** SEC light scattering chromatograms exhibited an increase in molecular weight with time in poly(UrMA- $b$ -DEGMEMA- $b$ -UrMA) triblock synthesis. (Molecular weight of DEGMEMA macroCTA was determined using aqueous SEC, but shown for comparison in DMF + 0.05 M LiBr SEC)

Thermogravimetric analysis demonstrated one-step thermal degradation for all the triblock copolymers, and the temperatures at 5 wt% weight loss ( $T_{d, 5\%}$ ) varied from 180 °C to 220 °C. The thermal degradation profile was consistent with earlier urea-containing polymers.<sup>7</sup> DSC highlighted two distinct  $T_g$ s associated with the soft central and hard external blocks, respectively (**Table 6.1**). The lower  $T_g$  at -25 °C corresponded to the  $T_g$

of the soft central polyDEGMEMA block with an elevation of 15 °C from polyDEGMEMA macroCTA ( $T_g$  -40 °C). This deviation was consistent with previous literature and was attributed to either more restricted segmental mobility near adjacent hard blocks<sup>6</sup> or phase mixing due to strong ether-urea interaction.<sup>33</sup> The second higher  $T_g$  agreed with the  $T_g$  of hard external block at 78 °C. The hard block  $T_g$  for poly(UrMA<sub>10</sub>-*b*-DEGMEMA<sub>58</sub>-*b*-UrMA<sub>10</sub>), 25 wt% hard blocks, was more than 10 °C lower than other triblock copolymers. It was presumed that the lower second  $T_g$  was due to a combination of short hard block length and microscopic phase-mixing. As described in the Flory-Huggins theory, long block lengths and high  $\chi$  parameters promote microphase separation.<sup>34-36</sup> In poly(UrMA<sub>10</sub>-*b*-DEGMEMA<sub>58</sub>-*b*-UrMA<sub>10</sub>), the molecular weight of the UrMA hard segment was short relative to other triblock copolymers in this study. As a result, the external hard block presumably partially phase-mixed with small amount of DEGMEMA segments, leading to a lower  $T_g$ . Nevertheless, two distinct  $T_g$ s in all triblock copolymers suggested microphase separation in all cases.

**Table 6.1** Molecular weight analysis of urea-containing ABA triblock copolymers

Polymer	$M_n$ (kg/mol) SEC	Weight percent (%)	PDI $M_w/M_n$	$T_g$ (°C)
PDEGMEMA macroCTA	58	N/A	1.06	-40
Poly(UrMA <sub>10</sub> - <i>b</i> -DEGMEMA <sub>58</sub> - <i>b</i> -UrMA <sub>10</sub> )	78	25	1.08	-25, 65
Poly(UrMA <sub>30</sub> - <i>b</i> -DEGMEMA <sub>58</sub> - <i>b</i> -UrMA <sub>30</sub> )	118	50	1.12	-27, 78
Poly(UrMA <sub>53</sub> - <i>b</i> -DEGMEMA <sub>58</sub> - <i>b</i> -UrMA <sub>53</sub> )	164	64	1.13	-24, 76

Poly(UrMA <sub>58</sub> - <i>b</i> -DEGMEMA <sub>58</sub> - <i>b</i> - UrMA <sub>58</sub> )	174	67	1.16	-24, 78
--	-----	----	------	---------

---

DMA elucidated the mechanical response of poly(UrMA-*b*-DEGMEMA-*b*-UrMA) triblock copolymers as a function of temperature. DMA in **Figure 6.3** supported the  $T_g$  values from DSC and indicated microphase separation of poly(UrMA-*b*-DEGMEMA-*b*-UrMA). For the triblock copolymer with 25 wt% hard blocks, the storage modulus ( $E'$ ) was approximately 3 GPa at -40 °C, which was expected for polymers in the glassy state.  $E'$  drastically decreased below 1 MPa at 30 °C. No modulus plateau appeared presumably due to phase mixing as supported by DSC measurement discussed above. In contrast, poly(UrMA-*b*-DEGMEMA-*b*-UrMA) containing 50 wt% hard segments demonstrated a modulus plateau from -10 °C to 90 °C before flow temperatures ( $T_f$ ) as the hard block molecular weight increased and resulted in better phase separation.  $T_g$ s in DMA were both slightly higher than those from DSC. As glass transition is a kinetic driven phenomena, DMA introduced additional frequency dependence and thermal gradient comparing to DSC, leading to a shift in  $T_g$  between two instruments. Triblock copolymers films with hard segments higher than 50 wt% were too brittle to yield reproducible data.

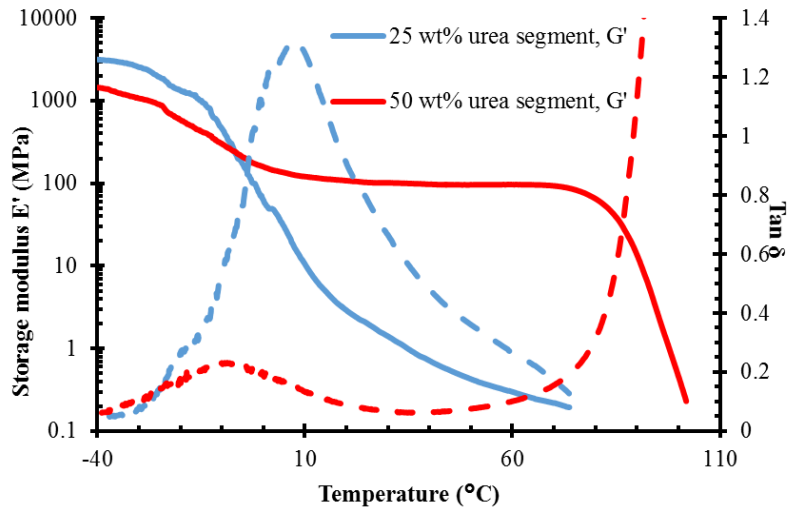


**Figure 6.3.** Dynamic mechanical analysis of poly(UrMA-*b*-DEGMEMMA-*b*-UrMA) with 25 and 50 wt% urea segment.

Thermomechanical analysis suggested microphase separation in the triblock copolymer films, and surface and bulk morphologies were investigated to elucidate the compositional dependence on microphase separated morphologies. Atomic force microscopy (AFM) revealed the influence of block compositions on surface morphology. As shown in **Figure 6.4**, increasing hard block length led to a transition of surface morphology from spherical/cylindrical morphologies to lamellar morphologies. At low hard block content (25 and 50 wt%), surface morphologies were less defined, and spherical/cylindrical features dominated with minimal long-range order. When the hard segment content increased to 64 wt%, a well-defined lamellar surface morphology appeared. The lamellar thickness was approximately 50 nm. The microphase separated lamellar morphology showed limited long-range order, owing to the lack of long-range parallel lamellar domains.<sup>10</sup> Upon increasing the hard segment (67 wt% UrMA), the triblock copolymer films showed a less defined lamellar thickness, and the potential

beginning of phase reversal. Further increases in the hard segment content also led to discontinuities in the observed lamellar structures.

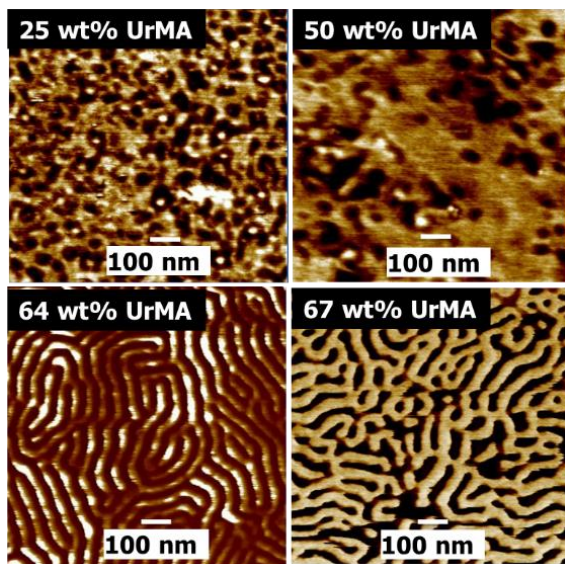


**Figure 6.4.** AFM revealed microphase-separated surface morphology: tapping mode, 42 N m<sup>-1</sup> high spin constant cantilever.

Small angle X-ray scattering further characterized the bulk morphologies of poly(UrMA-*b*-DEGMEMMA-*b*-UrMA) triblock copolymer films. **Figure 6.5** shows only one scattering peak without higher order peaks for both triblock copolymer films with lamellar surface morphologies in AFM. **Table 6.2** displayed similar Bragg spacing ( $D = 2\pi/q$ ) in both samples between 50 to 60 nm. The Bragg spacing corresponded well with the lamellar thickness in AFM. The absence of higher order SAXS peaks is indicative of the lack of long-range order,<sup>37</sup> corresponding well with AFM images. Since triblock copolymers with lamellar surface morphology (64 wt% and 67 wt% hard segment in AFM) did not exhibit higher order scattering peaks, triblock copolymers with less defined morphologies in AFM (25 wt% and 50 wt%) were not subjected to SAXS measurements. Attempts of

transmission electron microscopy (TEM) did not convey meaningful data due to the difficulty of properly staining microtomed samples.

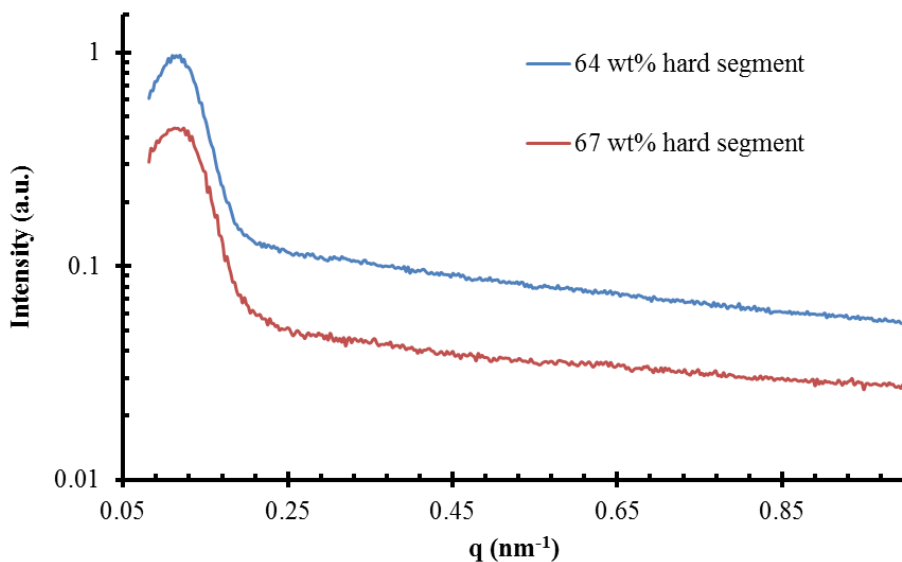


**Figure 6.5.** SAXS of cast films exhibited distinct first-order interference peaks without higher order peaks.

**Table 6.2.** SAXS  $q$  values and Bragg spacing for triblock copolymers with lamellar morphology in AFM

Polymer	Weight percent (%)	$q$ ( $\text{nm}^{-1}$ )	Distance (nm)
Poly(UrMA <sub>53</sub> - <i>b</i> -DEGMEMA <sub>58</sub> - <i>b</i> -UrMA <sub>53</sub> )	64	0.110	57.1
Poly(UrMA <sub>58</sub> - <i>b</i> -DEGMEMA <sub>58</sub> - <i>b</i> -UrMA <sub>58</sub> )	67	0.117	53.7

Variable temperature FTIR revealed the evolution of hydrogen bonding structure as a function of temperature. **Figure 6.6** depicts a typical VT-FTIR spectrum of triblock copolymers containing 64 wt% hard segments, poly(UrMA<sub>53</sub>-*b*-DEGMEMA<sub>58</sub>-*b*-UrMA<sub>53</sub>). Monitoring the shifts of carbonyl stretching vibrating peaks using VT-FTIR

provided an insight of ordered-disordered hydrogen-bonding transition. At 25 °C, an ordered hydrogen-bonded carbonyl stretching peak appeared at 1640 cm<sup>-1</sup>, corresponding to a bidentate hydrogen bond (structure **a** in **Figure 6.6**). A secondary carbonyl stretching peak also appeared at 1648 cm<sup>-1</sup>, corresponding to monodentate hydrogen bond (structure **b** in **Figure 6.6**).<sup>38</sup> Monodentate hydrogen bonding has only one hydrogen bond for each urea site compared to two hydrogen bonds in bidentate hydrogen bonding. As a result, the carbonyl bonds in monodentate hydrogen bonding are less stretched and stronger than those in bidentate hydrogen bonding, leading to a blue shift in FTIR from 1640 cm<sup>-1</sup> to 1648 cm<sup>-1</sup>. At 75 °C, both ordered hydrogen-bonded carbonyl peaks (1640 and 1648 cm<sup>-1</sup>) started to shift to higher wavenumbers, i.e. 1656 and 1680 cm<sup>-1</sup>, respectively. We attributed this transition to the increase of segmental mobility as temperature approaching the hard domain T<sub>g</sub> (78 °C). Dissociation of hydrogen bonds leads to stronger carbonyl double bonds. Therefore, the FTIR peaks further moved towards high wavenumber (blue shift). Further increase of temperature led to a higher population of disordered hydrogen-bonded carbonyls and free carbonyls (1692 cm<sup>-1</sup>). However, at 165 °C, the intensity of ordered carbonyl stretching peaks (1640 and 1648 cm<sup>-1</sup>) remained significant compared to the disordered carbonyl peaks, indicating the retention of ordered hydrogen bonding. In summary, upon increasing temperature, only a limited amount of hydrogen bonds transitioned from ordered structures (1640 cm<sup>-1</sup>) to disordered structures (1656 cm<sup>-1</sup>) and eventually fully dissociated (1692 cm<sup>-1</sup>).

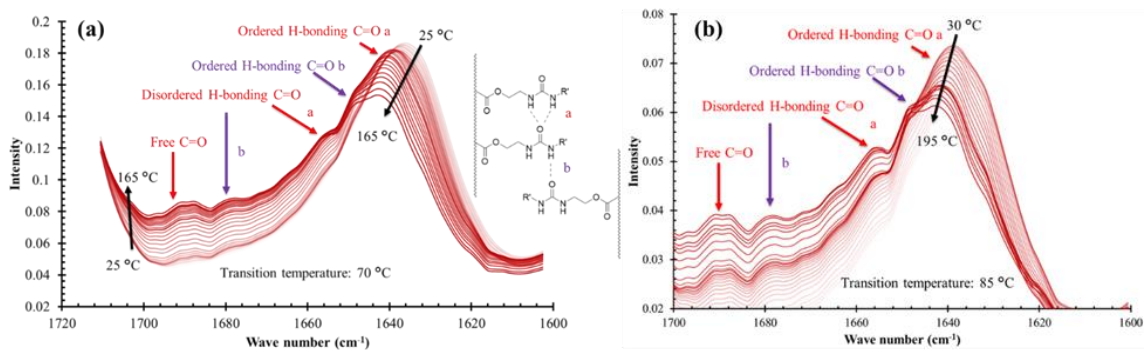


**Figure 6.6** Variable temperature Fourier transform infrared spectroscopy illustrated the transition from ordered hydrogen bonding to disordered hydrogen bonding with increasing temperature in (a) poly(UrMA<sub>50</sub>-*b*-DEGMEMA<sub>58</sub>-*b*-UrMA<sub>50</sub>), 64 wt% hard block and (b) poly(UrMA<sub>30</sub>-*b*-DEGMEMA<sub>58</sub>-*b*-UrMA<sub>30</sub>), 50 wt% hard block. Hydrogen bonding structure: **a**, bidentate hydrogen bonding; **b**, mono-dentate hydrogen bonding.

**Figure 6.6b** depicted the dissociation of hydrogen bonding in triblock copolymers with 50 wt% urea content, poly(UrMA<sub>30</sub>-*b*-DEGMEMA<sub>58</sub>-*b*-UrMA<sub>30</sub>). Triblock copolymers with 50 wt% urea content showed both monodentate and bidentate hydrogen bonding and demonstrated similar temperature response compared to the triblock copolymer with 64 wt% urea content. Yet, the intensity of ordered hydrogen bonding experienced a more prominent decrease starting at 85 °C, which corresponded with the  $T_f$  in DMA (90 °C). The different dissociation profiles of triblock copolymers with 50 wt% and 64 wt% urea content was ascribed to morphological changes. As shown in **Figure 6.4**, triblock copolymers with 64 wt% urea content demonstrated ordered lamellar morphology while triblock copolymers with 50 wt% urea content showed less ordered phase separation. Well aligned hydrogen bonds in ordered lamellar morphology required higher temperature to dissociate. Nevertheless, block copolymers with 50 wt% still retained ~ 70% ordered structure at 195 °C.

The presence of monodentate hydrogen bonding and the retention of the majority of ordered hydrogen bonds at high temperature are unique for the pendant urea sites compared to backbone urea sites, which demonstrated almost complete disappearance of ordered hydrogen bonding at 120 to 160 °C depending on specific backbone structures<sup>1-2</sup>. As proposed in **Figure 6.7**, the main chain hydrogen bonds dissociate more readily at high temperature due to the cooperative effect.<sup>1-2</sup> Yet, the absence of cooperativity in pendant hydrogen bonds may lead to more ordered hydrogen bonds at high temperatures. It was assumed that the lack of cooperativity competes with increased mobility from pendant hydrogen bonding. In our case, pendant urea hydrogen bonding is strong enough to overcome increased mobility and maintains more ordered hydrogen bonds at high temperatures. Future studies will include the synthesis of backbone urea block copolymers with similar molecular weight and molecular weight distribution to further validate our hypothesis on the origin of monodentate hydrogen bonding and the retention of ordered hydrogen bonding at high temperature.

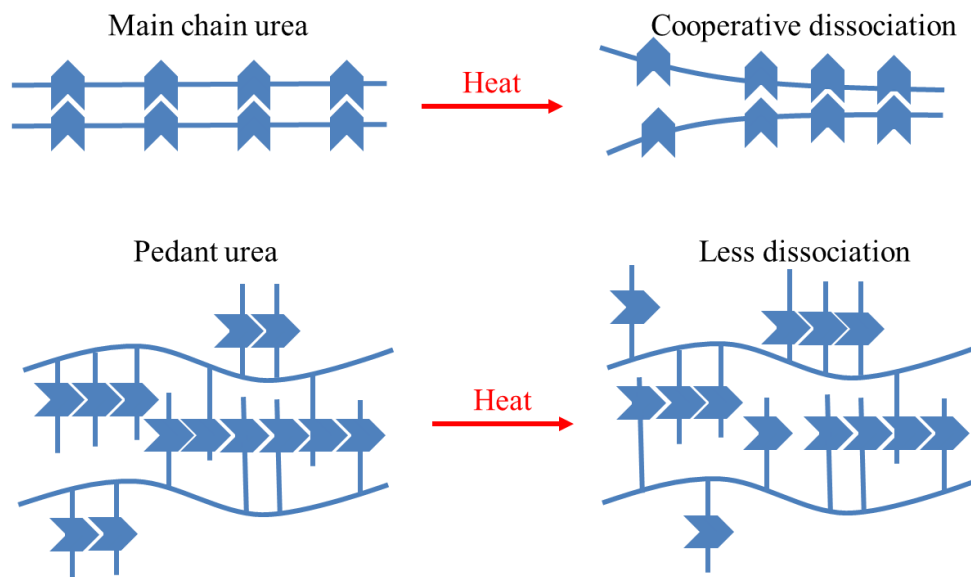


**Figure 6.7.** Schematic illustration of the dissociation of main chain urea sites and pendant urea side sites.

## 6.5 Conclusions

RAFT polymerization allowed the successful synthesis of ABA triblock copolymers with pendant urea sites. Random copolymerization of two urea-containing monomers afforded a hard, external block with tunable  $T_g$ s. A kinetic study and molecular weight characterization demonstrated well-controlled chain growth throughout the entire polymerization. Two distinct  $T_g$ s in DSC and DMA suggested the microphase separated morphologies of the triblock copolymers with pendant urea sites. AFM further supported the microphase separation conclusion from thermomechanical analysis and showed compositional dependence on surface morphologies. Poly(UrMA-*b*-DEGMEMA-*b*-UrMA) triblock copolymers achieved various surface morphologies with limited long-range order. SAXS further supported the lack of long-range orders in microphase separated morphologies, where only one scattering peak appeared.

From VT-FTIR, the presence of monodentate hydrogen bonding confirmed pendant hydrogen bonding exhibited less ordered structure compared to main chain hydrogen

bonding. At elevated temperatures, the majority of pendant hydrogen bonds still retained ordered structures in contrast to an obvious shift from ordered to less ordered structures in main chain hydrogen bonds. We attribute this difference at high temperatures to the cooperativity that is unique for main chain hydrogen bonding. This study advanced the understanding in temperature response of pendant hydrogen bonding and demonstrated the potential of pendant hydrogen bonding to retain ordered morphologies at elevated temperatures.

## 6.6 Acknowledgements

We acknowledge the Institute of Critical Technology and Applied Science (ICTAS) and ICTAS Nanoscale Characterization and Fabrication Laboratory (NCFL) at Virginia Tech for instrumental support (AFM and TEM). We also acknowledge Stephen McCartney and Christopher Winkler for training and performing AFM. We thank Dr. Bruce Orlor for help in the review of this manuscript.

## 6.7 References

1. Buckwalter, D. J.; Inglefield, D. L.; Enokida, J. S.; Hudson, A. G.; Moore, R. B.; Long, T. E., Effects of Copolymer Structure on the Mechanical Properties of Poly(dimethyl siloxane) Poly(oxamide) Segmented Copolymers *Macromol. Chem. Phys.* **2013**, *214*, 2073-2082.
2. Buckwalter, D. J.; Zhang, M. Q.; Inglefield, D. L.; Moore, R. B.; Long, T. E., Synthesis and characterization of siloxane-containing poly(urea oxamide) segmented copolymers *Polymer* **2013**, *54*, 4849-4857.
3. Komatsu, H.; Ikeda, M.; Hamachi, I., Mechanical Reinforcement of Supramolecular Hydrogel through Incorporation of Multiple Noncovalent Interactions *Chem. Lett.* **2011**, *40*, 198-200.
4. Neal, J. A.; Mozhdehi, D.; Guan, Z. B., Enhancing Mechanical Performance of a Covalent Self-Healing Material by Sacrificial Noncovalent Bonds *J. Am. Chem. Soc.* **2015**, *137*, 4846-4850.
5. Wilson, G. O.; Caruso, M. M.; Schelkopf, S. R.; Sottos, N. R.; White, S. R.; Moore, J. S., Adhesion Promotion via Noncovalent Interactions in Self-Healing Polymers *ACS Appl. Mater. Interfaces* **2011**, *3*, 3072-3077.
6. Allen, M. H.; Hemp, S. T.; Zhang, M. S.; Zhang, M. Q.; Smith, A. E.; Moore, R. B.; Long, T. E., Synthesis and characterization of 4-vinylimidazole ABA triblock

- copolymers utilizing a difunctional RAFT chain transfer agent *Polym. Chem.* **2013**, *4*, 2333-2341.
7. Inglefield, D. L.; Merritt, T. R.; Magill, B. A.; Long, T. E.; Khodaparast, G. A., Upconverting nanocomposites dispersed in urea-containing acrylics *J. Mater. Chem. C* **2015**, *3*, 5556-5565.
  8. Jimenez, Z. A.; Yoshida, R., Temperature Driven Self-Assembly of a Zwitterionic Block Copolymer That Exhibits Triple Thermoresponsivity and pH Sensitivity *Macromolecules* **2015**, *48*, 4599-4606.
  9. Wang, F.; Pu, H. T.; Jin, M.; Pan, H. Y.; Chang, Z. H.; Wan, D. C.; Du, J., From single-chain folding to polymer nanoparticles via intramolecular quadruple hydrogen-bonding interaction *J. Polym. Sci. Pol. Chem.* **2015**, *53*, 1832-1840.
  10. Zhang, K. R.; Fahs, G. B.; Aiba, M.; Moore, R. B.; Long, T. E., Nucleobase-functionalized ABC triblock copolymers: self-assembly of supramolecular architectures *Chem. Commun.* **2014**, *50*, 9145-9148.
  11. Jangu, C.; Savage, A. M.; Zhang, Z. Y.; Schultz, A. R.; Madsen, L. A.; Beyer, F. L.; Long, T. E., Sulfonimide-Containing Triblock Copolymers for Improved Conductivity and Mechanical Performance *Macromolecules* **2015**, *48*, 4520-4528.
  12. Jangu, C.; Wang, J. H. H.; Wang, D.; Sharick, S.; Heflin, J. R.; Winey, K. I.; Colby, R. H.; Long, T. E., Well-Defined Imidazolium ABA Triblock Copolymers as Ionic-Liquid-Containing Electroactive Membranes *Macromol. Chem. Phys.* **2014**, *215*, 1319-1331.
  13. Kopec, M.; Niemiec, W.; Laschewsky, A.; Nowakowska, M.; Zapotoczny, S., Photoinduced Energy and Electron Transfer in Micellar Multilayer Films *J. Phys. Chem. C* **2014**, *118*, 2215-2221.
  14. Wolski, K.; Szuwarzynski, M.; Kopec, M.; Zapotoczny, S., Ordered photo- and electroactive thin polymer layers *Eur. Polym. J.* **2015**, *65*, 155-170.
  15. Berl, V.; Schmutz, M.; Krische, M. J.; Khoury, R. G.; Lehn, J. M., Supramolecular polymers generated from heterocomplementary monomers linked through multiple hydrogen-bonding arrays - Formation, characterization, and properties *Chem. Eur. J.* **2002**, *8*, 1227-1244.
  16. Herbst, F.; Schroter, K.; Gunkel, I.; Groger, S.; Thurn-Albrecht, T.; Balbach, J.; Binder, W. H., Aggregation and Chain Dynamics in Supramolecular Polymers by Dynamic Rheology: Cluster Formation and Self-Aggregation *Macromolecules* **2010**, *43*, 10006-10016.
  17. Park, T.; Zimmerman, S. C., Formation of a miscible supramolecular polymer blend through self-assembly mediated by a quadruply hydrogen-bonded heterocomplex *J. Am. Chem. Soc.* **2006**, *128*, 11582-11590.
  18. Roy, N.; Buhler, E.; Lehn, J. M., Double dynamic self-healing polymers: supramolecular and covalent dynamic polymers based on the bis-iminocarbohydrazide motif *Polym. Int.* **2014**, *63*, 1400-1405.
  19. Akutagawa, T.; Iuchi, K.; Matsunaga, Y., Mesomorphic behaviour of N,N'-dialkanoyl-3,4,5,6-tetramethylbenzene-1,2-diamines and related compounds *Liq. Cryst.* **2000**, *27*, 1399-1403.
  20. Fukumasa, M.; Takeuchi, K. I.; Kato, T., Miscibility of a hydrogen-bonded mesogenic complex with normal liquid crystals *Liq. Cryst.* **1998**, *24*, 325-327.

21. He, W. L.; Huang, Q.; Yang, Z.; Cao, H.; Wang, D.; Yang, H., Effect of bent-shape and calamitic-shape of hydrogen-bonded mesogens on the liquid crystalline properties *Liq. Cryst.* **2015**, *42*, 1191-1200.
22. Xu, H.; Kang, N.; Xie, P.; Zhang, R. B.; Xu, D. F., Synthesis and characterization of a hydrogen-bonded nematic network based on 4-propoxybenzoic acid side groups grafted onto a polysiloxane *Liq. Cryst.* **2000**, *27*, 169-176.
23. Teo, L.-S.; Chen, C.-Y.; Kuo, J.-F., Fourier Transform Infrared Spectroscopy Study on Effects of Temperature on Hydrogen Bonding in Amine-Containing Polyurethanes and Poly(urethane-urea)s *Macromolecules* **1997**, *30*, 1793-1799.
24. Mattia, J.; Painter, P., A Comparison of Hydrogen Bonding and Order in a Polyurethane and Poly(urethane-urea) and Their Blends with Poly(ethylene glycol) *Macromolecules* **2007**, *40*, 1546-1554.
25. Anastasaki, A.; Nikolaou, V.; McCaul, N. W.; Simula, A.; Godfrey, J.; Waldron, C.; Wilson, P.; Kempe, K.; Haddleton, D. M., Photoinduced Synthesis of alpha,omega-Telechelic Sequence-Controlled Multiblock Copolymers *Macromolecules* **2015**, *48*, 1404-1411.
26. Ladmiral, V.; Charlot, A.; Semsarilar, M.; Armes, S. P., Synthesis and characterization of poly(amino acid methacrylate)-stabilized diblock copolymer nano-objects *Polym. Chem.* **2015**, *6*, 1805-1816.
27. Moraes, J.; Simionca, I. M.; Ketari, H.; Klok, H. A., Avoiding compositional drift during the RAFT copolymerization of N-(2-hydroxypropyl)methacrylamide and N-acryloxysuccinimide: towards uniform platforms for post-polymerization modification *Polym. Chem.* **2015**, *6*, 3245-3251.
28. Holmberg, A. L.; Karavolias, M. G.; Epps, T. H., RAFT polymerization and associated reactivity ratios of methacrylate-functionalized mixed bio-oil constituents *Polym. Chem.* **2015**, *6*, 5728-5739.
29. Lovett, J. R.; Warren, N. J.; Ratcliffe, L. P. D.; Kocik, M. K.; Armes, S. P., pH-Responsive Non-Ionic Diblock Copolymers: Ionization of Carboxylic Acid End-Groups Induces an Order-Order Morphological Transition *Angew. Chem. Int. Edit.* **2015**, *54*, 1279-1283.
30. Wang, W.; Liu, H.; Mu, M.; Yin, H.; Feng, Y., CO<sub>2</sub>-induced reversible morphology transition from giant worms to polymersomes assembled from a block-random segmented copolymer *Polym. Chem.* **2015**, *6*, 2900-2908.
31. Matsushita, Y.; Noro, A.; Iinuma, M.; Suzuki, J.; Ohtani, H.; Takano, A., Effect of Composition Distribution on Microphase-Separated Structure from Diblock Copolymers *Macromolecules* **2003**, *36*, 8074-8077.
32. Vandenberg, J.; Junkers, T., Alpha and Omega: Importance of the Nonliving Chain End in RAFT Multiblock Copolymerization *Macromolecules* **2014**, *47*, 5051-5059.
33. Yilgör, I.; Yilgör, E.; Wilkes, G. L., Critical parameters in designing segmented polyurethanes and their effect on morphology and properties: A comprehensive review *Polymer* **2015**, *58*, A1-A36.
34. Bates, F. S.; Fredrickson, G. H., Block Copolymer Thermodynamics: Theory and Experiment *Annu. Rev. Phys. Chem.* **1990**, *41*, 525-557.
35. Leibler, L., Theory of Microphase Separation in Block Copolymers *Macromolecules* **1980**, *13*, 1602-1617.

36. Sinturel, C.; Bates, F. S.; Hillmyer, M. A., High  $\chi$ -Low N Block Polymers: How Far Can We Go? *ACS Macro Lett.* **2015**, *4*, 1044-1050.
37. Nykaza, J. R.; Savage, A. M.; Pan, Q. W.; Wang, S. J.; Beyer, F. L.; Tang, M. H.; Li, C. Y.; Elabd, Y. A., Polymerized ionic liquid diblock copolymer as solid-state electrolyte and separator in lithium-ion battery *Polymer* **2016**, *101*, 311-318.
38. Sheth, J. P.; Wilkes, G. L.; Fornof, A. R.; Long, T. E.; Yilgor, I., Probing the hard segment phase connectivity and percolation in model segmented poly(urethane urea) copolymers *Macromolecules* **2005**, *38*, 5681-5685.

## Chapter 7: Block Copolymers Containing Pyridinium and

## Urea: A Unique Example of Charged Hydrogen Bonding

### Materials

*(Manuscript in preparation for publication)*

*Mingtao Chen, Samantha J. Talley, Maruti Hegde, Lindsey J. Anderson, Keren Zhang, Robert B. Moore, and Timothy E. Long\**

Department of Chemistry, Virginia Tech, Blacksburg, VA, 24061, US

Macromolecules Innovation Institute, Virginia Tech, Blacksburg, VA, 24061, US

\*To whom correspondence should be addressed: [telong@vt.edu](mailto:telong@vt.edu)

### 7.1 Abstract

Reversible addition-fragmentation chain transfer (RAFT) polymerization afforded novel ABA block copolymers containing both urea and pyridine groups in the external hard blocks as the first example to study the interaction between hydrogen bonding and electrostatic interaction in polymers. Before quaternization, **pyridine enhanced the hydrogen bonding of urea sites to form highly ordered morphology** in small angle X-ray scattering (SAXS) extending rubbery plateau 80 °C above hard block  $T_g$  in dynamic mechanical analysis (DMA). With the introduction of electrostatic interaction after quaternization of pyridine groups, the diminish of higher order scattering peaks in SAXS

indicated that extra physical crosslinking disrupted ordered morphology, leading to a decrease of flow temperature ( $T_f$ ) from  $\sim 180$  °C to  $\sim 100$  °C. Variable temperature FTIR (VT-FTIR) compared the temperature response of hydrogen bonding before and after quaternization and demonstrated extra electrostatic interactions delayed the disorder transition of hydrogen bonding. As a result, quaternized block copolymers showed improved stress-relaxation behavior.

## 7.2 Introduction

Common strategies to enhance inter- or intra-chain interactions in macromolecules includes the incorporation of non-covalent functionalities including H-bonding, ionic interactions,  $\pi$ - $\pi$  stacking, etc. Corresponding properties gained from non-covalent interactions include ion conductivity,<sup>1-6</sup> selective gas permeability,<sup>7-12</sup> enhanced mechanical properties,<sup>13-15</sup> anti-bacterial barrier,<sup>16</sup> specific binding to biomacromolecules,<sup>17</sup> electro-response,<sup>18-20</sup> and luminescence.<sup>21-22</sup> Current research primarily focuses on further improving these properties through incorporating multiple complimentary non-covalent interactions. For example, multiple hydrogen-bonding sites improve material mechanical properties,<sup>23</sup> facilitate exceptionally ordered micro-phase separation,<sup>13</sup> and allows strong supra-molecular assembly<sup>24</sup> compared to single hydrogen-bonding sites. Similarly, polymers with high charge density, such as zwitter-ionic polymers and doubly-charged polymers, exhibited promising improvement in mechanical performance,<sup>25</sup> ion conductivities,<sup>3-4</sup> and anti-fouling properties.<sup>26</sup> Our group has extensively studied polymers with multiple hydrogen bonding and ionic interactions, and demonstrated unique benefits from multiple non-covalent interactions. For instance, nucleobase pendant groups with multiple hydrogen bonds improved promoted micro-

phase separation including ordered lamellar morphology up to  $\mu\text{m}$ .<sup>13</sup> Similarly, polymers with doubly charged pendant groups extended rubbery plateau 50 °C compared to their single-ion counterparts.<sup>27</sup>

However, the study of macromolecules that combine different types of non-covalent interactions remains limited due to synthetic challenges and analytical obstacles to deconvolute the influence of different non-covalent interactions. Different types of non-covalent interactions do not necessarily synergistically enhance properties, but the right combination of functionality produces polymers with complex stimuli responses, *i.e.* multi-responsive materials. Previous research on multi-responsive materials normally involve polymer solutions with pH and temperature response. Sumerlin *et al.* achieved pH and temperature responsive polymers through incorporating boronic acid to poly(N-isopropylarylamide) (NIPAM), which underwent self-assembly upon heating.<sup>18</sup> Boronic acid functionality allowed tunable cloud points depending on the pH. Lodge and coworkers' investigation on thermally reversible and conductive ion gels showcased the synergistic effect of thermal and electric stimuli response.<sup>28-29</sup> NIPAM-containing triblock copolymers aggregated to form gels within ionic liquid solvent while maintaining high ion conductivities. Upon heating the gels above the upper critical solution temperature (UCST), the ion gels transformed to a liquid. However, the limited mechanical integrity at high temperature severely restricted the applications of those materials, such as transducer or ion exchange membranes (at high temperatures). To design mechanically robust, multi-responsive materials, we envisaged that polymers with both hydrogen bonding and ionic interactions could serve as the first example to understand the interactive effect from different non-covalent interactions at meso-scale,

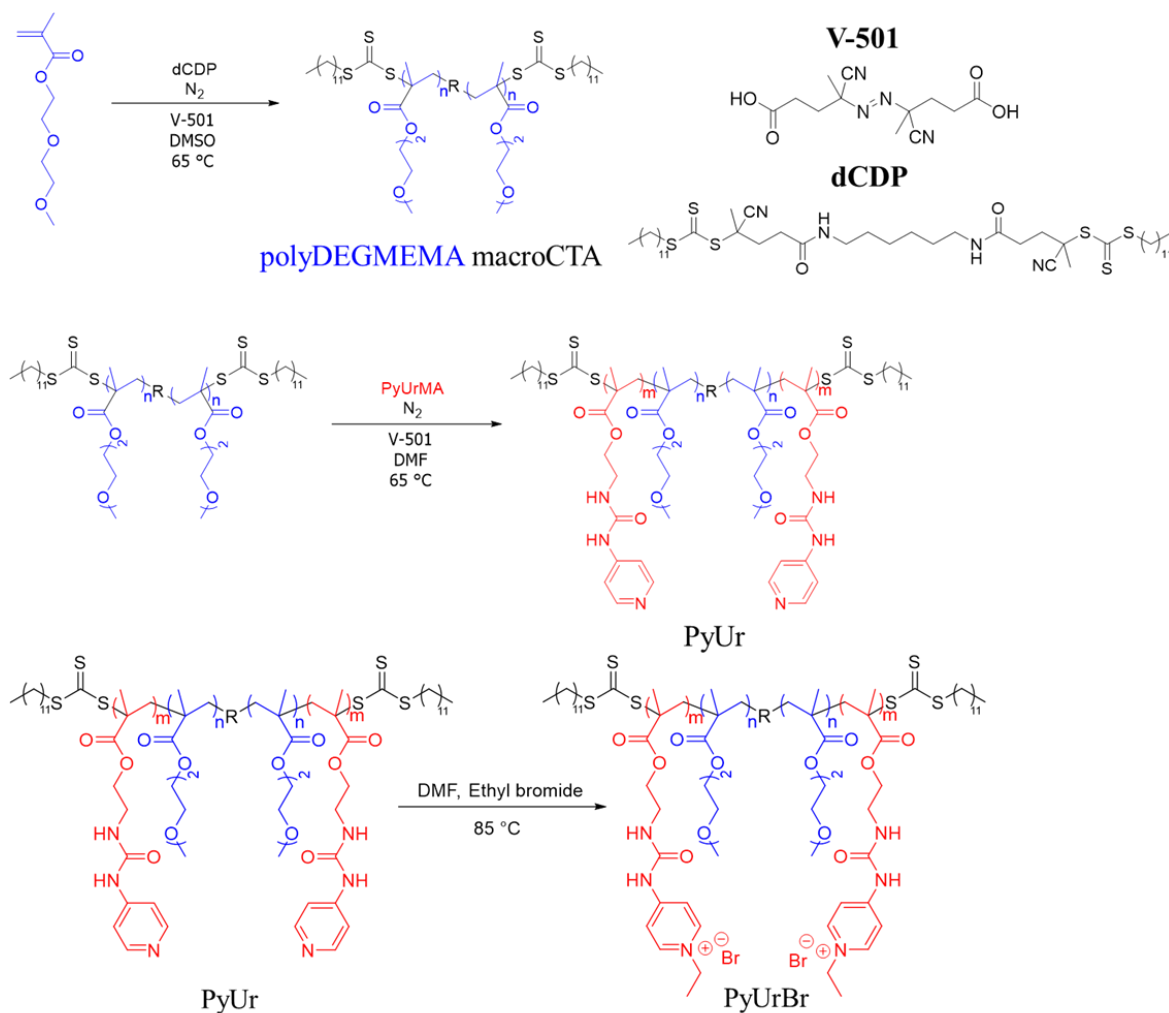
and further research endeavor towards mechanically robust materials with both thermal and electro response. In this case, hydrogen bonding will impart thermal response and mechanical properties to polymers, while ionic interactions offer electric stimuli response.

Herein, we describe the synthesis of ABA triblock copolymers (BCPs) with a low glass transition temperature ( $T_g$ ) and soluble middle block and pyridine-/pyridinium- urea functionalized outer blocks. Reversible addition-fragmentation chain transfer (RAFT) polymerization afforded controlled molecular weights and molecular weight distribution. Morphological and physical property analysis enabled structure-property-morphology relationships of urea hydrogen-bonding polymers with and without the synergistic neighboring ionic functionality.

### 7.3 Results and Discussion

Reaction between 4-amino pyridine (4-AP) and 2-isocyanatoethyl methacrylate (2-ICMA) quantitatively produced methacrylate monomers with pyridine and urea pendant sites (PyUrMA).<sup>30</sup> Pyridine groups in PyUrMA served as a function site to impart ionic interaction via post-polymerization quaternization. As seen in **Scheme 7.1**, sequential RAFT polymerization of di(ethylene glycol) methyl ether methacrylate (DEGMEMA) and PyUrMA produced a series of triblock copolymers, poly(PyUrMA-*b*-DEGMEMA-*b*-PyUrMA). The synthesis of difunctional poly(DEGMEMA) macromolecular chain transfer agent (macroCTA) exhibited a well-controlled polymerization, evident by the low PDI (1.07) and targeted number average molecular weight ( $M_n$ ) of 63 kg/mol according to size exclusion chromatography (SEC) (**Figure S7.1**). Poly(DEGMEMA) macroCTA featured flexibility and good solubility as the middle soft block. Reinitiation

of poly(DEGMEMA) macroCTA and addition of PyUrMA monomer afforded ABA symmetric triblock copolymers with varying block lengths dependent on the propagation time.



**Scheme 7.1** Synthesis of PyUrMA triblock copolymers and corresponding quaternization.

The resulting BCPs demonstrated low signal-to-noise ratio in both RI and LS detectors during SEC measurements with common eluent solvents. Instead, <sup>1</sup>H NMR spectroscopy determined the relative molar ratio of DEGMEMA and PyUrMA (Figure S2). Based on the absolute M<sub>n</sub> of poly(DEGMEMA), the molecular weight of triblock copolymers, shown in Table 1, ranged from 95 kg/mol to 165 kg/mol. The nomenclature, PyUr# (# =

1/2/3/4), represented the synthesized neutral triblock copolymers with an increasing PyUrMA block length. Post-polymerization quaternization of PyUr triblock copolymers produced their charged counterparts with bromide (Br) counter anions (PyUrBr #), as seen in **Scheme 7.1** and **Table 7.1**.  $^1\text{H}$  NMR spectroscopy confirmed quantitative quaternization (**Figure S7.3**).

**Table 7.1** Molecular weight and thermal analysis of triblock copolymers.  $M_n$  was determined by aqueous SEC and  $^1\text{H}$  NMR spectroscopy.  $T_{d,5\%}$  was calculated using TGA.  $T_g$ , endothermic transition, and exothermic transition were measured by DSC.

<b>Triblock copolymers</b>	<b><math>M_n</math> (kg/mol)</b>	<b><math>T_{d,5\%}</math> (<math>^{\circ}\text{C}</math>)</b>	<b><math>T_g</math> (<math>^{\circ}\text{C}</math>)</b>	<b>Endothermic transition (<math>^{\circ}\text{C}</math>)</b>	<b>Exothermic transition (<math>^{\circ}\text{C}</math>)</b>
PyUr1	16-63-16	187	-32, 99	ND	ND
PyUr2	30-63-30	186	-29, 91	ND	ND
PyUr3	45-63-45	205	-31, 95	ND	ND
PyUr4	51-63-51	208	-34, 96	ND	ND
PyUrBr1	16-63-16	254	-20	ND	ND
PyUrBr2	30-63-30	214	-20	81	123
PyUrBr3	45-63-45	230	-20	103	123
PyUrBr4	51-63-51	239	-20, 88	ND	ND

Thermogravimetric analysis (TGA) demonstrated an increase in onset of thermal weight loss upon quaternization. The temperature at 5 wt% loss ( $T_{d,5\%}$ ) increased 20 to 70  $^{\circ}\text{C}$  after quaternization, contradictory to previous literature.<sup>31</sup> Ammonium salts typically undergo Hofmann elimination around 180  $^{\circ}\text{C}$ , which is detrimental to the thermal stability of PyUrBr considering their  $T_{d,5\%}$  are higher than 180  $^{\circ}\text{C}$ . We attribute the

improved thermal stability to additional physical crosslinking arising from ionic interactions, discussed in greater detail later.

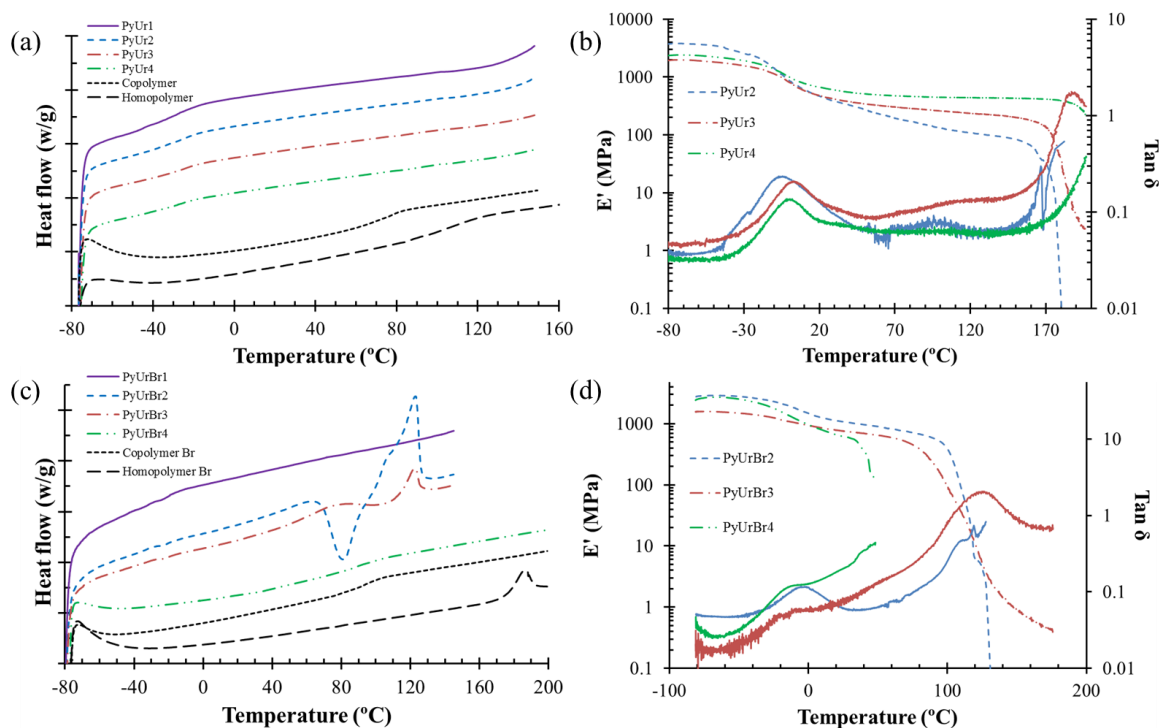


**Figure 7.1** Thermomechanical performance of PyUr and PyUrBr triblock copolymers: (a) DSC and (b) DMA of PyUr triblock copolymers; (c) DSC and (d) DMA of PyUrBr triblock copolymers. Homopolymer: poly(PyUrMA) homopolymer; Copolymer: poly(PyUrMA-*co*-DEGMEMA), 55 wt % of PyUrMA). Exo up for DSC.

Differential scanning calorimetry (DSC) showed two distinct  $T_g$ s for PyUr, suggesting microphase separation. The lower  $T_g$  corresponded to poly(DEGMEMA), while the higher  $T_g$  agreed with that of a poly(PyUrMA) homopolymer control as seen in **Figure 7.1a**. The statistic copolymer of DEGMEMA and PyUrMA (55 wt % PyUrMA) demonstrated a  $T_g$  in between the  $T_g$ s of two corresponding homopolymers as expected. Dynamic mechanical analysis (DMA) revealed a similar lower  $T_g$  at  $-25$  °C (the peak temperature of  $\tan \delta$ ) in all PyUr polymers. (free-standing films thermally annealed at  $150$  °C), as shown in **Figure 7.1b**. All PyUrBr polymers demonstrated a well-defined elastic modulus ( $E'$ ) plateau from  $0$  °C to  $180$  °C, further supporting microphase

separation. The plateau modulus increased with longer hard block length as expected. The flow temperature ( $T_{\text{flow}}$ ) of PyUr polymers exceeded the  $T_g$  of hard segments by 70 °C, from 91-99 °C to 170-200 °C, indicating strong hydrogen bonding association. We ascribed this exceptionally strong hydrogen bonding to the preorganization effect from pyridine ring, where the pyridine ring stacked periodically to align the urea groups for tight hydrogen bonding.<sup>32</sup> Another possible explanation originated from direct participation of pyridine in hydrogen bonding. Mattei *et al.* showed pyridine was a better hydrogen bonding acceptor than a carbonyl in carboxylic acid groups.<sup>33</sup> However, this phenomena is most efficient when the pyridine nitrogen is well-aligned with hydrogen bonding groups, which normally requires *ortho*-substituents of the hydrogen bonding sites.<sup>34-35</sup> Considering the fact that pyridine nitrogen in PyUr is *para* to urea sites, the direct participation of pyridine ring is most likely limited.

The quaternization of PyUr generated new thermal transitions in DSC thermograms, as seen in **Figure 7.1c**. The lower  $T_g$  of PyUrBr (-20 °C) increased due to slight phase mixing caused by the ethylene oxide units in DEGMEMA interacting with the pyridinium. The higher  $T_g$  diminished, and was only determinable in PyUrBr4. Both PyUrBr2 and PyUrBr3 showed an extra endothermic and exothermic transition compared to their neutral counterparts regardless of the cooling rate (**Figure S7.4**). Isotherm test during cooling cycles demonstrated strong crystallization transitions indicative of possible crystalline structure, as shown in **Figure S7.5a**. Further wide angle X-ray scattering (WAXS) studies in **Figure S7.5b**. revealed a sharp crystalline peak in PyUr2 besides a broad scattering peak attributing to  $\pi$ - $\pi$  stacking, which further validated the presence of crystalline regions. The  $T_{\text{flow}}$  of PyUrBr in DMA decreased significantly

compared to their neutral counterparts as a result of additional physical crosslinks disrupting hydrogen bonding, which agreed with later variable temperature FTIR (VT-FTIR). The flow temperatures were also close to the hard segment  $T_g$ , which is consistent with typical thermoplastic elastomer behavior indicating the loss of ordered hydrogen bonding.

To further compare PyUr and PyUrBr at meso-scale, we employed small angle X-ray scattering (SAXS) and wide angle X-ray scattering (WAXS) to probe the morphologies of their free-standing films. **Figure 7.2** showed the SAXS and WAXS profiles of thermally annealed PyUr and PyUrBr films with various compositions. As depicted in **Figure 7.2a**, PyUr polymers self-assembled into ordered lamellar morphology with distinct higher order scattering peaks. The Bragg spacing ( $d = 2\pi/q$ ) of PyUr polymers showed lamellar thickness to be between 30 and 40 nm (**Table 7.2**). PyUr2 had one distinct high order scattering peak ( $3q^*$ ), and another peak with lower intensity at  $5q^*$  (Table 2). PyUr3 and PyUr4 both featured three distinct high order scattering peaks ( $2q^*$ ,  $3q^*$ , and  $4q^*$ ). Increasing the hydrogen bonding content resulted in well-defined high order scattering patterns, demonstrating enhanced microphase separation. The block structures were necessary to achieve ordered morphologies as the statistic copolymer showed no distinct scattering peaks in SAXS. While SAXS identified long range order, WAXS explored local chain packing. Illustrated in **Figure 7.2b**, PyUr2, PyUr4, and the statistic copolymer control exhibited a primary peak around  $14^\circ 2\theta$ , and two smaller shoulders around  $24^\circ 2\theta$  and  $35^\circ 2\theta$ . The primary peaks represented 0.57 to 0.60 nm in real space, and we ascribed this spacing to the distance between two adjacent pyridine rings. The interdigitated spacing between polymer backbone and urea hydrogen bonding

would be longer than 0.60 nm.<sup>36</sup> The fact that the statistical copolymer control exhibited similar WAXS profile as PyUr block copolymers revealed that the peaks in WAXS correlated to short-range packing.

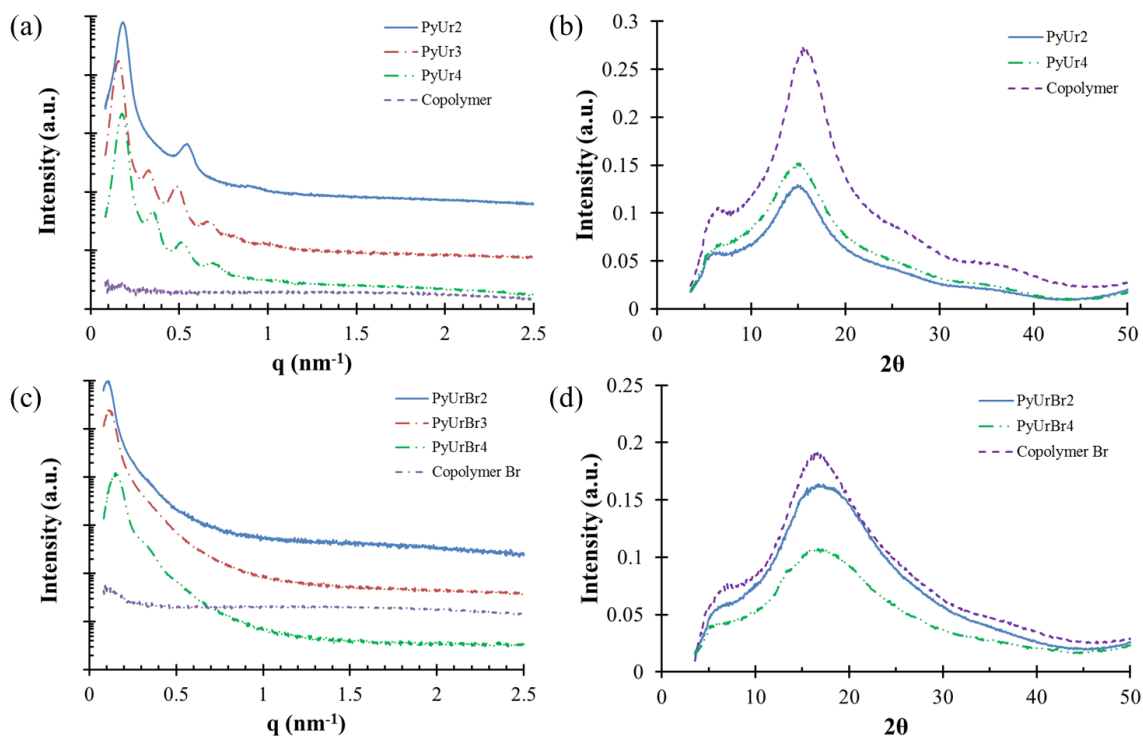


**Figure 7.2** Bulk morphologies of PyUr and PyUrBr triblock copolymer films: (a) SAXS and (b) WAXS of PyUr triblock copolymers; (c) SAXS and (d) WAXS of PyUrBr triblock copolymers. Copolymer: poly(PyUrMA-*co*-DEGMEMA), 55 wt% PyUrMA.

The quaternized PyUrBr block copolymers received significant loss in long-range order, as evidenced by the diminished high order scattering peaks in SAXS, illustrated in **Figure 7.2c**. Distinct high order peaks disappeared in SAXS for all PyUrBr block copolymers compared to PyUr. The diminished high order scattering peaks indicated disrupted hydrogen bonding in PyUrBr polymers, corresponding well with their inferior mechanical properties shown in DMA. The Bragg spacing of the primary scattering peak of the PyUrBr specimens (43 to 60 nm) also expanded compared to their neutral counterparts. For short-range packing, PyUrBr demonstrated an obvious broadening of

primary peaks in WAXS, suggesting a disruption of ordered packing, as seen in **Figure 7.2d**. PyUrBr demonstrated a slight shift of primary peaks to smaller scattering angle, which correspond to a looser packing of 0.53 nm in real space, as seen in **Figure 7.2d**. However this shift is insignificant considering the peaks are broad.

**Table 7.2** Bragg spacing and higher order peaks of triblock copolymers in SAXS

<b>Triblock copolymers</b>	<b>Bragg spacing of <math>q^*</math> (nm)</b>	<b>SAXS peaks</b>	<b>SAXS morphology</b>
PyUr2	34.4	$q^*$ , $3q^*$ , $5q^*$	Lamellae
PyUr3	40.7	$q^*$ , $2q^*$ , $3q^*$ , $4q^*$	Lamellae
PyUr4	36.2	$q^*$ , $2q^*$ , $3q^*$ , $4q^*$	Lamellae
Copolymer	N/A	N/A	N/A
PyUrBr2	59.9	$q^*$ , $3q^*$	Lamellae
PyUrBr3	58.6	$q^*$ , $3q^*$	Lamellae
PyUrBr4	43.3	$q^*$ , $2q^*$	Lamellae
Copolymer Br	N/A	N/A	N/A

**Figure 7.3** depicted the direct imaging of bulk morphologies in PyUr2 and PyUrBr2 through transmission electron microscopy. The urea sites in PyUr2 adopted long-range ordered lamellar morphology through ordered hydrogen bonding enhanced by the  $\pi$ - $\pi$  stacking of pyridine ring. As a result, PyUr showed exceptional high  $T_{flow}$  in DMA and prominent higher order scattering peaks in SAXS. After quaternization, PyUrBr2 showed no distinct morphologies. Ionic interaction introduced additional physical crosslinking in PyUrBr2, disrupting ordered packing as evidenced by the loss of higher order scattering peaks in SAXS and the peak broadening in WAXS. As a result, the corresponding  $T_{flow}$  in

DMA decreased substantially from 170 °C to 100 °C.

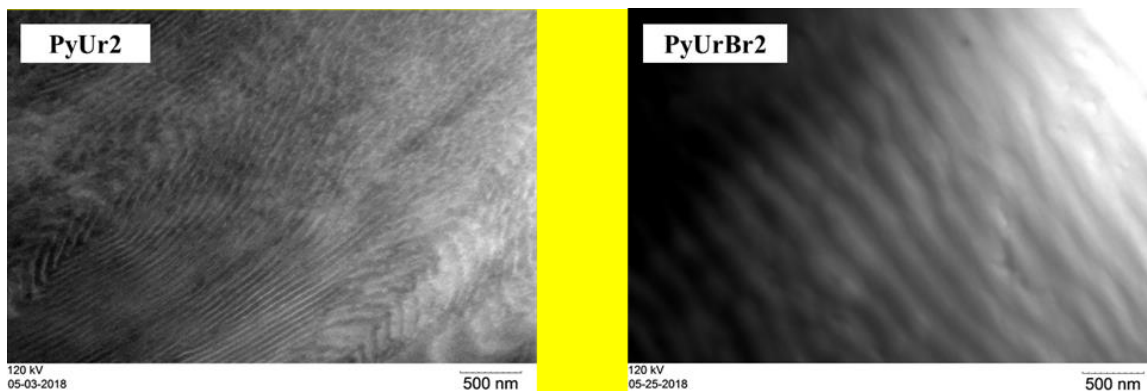


**Figure 7.3** TEM images of PyUr2 and PyUrBr2 (scale bar: 500 nm).

As seen in **Figure 7.4**, variable temperature Fourier transfer infrared spectroscopy (VT-FTIR) revealed identical carbonyl peaks for PyUr2 and PyUrBr2 at circa  $1640\text{ cm}^{-1}$  at  $30\text{ }^{\circ}\text{C}$ , corresponding well with hydrogen bonded carbonyl groups.<sup>37</sup> **Figure 7.4a** and **7.4b** showed the absorbance of hydrogen bonded carbonyl as a function of elevating temperature. Illustrated in **Figure 7.4a** and **7.4b**, PyUr hydrogen bonding underwent three major stages: 1) hydrogen bonding became more ordered with increasing temperature from  $30\text{ }^{\circ}\text{C}$  to  $90\text{ }^{\circ}\text{C}$  as increased thermal energy facilitated better pendant group packing through urea sites reorganization; 2) after the reorganization in stage 1 completed, ordered hydrogen bonding remained unchanged, and its intensity reached a plateau between  $100\text{ }^{\circ}\text{C}$  and  $150\text{ }^{\circ}\text{C}$ ; 3) starting at  $160\text{ }^{\circ}\text{C}$ , the hydrogen bonds started to dissociate, evidenced by the decreased absorbance of the peak at  $1640\text{ cm}^{-1}$  and the emergence of less associated carbonyl stretching peak at  $1652\text{ cm}^{-1}$ .<sup>37</sup> The onset temperature of hydrogen bonding dissociation correlated well with the  $T_{\text{flow}}$  of PyUr2 ( $170\text{ }^{\circ}\text{C}$ ).

For charged PyUrBr<sub>2</sub>, reorganization of hydrogen bonding happened between 30 °C and 90 °C, similar to the stage 1 in PyUr, as seen in **Figure 7.4b**. However, as shown in **Figure 7.4c**, the ordered hydrogen bonding intensity retained its plateau peak absorbance value even at 190 °C. Ionic interaction endowed additional physical crosslinks, and prevented the dissociation of hydrogen bonding.

Stress relaxation in DMA also recognized a similar hydrogen bonding dissociation difference between PyUr and PyUrBr. **Figure 7.4d** illustrated the relaxation modulus of PyUr<sub>2</sub> and PyUrBr<sub>2</sub> as a function of time at 35 °C. In PyUr<sub>2</sub>, the relaxation of soft internal block poly(DEGMEMMA) was responsible for the instantaneous decrease in relaxation modulus,  $E'(t)$ , before 5 min. Then  $E'(t)$  further decreased as the cooperative “unzipping” effect of well-aligned hydrogen bonding caused a continuous relaxation.<sup>14-15</sup> However, additional ionic interaction in PyUrBr<sub>2</sub> imparted extra physical crosslinking, permitting no stress relaxation during the course of DMA measurements after the initial relaxation from poly(DEGMEMMA) soft block. The neutral homopolymers and statistic copolymers showed no stress relaxation after 1 h in **Figure 7.4d**, indicating segmented poly(DEGMEMMA) block is responsible for the initial relaxation before 5 min and microphase separated morphology is necessary for the continuous decrease of  $E'(t)$  in PyUr<sub>2</sub>. Quaternized homopolymer and statistic copolymer controls were too brittle for stress relaxation tests due to additional physical crosslinks from electrostatic interaction.

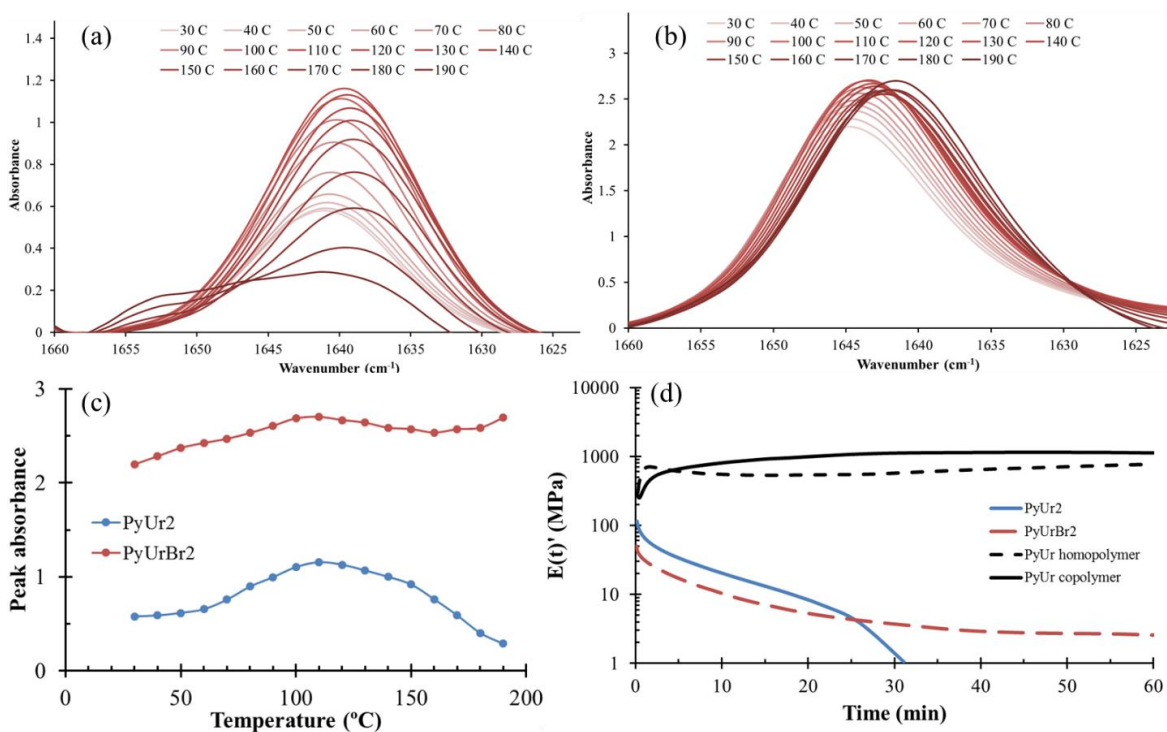


**Figure 7.4** VT-FTIR of PyUr2 (a), PyUrBr (b), and the peak absorbance of carbonyl stretching at various temperature (c) coupled with corresponding stress-relaxation of PyUr2 and PyUrBr2 (d).

## 7.4 Conclusions

In summary, we successfully synthesized methacrylate monomers with urea and pyridine sites in the pendant groups. RAFT polymerization readily afforded ABA triblock copolymers (PyUr) with pyridine urea pendant sites on the external hard block. Post-polymerization quaternization produced their charged counterparts (PyUrBr) with quantitatively efficiency.

PyUr exhibited exceptionally ordered lamellar morphology and extended the elastic modulus plateau 70 °C above the hard block  $T_g$ . The strong hydrogen bonding in PyUr started to dissociate at 160 °C, and relaxed under stress within 30 min at 35 °C. Alternatively, PyUrBr showed limited long-range order at the mesoscale, and lost mechanical integrity at the hard block  $T_g$ . However, the introduction of ionic interactions

introduced a second physical crosslinking mechanism, and led to no stress relaxation and higher dissociation temperature of hydrogen bonding.

To the best of our knowledge, this work addressed the first example of polymers with both hydrogen bonding and ionic interaction, and demonstrated the cooperative and disruptive properties by incorporating two different non-covalent interaction. It is our goal to further the development of polymers with multiple non-covalent interactions, and eventually impart multiple functionality to stimuli-responsive materials.

## **7.5 Experimental**

### **7.5.1 Materials**

N,N-dimethylformamide (DMF, anhydrous, 99.8%), chloroform (anhydrous), dimethyl sulfoxide (DMSO, anhydrous,  $\geq 99.9\%$ ), bromoethane (reagent grade, 98%), tetrahydrofuran (unstabilized), 4-aminopyridine (4-AP) and methanol were purchased from Sigma-Aldrich and used without further purification. 2,2'-Azobis(2-methylpropionitrile) (AIBN), 4,4'-Azobis(4-cyanovaleric acid) (V-501) and 4-cyano-4-[(dodecylsulfanylthiocarbonyl)sulfanyl]pentanoic acid (CDP) were purchased from Sigma-Aldrich and recrystallized from methanol prior to use. Di(ethylene glycol) methyl ether methacrylate (DEGMEMA) was purchased from Sigma-Aldrich and passed through neutral aluminum oxide (activated) prior to use. 2-Isocyanatoethyl methacrylate (2-ICMA,  $> 98\%$ ) was purchased from TCI America and used as received. Difunctional CTA were synthesized based on previous literature using CDP as starting reagents.<sup>38</sup>

### **7.5.2 Instruments**

<sup>1</sup>H nuclear magnetic resonance (NMR) spectroscopy samples were prepared in deuterated DMSO, and measured on a Varian Unity 400 MHz NMR spectrometer (128 scans) at 23

°C. Molecular weight and molecular weight distribution of poly(DEGMEMA) macroCTA were determined by size exclusion chromatography (SEC) using a Waters 515 HPLC pump equipped with a Waters 717 plus auto sampler. Absolute molecular weight was determined through a Wyatt Technology miniDawn MALLS detector operating at 690 nm coupled with a Waters 2414 refractive index detector operating at 880 nm with a flow rate of 1 mL/min in aqueous solution (54/23/23 v/v/v% water/methanol/acetic acid with 0.1 M sodium acetate). Specific refractive index value ( $dn/dc$ ) was determined offline using an Optilab T-rEX refractometer ( $\lambda = 658$  nm) and was employed to calculate weight-average molecular weight ( $M_w$ ) from SEC. Thermal degradation was determined using thermogravimetric analyzer (TGA) using a TA Instruments Q500 with a heating rate of 10 °C/min under N<sub>2</sub> atmosphere. Glass transition temperatures were measured by a TA Instruments Q2000 differential scanning calorimeter (DSC), and reported as the middle point of the thermal transition in the second heat during a heat/cool/heat procedure (10 °C/min heating rate and quench cool, N<sub>2</sub> purge). Dynamic mechanical analysis (DMA) was performed using a TA Instruments Q800 in film tension mode (3 °C/min heating ramp and 1 Hz frequency). Stress relaxation was also conducted on a TA Instruments Q800 DMA through a stress relaxation process with 0.5% strain. The temperature was set to 35 °C, and the relaxation time was 60 min. Variable temperature Fourier transfer infrared spectroscopy (VT-FTIR) was employed to evaluate the temperature response of hydrogen bonding. The instruments are consisted of a Varian 670-IR with a PIKE GladiATR attachment with a scan range 4000-400 cm<sup>-1</sup> and resolution of 4 cm<sup>-1</sup>. Spectra were collected every 5 °C as an average of 32 scans with a temperature ramp from 25 °C to 165 °C (1 °C/min).

Small angle X-ray scattering (SAXS) and wide-angle X-ray diffraction (WAXS) experiments were performed using a Rigaku S-Max 3000 3 pinhole SAXS system, equipped with a rotating anode emitting X-ray with a wavelength of 0.154 nm (Cu K $\alpha$ ). The sample-to-detector distance was 1603 mm for SAXS and 110 mm for WAXS, and the q-range was calibrated using a silver behenate standard. Two-dimensional SAXS patterns were obtained using a fully integrated 2D multiwire, proportional counting, gas-filled detector, with an exposure time of 2 h. WAXS two-dimensional diffraction patterns were obtained using an image plate with an exposure time of 1 h. The SAXS data were corrected for sample thickness, sample transmission and background scattering. All of the SAXS and WAXS data were analyzed using the SAXSGUI software package to obtain radially integrated SAXS and WAXS intensity versus the scattering vector q (SAXS) or  $2\theta$  (WAXS), where  $q=(4\pi/\lambda)\sin(\theta)$ ,  $\theta$  is one half of the scattering angle and  $\lambda$  is the wavelength of X-ray.

### **7.5.3 Synthesis of PyUrMA monomer**

4-Amino pyridine (10.0 g, 0.107 mol) and anhydrous chloroform (40.0 g) were charged in a two-necked, round-bottomed flask. The solution was purged with N<sub>2</sub> for 15 min, and cooled in an ice bath. 2-Isocyanatoethyl methacrylate (16.5 g, 0.107 mol) was added dropwise through an additional funnel with strong stirring. The reaction proceeded at 0 °C for 4 h, and was allowed to warm up to 23 °C for 20 h. White solid crashed out of solution. After filtration, the white solid was further washed with chloroform twice. After drying under vacuum for 12 h at 23 °C, the final product was a white solid with quantitative yield (95%). <sup>1</sup>H NMR (DMSO-*d*<sub>6</sub>, 25 °C,  $\delta$ ): 1.85 (3H, -CH<sub>3</sub>, vinyl methyl protons), 3.35 (2H, -CH<sub>2</sub>-N, methylene protons), 4.11 (2H, -CH<sub>2</sub>-O, methylene protons),

5.65 (1H, =CH<sub>2</sub>, vinyl proton), 6.04 (1H, =CH<sub>2</sub>, vinyl proton), 6.48 (1H, -CH<sub>2</sub>-NH-, amine protons), 7.34 & 8.24 (4H, aromatic protons), 8.99 (1H, -NH-Ar, amine proton).

#### **7.5.4 Synthesis of poly(DEGMEMA) macroCTA**

DEGMEMA monomer (7 g), dCDP difunctional CTA (94.1 mg) and initiator V-510 (14.9 mg) was dissolved in DMSO (74.4 mL) at 0.5 M monomer concentration. The [dCDP]/[V-501] ratio was set to 2:1 (the actual CTA/initiator ratio was 4:1) and the degree of polymerization at 100% monomer conversion was 350. The solution was sparged with nitrogen for 45 min and stirred at 65 °C for a given time to obtain macroCTA with specific molecular weights. The polymerization was quenched by exposing to air. Polymers were dialyzed against unstabilized THF three times. The dialysis solvent was replaced every 8 h. After removal of solvent and drying *in vacuo* (25 °C for 12 h and 50 °C for 12 h), the product was sticky yellow glue-like materials.

#### **7.5.5 Synthesis of PyUr triblock copolymers**

A 100-mL, one-necked, round-bottomed, flask was charged with PyUrMA monomer (6 g), poly(DEGMEMA) macroCTA (2.33 g, 63 kg/mol), and V-501 initiator (3.46 mg) in 48.1 mL DMF at 0.5 M monomer concentration. The CTA/initiator ratio ([dCDP]/[V-501]) was set to 2.5. The solution was sparged with nitrogen for 40 min, and then stirred at 65 °C for a given time interval. The polymerization was quenched by exposing to air and cooling to 0 °C. The polymers were purified by dialysis against methanol three times with solvent change every 8 h. After removal of solvent, the pale yellow polymers were further dried *in vacuo* at 25 °C for 24 h and 50 °C for 12 h.

#### **7.5.6 Synthesis of PyUrBr triblock copolymers**

PyUr triblock copolymer (0.34 g, 0.46 mmol of PyUrMA repeating units, 16-63-16 kg/mol) was dissolved in 5 mL DMF, and purged with Ar for 5 min. Bromoethane (0.104 mL, 1.38 mmol) was injected into the solution all at once. The reaction was performed at 85 °C for 3 d with strong stirring. The resulting PyUrBr was purified through dialysis against methanol. The dialysis solvent was switched three times with 8 h interval. After drying under vacuum at 50 °C for 24 h, the resulting product was a brown solid.

### 7.5.7 Film casting

Both PyUr and PyUrBr polymers were dissolved in DMF at circa 15 wt%. The polymer solution was cast onto Mylar<sup>®</sup> films with slow drying process (24 h at ambient condition, 24 h at 50 °C, and 24 h at 50 °C under vacuum). Then the films were thermally annealed at 150 °C for 48 h *in vacuo*, and peeled off Mylar<sup>®</sup> as free-standing films.

## 7.6 Reference

1. Allen, M. H.; Wang, S.; Hemp, S. T.; Chen, Y.; Madsen, L. A.; Winey, K. I.; Long, T. E., Hydroxyalkyl-Containing Imidazolium Homopolymers: Correlation of Structure with Conductivity *Macromolecules* **2013**, *46*, 3037-3045.
2. Jourdain, A.; Serghei, A.; Drockenmuller, E., Enhanced Ionic Conductivity of a 1,2,3-Triazolium-Based Poly(siloxane ionic liquid) Homopolymer *ACS Macro Lett.* **2016**, *5*, 1283-1286.
3. Obadia, M. M.; Jourdain, A.; Serghei, A.; Ikeda, T.; Drockenmuller, E., Cationic and dicationic 1,2,3-triazolium-based poly(ethylene glycol ionic liquid)s *Polym. Chem.* **2017**, *8*, 910-917.
4. Shaplov, A. S.; Lozinskaya, E. I.; Losada, R.; Wandrey, C.; Zdvizhkov, A. T.; Korlyukov, A. A.; Lyssenko, K. A.; Malyshkina, I. A.; Vygodskii, Y. S., Polymerization of the new double-charged monomer bis-1,3(N,N,N-trimethylammonium dicyanamide)-2-propylmethacrylate and ionic conductivity of the novel polyelectrolytes *Polym. Adv. Technol.* **2011**, *22*, 448-457.
5. Shaplov, A. S.; Lozinskaya, E. I.; Ponkratov, D. O.; Malyshkina, I. A.; Vidal, F.; Aubert, P.-H.; Okatova, O. g. V.; Pavlov, G. M.; Komarova, L. I.; Wandrey, C.;

- Vygodskii, Y. S., Bis(trifluoromethylsulfonyl)amide based “polymeric ionic liquids”: Synthesis, purification and peculiarities of structure–properties relationships *Electrochimica Acta* **2011**, *57*, 74-90.
6. Wang, A. L.; Xu, H.; Liu, X.; Gao, R.; Wang, S.; Zhou, Q.; Chen, J.; Liu, X. F.; Zhang, L. Y., The synthesis of a hyperbranched star polymeric ionic liquid and its application in a polymer electrolyte *Polym. Chem.* **2017**, *8*, 3177-3185.
  7. Bara, J. E.; Hatakeyama, E. S.; Gin, D. L.; Noble, R. D., Improving CO<sub>2</sub> permeability in polymerized room-temperature ionic liquid gas separation membranes through the formation of a solid composite with a room-temperature ionic liquid *Polym. Adv. Technol.* **2008**, *19*, 1415-1420.
  8. Cheng, J.; Hu, L. Q.; Li, Y. N.; Liu, J. Z.; Zhou, J. H.; Cen, K. F., Improving CO<sub>2</sub> permeation and separation performance of CO<sub>2</sub>-philic polymer membrane by blending CO<sub>2</sub> absorbents *Appl. Surf. Sci.* **2017**, *410*, 206-214.
  9. Estahbanati, E. G.; Omidkhah, M.; Arnooghint, A. E., Interfacial Design of Ternary Mixed Matrix Membranes Containing Pebax 1657/Silver-Nanopowder/ BMIM BF<sub>4</sub> for Improved CO<sub>2</sub> Separation Performance *ACS Appl. Mater. Interfaces* **2017**, *9*, 10094-10105.
  10. Fam, W.; Mansouri, J.; Li, H. Y.; Chen, V., Improving CO<sub>2</sub> separation performance of thin film composite hollow fiber with Pebax (R) 1657/ionic liquid gel membranes *J. Membr. Sci.* **2017**, *537*, 54-68.
  11. Moghadam, F.; Kamio, E.; Yoshioka, T.; Matsuyama, H., New approach for the fabrication of double-network ion-gel membranes with high CO<sub>2</sub>/N<sub>2</sub> separation performance based on facilitated transport *J. Membr. Sci.* **2017**, *530*, 166-175.
  12. Nguyen, P. T.; Voss, B. A.; Wiesenauer, E. F.; Gin, D. L.; Nobe, R. D., Physically Gelled Room-Temperature Ionic Liquid-Based Composite Membranes for CO<sub>2</sub>/N<sub>2</sub> Separation: Effect of Composition and Thickness on Membrane Properties and Performance *Ind. Eng. Chem. Res.* **2013**, *52*, 8812-8821.
  13. Zhang, K. R.; Talley, S. J.; Yu, Y. P.; Moore, R. B.; Murayama, M.; Long, T. E., Influence of nucleobase stoichiometry on the self-assembly of ABC triblock copolymers *Chem. Commun.* **2016**, *52*, 7564-7567.
  14. Buckwalter, D. J.; Zhang, M. Q.; Inglefield, D. L.; Moore, R. B.; Long, T. E., Synthesis and characterization of siloxane-containing poly(urea oxamide) segmented copolymers *Polymer* **2013**, *54*, 4849-4857.
  15. Buckwalter, D. J.; Inglefield, D. L.; Enokida, J. S.; Hudson, A. G.; Moore, R. B.; Long, T. E., Effects of Copolymer Structure on the Mechanical Properties of Poly(dimethyl siloxane) Poly(oxamide) Segmented Copolymers *Macromol. Chem. Phys.* **2013**, *214*, 2073-2082.
  16. Qin, J.; Guo, J. N.; Xu, Q. M.; Zheng, Z. Q.; Mao, H. L.; Yan, F., Synthesis of Pyrrolidinium-Type Poly(ionic liquid) Membranes for Antibacterial Applications *ACS Appl. Mater. Interfaces* **2017**, *9*, 10504-10511.
  17. Jung, S.; Lodge, T. P.; Reineke, T. M., Complexation between DNA and Hydrophilic-Cationic Diblock Copolymers *J. Phys. Chem. B* **2017**, *121*, 2230-2243.
  18. Brooks, W. L. A.; Vancoillie, G.; Kabb, C. P.; Hoogenboom, R.; Sumerlin, B. S., Triple Responsive Block Copolymers Combining pH-Responsive, Thermoresponsive, and Glucose-Responsive Behaviors *J. Polym. Sci. Pol. Chem.* **2017**, *55*, 2309-2317.

19. Li, W.; Kuang, T. R.; Jiang, X. P.; Yang, J. T.; Fan, P.; Zhao, Z. P.; Fei, Z. D.; Zhong, M. Q.; Chang, L. Q.; Chen, F., Photoresponsive polyelectrolyte/mesoporous silica hybrid materials with remote-controllable ionic transportation *Chem. Eng. J.* **2017**, *322*, 445-453.
20. Niu, Y. L.; Yuan, X. Y.; Zhao, Y. H.; Zhang, W. Y.; Ren, L. X., Temperature and pH Dual-Responsive Supramolecular Polymer Hydrogels Hybridized with Functional Inorganic Nanoparticles *Macromol. Chem. Phys.* **2017**, *218*, 8.
21. Cheng, C. C.; Chu, C. W.; Huang, J. J.; Liao, Z. S., Complementary hydrogen bonding interaction-mediated hole injection in organic light-emitting devices *J. Mater. Chem. C* **2017**, *5*, 4736-4741.
22. Morisue, M.; Hoshino, Y.; Shimizu, M.; Nakanishi, T.; Hasegawa, Y.; Hossain, M. A.; Sakurai, S.; Sasaki, S.; Uemura, S.; Matsui, J., Supramolecular Polymer of Near-Infrared Luminescent Porphyrin Glass *Macromolecules* **2017**, *50*, 3186-3192.
23. Guo, M.; Pitet, L. M.; Wyss, H. M.; Vos, M.; Dankers, P. Y. W.; Meijer, E. W., Tough Stimuli-Responsive Supramolecular Hydrogels with Hydrogen-Bonding Network Junctions *J. Am. Chem. Soc.* **2014**, *136*, 6969-6977.
24. Folmer, B. J. B.; Sijbesma, R. P.; Versteegen, R. M.; van der Rijt, J. A. J.; Meijer, E. W., Supramolecular Polymer Materials: Chain Extension of Telechelic Polymers Using a Reactive Hydrogen-Bonding Synthone *Adv. Mater.* **2000**, *12*, 874-878.
25. Zhang, K. R.; Fahs, G. B.; Drummey, K. J.; Moore, R. B.; Long, T. E., Doubly-Charged Ionomers with Enhanced Microphase-Separation *Macromolecules* **2016**, *49*, 6965-6972.
26. Li, G.; Cheng, G.; Xue, H.; Chen, S.; Zhang, F.; Jiang, S., Ultra low fouling zwitterionic polymers with a biomimetic adhesive group *Biomaterials* **2008**, *29*, 4592-4597.
27. Zhang, K.; Drummey, K. J.; Moon, N. G.; Chiang, W. D.; Long, T. E., Styrenic DABCO salt-containing monomers for the synthesis of novel charged polymers *Polym. Chem.* **2016**, *7*, 3370-3374.
28. Hall, C. C.; Zhou, C.; Danielsen, S. P. O.; Lodge, T. P., Formation of Multicompartment Ion Gels by Stepwise Self-Assembly of a Thermoresponsive ABC Triblock Terpolymer in an Ionic Liquid *Macromolecules* **2016**, *49*, 2298-2306.
29. Lodge, T. P.; Ueki, T., Mechanically Tunable, Readily Processable Ion Gels by Self-Assembly of Block Copolymers in Ionic Liquids *Acc. Chem. Res.* **2016**, *49*, 2107-2114.
30. Inglefield, D. L.; Merritt, T. R.; Magill, B. A.; Long, T. E.; Khodaparast, G. A., Upconverting nanocomposites dispersed in urea-containing acrylics *J. Mater. Chem. C* **2015**, *3*, 5556-5565.
31. Schultz, A. R.; Jangu, C.; Long, T. E., Thermal and living anionic polymerization of 4-vinylbenzyl piperidine *Polym. Chem.* **2014**, *5*, 6003-6011.
32. Bell, T. W.; Khasanov, A. B.; Drew, M. G. B., Role of Pyridine Hydrogen-Bonding Sites in Recognition of Basic Amino Acid Side Chains *J. Am. Chem. Soc.* **2002**, *124*, 14092-14103.
33. Li, T.; Zhou, P.; Mattei, A., Electronic origin of pyridinyl N as a better hydrogen-bonding acceptor than carbonyl O *CrystEngComm* **2011**, *13*, 6356-6360.
34. Borah, P.; Mondal, J.; Zhao, Y., Urea-pyridine bridged periodic mesoporous organosilica: An efficient hydrogen-bond donating heterogeneous organocatalyst for Henry reaction *Journal of Catalysis* **2015**, *330*, 129-134.

35. Yabuuchi, K.; Marfo-Owusu, E.; Kato, T., A new urea gelator: incorporation of intra- and intermolecular hydrogen bonding for stable 1D self-assembly *Organic & Biomolecular Chemistry* **2003**, *1*, 3464-3469.
36. Cheng, S.; Zhang, M.; Wu, T.; Hemp, S. T.; Mather, B. D.; Moore, R. B.; Long, T. E., Ionic aggregation in random copolymers containing phosphonium ionic liquid monomers *Journal of Polymer Science Part A: Polymer Chemistry* **2012**, *50*, 166-173.
37. Sheth, J. P.; Wilkes, G. L.; Fornof, A. R.; Long, T. E.; Yilgor, I., Probing the hard segment phase connectivity and percolation in model segmented poly(urethane urea) copolymers *Macromolecules* **2005**, *38*, 5681-5685.
38. Allen, M. H.; Hemp, S. T.; Zhang, M. S.; Zhang, M. Q.; Smith, A. E.; Moore, R. B.; Long, T. E., Synthesis and characterization of 4-vinylimidazole ABA triblock copolymers utilizing a difunctional RAFT chain transfer agent *Polym. Chem.* **2013**, *4*, 2333-2341.

## 7.7 Supporting information

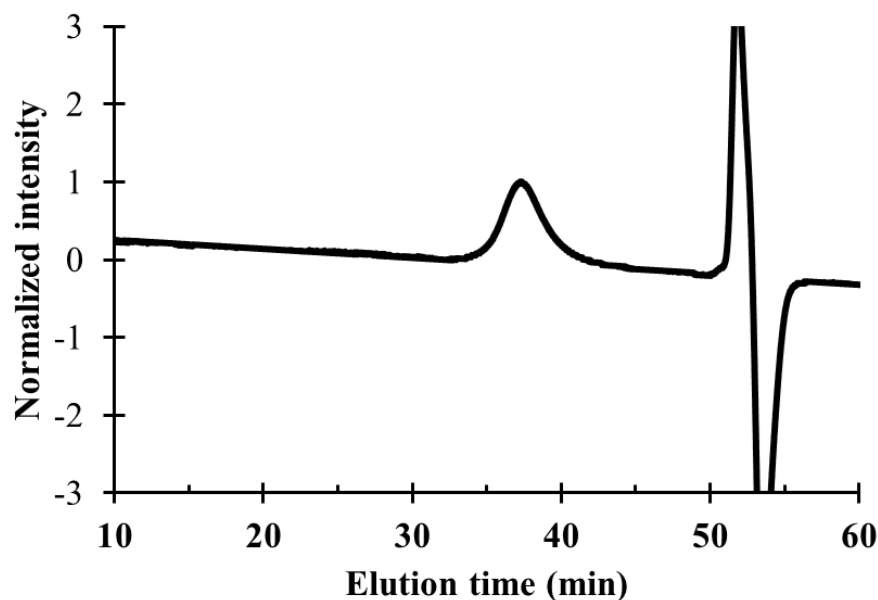


**Figure S7.1** Size exclusion chromatography (SEC) trace of poly(DEGMEMA) macrCTA. Elution solvent: DMF + 0.05 M LiBr at 60 °C.

PyUrMA molecular weight calculation:

$$M_n(\text{PyUrMA}) = \frac{b}{e-b} \times M_n(\text{DEGMEMA})$$

$$M_n(\text{DEGMEMA}) = 63 \text{ kg/mol}$$

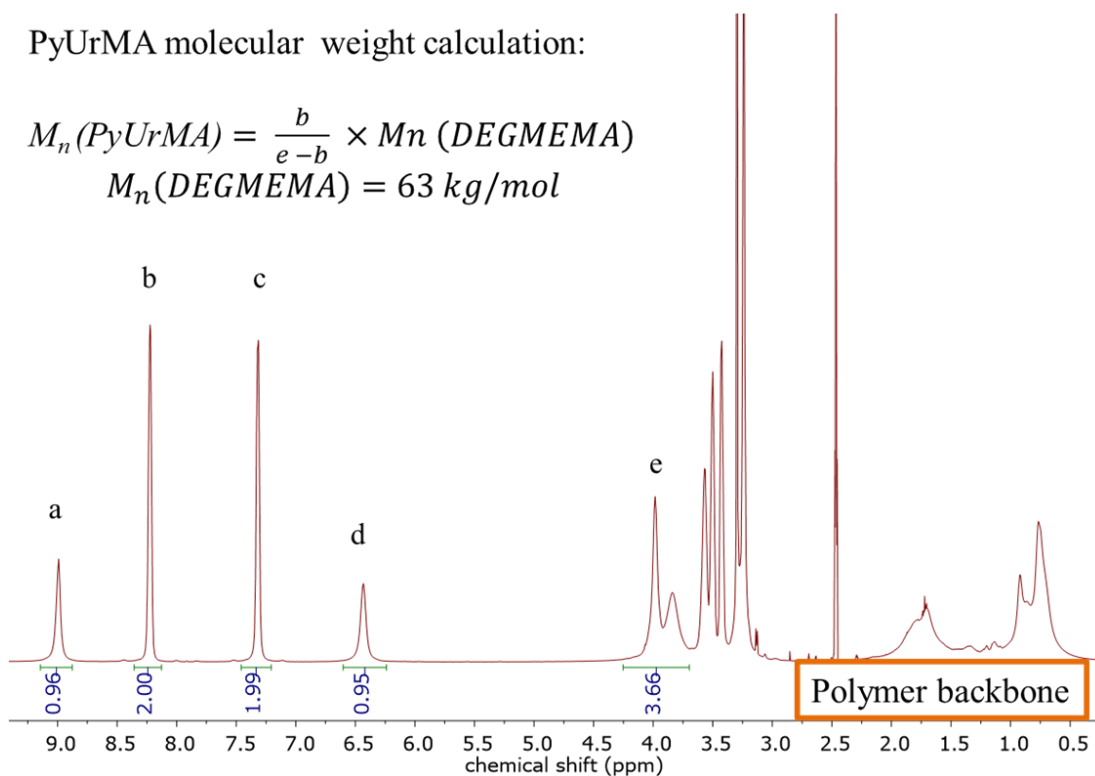


**Figure S7.2** Molecular weight determination of poly(PyUrMA) block through  $^1\text{H}$  NMR spectroscopy.

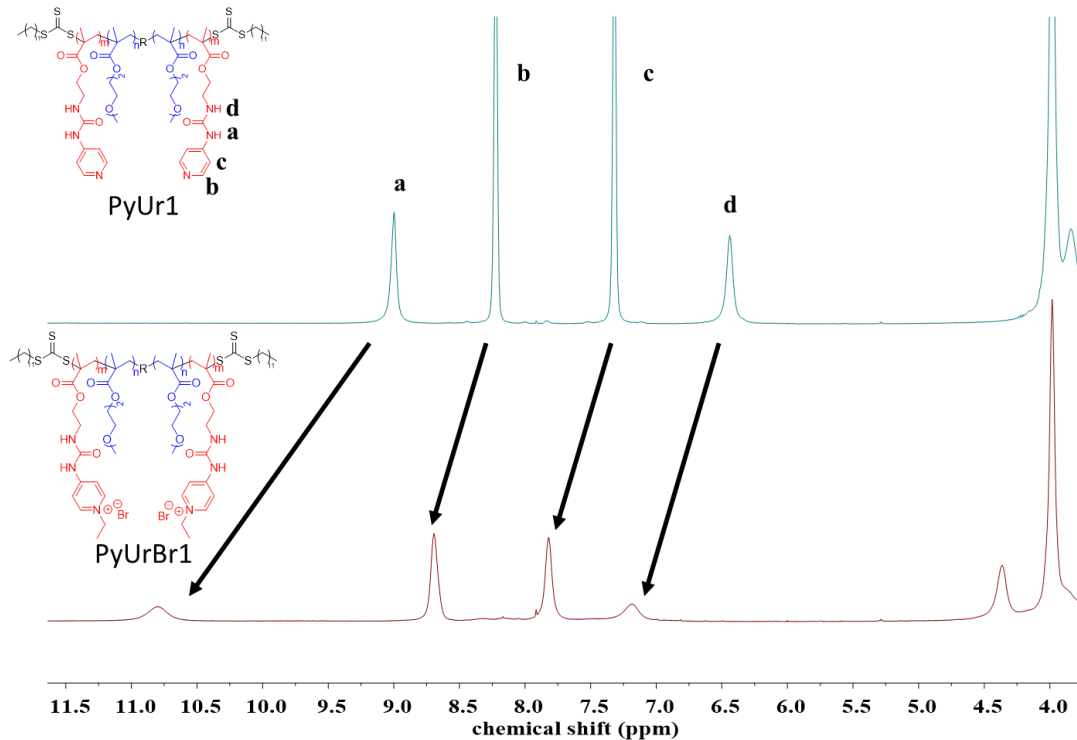


**Figure S7.3** Comparison of  $^1\text{H}$  NMR spectroscopies before and after quaternization.

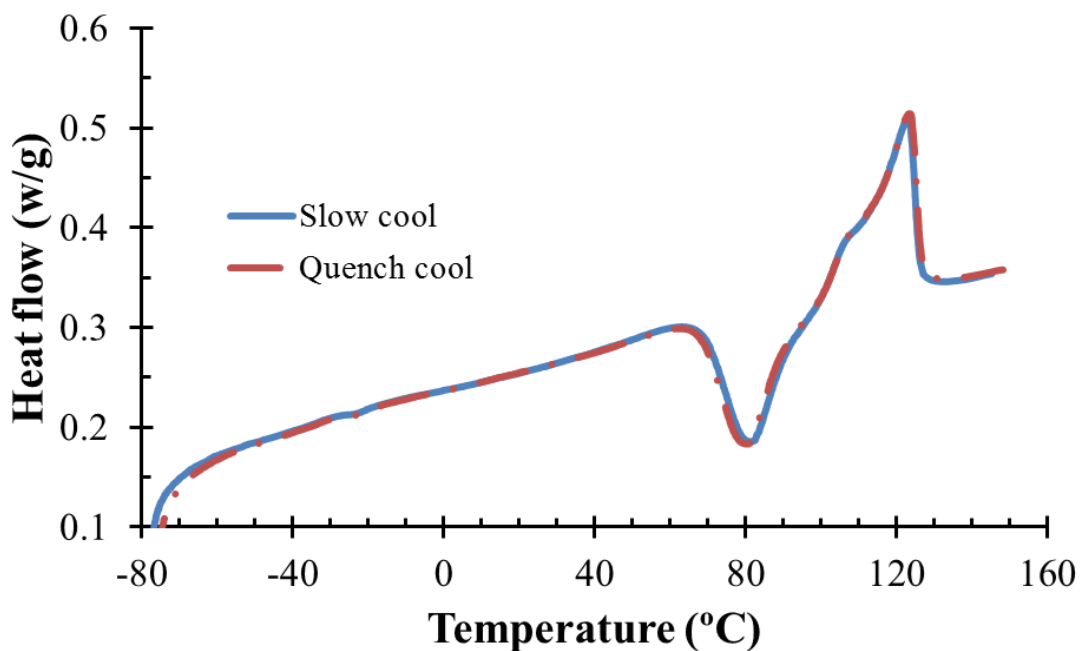


**Figure S7.4** Second heat of differential scanning calorimetry (DSC) at different cooling rate: slow cool: 5 °C/min; quench cool: 100 °C/min.

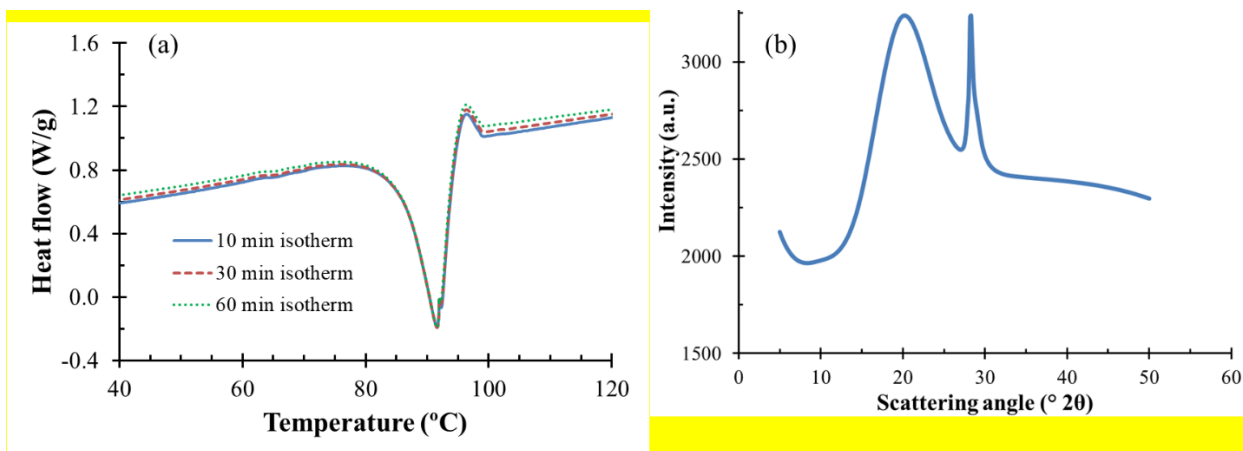


**Figure S7.2** (a) Cooling traces of PyUr2 in DSC isotherming at 92 °C for 10, 30, and 60 min; (b) WAXS profiles of PyUr2 when annealed at 92 °C.

## Chapter 8: Polymerized Ionic Liquids: Effects of Counter-Anions on Ion Conduction and Polymerization Kinetics

*(Published in Journal of Polymer Science, Part A: Polymer Chemistry, ASAP)*

Mingtao Chen,<sup>†,‡</sup> Jason W. Dugger,<sup>§</sup> Xiuli Li,<sup>†,‡</sup> Yangyang Wang,<sup>§</sup> Rajeev Kumar,<sup>§,|</sup> Kelly M. Meek,<sup>||</sup> David W. Uhrig,<sup>§</sup> James F. Browning,<sup>|||</sup> Louis A. Madsen,<sup>†,‡</sup> Timothy E. Long,<sup>†,‡</sup> and Bradley S. Lokitz<sup>§,\*</sup>

<sup>†</sup> Department of Chemistry, Virginia Tech., Blacksburg, VA 24061, USA.

<sup>‡</sup> Macromolecules Innovation Institute (MII), Virginia Tech., Blacksburg, VA 24061, USA.

<sup>§</sup> Center for Nanophase Materials Sciences, Oak Ridge National Laboratory, One Bethel Valley Road, Oak Ridge, TN 37831, USA.

<sup>|</sup> Computational Sciences and Engineering Division, Oak Ridge National Laboratory, Oak Ridge, TN 37831, USA.

<sup>||</sup> Materials Sciences and Technology Division, Oak Ridge National Laboratory, One Bethel Valley Road, Oak Ridge, TN 37831, USA.

<sup>|||</sup> Neutron Scattering Division, Oak Ridge National Laboratory, One Bethel Valley Road, Oak Ridge, TN 37831, USA.

\*To whom correspondence should be addressed: lokitzbs@ornl.gov

*This manuscript has been authored by UT-Battelle, LLC under Contract No. DE-AC05-00OR22725 with the U.S. Department of Energy. The United States Government retains and the publisher, by accepting the article for publication, acknowledges that the United States Government retains a non-exclusive, paid-up, irrevocable, world-wide license to publish or reproduce the published form of this manuscript, or allow others to do so, for United States Government purposes. The Department of Energy will provide public access to these results of federally sponsored research in accordance with the DOE Public Access Plan (<http://energy.gov/downloads/doe-public-access-plan>).*

### 8.1 Abstract

A novel imidazolium-containing monomer, 1-[ $\omega$ -methacryloyloxydecyl]-3-(*n*-butyl)-imidazolium (1BDIMA), was synthesized and polymerized using free radical and controlled free radical polymerization followed by post-polymerization ion exchange with bromine (Br), tetrafluoroborate (BF<sub>4</sub>), hexafluorophosphate (PF<sub>6</sub>), or bis(trifluoromethylsulfonyl)imide (Tf<sub>2</sub>N). The thermal properties and ionic conductivity of the polymers showed a strong dependence on the counter-ions and had glass transition temperatures ( $T_g$ ) and ion conductivities at room temperature ranging from 10 °C to -42 °C and  $2.09 \times 10^{-7} \text{ S cm}^{-1}$  to  $2.45 \times 10^{-5} \text{ S cm}^{-1}$ . In particular, PILs with Tf<sub>2</sub>N counter-ions showed excellent ion conductivity of  $2.45 \times 10^{-5} \text{ S cm}^{-1}$  at room temperature without additional ionic liquids (ILs) being added to the system, making them suitable for further study as electro-responsive materials. In addition to the counter-ions, solvent was found to have a significant effect on the reversible addition-fragmentation chain-transfer polymerization (RAFT) for 1BDIMA with different counter-ions. For example, 1BDIMATf<sub>2</sub>N would not polymerize in acetonitrile (MeCN) at 65 °C and only achieved low monomer conversion (< 5%) at 75 °C. However, 1BDIMATf<sub>2</sub>N proceeded to high conversion in dimethylformamide (DMF) at 65 °C and 1BDIMABr polymerized significantly faster in DMF compared to MeCN. NMR diffusometry was used to investigate the kinetic differences by probing the diffusion coefficients for each monomer and counter-ion in MeCN and DMF. These results indicate that the reaction rates are not diffusion limited, and point to a need for deeper understanding of the role electrostatics plays in the kinetics of free radical polymerizations.

## 8.2 Introduction

Ionic liquids (ILs) have attracted significant attention both as solvents<sup>1-3</sup> and as materials<sup>4</sup> due to their unique properties, such as negligible vapor pressure, excellent electrochemical stability, and high ion conductivity. Poly(ionic liquid)s (PILs), the macromolecular form of ILs, provide a path to coupling the advantages of ILs with polymeric materials. By introducing mechanically reinforcing components (either through the synthesis of block copolymers or via blending with other polymers), PILs have several potential applications in a wide range of areas including actuation devices,<sup>5-6</sup> separation membranes,<sup>7-13</sup> supercapacitors,<sup>14-16</sup> sea water and biomass remediation,<sup>17</sup> nanoscale lithography<sup>18</sup> and as flocculants for oil recovery.<sup>19</sup> Typical synthesis of PILs involves either conventional free radical polymerization or controlled radical polymerization (CRP). While conventional free radical polymerization finds most applications in crosslinked polymer matrices, CRP affords defined block copolymer structures, which is critical for applications that require control over morphology.

Coulombic interactions among ions undoubtedly direct the physical properties of PILs. To manipulate the Coulombic interactions, researchers routinely capitalize on monomer design and counter-ion effect. For example, spatial separation between ions and polymer backbones is a common strategy to achieve lower glass transition temperatures ( $T_g$ ) and faster ionic conduction at room temperature.<sup>20-21</sup> Counter-ion identity also affects the mobility of segments, which has a profound influence on material properties. Wang *et al.* synthesized imidazolium-containing hyperbranched PILs for polymer electrolytes through reversible addition-fragmentation chain-transfer polymerization (RAFT).<sup>22</sup> PILs with bromine (Br) counter-ions demonstrated a  $T_g$  significantly higher than bis(trifluoromethylsulfonyl)imide (Tf<sub>2</sub>N) counter-ions (79 °C and -6 °C, respectively).

After swelling with an optimized amount of LiTf<sub>2</sub>N salts, the ion conductivity of the PIL with Tf<sub>2</sub>N counter-ion reached  $4.76 \times 10^{-5} \text{ S cm}^{-1}$  at 30 °C. Lee and coworkers extended the distance between the imidazolium moiety and the polymer backbone with an ethylene glycol linker to achieve PILs with even lower T<sub>g</sub>s and higher ion conductivity.<sup>20-21</sup> PILs with hexafluorophosphate (PF<sub>6</sub>) and Tf<sub>2</sub>N counter-ions exhibited T<sub>g</sub>s at -18 °C and -50 °C, respectively. Without any addition of lithium salts, the ion conductivity of PILs with Tf<sub>2</sub>N counter-ions reached  $1.8 \times 10^{-5} \text{ S cm}^{-1}$  at 25 °C. Additionally, PILs with PF<sub>6</sub> counter-ions showed lower ion conductivity than Tf<sub>2</sub>N due to differences in polymer chain mobility arising from the variation in T<sub>g</sub>s and ion association differences derived from specific molecular interactions.<sup>23</sup> Jangu *et al.* also reported the T<sub>g</sub> and effects of counter-ion identity in styrenic PILs.<sup>24</sup> Those findings showed that T<sub>g</sub>s decreased in the order: Br > BF<sub>4</sub> > TfO (trifluoromethanesulfonate) > Tf<sub>2</sub>N, probably due to counter-ion size effects and weakened Columbic interactions, while thermal degradation exhibited the reverse order.

Despite a large number of literature reports focused on correlating the counter-ion and properties of PILs, a relatively less studied aspect is the role that counter-ion identity plays during polymerization. A few studies have focused on the influence of IL on polymerization kinetics as a solvent.<sup>25-29</sup> Mori *et al.* demonstrated that the choice of ILs as solvent affected the kinetics of ring opening polymerization (ROP) due to the interaction between IL molecules and amine additives. While the propagation rates were different for the three ILs studied, the molecular weight distribution did not change significantly. Additionally, ILs led to slower polymerization rates and lower final monomer conversion, but experienced shorter induction times.<sup>26</sup> Conversely, Zhang *et al.*

showed that the use of ILs as solvent media led to accelerated polymerization rates of methyl methacrylate compared to acetonitrile (MeCN) during atom transfer radical polymerization (ATRP).<sup>29</sup> In RAFT polymerization, Hou *et al.* compared the polymerization kinetics of acrylonitrile in IL solvent and in bulk (solvent-free).<sup>27</sup> When ILs were used as the solvent, both the polymerization rate and molecular weight distribution increased. He *et al.* studied the influence of salt addition during the homopolymerization of an imidazolium-containing IL monomer using ATRP.<sup>30</sup> Starting from the same IL monomer (imidazolium-Tf<sub>2</sub>N), the addition of various lithium salts showed limited influence on ATRP kinetics. This study was a preliminary effort to understand the role of counter-ions on polymerization kinetics. However, the lack of control over the degree of ion exchange during the polymerization made it hard for the authors to make any general conclusions.

The role of charged species (either as solvents or monomers) in polymerization kinetics has been attributed to “protected radicals” and/or “propagation with aggregation” mechanisms. For example, Thurecht and coworkers claimed the accelerated polymerization rate of methyl methacrylate (MMA) in ionic liquids compared to organic solvents was due to “protected radicals”.<sup>31</sup> Their hypothesis is that radicals are “protected” by the ionic liquids from termination, which results in faster polymerization rates and higher monomer conversions. The “propagation with aggregation” mechanism proposed by Biela *et al.* investigated the aggregation behavior of caprolactone during ring opening polymerization (ROP), and suggested that an equilibrium between active propagating chains and inactive aggregates of propagating chains existed. The polymerization rate strongly depended on deaggregation equilibrium constants, which

varied among solvents. These previous studies are notable in that the effect of counter-ion, the use of ILs, and solvent choice are all variables capable of impacting polymerization kinetics. Therefore, ionic-liquid monomers with different counter-ions will be of great interest for understanding the influence of Coulombic interactions on polymerization kinetics.

Herein, we describe the synthesis of imidazolium-containing IL monomers with identical cations but different counter-ions, and the use of either conventional free radical polymerization or reversible addition-fragmentation chain-transfer (RAFT) polymerization to synthesize PIL homopolymers. This study aimed (1) to synthesize PILs with low glass transition temperatures and high ion conductivity, (2) to confirm the influence of counter-ions on thermomechanical properties and ion conduction, and (3) to investigate the effect of counter-ions on polymerization rates. Novel PILs were successfully designed and synthesized with  $T_g$ s as low as  $-40\text{ }^\circ\text{C}$ , and these PILs demonstrated excellent ion conductivity ( $2.45 \times 10^{-5}\text{ S cm}^{-1}$ ) at room temperature without adding additional ionic liquid salts. As expected, both  $T_g$  and ion conductivity showed a strong dependence on counter-ion identity; polymers with lower  $T_g$ s had higher ionic conductivities at the room temperature. *In situ* FTIR results indicated that the counter-ions of ionic-liquid monomers have a significant impact on the kinetics of RAFT polymerization. NMR diffusometry studies indicated that neither the monomer diffusion coefficient nor degree of aggregation could account for differences in the kinetic behavior of these systems. The monomer under study here (1BDIMA, see Scheme 1) reaches high monomer conversion with Br, BF<sub>4</sub>, and Tf<sub>2</sub>N counter-ions via conventional free radical polymerization in MeCN but no monomer conversion is seen for 1BDIMATf<sub>2</sub>N in

MeCN using RAFT polymerization. The differences in polymerization kinetics resulting from solvent and counter-ion choice may lie in electron transfer processes such as free radical generation and propagation that were described by Marcus<sup>32-35</sup>. The preliminary investigations into the factors that dictate polymerization kinetics demonstrate not only the complexity of these systems, but also uncover a rich area of research that has yet to be fully explored.

### **8.3 Experimental**

#### **8.3.1 Materials**

10-Bromo-1-decanol (technical grade, 90%), 1-butyylimidazole, lithium tetrafluoroborate (98%), lithium hexafluorophosphate (98%), and bis(trifluoromethane)sulfonimide lithium salt were ordered from Sigma-Aldrich and used without further purification. N,N-dimethylformamide (DMF, anhydrous, 99.8%), acetonitrile (MeCN, anhydrous,  $\geq$  99.8%), ethyl acetate, triethylamine, and unstabilized tetrahydrofuran (THF) were purchased from Sigma-Aldrich and used as received. Aluminum oxide (neutral, activated) was purchased from Sigma-Aldrich and used as received. 4-Cyano-4-[(dodecylsulfanylthiocarbonyl)sulfanyl]pentanoic acid (CDP, 97%, HPLC) from Sigma-Aldrich was stored at -20 °C and used without purification. 2,2'-Azobis(2-methylpropionitrile) (AIBN, 98%) was purchased from Sigma-Aldrich and recrystallized once from methanol prior to use. All imidazolium-containing IL monomers were synthesized and passed through aluminum oxide columns before use. Methacryloyl chloride ( $\geq$ 97.0%, GC, contains ~0.02% 2,6-di-*tert*-butyl-4-methylphenol as stabilizer) was ordered from Sigma-Aldrich, and stored under inert atmosphere at 2 °C.

#### **8.3.2 Instrumentation**

$^1\text{H}$  and  $^{19}\text{F}$  nuclear magnetic resonance (NMR) spectroscopy measurements were conducted on a 400 MHz Bruker Advance III WB NMR spectrometer. Samples were prepared in deuterated MeCN and data was collected from 128 scans. *In situ* Fourier transform infrared spectroscopy (FTIR) experiments were performed on a Bruker Matrix-MF FTIR equipped with a diamond probe. Both peak intensity and integrated area of the vinyl methyl group stretching were monitored in the range of 1289 - 1308  $\text{cm}^{-1}$  to track monomer concentration over time. The peak resolution was set to 4  $\text{cm}^{-1}$ , and each spectra was an average of 64 scans within 50 S. Pure solvent background was collected every time before the tests. Thermal degradation was determined by a TA Q500 thermogravimetric analyzer (TGA) under  $\text{N}_2$  at 10  $^\circ\text{C}/\text{min}$  ramp rate. Thermal transition was measured by a TA Q2000 differential scanning calorimeter (DSC) under  $\text{N}_2$ . Reported values (middle point) were from the second heating cycle of a heat/cool/heat procedure: (1) 10  $^\circ\text{C}/\text{min}$  ramp from 23  $^\circ\text{C}$  to 120  $^\circ\text{C}$ , isotherm at 120  $^\circ\text{C}$  for 30 min, (2) 100  $^\circ\text{C}/\text{min}$  quench cool to -80  $^\circ\text{C}$ , and (3) 10  $^\circ\text{C}/\text{min}$  ramp to 50  $^\circ\text{C}$ . Molecular weight and molecular weight distribution were determined via size exclusion chromatography (SEC) in DMF (with 0.05 mol LiBr) at 60  $^\circ\text{C}$  and a flowrate of 1  $\text{mL min}^{-1}$ . The SEC system consisted of a Waters 1515 Isocratic HPLC pump equipped with 2414 Refractive Index (RI) detector. Poly(ethylene oxide)/poly(ethylene glycol) standards were used with Styragel HR 3 and HR 4 columns maintained in a column heater compartment.

Broadband dielectric spectroscopy (BDS) measurements of the polymerized ILs were performed with an Alpha-A analyzer, a ZGS active sample cell interface, and a Quatro Cryosystem temperature control unit (Novocontrol), in the frequency range of 0.1 –  $10^7$  Hz. Prior to the dielectric tests, the samples were heated to 120  $^\circ\text{C}$  under vacuum to

completely remove volatile impurities. In each experiment, the sample was sandwiched between two gold-plated round electrodes and a thin PTFE ring spacer was used to maintain the gap (76  $\mu\text{m}$ ). The sample thickness (gap) was 76  $\mu\text{m}$  and the sample area was 38.5  $\text{mm}^2$ . DC conductivity was defined as the value at the middle point of the plateau in the Bode plots at low frequency. Samples were equilibrated at each temperature for 20 mins prior to the test. BDS was repeated twice for all the samples from two different batches, and the results showed excellent agreement (within 5%).

### **8.3.3 Synthesis of 1-butyl-3-(10'-hydroxydecyl)-1*H*-imidazolium bromide (1BDIBr)**

This procedure was modified based on previous literature.<sup>20</sup> A solution of 1-butyl imidazole (5.5 mL, 0.042 mol) and 10-bromo-1-decanol (10.0g, 0.042 mol) in 45 mL THF was refluxed for three days at 65 °C with vigorous stirring (two-neck, round-bottomed, flask with condenser). Upon cooling to room temperature, the product formed a separate layer from the THF. THF was decanted and the product was washed with THF (45 mL) three times. The bromide salt was further dried under vacuum at 50 °C for 24 h, and appeared as a light-yellow wax at room temperature. The isolation yield was 68% (10.39 g) and <sup>1</sup>H NMR spectroscopy (400 MHz Bruker Advance III WB NMR spectrometer, MeCN-*d*<sub>3</sub>) results were as follows:  $\delta$  9.21 (t, 1H, imidazolium proton), 7.51 (d, 2H, imidazolium protons), 4.22 (d, 4H, CH<sub>2</sub>-N), 3.49 (d, 2H, CH<sub>2</sub>-OH), 2.97 (d, 1H, CH<sub>2</sub>-OH), 1.93-1.79 (m, 4H, CH<sub>2</sub>-CH<sub>2</sub>-N), 1.49 (m, 2H, CH<sub>2</sub>-CH<sub>2</sub>-OH), 1.34 (m, 14H, methylene protons in alkyl chains), 0.97 (t, 3H, -CH<sub>3</sub>).

### **8.3.4 Synthesis of 1-butyl-3-(10'-hydroxydecyl)-1*H*-imidazolium tetrafluoroborate (1BDIBF<sub>4</sub>), 1-butyl-3-(10'-hydroxydecyl)-1*H*-imidazolium hexafluorophosphate**

**(1BDIPF<sub>6</sub>), and 1-butyl-3-(10'-hydroxydecyl)-1*H*-imidazolium bis(trifluoromethane)sulfonimide (1BDITf<sub>2</sub>N)**

For 1BDIBF<sub>4</sub> synthesis, 1BDIBr (10.39 g, 0.029 mol) was dissolved in 100 mL DI water (one-neck, round-bottomed, flask) and lithium tetrafluoroborate (LiBF<sub>4</sub>) (3.23 g, 0.035 mol) was added to the aqueous solution all at once with vigorous stirring for 24 h. The precipitated salt was washed with DI water three times and dried under vacuum at 50 °C for 24 h. The product was a yellow viscous oil, and the isolation yield was 75% (7.94 g). <sup>1</sup>H NMR spectroscopy (400 MHz Bruker Advance III WB NMR spectrometer, MeCN-*d*<sub>3</sub>): δ 8.51 (t, 1H, imidazolium proton), 7.40 (d, 2H, imidazolium protons), 4.12 (q, 4H, CH<sub>2</sub>-N), 3.47 (q, 2H, CH<sub>2</sub>-OH), 2.50 (t, 1H, CH<sub>2</sub>-OH), 1.87-1.77 (m, 4H, CH<sub>2</sub>-CH<sub>2</sub>-N), 1.46 (p, 2H, CH<sub>2</sub>-CH<sub>2</sub>-OH), 1.37-1.24 (m, 14H, methylene protons in alkyl chains), 0.94 (t, 3H, -CH<sub>3</sub>).

The synthesis of 1BDIPF<sub>6</sub> and 1BDITf<sub>2</sub>N followed the same procedure as 1BDIBF<sub>4</sub>, and both chemical structures were confirmed by <sup>1</sup>H NMR spectroscopy with similar chemical shifts (except imidazolium protons, see Figure 1). The isolation yields for 1BDIPF<sub>6</sub> and 1BDITf<sub>2</sub>N were 76% and 83%, respectively.

**8.3.5 Synthesis of 1-[ω-methacryloyloxydecyl]-3-(*n*-butyl)-imidazolium bromide (1BDIMABr), 1-[ω-methacryloyloxydecyl]-3-(*n*-butyl)-imidazolium tetrafluoroborate (1BDIMABF<sub>4</sub>), 1-[ω-methacryloyloxydecyl]-3-(*n*-butyl)-imidazolium hexafluorophosphate (1BDIMAPF<sub>6</sub>), and 1-[ω-methacryloyloxydecyl]-3-(*n*-butyl)-imidazolium bis(trifluoromethane)sulfonimide (1BDIMATf<sub>2</sub>N)**

For 1BDIMABr preparation, 1BDIBr (11.60 g, 0.032 mol) and triethylamine (TEA) (8.95 mL, 0.064 mol) were charged in a two-neck, round-bottomed, flask with 90 mL

acetonitrile (MeCN, anhydrous). The system was purged with nitrogen gas for 15 min and cooled down to 0 °C using an ice bath. An addition funnel was charged with methacryloyl chloride (0.37 mL, 0.038 mol) and MeCN (40 mL, anhydrous). Next, the methacryloyl chloride solution was added to the reaction flask dropwise under strong stirring. The reaction was kept at 0 °C for 4 h, and then warmed back to 23 °C for 20 h. The reaction was quenched with 30 mL deionized water, and MeCN was removed under reduced pressure. The product was extracted three times from aqueous solution using ethyl acetate (EA), and dried over MgSO<sub>4</sub> for 1 h. After filtration, the EA solution was passed through an Al<sub>2</sub>O<sub>3</sub> column to remove potential inhibitors. Finally, EA was removed under reduced pressure and the product was dried under vacuum at 23 °C for 48 h. The resulting product was a yellow liquid and the isolation yield was 49% (6.78 g) with the following <sup>1</sup>H NMR spectroscopy (400 MHz Bruker Advance III WB NMR spectrometer, MeCN-*d*<sub>3</sub>) chemical shifts: δ 9.32 (t, 1H, imidazolium proton), 7.47 (p, 2 H, imidazolium protons), 6.02 (p, 1H, CH<sub>2</sub>=C), 5.58 (p, 1H, CH<sub>2</sub>=C), 4.19 (q, 4H, CH<sub>2</sub>-N), 4.09 (t, 2H, CH<sub>2</sub>-OH), 1.89 (t, 3H, CH<sub>2</sub>=C-CH<sub>3</sub>), 1.87-1.79 (m, 4H, CH<sub>2</sub>-CH<sub>2</sub>-N), 1.67-1.59 (m, 2H, CH<sub>2</sub>-CH<sub>2</sub>-OH), 1.39-1.23 (m, 14H, methylene protons in alkyl chains), 0.93 (t, 3H, -CH<sub>3</sub>).

The synthesis of 1BDIMABF<sub>4</sub>, 1BDIMAPF<sub>6</sub>, and 1BDIMATf<sub>2</sub>N followed the same procedure as 1BDIMABr, and their chemical structures were confirmed by <sup>1</sup>H NMR spectroscopy with similar chemical shifts (except imidazolium protons, see Figure 1). The isolation yields were 78% on average for all three monomers (red to pink liquid). <sup>19</sup>F NMR spectroscopy (400 MHz Bruker Advance III WB NMR spectrometer, MeCN-*d*<sub>3</sub>)

chemical shifts: 1BDIPF<sub>6</sub>: 72.17 and 73.82 ppm; 1BDIBF<sub>4</sub>: -151.57 ppm; 1BDITf<sub>2</sub>N: -80.18 ppm.

### **8.3.6 Conventional free radical polymerization of 1BDIMA IL monomers (*in situ* FTIR)**

1BDIMABr (1.28 g, 3.0 mmol) and corresponding amount of AIBN initiator (1 or 3 mol%) were charged in a 25-mL two-neck, round-bottomed, flask. The initial monomer concentration was kept at 0.5 M (5.98 mL MeCN). The *in situ* FTIR probe was submerged into pure solvent (MeCN) first to collect a background spectrum. The probe was then inserted into the reaction flask with a Teflon adapter and the diamond probe head below the solution surface. The joint between the Teflon adapter and reaction flask was further sealed by Teflon tape and parafilm. The third neck of the reaction flask was capped with a rubber stopper, and sealed by Teflon tape and parafilm. The reaction flask was then sparged for 20 min using Argon and a static argon pressure was maintained throughout the reaction. The reaction temperature was set to 65 °C at the beginning of data collection. Due to the overlap of the IR peak for the carbon double bond stretching modes, the vibration mode of vinyl methyl groups (C=C-CH<sub>3</sub>) was used to track monomer consumption. The peak intensity and integrated area showed good correlation (1289 to 1308 cm<sup>-1</sup>) throughout the experiment. The integrated peak area was used to calculate conversion due to its superior signal-to-noise ratio. The reaction was quenched by exposure to air and the resulting homopolymer, poly(1BDIMABr), was precipitated into EA (ethyl acetate), and washed with EA three times before being dried under vacuum at 50 °C. The pure homopolymer appeared as a yellow viscous oil with quantitative isolation yield and the following <sup>1</sup>H NMR spectroscopy (400 MHz, MeCN-

$d_3$ ) shifts:  $\delta$  10.08 (1H), 7.86 and 7.77 (2 H), 4.34 (4H), 3.94 (2H), 4.19 (q, 4H), 1.93-1.87 (4H), 1.34 (2H), 1.38-1.25 (17H), 0.95 (3H).

The conventional free radical polymerization of 1BDIMABF<sub>4</sub>, 1BDIMAPF<sub>6</sub>, and 1BDIMATf<sub>2</sub>N followed the same procedure as 1BDIMABr, and their chemical structures were confirmed by <sup>1</sup>H NMR spectroscopy with similar chemical shifts with the exception of imidazolium protons (Figure 1).

### **8.3.7 RAFT polymerization of 1BDIMA IL monomers (*in situ* FTIR)**

The RAFT polymerization of 1BDIMA IL monomers shared the same *in situ* FTIR set-up and purification procedure as above, but had slightly different polymerization conditions – the addition of the RAFT CTA: a solution of 1BDIMABr (2.02 g, 4.7 mmol), CDP (12.7 mg, 0.03 mmol), and AIBN (1.7 mg, 0.01 mmol) in 4.7 mL MeCN or DMF was sparged with Argon for 20 min prior to the polymerization. The polymerization was performed at 65 °C for 24 or 48 h and all chemical structures were confirmed by <sup>1</sup>H NMR spectroscopy.

### **8.3.8 Conventional free radical polymerization of 1BDIMABr (thermal properties and conductivity)**

A solution of 1BDIMABr (4.83 g, 0.011 mol) and a corresponding amount of AIBN (1 or 3 mol%) in MeCN (22.50 mL, 0.5 M) was sparged for 40 min using argon (50-mL, one-neck, round-bottomed flask). The polymerization was then performed at 65 °C for 24 h. The resulting polymer was precipitated into EA and washed with EA three times. The EA was removed under reduced pressure and the sample was dried under vacuum at 50 °C. The pure homopolymer appeared as yellow viscous oil with quantitative isolation yield. For characterization of thermal properties and conductivity, homopolymers with different

counter-ions were synthesized from the same batch of poly(1BDIMABr) to achieve identical repeating units number.

### 8.3.9 Post-polymerization ion exchange of poly(1BDIMABr)

The post-polymerization ion exchange of poly(1BDIMABr) with LiBF<sub>4</sub>, LiPF<sub>6</sub> and LiTf<sub>2</sub>N shared the same procedure. For the example of LiBF<sub>4</sub> ion-exchange: poly(1BDIMABr) (0.31 g, 0.72 mmol repeating unit) was dissolved in 8 mL DI water with vigorous stirring. LiBF<sub>4</sub> (96.5 mg, 1.03 mmol) was added to the reaction all at once. The reaction was performed at 23 °C for 24 h and the resulting poly(1BDIMABF<sub>4</sub>) was washed with DI water three times and dried under vacuum at 50 °C for 24 h. The isolation yield was 95% (yellow viscous oil). The chemical structure of poly(1BDIMABF<sub>4</sub>) was confirmed by <sup>1</sup>H NMR spectroscopy with similar chemical shifts with the exception of imidazolium protons (Figure 1).

### 8.3.10 NMR Diffusometry

The self-diffusion coefficients of monomer and solvent in solutions were determined using a 400 MHz Bruker Advance III WB NMR spectrometer equipped with a MIC probe, a Micro5 triple-axis gradient, and a 5 mm <sup>1</sup>H/<sup>19</sup>F detection coil. In the NMR diffusometry experiment, signal amplitude *I* was measured as a function of gradient strength (*g*) and was fit using the Stejskal-Tanner equation (Equation 1),<sup>23, 36-37</sup>

$$I = I_0 \exp[-\gamma^2 \delta^2 g^2 (\Delta - \delta/3) D], \quad (1)$$

where *I*<sub>0</sub> is the signal amplitude at *g* = 0,  $\gamma$  is the gyromagnetic ratio,  $\delta$  is the gradient pulse length,  $\Delta$  is the diffusion time between gradient pulses, and *D* is the self-diffusion coefficient. By varying the known NMR-specific parameters, diffusion coefficients were

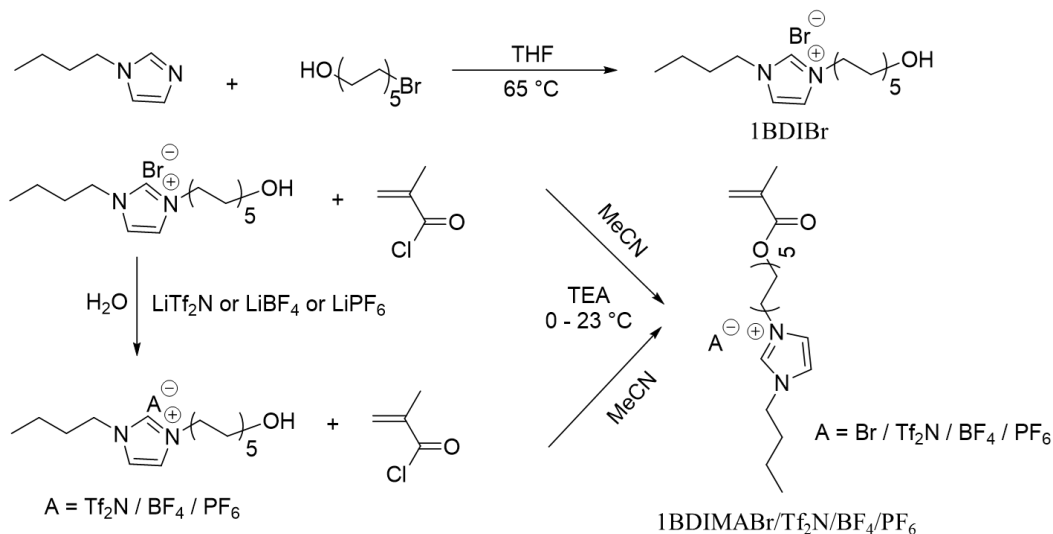
quantified by the simple and robust pulsed-gradient stimulated echo (PGSTE) sequence.<sup>38</sup> A 90° RF pulse length of 4.5  $\mu$ s, a half sinusoid gradient pulse length ( $\delta$ ) of 3.14 ms (effective rectangular pulse length of 2 ms), diffusion time ( $\Delta$ ) of 25 ms, and post-gradient delay of 1 ms were used for diffusometry measurements. Maximum gradient strengths were in the range 45 – 240 G·cm<sup>-1</sup> to attenuate signals to 90 – 99% in 16 gradient steps. Sufficient signal-to-noise ratio (SNR) for each data point was achieved with 4 – 8 scans. Acquisition times and relaxation delay times were each 1 s, and 0.3 Hz line broadening was applied during data processing. Deuterated solvents (MeCN<sub>d3</sub> and DMF<sub>d7</sub>) were used to reduce <sup>1</sup>H solvent signal interference. All NMR tubes were flame sealed to prevent solvent evaporation. The NMR measurements were performed at 21 and 62 ( $\pm$  1) °C, where the samples were equilibrated at each temperature for > 5 min. Four capillary tubes (1.2 mm in diameter) were added into the 5 mm NMR tube to suppress thermal convection at higher temperature. The diffusion coefficients reported were the average of x and y axes instead of z axis to minimize experimental errors caused by convective flow. The monomer diffusion coefficient was determined by the imidazolium proton peak at 8.0 ppm for both 1BDIMABr and 1BIDMATf<sub>2</sub>N.

## **8.4 Results and Discussion**

### **8.4.1 Synthesis of IL monomer**

We designed the PIL homopolymers discussed below as soft, conductive blocks for future studies on electro-responsive materials. Thus, a low glass transition temperature ( $T_g$ ) was an essential property in the design of the PILs in order to maintain some degree of polymer chain mobility at room temperature. A common strategy to achieve low  $T_g$  involves separation between charged moieties and polymer backbones. Lee *et al.*

demonstrated an approach to insert an ethylene oxide linker between an imidazolium ring and acrylate polymer backbone.<sup>21</sup> However, this method required multi-step synthesis and relatively harsh reaction conditions. Hence, we proposed a new scheme with a two-step synthesis (**Scheme 8.1**).



**Scheme 8.1** Synthesis of imidazolium-containing monomer with different counter-ions.

The monomers contained three major parts: A N-substituted imidazolium salt with four different counter-ions (Br, BF<sub>4</sub>, PF<sub>6</sub>, and Tf<sub>2</sub>N), polymerizable methacrylate groups, and long alkyl linkers between the imidazolium salts and methacrylate groups. A simple reflux reaction between 1-butylimidazole and 10-bromo-1-decanol was employed to yield the imidazolium salt 1BDIBr. The Br counter-ion of 1BDIBr was exchanged with various lithium salts to yield similar charged precursors with different counter-ions. Only the imidazolium salt with Br counter-ion was soluble in aqueous solution, therefore the ion exchange was performed in deionized water. As the reaction proceeded, imidazolium salts with BF<sub>4</sub>, PF<sub>6</sub>, and Tf<sub>2</sub>N counter-ions precipitated out of the aqueous solution. The resulting salts were washed with copious amounts of deionized water and dried at 50 °C

under vacuum.  $^1\text{H}$  and  $^{19}\text{F}$  NMR spectroscopy confirmed the successful synthesis of the four IL precursors and corresponding monomers (**Figure 8.1, S8.1, and S8.2**). As shown in **Figure 8.1**, proton *a* shifted from  $\delta$  9.2 (Br) to  $\delta$  8.5-8.4 ( $\text{BF}_4$ ,  $\text{PF}_6$ , and  $\text{Tf}_2\text{N}$ ) in  $^1\text{H}$  NMR spectroscopy suggesting complete ion exchange. Proton *b* also shifted due to resonance of the aromatic ring, but these shifts were less significant compared to proton *a*, due to the longer distance between the counter-ion and proton *b*. As expected,  $^{19}\text{F}$  NMR spectroscopy showed no fluorine peak for 1BDIBr, but had characteristic fluorine peaks for 1BDIBF<sub>4</sub>, 1BIDPF<sub>6</sub>, and 1BIDTf<sub>2</sub>N, further confirming successful ion exchange (**Figure S8.2**).

The polymerizable methacrylate units were introduced by a nucleophilic attack from the terminal alcohol of the IL to methacryloyl chloride. After the removal of solvent, MeCN, ethyl acetate (EA) extraction yielded the polymerizable IL monomers (1BDIMABr, 1BDIMABF<sub>4</sub>, 1BIDMAPF<sub>6</sub>, and 1BIDMATf<sub>2</sub>N), and  $^1\text{H}$  and  $^{19}\text{F}$  NMR spectroscopy confirmed their structures.

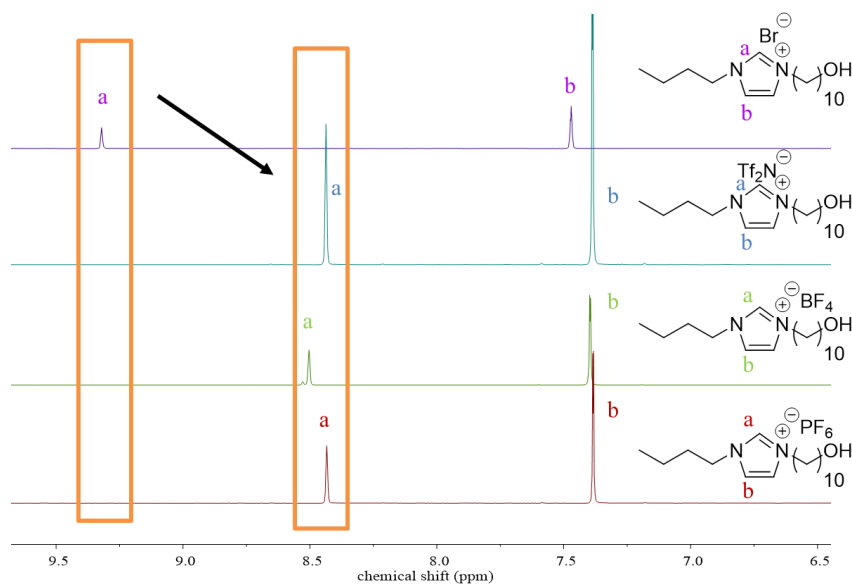
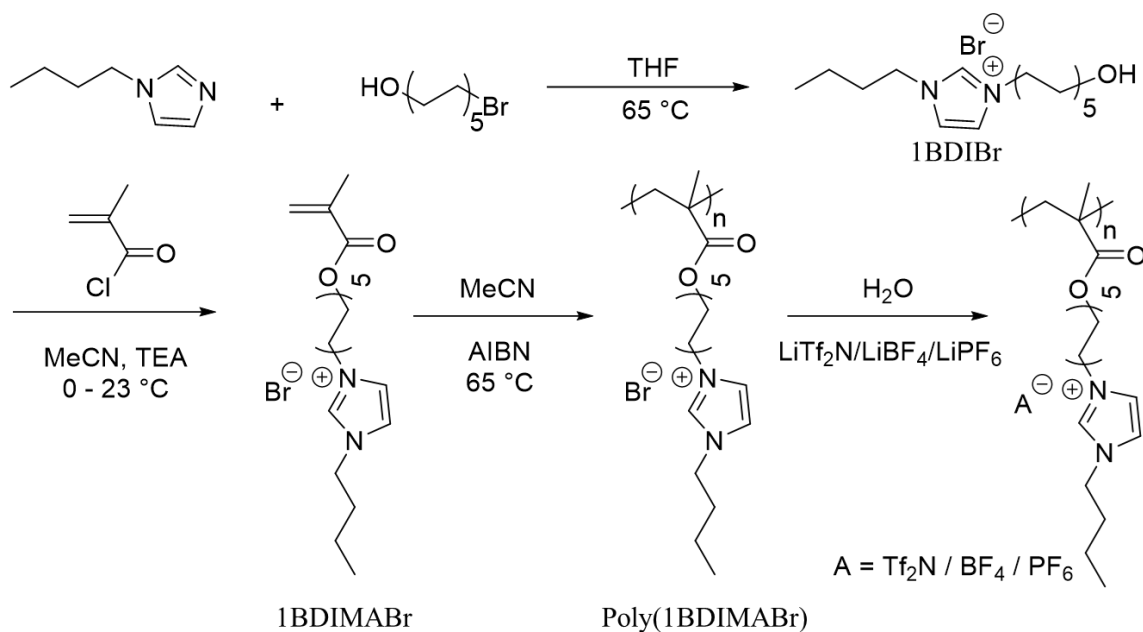


**Figure 8.1**  $^1\text{H}$  NMR of imidazolium-containing precursors (1BDIBr) demonstrated complete ion-exchange from Br anion to  $\text{Tf}_2\text{N}$ ,  $\text{BF}_4$  and  $\text{PF}_6$  anions (500 MHz).

### 8.4.2 Thermal properties and ion conductivity

The counter-ion effect on the physical properties of PILs is a well-known phenomenon.<sup>24,</sup>

<sup>39</sup> However, to compare the thermal properties and ion conductivity performance of PILs with four different counter-ions, the molecular weight should ideally be similar. Instead of pre-polymerization ion exchange, we applied a different synthetic strategy to eliminate any molecular weight differences from the discussion of thermal properties and ion conductivity (**Scheme 8.2**). The post-polymerization ion exchange approach is shown in Scheme 2 and results in identical polymer backbones for all four PILs.



**Scheme 8.2** Synthesis of poly(1BDIMABr) and post-polymerization ion-exchange.

For ionic polymers, the molecular weight characterization from SEC is difficult and not generally accurate due to strong Coulombic interactions. Nevertheless, we applied SEC to qualitatively compare the molecular weight and molecular weight distribution between samples without considering absolute values. Using SEC analysis the relative molecular weights of the two homopolymers with Br<sup>-</sup> counter-ions synthesized through

conventional free radical polymerization were determined to be 26.8 kg/mol (PDI = 2.9) and 32.1 kg/mol (PDI = 2.6) (Figure S3). The targeted number average molecular weights were 14 kg/mol and 40 kg/mol, respectively; however, due to the Columbic interactions, the molecular weight data appears skewed. Additionally, the absolute molecular weight could not be determined because no peaks were observed from the light scattering detector. After ion exchange, the effects of counter-ion on the physical properties for two sets of PILs with different molecular weights were examined (**Table 8.1**).

**Table 8.1** Thermal properties and conductivity of PIL homopolymers with different counter-ions.  $T_{d,5\%}$ ,  $T_g$  and  $\sigma_{dc}$  were determined by TGA, DSC, and BDS, respectively. Samples were dried in a vacuum oven at 120 °C overnight before the DSC and BDS tests.

	$T_{d,5\%}$ (°C)	$T_g$ (°C) 1 mol% [AIBN]	$T_g$ (°C) 3 mol% [AIBN]	$\sigma_{dc}$ (30 °C) (S/cm)	$\sigma_{dc}$ (80 °C) (S/cm)
Poly(1BDIMABr)	249	10	-3	$2.09 \times 10^{-7}$	$2.19 \times 10^{-5}$
Poly(1BDIMAPF <sub>6</sub> )	300	-8	-10	$1.32 \times 10^{-7}$	$2.57 \times 10^{-5}$
Poly(1BDIMABF <sub>4</sub> )	325	-30	-24	$9.77 \times 10^{-7}$	$6.61 \times 10^{-5}$
Poly(1BDIMATf <sub>2</sub> N)	372	-42	-39	$2.45 \times 10^{-5}$	$4.17 \times 10^{-4}$

TGA results (**Figure S8.4**) yielded 5 wt% degradation temperatures ( $T_{d,5\%}$ ) of 372, 325, 300, and 249 °C for poly(1BDIMATf<sub>2</sub>N), poly(1BDIMABF<sub>4</sub>), poly(1BDIMAPF<sub>6</sub>), and poly(1BDIMABr), respectively (**Table 8.1**). As expected, the less nucleophilic and less basic counter-ions had higher degradation temperatures.<sup>24, 40-42</sup> Only 1BDIMABr demonstrated an obvious water weight loss (~ 2 wt%) during the 120 °C isotherm step, as the other three ion pairs were hydrophobic. Since the water content had the potential to

affect thermal transition and ion conductivity data through plasticization, the preparation of DSC and conductivity samples went through an additional drying process at 120 °C under vacuum overnight.

DSC data shown in **Table 8.1** and **Figure S8.5** confirms the  $T_g$ s were dependent on the counter-ion and varied from 10 °C (1BDIMABr) to -42 °C (1BDIMATf<sub>2</sub>N), where larger counter-ion size facilitated long range segmental motion and led to weaker ion associations, resulting in a lower  $T_g$ .<sup>24, 40-45</sup> Previous works have attributed the counter-ion effect on  $T_g$  to size, where larger counter-ions (Tf<sub>2</sub>N) tended to plasticize the polymer matrices more than smaller, tightly-bound ions (Br), leading to a decrease in  $T_g$ .<sup>24</sup> When comparing PILs with the same counter-ions but different molecular weights, the  $T_g$  showed no significant variation. This result wasn't surprising when one considers the Flory-Fox equation since the molecular weight for both series of polymers was large enough (above 25 kg/mol) to exhibit any molecular weight dependence and only differ by approximately 5 kg/mol.<sup>46</sup>

The ion conductivity of PILs varied significantly depending on the counter-ions - especially at low temperatures (**Figure 8.2**). To determine the dc conductivity  $\sigma_{dc}$ , the measured dielectric spectra were presented in the form of complex conductivity:  $\sigma^* = \sigma' + i\sigma'' = i\omega\varepsilon_0\varepsilon^*$ , where  $\varepsilon^*$  is the complex permittivity and  $\varepsilon_0$  is the permittivity of vacuum.  $\sigma_{dc}$  was taken as the plateau value of  $\sigma'$ , before the effect of electrode polarization sets in at low frequencies.

At 30 °C, 1BDIMATf<sub>2</sub>N demonstrated superior conductivity compared to the other three PILs (**Figure 8.2** and **Table 8.1**). The high conductivity of 1BDIMATf<sub>2</sub>N at low temperatures was likely due to its low  $T_g$  and weaker ion associations, which facilitated

faster ion migration. Typical ILs and polymeric materials with low molecular weight IL additives reach conductivities as high as  $10^{-3}$  S/cm at room temperature but can suffer from leaching issues as the ILs are not covalently bonded to the polymeric matrices.<sup>2, 47</sup> However, PILs with no additives normally suffer from decreased conductivity. In this study, the conductivity of 1BDIMATf<sub>2</sub>N ( $2.45 \times 10^{-5}$  S/cm) approached the highest reported literature value ( $6.7 \times 10^{-5}$  S/cm) at room temperature for bulk PILs without any low molecular weight ILs and/or lithium salt additives.<sup>48</sup> Differences in conductivities due to counter-ion identity diminished with increasing temperature as thermal energy activated molecular motion, and thus reduced the molecular motion differences among PILs, leading to a convergence of conductivities. After normalizing the conductivity to  $T_g$  to account for mobility differences, the conductivity followed the order: 1BDIMABr ~ 1BDIMATf<sub>2</sub>N > 1BDIMAPF<sub>6</sub> ~ 1BDIMABF<sub>4</sub> (**Figure S8.6**). We attributed the remaining conductivity difference after normalization of mobility to the additional effects such as decoupling of segmental dynamics from the counter-ion dynamics.<sup>49-50</sup> This trend agrees well with PILs in which ionic groups are separated from the polymer backbone.<sup>21</sup> However, when ionic groups are closer to the polymer backbone, this trend may reverse.<sup>51</sup> Detailed BDS studies are planned to investigate the origin of these trend differences and their dependence on the spacing between ionic moiety and polymer backbone.

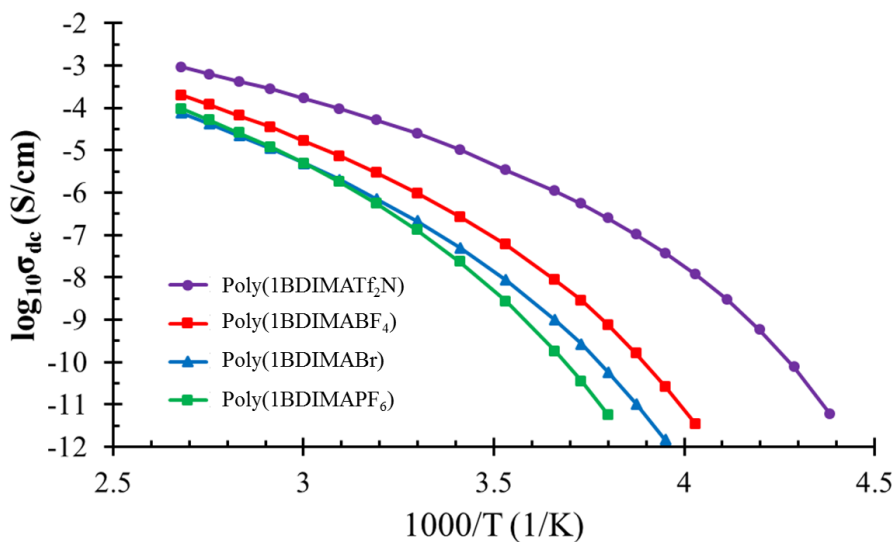


**Figure 8.2** Temperature dependent dc ionic conductivity of PIL homopolymers.

### 8.4.3 Polymerization kinetics of ILs

Post-polymerization ion exchange provided a facile approach to deconvolute the effect of counter-ion identity and molecular weight. However, ion exchange of polymers is challenging in some cases due to polymers' complicated solubility before and after ion exchange. A common synthetic approach to circumvent this challenge is to perform ion exchange before polymerization. During the process of synthesizing the 1BDIMA ionic-liquid blocks, it was noticed that the counter-ion identity significantly influenced the polymerization kinetics. During RAFT polymerization, 1BDIMATf<sub>2</sub>N failed to polymerize after 24 h even when aggressive conditions were employed (CTA/I (chain transfer agent/initiator) = 1, [IBDIMA] = 2M), while 1BDIMABr was able to reach a reasonable monomer conversion. *In situ* FTIR was used to provide insight into the differences in radical polymerization kinetics resulting from the use of different counter-ion species. The kinetic study of both conventional free radical polymerization and reversible addition-fragmentation chain-transfer polymerization (RAFT) covered a wide

range of polymerization rates. As conventional free radical polymerization is fast and uncontrolled, the kinetic differences due to counter-ion identity were expected to be subtle. As a controlled radical polymerization technique, RAFT polymerization was expected to slow down the polymerization rate enough to observe kinetic differences due to counter-ion identity.

We observed no significant kinetic differences during the conventional free radical polymerization of the imidazolium-containing monomer with different counter-ions even at low initiator concentrations. Figure 3a depicts representative spectra of experiments that were repeated at least two times. For the conventional free radical polymerization of IL monomers at 3 mol% initiator concentration, the kinetic differences were negligible (**Figure S8.7**). The time required for each monomer to reach half its initial concentration ( $t_{1/2}$ ) had a maximum difference of 1 h. However, the relative error in the  $t_{1/2}$  determination was 0.5 h, indicating that the free radical polymerization kinetics did not exhibit a significant difference in polymerization kinetics. It is possible that the fast and uncontrolled nature of free radical polymerization diminished the kinetic differences that might arise from counter-ion identity, and thus, another series of free radical polymerizations with lower initiator concentrations (1 mol%) was conducted in order to slow down the polymerization kinetics. As shown in **Figure 8.3a & 8.3b**, 1BDIMAPF<sub>6</sub> and 1BDIMABF<sub>4</sub> exhibit the fastest propagation rates, followed by 1BDIMATf<sub>2</sub>N, while 1BDIMABr was the slowest. A typical *in situ* FTIR waterfall spectrum and plot of the normalized IR intensity as a function of time are shown in Figure 3a. Figure 3b demonstrated the change of monomer concentration over time assuming a direct proportional relationship between normalized intensity and monomer concentration. The

normalized intensity (proportional to monomers left in solution) was calculated as the ratio of the integral for the peak area between 1289 - 1308  $\text{cm}^{-1}$  at time  $t$ , and at time  $t_0 = 5$  min (after the temperature stabilized at 65  $^{\circ}\text{C}$ )  $[M]_0$  and  $[M]$ , which represents the monomer concentration at time  $t_0 = 5$  min and time  $t$ , were calculated from the integral between 1289 - 1308  $\text{cm}^{-1}$  at time  $t_0 = 5$  min and time  $t$ , respectively. The largest  $t_{1/2}$  difference for these experiments was 1.7 h - 1BDIMAPF<sub>6</sub> to 1BDIMABr. While these results were promising, the differences due to counter-ion identity were still within the relative error of the experiment. Comparing PILs synthesized from pre-polymerization and post-polymerization ion exchanges, their  $T_g$  and ion conductivities showed no statistical difference.

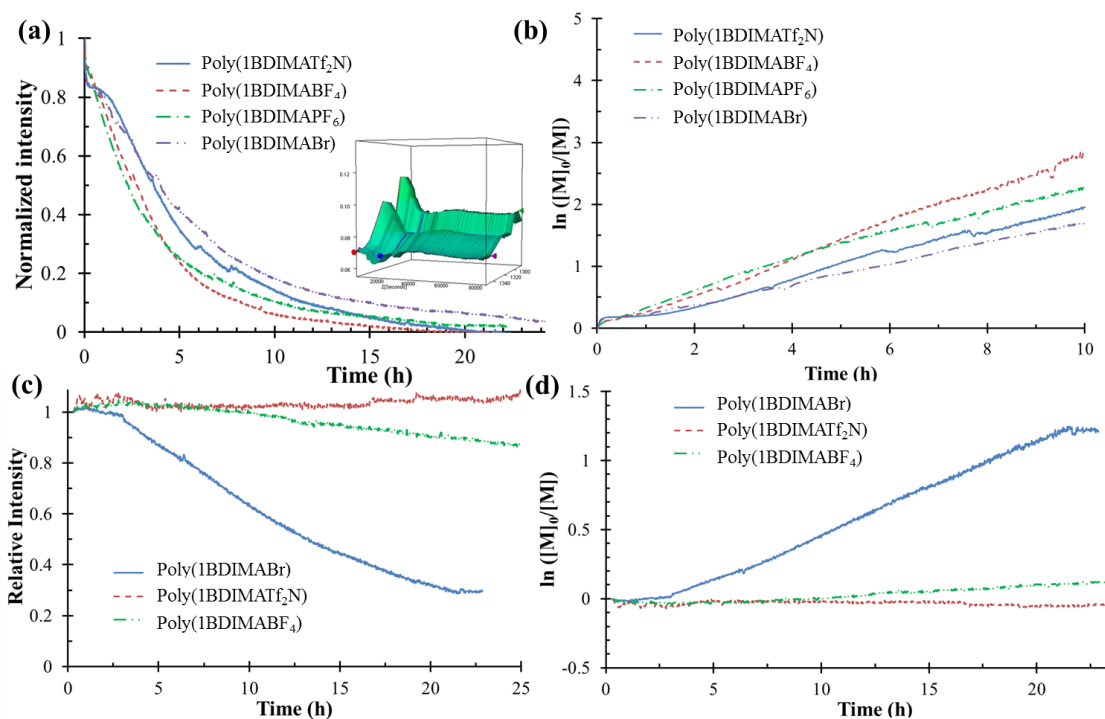


**Figure 8.3** Polymerization kinetics through *in situ* FTIR: (a) & (b) Free radical polymerization of IL monomer that shows similar polymerization kinetics. *In situ* FTIR: Matrix-MF, [1BDIMA] = 0.5 M, AIBN = 1 mol%, T = 65  $^{\circ}\text{C}$ , MeCN, 1289 - 1308  $\text{cm}^{-1}$ ; (c) & (d) RAFT polymerization of IL monomers that show obvious differences in polymerization kinetics. *In situ* FTIR: Matrix-MF, [1BDIMA] = 1 M, [CTA]/[I] = 3, T = 65  $^{\circ}\text{C}$ , MeCN, 1289 - 1308  $\text{cm}^{-1}$ .

To circumvent the fast and uncontrolled nature of free radical polymerization, RAFT polymerization was employed. These studies showed significant kinetic differences based on the counter-ions (**Figure 8.3c & 8.3d**). The CTA/I ratio and monomer concentration were set to be 3 and 1 M, respectively, to guarantee a reasonable amount of monomer conversion in 24 h. 1BDIMATf<sub>2</sub>N exhibited no obvious polymerization after 24 h, while 1BDIMABr reached 70% monomer conversion in 20 h. 1BDIMABF<sub>4</sub> monomer conversion was apparent, but much slower than 1BDIMABr, and 1BDIMAPF<sub>6</sub> failed to produce meaningful results due to reproducibility issues. Both 1BDIMABr and 1BDIMABF<sub>4</sub> demonstrated pseudo-first order kinetics as a characteristic behavior in CRPs. To promote the polymerization of 1BDIMATf<sub>2</sub>N, the RAFT polymerization was performed at elevated temperature (75 °C). However, as depicted in Figure S7, only a small amount of monomer was consumed (< 5%). Due to the boiling point of MeCN (82 °C), a further increase in temperature was not feasible. Even when a polymeric 1BDIMATf<sub>2</sub>N CTA (macroCTA) was employed, no monomer conversion was observed, indicating that the lack of polymerization could not be attributed solely to induction. Hence, we opted to switch to DMF as the polymerization media due to its similar polarity and higher boiling point (152 °C). Variation of the CTA/I ratio caused either slow polymerization (less than 20% monomer conversion in DMF after 48 h when CTA/I changed to 5) or introduced difficulties in

reproducibility.

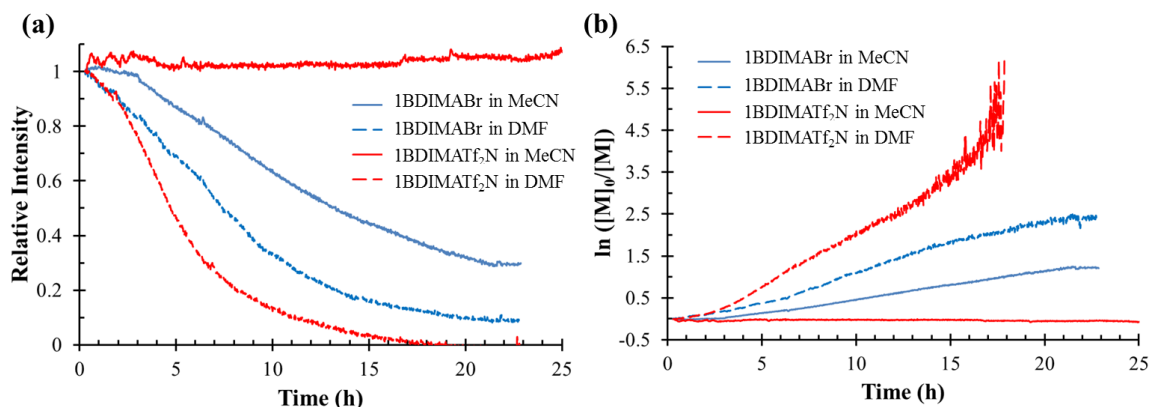


**Figure 8.4** DMF accelerated RAFT polymerization of 1BDIMABr and 1BDIMATf<sub>2</sub>N compared to MeCN as solvent. *In situ* FTIR: [M] = 1 M, [CTA]/[I] = 3, T = 65 °C, 1289 - 1308 cm<sup>-1</sup>.

Surprisingly, 1BDIMATf<sub>2</sub>N not only polymerized in DMF at 65 °C but was faster than 1BDIMABr in MeCN and DMF. The *in situ* FTIR experiments for 1BDIMABr and 1BDIMATf<sub>2</sub>N in DMF and MeCN are shown in **Figure 8.4a** & **8.4b**. While 1BDIMATf<sub>2</sub>N does not polymerize in MeCN, it reaches 100% monomer conversion in 17 h in DMF. The use of DMF also resulted in a rate increase for 1BDIMABr compared to MeCN. Biela and coworkers' saw a similar trend for the polymerization of caprolactone and concluded that the kinetic differences were a result of the propagating chains aggregating and hindering propagation.<sup>52</sup> The RAFT polymerizations showed pseudo-first order kinetics (**Figure 8.4b**); however, the polymerization of 1BDIMATf<sub>2</sub>N in DMF deviated slightly at high monomer conversion. The faster polymerization rates in DMF also led to a higher degree of monomer conversion before the reaction plateaued. Efforts to find additional polymerization solvents were not successful as only DMF, MeCN and DMSO were determined to be universal solvents that would dissolve both

monomers and polymers. Because DMSO is very similar to DMF in terms of polarity and polarizability, additional polymerizations in DMSO were not performed.<sup>53</sup>

Initially, it was suspected that the observed kinetic differences were related to Columbic interactions in the system impacting 1) the diffusion rate of monomers and/or 2) monomer aggregation hindering polymerization/propagation. <sup>1</sup>H NMR diffusometry was used to probe the solvent and counter-ion effects on the diffusive behavior of ionic-liquid monomers (**Figure 8.5**) and to determine if monomer aggregation was occurring. To mimic the RAFT polymerization conditions, the monomer concentration and temperature were set to 1 M and 62 °C. The monomer diffusion for both 1BDIMA-Br and 1BDIMA-Tf<sub>2</sub>N in MeCN was more than twice as fast compared to DMF due to MeCN's lower viscosity (0.343 mPa·s, 25 °C for MeCN, and 0.802 mPa·s, 25 °C for DMF). Additionally, the monomers with Tf<sub>2</sub>N counter-ions diffused faster than monomers with Br counter-ions in both solvents. The faster diffusion was attributed to the weak interactions between imidazolium and Tf<sub>2</sub>N, resulting from the delocalization of negative charge on Tf<sub>2</sub>N. Notably, the ionic monomers with Tf<sub>2</sub>N in MeCN diffuse at the fastest rate; however, the *in situ* FTIR results showed no monomer conversion taking place (**Figure 8.4**), suggesting that the RAFT polymerization rate of ionic-liquid monomers is not simply diffusion-controlled.

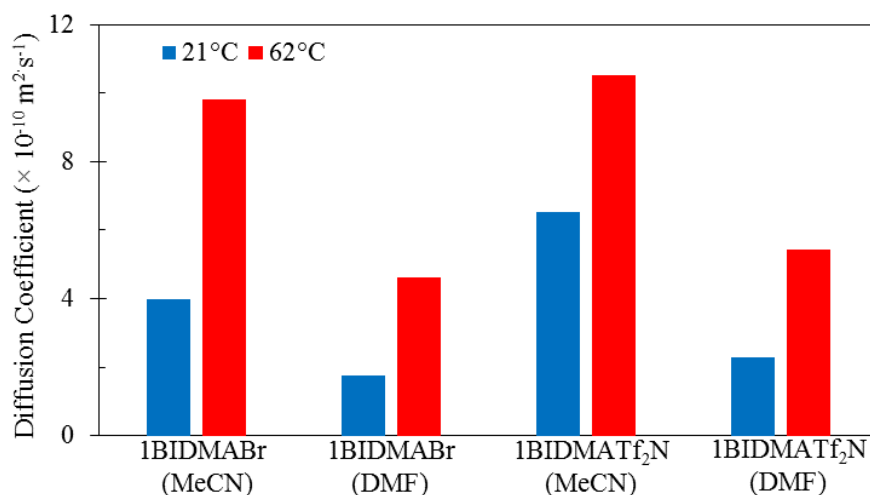


**Figure 8.5** Diffusion coefficients of IL monomers with different counter-anions and in different solvents. NMR diffusometry measurements were done at 21 °C and 62 °C, respectively. Errors in  $D$  values are  $\pm 5$  %.

Eliminating differences in monomer diffusion as the underlying cause of the polymerization rate differences, we then investigated the monomer aggregation behavior in solution. The Stokes-Einstein equation (Equation 2)<sup>54-55</sup> was used to assess how counter-ion and solvent affected the relative sizes of the monomers:

$$D = \frac{kT}{c\eta R_h} \quad (2)$$

where  $D$  is the diffusion coefficient,  $k$  is the Boltzmann constant,  $T$  is the temperature,  $\eta$  is the solution viscosity,  $R_h$  is the hydrodynamic radius of a diffusing species, and  $c$  is a correction factor ( $2\pi - 6\pi$ ). It is well known that the Stokes-Einstein equation shows non-ideal behavior for charged species.<sup>23, 56-59</sup> However, the Stokes-Einstein equation was still employed to provide a qualitative comparison. A small difference in the effective  $R_h$  of the monomer as a function of counter-ion was observed, but no large self-assembled aggregates were detected under the measured conditions (**Table 8.2**). The calculated monomer sizes were all approximately 1 nm, which is roughly the hydrodynamic size of a typical monomer. This indicates a lack of monomer aggregation in the samples and

excludes aggregate formation as a major factor in the kinetic differences seen in the 1BDIMA monomer studies presented here. Dynamic light scattering studies revealed similar hydrodynamic sizes in dilute conditions (10 mg/ml). However, the polymerization concentration (1M) exceeded the limit of DLS, and so it is difficult to draw meaningful conclusions from this data. Future studies will include Raman spectroscopy and wide angle X-ray scattering (WAXS) to further substantiate the conclusions from NMR diffusometry. Additionally, in situ NMR diffusometry can be used to elucidate size and diffusion coefficient changes during polymerization.

**Table 8.2** Diffusion coefficients of solvents and sizes of monomers in different solutions at 62 °C.

	<b>1BIDMABr</b> (MeCN)	<b>1BIDMABr</b> (DMF)	<b>1BIDMATf<sub>2</sub>N</b> (MeCN)	<b>1BIDMATf<sub>2</sub>N</b> (DMF)
$D_{\text{solvent}}$ (m <sup>2</sup> .s <sup>-1</sup> )	$4.57 \times 10^{-9}$	$1.94 \times 10^{-9}$	$4.44 \times 10^{-9}$	$1.87 \times 10^{-9}$
$2R_{\text{h monomer}}$ (nm)	1.15	1.18	1.05	0.97

Note:  $R_{\text{h monomer}} = D_{\text{solvent}} \times R_{\text{h solvent}} / D_{\text{monomer}}$  based on Equation 2 ( $D_{\text{solvent}}$  and  $D_{\text{monomer}}$  were experimentally determined using diffusion NMR by following the proton peaks at 1.9 ppm (MeCN), 2.8 ppm (DMF) and 8.0 ppm (monomers) associated with the solvent and monomer). A hydrodynamic diameter of 1.2 Å for MeCN and 1.4 Å for DMF were used in the calculations.

NMR experiments showed that variations in neither monomer diffusion coefficients nor aggregation could adequately explain the observed differences in polymerization rates. This led us to propose that electron transfer differences originating from solvent and counter-ion choice, as described in theoretical work by Marcus, could provide a reasonable explanation for the kinetic differences.<sup>32-35</sup> Marcus discusses the influence of solvent on the rate of electron transfer, leading to changes in reaction rates. In our free radical polymerization study, monomers with all four counter-ions polymerized readily in MeCN. Hence the electron transfer to initiator (to form active radicals) and the electron transfer between propagating radicals and monomers (propagation) proceeded as expected for an uncontrolled free radical process. However, in RAFT polymerization, radicals are in a dormant state for the majority of the time, causing a competition between electron transfer from active radicals to either monomers (propagation) or to CTAs (back to dormant state). Based on our observed *in situ* FTIR data, 1BDIMATf<sub>2</sub>N in MeCN apparently has a much slower electron transfer rate from active radicals to monomers compared to the electron transfer rate from active radicals to CTAs, resulting in an equilibrium between active radicals and dormant states with negligible monomer insertion. Calculations based on Marcus theory are explained in the supporting information suggest that polymerization rates in DMF and MeCN could differ by several orders of magnitude, depending on the radii of reacting species and the distance between an electron donor and acceptor (**Figure S8.9**). Although the time scale for electron transfer processes calculated from Marcus theory is in picoseconds, it would still have a significant impact on the polymerization if the active radicals strongly favored

recombination with CTA, which would result in little to no monomer insertion for 1BDIMATf<sub>2</sub>N in MeCN.

Marcus theory explains the effects of solvent polarity on the rate of electron transfer from an electron donor to an acceptor. The solvent polarity appears via its high frequency dielectric response, which is related to its refractive index. It should be noted that DMF is a more polarizable solvent than MeCN based on their refractive indices (1.34 for MeCN, 1.43 for DMF at T= 20° C),<sup>53</sup> and in DMF the electron transfer from active radicals to monomers would be accelerated, making it comparable to the electron transfer rate between active radicals and CTAs, which would lead to propagation. Furthermore, the degree of ionization of monomers tends to have a significant effect on their polymerization. For example, it has been reported that increasing the degree of ionization can lead to an order of magnitude enhancement in the rate of free radical polymerization for methacrylic acid (MAA).<sup>60</sup> Similarly, Tf<sub>2</sub>N counter-ions are more polarizable than Br counter-ions due to their larger size and the polymers bearing Tf<sub>2</sub>N counter-ions would have a larger degree of ionization (cation-anion dissociation) in the same solvent. Thus, the difference in polymerization kinetics for 1BDIMATf<sub>2</sub>N in MeCN versus DMF is more dramatic than for 1BDIMABr. To better understand the impact of electron transfer processes on the polymerization kinetics of 1BDIMA, additional experiments including cyclic voltammetry (CV) studies are currently under development.<sup>34</sup>

## 8.5 Conclusion

This work demonstrates the successful synthesis of four novel PILs through two different approaches: pre- and post-polymerization ion-exchange. The thermal degradation and

glass transition temperature of 1BDIMA homopolymers was shown to be strongly dependent on the choice of counter-ion. Notably, 1BDIMATf<sub>2</sub>N has a conductivity of  $2.45 \times 10^{-5} \text{ S cm}^{-1}$  at room temperature and a  $T_g$  of  $-42 \text{ }^\circ\text{C}$ . The conductivity differences due to counter-ions decreased with increasing temperature as thermal energy facilitated molecular motion and diminished the mobility differences due to counter-ion size. These conductivity measurements establish a foundation for further electro-responsive studies of block copolymers containing these PILs as the soft, conducting segments.

*In situ* FTIR showed that the influence of counter-ions on polymerization kinetics was insignificant in conventional free radical polymerization, but showed an obvious dependence on counter-ion identity for RAFT polymerizations. To our knowledge, this is the first report of a counter-ion effect on controlled radical polymerization rates. *In situ* FTIR measurements in DMF had faster polymerization rates compared to MeCN. NMR diffusometry ruled out monomer diffusion and/or aggregation as major contributors to the differences in polymerization kinetics. A possible explanation lies in Marcus theory, where the influence of solvent and counter-ions on the electron transfer process may be critical for polymerization, especially in a controlled process like RAFT. Future experiments are under development to better elucidate the differences in polymerization kinetics for these systems.

This work extends efforts to investigate the impact counter-ions have on the physical properties of polymerized ionic liquid based materials. Conductivity results suggest 1BDIMA-based polymers could have a role in various energy-related applications, such as transducers, barrier membranes, and batteries. The  $T_g$  and hydrophilicity of poly(1BDIMA) is tunable through post-polymerization counter-ion exchange. While

more experiments are necessary in order to understand the delicate nature of how counter-ions and solvents influence the controlled radical polymerization kinetics of ionic monomers, this work helps guide future research into this relatively unexplored area.

## 8.6 Acknowledgments

The authors would like to thank, Dr. Balaka Barkakaty and Dr. Peter V. Bonnesen, in CNMS ORNL for synthesis discussion and instrumental assistance. This research was sponsored by the Laboratory Directed Research and Development Program of Oak Ridge National Laboratory, managed by UT-Battelle, LLC, for the U. S. Department of Energy. A portion of this research was conducted at the Center for Nanophase Materials Sciences, which is a DOE Office of Science User Facility. This work was also partially supported by the US National Science Foundation under award number DMR 1507764 (X.L. and L.A.M.).

## 8.7 Supporting information

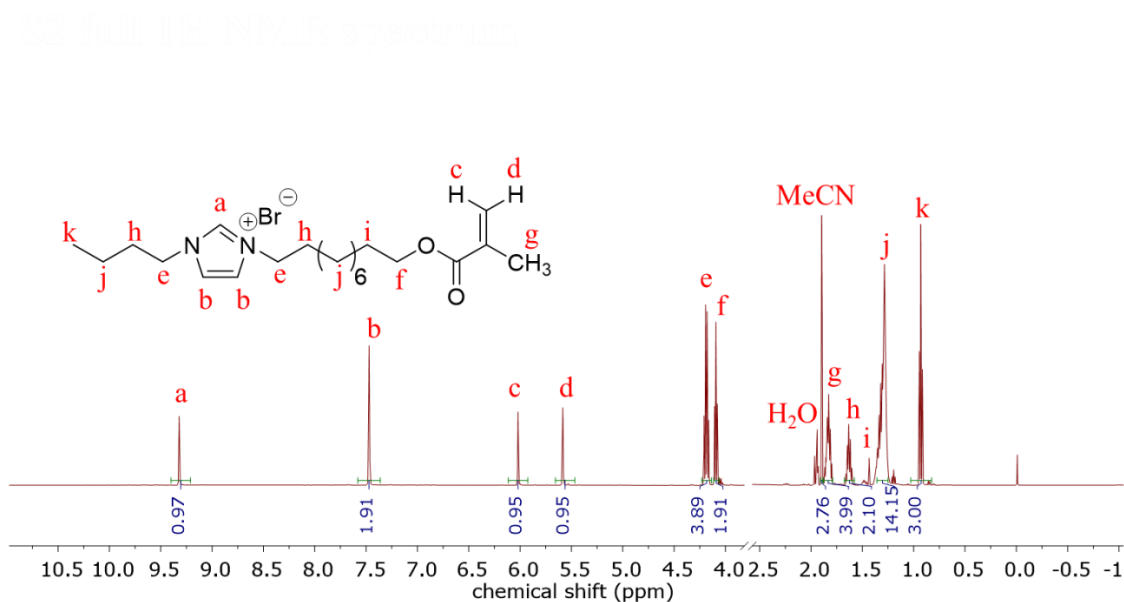


**Figure S8.1** Full <sup>1</sup>H NMR spectrum of 1BDIMABr (500 MHz).

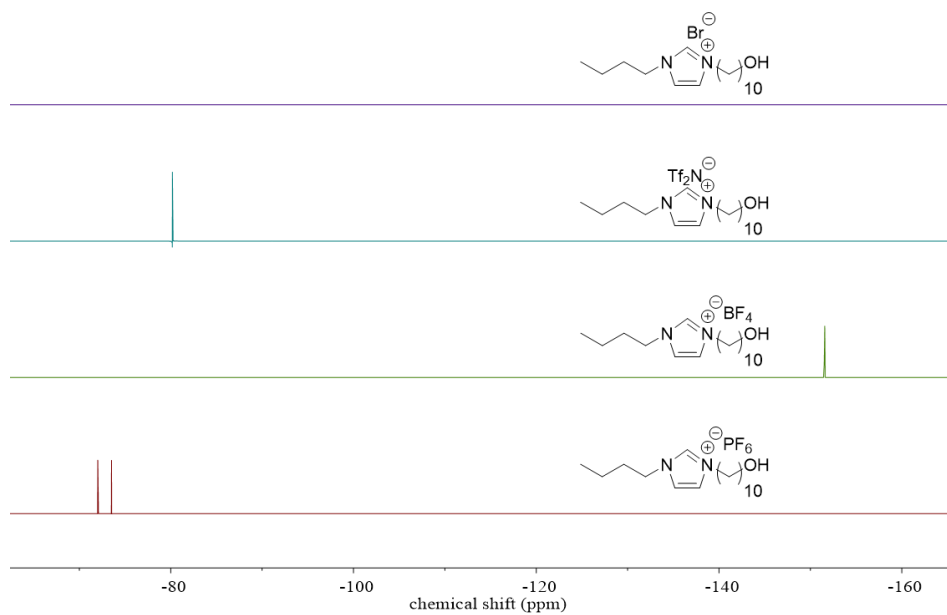


**Figure S8.2**  $^{19}\text{F}$  NMR spectra of the four IL precursors (470 MHz).

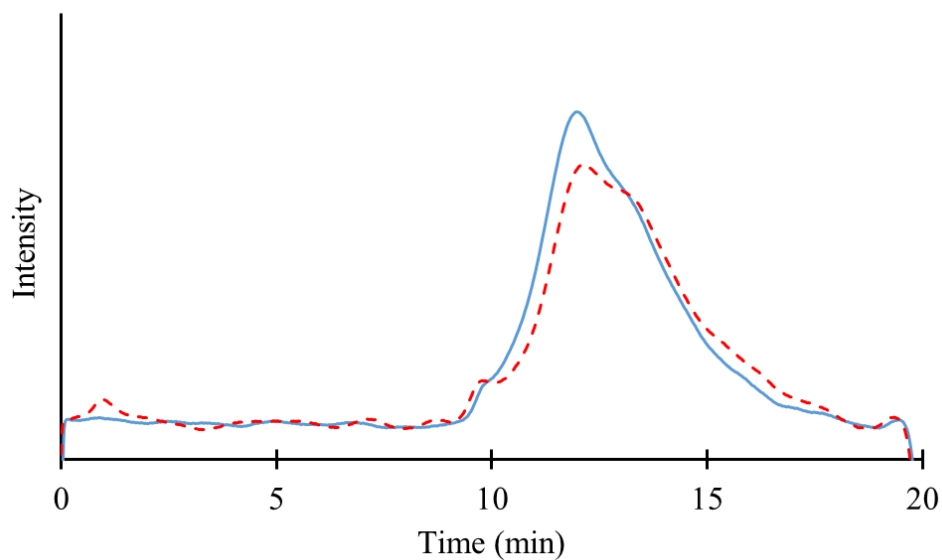


**Figure S8.3** SEC trace (dRI) of poly(1BIDMABr) homopolymers in DMF + 0.05 M LiBr. Blue solid line: 3 mol% AIBN; Red dash line: 1 mol% AIBN.

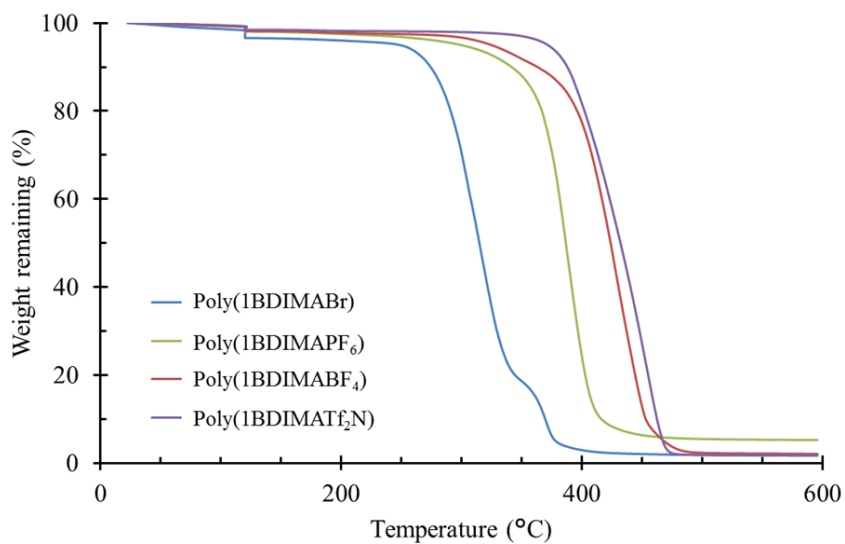


**Figure S8.4** Thermal degradation of PIL homopolymers. TGA: 10 °C/min heating rate, N<sub>2</sub>, isotherm at 120 °C for 30 min.

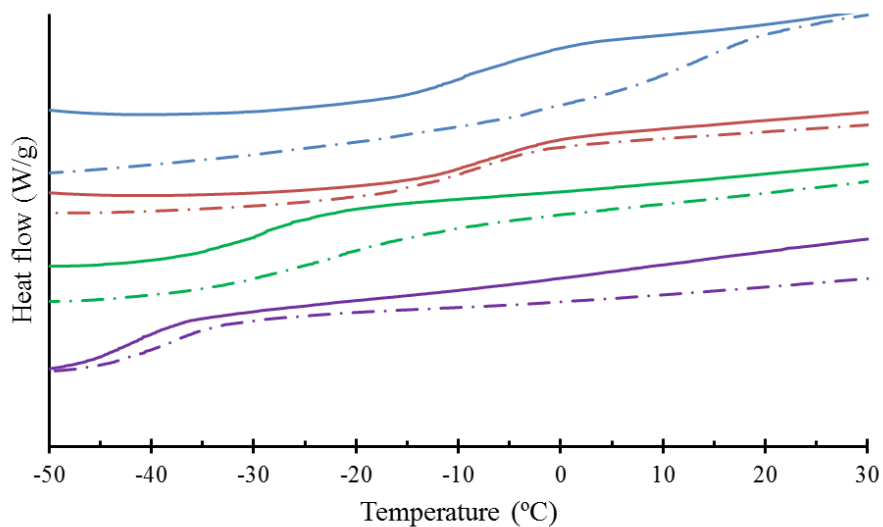


**Figure S8.5** T<sub>g</sub>s of PILs with different counter-ions. Solid line: 32.1 kg/mol (SEC, relative molecular weight); Dash line: 26.8 kg/mol (SEC, relative molecular weight). Blue: 1BDIMABr; Red: 1BDIMAPF<sub>6</sub>; Green: 1BDIMABF<sub>4</sub>; Purple: 1BDIMATf<sub>2</sub>N. Exo down.

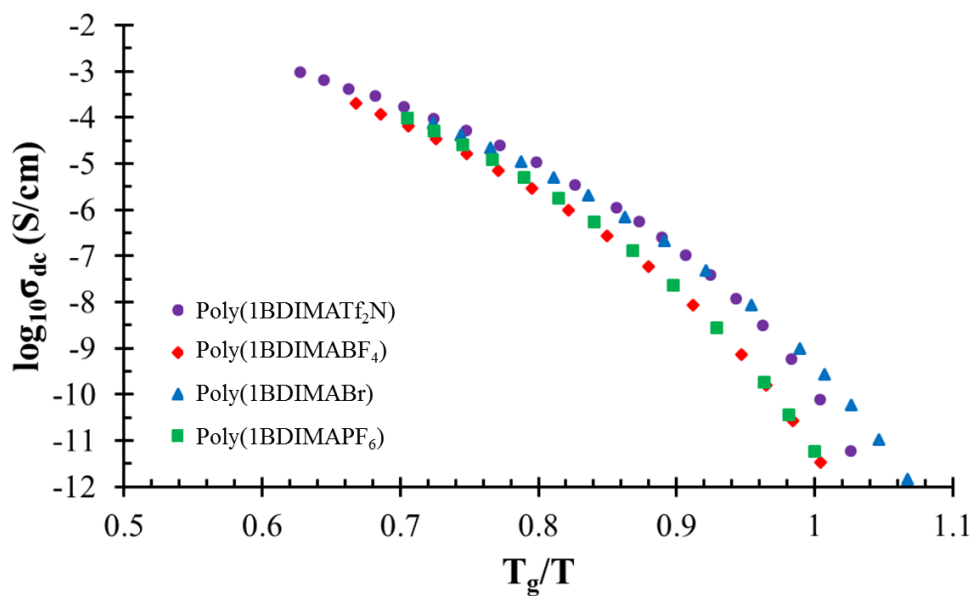


**Figure S8.6** Conductivities of PIL homopolymers at similar chain mobility.

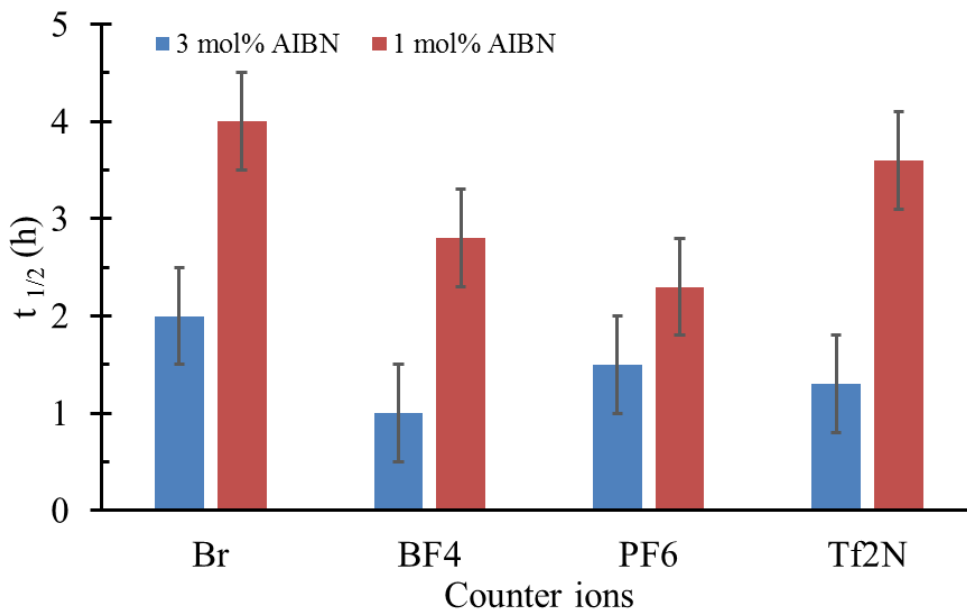


**Figure S8.7** Free radical polymerization showed similar kinetics regardless of the counter-ion species. Definition of  $t_{1/2}$ : Time for the system to consume half of the initial monomers (50% of initial monomer intensity in *in situ* FTIR). *In situ* FTIR: [IBDIMA] = 0.5 M.

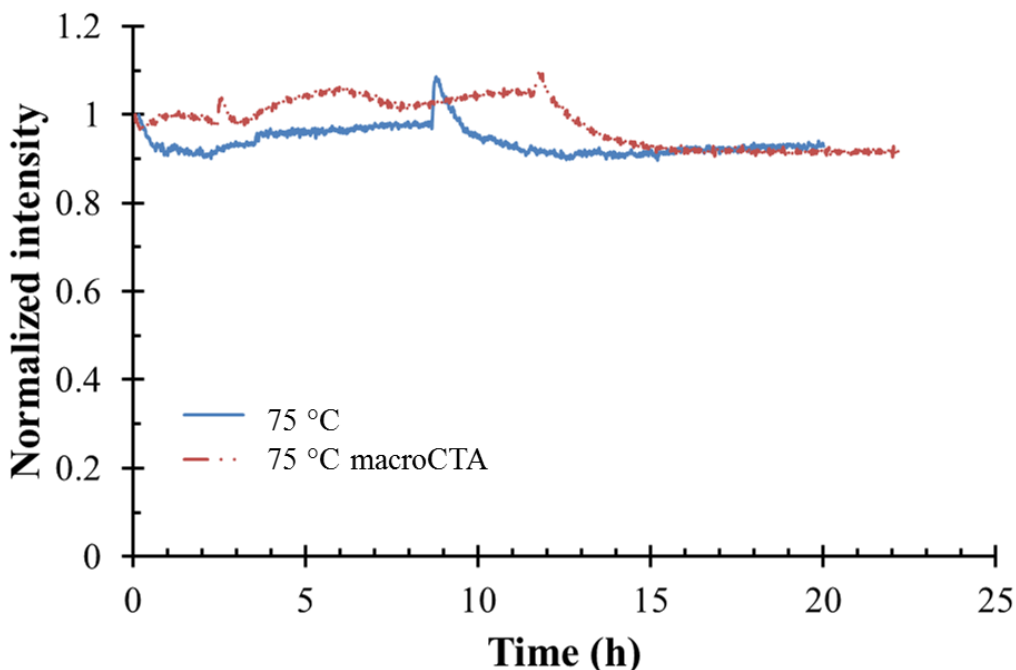


**Figure S8.8** *In situ* FTIR at 75 °C exhibited no monomer conversion during RAFT polymerization. *In situ* FTIR: [CTA]/[I] = 3, [M] = 1M. MacroCTA: poly(IBDIMATf2N) macro CTA.

#### **Electron Transfer Rates in Ionic Fluids and Figure S8.9:**

The rate of electron transfer<sup>61-63</sup> (i.e., number of electron transfers per unit time) in solutions can be estimated by assuming that it is a two-step process.<sup>64-65</sup> In the first step, the electron donor and the acceptor has to approach each other within a certain distance range. In the second step, bimolecular electron transfer takes place within a range of separation distances. The net rate of electron transfer can be obtained by integrating over the distribution of separation distances among the donors and the acceptors. The standard procedure<sup>64-65</sup> is to fix one reactant of a given size (either the donor or the acceptor) at the origin and then find the number density of the other type of reactants ( $c(r)$ ) as a function of radial distance ( $r$ ) from the origin. If  $k_{el}(r)$  is the rate of electron transfer at that radial distance then the number of electron transfers occurring per unit time can be written as

$$\begin{aligned}
 k &= 4\pi \int_0^{\infty} dr r^2 c(r) k_{el}(r) \\
 &= 4\pi \int_0^{\infty} dr r^2 c_o \exp[-w(r)] k_{el}(r)
 \end{aligned}
 \tag{1}$$

where we have introduced  $w(r)$  as the work required or the energy barrier to bring the reactants to a separation distance  $r$  and  $c_o$  is the concentration far from the reactant centered at the origin.

If the electron transfer processes are occurring predominately at  $r = \bar{r}$  in a range  $\delta r$  then

$$\begin{aligned}
 k &\cong 4\pi \delta r \bar{r}^2 c_o \exp[-w(\bar{r})] k_{el}(\bar{r}) \\
 &= n_{complex}(\bar{r}) k_{el}(\bar{r})
 \end{aligned}
 \tag{2}$$

where we have defined  $n_{complex}(\bar{r})$  as number of the so-called “complexes” of two reactants (electron donor and acceptor) at a distance ( $\bar{r}$ ) from the reactant centered at the origin. It is to be noted that  $w(\bar{r})$  depends on the size of the reactants, degree of ionization, solvent properties etc. Various approximate expressions for  $w(\bar{r})$  can be taken from the literature.<sup>4-5</sup> Physically, Eq. 2 means that the rate constant for an electron transfer depends on number of complexes/precursors and the rate of electron transfer when the donor and the acceptor are located at  $\bar{r}$  with a separation distance of  $\delta r$

Marcus derived an expression for the rate of electron transfer[1-3], which reads as

$$k_{el}(\bar{r}) = \frac{|V|^2 \sqrt{\pi}}{h \sqrt{\lambda kT}} \exp \left[ -\frac{\lambda(\bar{r})}{4kT} \left( 1 + \frac{\Delta G}{\lambda(\bar{r})} \right)^2 \right]
 \tag{4}$$

so that  $h$  is the Planck's constant,  $\lambda$  is the reorganization energy, given by

$$\lambda(\bar{r}) = \frac{e^2}{2} \left[ \frac{1}{r_d} + \frac{1}{r_a} + \frac{1}{\bar{r}} \right] \left[ \frac{1}{\epsilon(\infty)} - \frac{1}{\epsilon(o)} \right]
 \tag{5}$$

and  $\Delta G = E_{acceptor} - E_{donor}$  is the change in the energy of an electron of charge  $e$  in going from a donor to an acceptor. Also,  $|V|$  is the magnitude of the interaction energy, which characterizes tunneling of electron between the two states, in going from a donor to an acceptor.  $r_d$  and  $r_a$  are the radii of the donor and the acceptor, respectively, involved in the electron transfer process.  $\varepsilon(\infty)$  and  $\varepsilon(0)$  are the high frequency and the low frequency dielectric of the solvent, respectively. High frequency response of the solvent is related to its optical properties and in particular,  $\varepsilon(\infty) = n^2$ ,  $n$  being the refractive index. Low frequency response of the solvent characterizes the static dielectric constant of the solvent.  $k$  and  $T$  are the Boltzmann constant and the temperature, respectively. For dimethyl formamide (DMF) and acetonitrile (MeCN), ratio of the rates of the electro transfer as functions of  $\Delta G/kT$  and  $\frac{1}{r_d} + \frac{1}{r_a} - \frac{2}{r}$  are plotted in Figure S8 at  $T=293\text{K}$ .

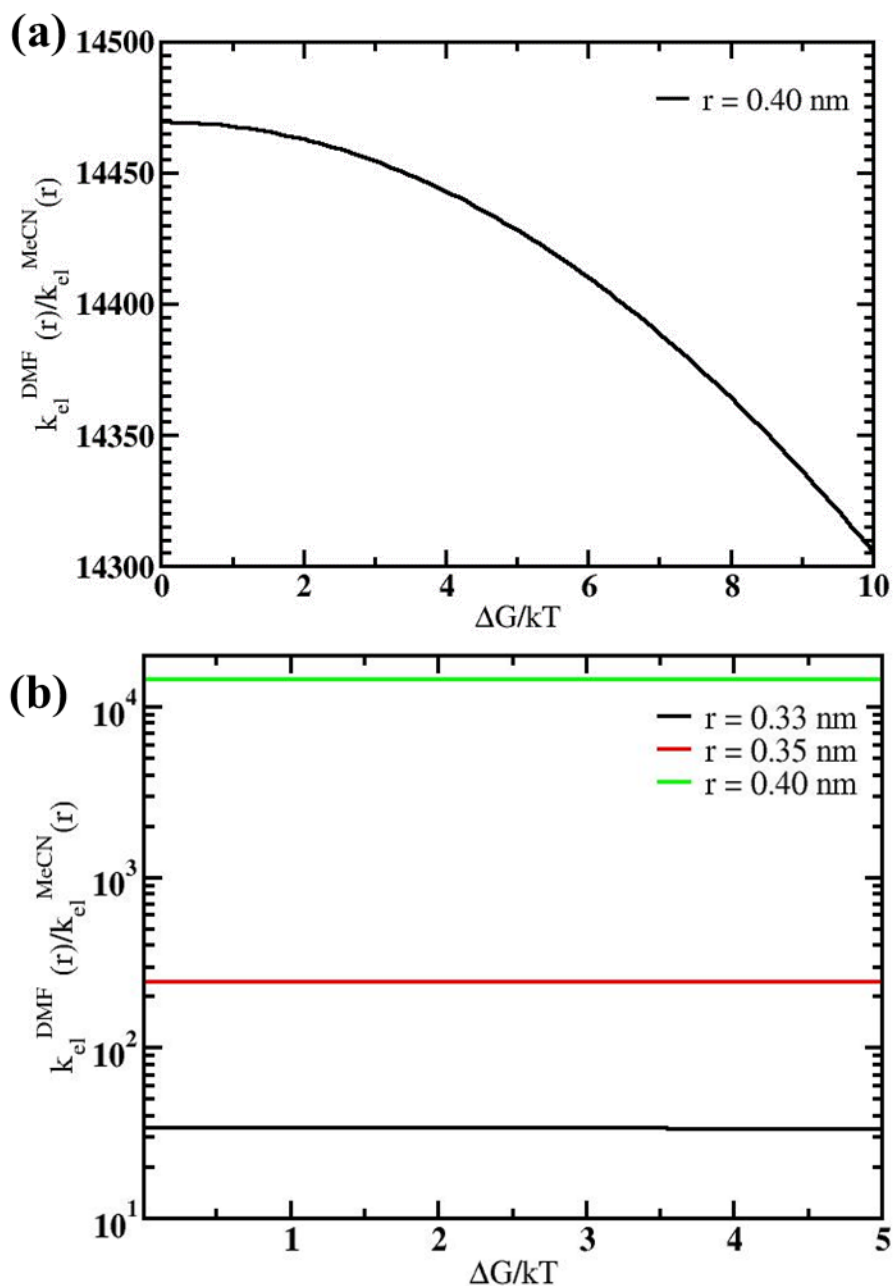


**Figure S8.9**  $k_{el}^{DMF}(\bar{r})/k_{el}^{MeCN}(\bar{r})$  obtained using Eq. 4 for the electron transfer occurring in DMF and MeCN.  $n_{DMF} = 1.43$ ,  $n_{MeCN} = 1.34$ ,  $T = 293K$ ,  $\epsilon_{DMF}(0) = \epsilon_{MeCN} = 37$ ,  $r_a = r_d = 0.3nm$  were used. The top panel shows the ratio for  $r \equiv \bar{r} = 0.4 nm$  and the bottom panel shows the ratio for various values of  $r$  on a semi-logarithmic plot to highlight changes in the ratio by

orders of magnitude.

## 8.8 References

1. He, Y. Y.; Li, Z. B.; Simone, P.; Lodge, T. P., Self-assembly of block copolymer micelles in an ionic liquid *J. Am. Chem. Soc.* **2006**, *128*, 2745-2750.
2. Lee, J.; Panzer, M. J.; He, Y. Y.; Lodge, T. P.; Frisbie, C. D., Ion gel gated polymer thin-film transistors *J. Am. Chem. Soc.* **2007**, *129*, 4532-4533.
3. Wasserscheid, P.; Keim, W., Ionic liquids - New "solutions" for transition metal catalysis *Angew. Chem. Int. Ed* **2000**, *39*, 3772-3789.
4. Schultz, A. R.; Lambert, P. M.; Chartrain, N. A.; Ruohoniemi, D. M.; Zhang, Z. Y.; Jangu, C.; Zhang, M.; Williams, C. B.; Long, T. E., 3D Printing Phosphonium Ionic Liquid Networks with Mask Projection Microstereolithography *ACS Macro Lett.* **2014**, *3*, 1205-1209.
5. Jangu, C.; Wang, J. H. H.; Wang, D.; Sharick, S.; Heflin, J. R.; Winey, K. I.; Colby, R. H.; Long, T. E., Well-Defined Imidazolium ABA Triblock Copolymers as Ionic-Liquid-Containing Electroactive Membranes *Macromol. Chem. Phys.* **2014**, *215*, 1319-1331.
6. Margaretta, E.; Fahs, G. B.; Inglefield, D. L.; Jangu, C.; Wang, D.; Heflin, J. R.; Moore, R. B.; Long, T. E., Imidazolium-Containing ABA Triblock Copolymers as Electroactive Devices *ACS Appl. Mater. Interfaces* **2016**, *8*, 1280-1288.
7. Navarra, M. A.; Manzi, J.; Lombardo, L.; Panero, S.; Scrosati, B., Ionic Liquid-Based Membranes as Electrolytes for Advanced Lithium Polymer Batteries *ChemSusChem* **2011**, *4*, 125-130.
8. Quinzeni, I.; Ferrari, S.; Quartarone, E.; Tomasi, C.; Fagnoni, M.; Mustarelli, P., Li-doped mixtures of alkoxy-N-methylpyrrolidinium bis(trifluoromethanesulfonyl)-imide and organic carbonates as safe liquid electrolytes for lithium batteries *J. Power Sources* **2013**, *237*, 204-209.
9. Sirisopanaporn, C.; Fernicola, A.; Scrosati, B., New, ionic liquid-based membranes for lithium battery application *J. Power Sources* **2009**, *186*, 490-495.
10. Miranda, D. F.; Versek, C.; Tuominen, M. T.; Russell, T. P.; Watkins, J. J., Cross-Linked Block Copolymer/Ionic Liquid Self-Assembled Blends for Polymer Gel Electrolytes with High Ionic Conductivity and Mechanical Strength *Macromolecules* **2013**, *46*, 9313-9323.
11. Lu, S. C.; Khan, A. L.; Vankelecom, I. F. J., Polysulfone-ionic liquid based membranes for CO<sub>2</sub>/N<sub>2</sub> separation with tunable porous surface features *J. Memb. Sci.* **2016**, *518*, 10-20.
12. Tome, L. C.; Mecerreyes, D.; Freire, C. S. R.; Rebelo, L. P. N.; Marrucho, I. M., Pyrrolidinium-based polymeric ionic liquid materials: New perspectives for CO<sub>2</sub> separation membranes *J. Memb. Sci.* **2013**, *428*, 260-266.
13. Zarca, G.; Home, W. J.; Ortiz, I.; Urriaga, A.; Bara, J. E., Synthesis and gas separation properties of poly(ionic liquid)-ionic liquid composite membranes containing a copper salt *J. Memb. Sci.* **2016**, *515*, 109-114.

14. Balducci, A.; Dugas, R.; Taberna, P. L.; Simon, P.; Plee, D.; Mastragostino, M.; Passerini, S., High temperature carbon-carbon supercapacitor using ionic liquid as electrolyte *J. Power Sources* **2007**, *165*, 922-927.
15. Fu, C. P.; Kuang, Y. F.; Huang, Z. Y.; Wang, X.; Yin, Y. F.; Chen, J. H.; Zhou, H. H., Supercapacitor based on graphene and ionic liquid electrolyte *J. Solid State Electrochem.* **2011**, *15*, 2581-2585.
16. Sathyamoorthi, S.; Suryanarayanan, V.; Velayutham, D., Organo-redox shuttle promoted protic ionic liquid electrolyte for supercapacitor *J. Power Sources* **2015**, *274*, 1135-1139.
17. Ambroggi, M.; Men, Y. J.; Polzer, F.; Yuan, J. Y., Salt-confinement enables production of nitrogen-doped porous carbons in an air oven *RSC Adv.* **2014**, *4*, 37714-37720.
18. Zhang, K. R.; Fahs, G. B.; Drummey, K. J.; Moore, R. B.; Long, T. E., Doubly-Charged Ionomers with Enhanced Microphase-Separation *Macromolecules* **2016**, *49*, 6965-6972.
19. Isik, M.; Fernandes, A. M.; Vijayakrishna, K.; Paulis, M.; Mecerreyes, D., Preparation of poly(ionic liquid) nanoparticles and their novel application as flocculants for water purification *Polym. Chem.* **2016**, *7*, 1668-1674.
20. Choi, U. H.; Mittal, A.; Price, T. L.; Gibson, H. W.; Runt, J.; Colby, R. H., Polymerized Ionic Liquids with Enhanced Static Dielectric Constants *Macromolecules* **2013**, *46*, 1175-1186.
21. Lee, M.; Choi, U. H.; Colby, R. H.; Gibson, H. W., Ion Conduction in Imidazolium Acrylate Ionic Liquids and their Polymers *Chem. Mater.* **2010**, *22*, 5814-5822.
22. Wang, A. L.; Xu, H.; Liu, X.; Gao, R.; Wang, S.; Zhou, Q.; Chen, J.; Liu, X. F.; Zhang, L. Y., The synthesis of a hyperbranched star polymeric ionic liquid and its application in a polymer electrolyte *Polym. Chem.* **2017**, *8*, 3177-3185.
23. Hou, J.; Zhang, Z.; Madsen, L. A., Cation/Anion Associations in Ionic Liquids Modulated by Hydration and Ionic Medium *J. Phys. Chem. B* **2011**, *115*, 4576-4582.
24. Jangu, C.; Schultz, A. R.; Wall, C. E.; Esker, A. R.; Long, T. E., Diphenylphosphino Styrene-Containing Homopolymers: Influence of Alkylation and Mobile Anions on Physical Properties *Macromol. Rapid Commun.* **2016**, *37*, 1212-1217.
25. Andrzejewska, E.; Podgorska-Golubska, M.; Stepniak, I.; Andrzejewski, M., Photoinitiated polymerization in ionic liquids: Kinetics and viscosity effects *Polymer* **2009**, *50*, 2040-2047.
26. Mori, H.; Iwata, M.; Ito, S.; Endo, T., Ring-opening polymerization of gamma-benzyl-L-glutamate-N-carboxyanhydride in ionic liquids *Polymer* **2007**, *48*, 5867-5877.
27. Hou, C.; Qu, R. J.; Ji, C. N.; Sun, C. M.; Wang, C. H., Reverse ATRP process of acrylonitrile in the presence of ionic liquids *J. Polym. Sci. A Polym. Chem.* **2008**, *46*, 2701-2707.
28. Li, D.; Zhang, Y. M.; Wang, H. P.; Tang, J. Z.; Wang, B., Free-radical copolymerization kinetics of acrylonitrile and methyl acrylate in BMIM BF<sub>4</sub> *J. Appl. Polym. Sci.* **2006**, *102*, 4254-4257.
29. Zhang, H. Y.; Zhang, Y. M.; Liu, W. W.; Wang, H. P., Kinetic study of atom transfer radical polymerization of methyl methacrylate in ionic liquids *J. Appl. Polym. Sci.* **2008**, *110*, 244-252.

30. He, H. K.; Zhong, M. J.; Luebke, D.; Nulwala, H.; Matyjaszewski, K., Atom Transfer Radical Polymerization of Ionic Liquid Monomer: The Influence of Salt/Counterion on Polymerization *J. Polym. Sci. A Polym. Chem.* **2014**, *52*, 2175-2184.
31. Thurecht, K. J.; Gooden, P. N.; Goel, S.; Tuck, C.; Licence, P.; Irvine, D. J., Free-Radical Polymerization in Ionic Liquids: The Case for a Protected Radical *Macromolecules* **2008**, *41*, 2814-2820.
32. Marcus, R. A., On The Theory of Oxidation—Reduction Reactions Involving Electron Transfer. V. Comparison and Properties of Electrochemical and Chemical Rate Constants *J. Phys. Chem.* **1963**, *67*, 853-857.
33. Paczkowski, J.; Kucybala, Z., Generalization of the Kinetic Scheme for a Dye-Photosensitized Free-Radical Polymerization Initiating System via an Intermolecular Electron-Transfer Process. Application of Marcus Theory *Macromolecules* **1995**, *28*, 269-273.
34. Clark, C. D.; Hoffman, M. Z., Ion-Pairing Control of Excited-State Electron-Transfer Reactions. Quenching, Charge Recombination, and Back Electron Transfer *J. Phys. Chem.* **1996**, *100*, 7526-7532.
35. Lynden-Bell, R. M., Can Marcus Theory Be Applied to Redox Processes in Ionic Liquids? A Comparative Simulation Study of Dimethylimidazolium Liquids and Acetonitrile *J. Phys. Chem. B* **2007**, *111*, 10800-10806.
36. Stejskal, E. O.; Tanner, J. E., Spin Diffusion Measurements: Spin Echoes in The Presence of A Time-dependent Field Gradient *J. Chem. Phys.* **1965**, *42*, 288-292.
37. Price, W. S., Pulsed-field gradient nuclear magnetic resonance as a tool for studying translational diffusion .1. Basic theory *Concepts Magn. Reson.* **1997**, *9*, 299-336.
38. Callaghan, P. T., *Principles of nuclear magnetic resonance microscopy*. Oxford University Press on Demand: New York, 1991.
39. Green, M. D.; Salas-de la Cruz, D.; Ye, Y. S.; Layman, J. M.; Elabd, Y. A.; Winey, K. I.; Long, T. E., Alkyl-Substituted N-Vinylimidazolium Polymerized Ionic Liquids: Thermal Properties and Ionic Conductivities *Macromol. Chem. Phys.* **2011**, *212*, 2522-2528.
40. Abdulahad, A. I.; Jangu, C.; Hemp, S. T.; Long, T. E., Influence of Counterion on Thermal, Viscoelastic, and Ion Conductive Properties of Phosphonium Ionenics *Macromol. Symp.* **2014**, *342*, 56-66.
41. Godeau, G.; Navailles, L.; Nallet, F.; Lin, X. R.; McIntosh, T. J.; Grinstaff, M. W., From Brittle to Pliant Viscoelastic Materials with Solid State Linear Polyphosphonium-Carboxylate Assemblies *Macromolecules* **2012**, *45*, 2509-2513.
42. Tudryn, G. J.; Liu, W. J.; Wang, S. W.; Colby, R. H., Counterion Dynamics in Polyester-Sulfonate Ionomers with Ionic Liquid Counterions *Macromolecules* **2011**, *44*, 3572-3582.
43. Fu, Y.; Bocharova, V.; Ma, M.; Sokolov, A.; Sumpter, B. G.; Kumar, R., Effects of counterion size and backbone rigidity on dynamics of ionic polymer melts and glasses *Phys. Chem. Chem. Phys.* **2017**, 27442-27451.
44. Simons, T. J.; Bayley, P. M.; Zhang, Z.; Howlett, P. C.; MacFarlane, D. R.; Madsen, L. A.; Forsyth, M., Influence of Zn<sup>2+</sup> and Water on the Transport Properties of a Pyrrolidinium Dicyanamide Ionic Liquid *J. Phys. Chem. B* **2014**, *118*, 4895-4905.
45. Zhang, Z.; Madsen, L. A., Observation of separate cation and anion electrophoretic mobilities in pure ionic liquids *J. Chem. Phys.* **2014**, *140*, 084204.

46. Fan, F.; Wang, W.; Holt, A. P.; Feng, H.; Uhrig, D.; Lu, X.; Hong, T.; Wang, Y.; Kang, N.-G.; Mays, J.; Sokolov, A. P., Effect of Molecular Weight on the Ion Transport Mechanism in Polymerized Ionic Liquids *Macromolecules* **2016**, *49*, 4557-4570.
47. He, Y. Y.; Lodge, T. P., A thermoreversible ion gel by triblock copolymer self-assembly in an ionic liquid *Chem. Commun.* **2007**, 2732-2734.
48. Jourdain, A.; Serghei, A.; Drockenmuller, E., Enhanced Ionic Conductivity of a 1,2,3-Triazolium-Based Poly(siloxane ionic liquid) Homopolymer *ACS Macro Lett.* **2016**, *5*, 1283-1286.
49. Wojnarowska, Z.; Knapik, J.; Jacquemin, J.; Berdzinski, S.; Strehmel, V.; Sangoro, J. R.; Paluch, M., Effect of Pressure on Decoupling of Ionic Conductivity from Segmental Dynamics in Polymerized Ionic Liquids *Macromolecules* **2015**, *48*, 8660-8666.
50. Wojnarowska, Z.; Feng, H.; Fu, Y.; Cheng, S.; Carroll, B.; Kumar, R.; Novikov, V. N.; Kisiuk, A. M.; Saito, T.; Kang, N.-G.; Mays, J. W.; Sokolov, A. P.; Bocharova, V., Effect of Chain Rigidity on the Decoupling of Ion Motion from Segmental Relaxation in Polymerized Ionic Liquids: Ambient and Elevated Pressure Studies *Macromolecules* **2017**, *50*, 6710-6721.
51. Jacob, C.; Matsumoto, A.; Brennan, M.; Liu, H.; Paddison, S. J.; Urakawa, O.; Inoue, T.; Sangoro, J.; Runt, J., Polymerized Ionic Liquids: Correlation of Ionic Conductivity with Nanoscale Morphology and Counterion Volume *ACS Macro Lett.* **2017**, *6*, 941-946.
52. Biela, T.; Duda, A., Solvent effect in the polymerization of  $\epsilon$ -caprolactone initiated with diethylaluminum ethoxide *J. Polym. Sci. A Polym. Chem.* **1996**, *34*, 1807-1813.
53. Polyanskiy, M. N., Refractive index database. <https://refractiveindex.info>, 2017.
54. Edward, J. T., Molecular volumes and the Stokes-Einstein equation *J. Chem. Educ.* **1970**, *47*, 261.
55. Hubbard, J.; Onsager, L., Dielectric dispersion and dielectric friction in electrolyte solutions. I *J. Chem. Phys.* **1977**, *67*, 4850-4857.
56. Zwanzig, R., Dielectric friction on a rotating dipole *J. Chem. Phys.* **1963**, *38*, 1605-1606.
57. Zwanzig, R., Dielectric friction on a moving ion 2. revised theory *J. Chem. Phys.* **1970**, *52*, 3625-3628.
58. Hubbard, J. B., Friction on a rotating dipole *J. Chem. Phys.* **1978**, *69*, 1007-1009.
59. Wolynes, P. G., Dynamics of Electrolyte Solutions *Annual Review of Physical Chemistry* **1980**, *31*, 345-376.
60. Beuermann, S.; Buback, M.; Hesse, P.; Kukuckova, S.; Lacik, I., Propagation kinetics of free-radical methacrylic acid polymerization in aqueous solution. The effect of concentration and degree of ionization *Macromol. Symp.* **2007**, *248*, 23-32.
61. Marcus, R. A., On the Theory of Oxidation-Reduction Reactions Involving Electron Transfer. I *J. Chem. Phys.* **1956**, *24*, 966-978.
62. Marcus, R. A., Exchange reactions and electron transfer reactions including isotopic exchange. Theory of oxidation-reduction reactions involving electron transfer. Part 4.-A statistical-mechanical basis for treating contributions from solvent, ligands, and inert salt *Discuss. Faraday Soc.* **1960**, *29*, 21-31.
63. Zwanzig, R., *Nonequilibrium Statistical Mechanics*. Oxford University Press: New York, 2001.
64. Debye, P. J., Reaction Rates in Ionic Solutions *Electrochem. Soc.* **1942**, 265.
65. Sutin, N., *Progress in Inorganic Chemistry*. John Wiley & Sons Inc.: 1983; Vol. 30.

# Chapter 9: Decoupling Ion Conduction from Structural Relaxation: Imidazolium-Containing Poly(Ionic Liquid)s

*(Manuscript in preparation for publication)*

Mingtao Chen<sup>1,#</sup>, Maximilian Heres<sup>2,#</sup>, Jason W. Dugger<sup>3</sup>, Timothy E. Long<sup>1</sup>, Joshua R. Sangoro<sup>2,\*</sup>, and Bradley S. Lokitz<sup>3,\*</sup>

<sup>1</sup> Department of Chemistry, Macromolecules Innovation Institute (MII), Virginia Tech, Blacksburg, VA 24061

<sup>2</sup> Department of Chemical and Biomolecular Engineering, University of Tennessee Knoxville, 1512 Middle Drive, Knoxville, TN 37996, USA

<sup>3</sup> Center for Nanophase Materials Sciences, Oak Ridge National Laboratory, One Bethel Valley Road, Oak Ridge, TN 3783

*#Those authors contributed equally to this work*

*\*To whom correspondence should be addressed: [jsangoro@utk.edu](mailto:jsangoro@utk.edu); [lokitzbs@ornl.gov](mailto:lokitzbs@ornl.gov)*

## 9.1 Abstract

Ion dynamics and mechanical properties in a series of imidazolium-based ABA ionic triblock copolymers were investigated using broadband dielectric spectroscopy (BDS), dynamic mechanical analysis (DMA), rheology and differential scanning calorimetry (DSC). Two glass transition temperatures ( $T_g$ s) were observed corresponding to the charged poly(ionic liquid) (PIL) block and the polystyrene block. Exchanging PIL block's counter-anion from Br to Tf<sub>2</sub>N led to an over 50 °C decrease in the  $T_g$  of the charged block and resulted in an increase in the room temperature ionic conductivity by over 6 orders of magnitude and an increase in viscosity. Increasing the molecular weight of the polystyrene block from 3kg/mol to 15kg/mol also led to an increase in viscosity by one order of magnitude and improved the elastic modulus plateau from 8 MPa to 60 MPa, with little impact on the ionic conductivity of the triblock copolymer. This work

demonstrates that it is possible to tune ion dynamics and mechanical properties independent of each other in ionic triblock copolymers, an aspect that to our knowledge has – so far – not been reported for PIL homopolymers.

## 9.2 Introduction

The interplay between ion conduction and mechanical strength has challenged researchers for decades in efforts to develop robust and efficient solid electrolytes<sup>1-6</sup>, ion exchange membranes (IEMs)<sup>7-8</sup>, actuators<sup>9-11</sup>, and gas separation membranes<sup>12-14</sup>. Ionic liquids (ILs) – molten salts with a melting temperature below 100 °C – continue to receive significant research interest because of their potential uses in energy storage devices, especially batteries.<sup>1, 5</sup> Besides their high ionic conductivity (in the mS/cm range), ILs' negligible volatility and high thermal- and electro-stability present significant advantages compared to conventional solvent-based electrolytes. However, if ILs are to be successfully used in IEMs and actuators, ion conduction and mechanical integrity must be properly balanced. Typically, efforts to improved mechanical integrity have almost always come at the cost of ionic conductivity.

A popular approach is to utilize the macromolecular form of ILs, i.e., poly(ionic liquid)s (PILs), to achieve high ionic conductivity and mechanical integrity simultaneously. PIL homopolymers or segmented copolymers have demonstrated reasonable mechanical integrity and ionic conductivity in the semi-conductor range at temperatures above glass transition temperature ( $T_g$ ). Long *et al.* synthesized ammonium- and phosphonium-containing PIL homopolymers with  $T_g$  ranging from 62 to 91 °C.<sup>15</sup> The polymers exhibited ionic conductivities from  $10^{-7}$  to  $10^{-5}$  S/cm at 100 °C. Colby *et al.* studied segmented polyurethanes and reported tunable  $T_g$ s depending on the counter ion

identity.<sup>16</sup> Similarly, the segmented polymers only reached ionic conductivities  $\sim 10^{-6}$  S/cm at high temperatures. By contrast, Drockenmuller *et al.* achieved high ionic conductivity ( $7 \times 10^{-5}$  S/cm) at room temperature using siloxane-based PILs but the mechanical integrity ( $T_g = -62$  °C) was poor.<sup>17</sup> In the cases of homopolymers and segmented copolymers, ion dynamics and structural relaxation are strongly correlated, leading to significant tradeoff between ionic conductivity and mechanical integrity.

Block copolymers with PIL segments allow ionic conductivity and mechanical integrity to be tuned separately, offering a potential solution to this problem. A PIL block with low  $T_g$  is used to achieve sufficient ionic conductivity while the uncharged block provides the necessary mechanical integrity to form free-standing films. Additionally, microphase separation in block copolymers offers ordered morphologies with well-defined ion conduction pathways. Park and coworkers reported an improvement in ionic conductivity when desired microphase morphologies were achieved.<sup>6</sup> For example, in PS-*b*-PEO diblock copolymers, PS blocks provided mechanical integrity while PEO segments swollen with Li salts increased the ionic conductivity. When comparing the different microphase morphologies, the ionic conductivity increased when comparing disordered systems to gyroid and lamellar morphologies, with lamellar films having ionic conductivities as high as  $10^{-2}$  S/cm at 100 °C.

While block copolymers with PILs offer the potential to tune ion dynamics and structural relaxation “separately”, a certain tradeoff between the two is still inevitable. However, we hypothesize that a long spacer between the ionic moiety and polymer backbone would improve the decoupling of ion dynamics and structural relaxation providing the ability to independently tune mechanical and viscoelastic properties with

limited impact on ionic conductivity. We previously reported the synthesis of a novel poly(ionic liquid)s (PILs) comprised of methacrylate backbones and imidazolium pendant groups spaced by a decyl linkage. The PILs showed promising ionic conductivities as high as  $2.45 \times 10^{-5}$  S/cm.<sup>18</sup>

In this work, we combine, dynamic mechanical analysis (DMA), rheology and differential scanning calorimetry (DSC) with broadband dielectric spectroscopy (BDS) to study ABA triblock copolymers synthesized by reversible addition-fragmentation chain transfer (RAFT) polymerization. The ABA triblock copolymers contain a polystyrene (S) block and an ionic liquid block, 1-[ $\omega$ -methacryloyloxydecyl]-3-(*n*-butyl)-imidazolium bromide (1BDIMABr) as the B block. In this manuscript, we investigate the influence of counter-ion identity and polymer composition on ionic conductivity; the effect of long spacer between ionic moieties and polymer backbones on decoupling the ion dynamics from structural relaxation; in a concerted effort to design materials with tunable viscoelastic properties and good ionic conductivity.

## 9.3 Experimental

### 9.3.1 Materials

Lithium tetrafluoroborate (98%), bis(trifluoromethane)sulfonimide lithium salt, 10-bromo-1-decanol (technical grade, 90%), 1-butylimidazole, triethylamine, and all common organic solvents were purchased from Sigma-Aldrich and used as received. Anhydrous solvents, N,N-dimethylformamide (DMF, anhydrous, 99.8%) and acetonitrile (MeCN, anhydrous,  $\geq 99.8\%$ ), were purchased from Sigma-Aldrich and used without further purification. 4-Cyano-4-[(dodecylsulfanylthiocarbonyl)sulfanyl]pentanoic acid (CDP, 97%, HPLC) and 2,2'-Azobis(2-methylpropionitrile) (AIBN, 98%) from Sigma-

Aldrich were stored at -20 °C and recrystallized once from methanol prior to use. Methacryloyl chloride ( $\geq 97.0\%$ , GC, contains  $\sim 0.02\%$  2,6-di-tert-butyl-4-methylphenol as stabilizer) was purchased from Sigma-Aldrich and stored under inert atmosphere at 2 °C. Styrene were purchased from Sigma-Aldrich and passed through aluminum oxide column to remove inhibitor before use. The 1BDIMABr monomer synthesis was described elsewhere. The difunctional chain transfer agent (CTA, dCDP) synthesis was reported in a previous literature.<sup>19</sup>

### 9.3.2 Instrumentation

<sup>1</sup>H and <sup>19</sup>F nuclear magnetic resonance (NMR) spectroscopy measurements were conducted on a Varian Unity 400 MHz NMR spectrometer (deuterated MeCN or DMSO, 128 scans). Thermal degradation under N<sub>2</sub> environment was determined by a TA Q500 thermogravimetric analyzer (TGA) at 10 °C/min ramp rate (25 to 600 °C). A TA Q2000 differential scanning calorimeter (DSC) was applied to investigate thermal transitions. Reported values (midpoint) were determined from the second heat cycle of a heat/cool/heat procedure: (1) 10 °C/min ramp from 23 °C to 150 °C, isotherm at 150 °C for 30 min, (2) 100 °C/min quench cool to -80 °C, and (3) 10 °C/min ramp to 150 °C. Dynamic mechanical analysis (DMA) were conducted on a TA Q800 instrument in multi-frequency (strain) module. The thermal mechanical response of polymer films were measured in a temperature ramp experiment with 3 °C/min heating rate from -60 to 150 °C (10  $\mu$ m amplitude). Viscoelastic properties were studied via a TA AR-G2 rheometer using disposable parallel plates (8 mm). Before time-temperature superposition (TTS) experiments, both strain sweep and frequency sweep were conducted at 100 °C and 180 °C. Strain sweep were performed from 0.1% to 10% strain at 1 Hz, and frequency sweep

were carried out from 0.01 Hz to 1 Hz. TTS experiments were performed from 100 °C to 180 °C with frequencies ranging from 0.1 Hz to 10 Hz (0.1% strain). TTS master curves were generated through TA Trios software using WLF fitting. Total molecular weight and molecular weight distribution of triblock copolymers were determined through size exclusion chromatography (SEC) in DMF (with 0.05 mol LiBr) at 60 °C at a flowrate of 1 mL/min. The SEC system consisted of a Waters 515 HPLC pump equipped with a Waters 717 plus autosampler. Absolute molecular weight was determined through a Wyatt Technology miniDawn MALLS detector operating at 690 nm and a Waters 2414 refractive index detector operating at 880 nm. Specific refractive index values ( $dn/dc$ ) were investigated via an offline Optilab T-rEX refractometer ( $\lambda = 658$  nm) and were used to calculate weight-average molecular weight ( $M_w$ ) from SEC. The molecular weight of individual blocks were determined by comparing the peak integral of aromatic peaks in styrene repeating units (6.5 to 7.5 ppm) and imidazolium peaks in ionic liquid repeating units (8.1 to 8.4 ppm) through  $^1\text{H}$  NMR spectroscopy.

Broadband dielectric spectroscopy (BDS) measurements were conducted on a Novocontrol Alpha analyzer. The sample was pressed between cylindrical brass electrodes to a thickness of 100  $\mu\text{m}$ . In order to insure consistent sample thickness, two silica spacer rods (100  $\mu\text{m}$  diameter) were inserted into the sample before pressing. To erase thermal history, the samples were thermally equilibrated at 150 °C after pressing and prior to the BDS measurement. The temperature was controlled by a Quatro cryostat with accuracy of  $\pm 0.1$  °C. Frequency sweeps over a range from 0.1 Hz to 10 MHz were measured between 430 K to 230 K in 5 K increments on a cooling-heating-cooling cycle in order to check for thermal stability and reproducibility.

### 9.3.3 Synthesis of poly(1BDIMABr) macroCTA

A solution of 1-[ $\omega$ -methacryloyloxydecyl]-3-(*n*-butyl)-imidazolium bromide (1BDIMABr) monomer (10.5 g, 24.5 mmol), dCDP (0.144 g, 0.16 mmol), and AIBN (13.4 mg, 0.08 mmol) in 24.5 mL MeCN ([1BDIMABr] = 1M) was sparged with Argon for 20 min prior to the polymerization. The polymerization was performed at 65 °C for a given time to target specific molecular weights. The resulting polymers were precipitated into ethyl acetate and washed with ethyl acetate twice to yield brown, glue-like product. The product was further dried under vacuum at 50 °C to yield a brown sticky solid. <sup>1</sup>H NMR spectroscopy (DMF-*d*7, 400 Hz): 0.8 – 2.2 ppm (polymer backbone and methylenes in pendant groups), 4.0 ppm (2H, CH<sub>2</sub>-O-C=O), 4.5 ppm (4H, CH<sub>2</sub>-N=C), 8.2 ppm (2H, CH=CH-N), 10.3 ppm (1H, N-CH=N).

### 9.3.4 Synthesis of poly(S-*b*-1BDIMABr-*b*-S) triblock copolymers

Styrene monomer (9.8 g), poly(1BDIMABr) macroCTA (5.9 g), and AIBN (12.9 mg) were dissolved in 47.05 mL DMF. The CTA/I ratio was set to 3/1, and monomer concentration [M] = 2 M. The reaction solution was sparged with Argon for 40 min prior to polymerization. The polymerization was conducted at 65 °C and quenched by exposing the reaction to air. The resulting polymers were precipitated into ethyl acetate and washed with ethyl acetate three times before drying under vacuum at 50 °C for 24 h. The final product was a light-brown solid. The ion exchange of block copolymers is described elsewhere.<sup>18</sup> <sup>1</sup>H NMR spectroscopy (DMF-*d*7, 400 Hz): 0.8 – 2.2 ppm (polymer backbone and methylene protons in pendant groups), 4.0 ppm (2H, CH<sub>2</sub>-O-C=O), 4.5 ppm (4H, CH<sub>2</sub>-N=C), 6.5 -7.5 ppm (aromatic protons, integral depends on composition), 8.2 ppm (2H, CH=CH-N), 10.3 ppm (1H, N-CH=N).

### 9.3.5 Film casting

All triblock copolymers were dissolved in DMF (~20 wt%) and cast into Teflon mode placed on a heat plate at 50 °C to allow slow evaporation of DMF for 2 d. The resulting polymers films were further dried under vacuum at 25 °C and 150 °C for 1 d, respectively. All polymer films were annealed under vacuum at 150 °C for 1 d before tests.

## 9.4 Results and Discussion

The synthesis of poly(S-*b*-1BDIMABr-*b*-S) triblock copolymers involved a two-step RAFT polymerization using a difunctional chain transfer agent (CTA). As illustrated in **Figure 9.1**, AIBN thermally initiated the polymerization of 1BDIMABr monomers resulting in a poly(1BDIMABr) macroCTA. The poly(1BDIMABr) macroCTA was chain extended from both the alpha and omega chain ends with styrene to form a poly(S-*b*-1BDIMABr-*b*-S) triblock copolymer. The targeted MW of the styrene blocks was varied to produce three ABA triblock copolymers with identical PIL B blocks and different PS A blocks. The Mw and dispersity of each polymer is listed in Table 1. The use of difunctional CTA allows minimal reinitiation times which is necessary to achieve narrow molecular weight distributions.<sup>20</sup> Post-polymerization ion exchange in DMF resulted in triblock copolymers with different counter anions but identical polymer backbones. Block copolymers with bromide (Br), tetrafluoroborate (BF<sub>4</sub>), and bis(trifluoromethane)sulfonimide (Tf<sub>2</sub>N) anions provided a wide range of ionic block T<sub>g</sub>s.

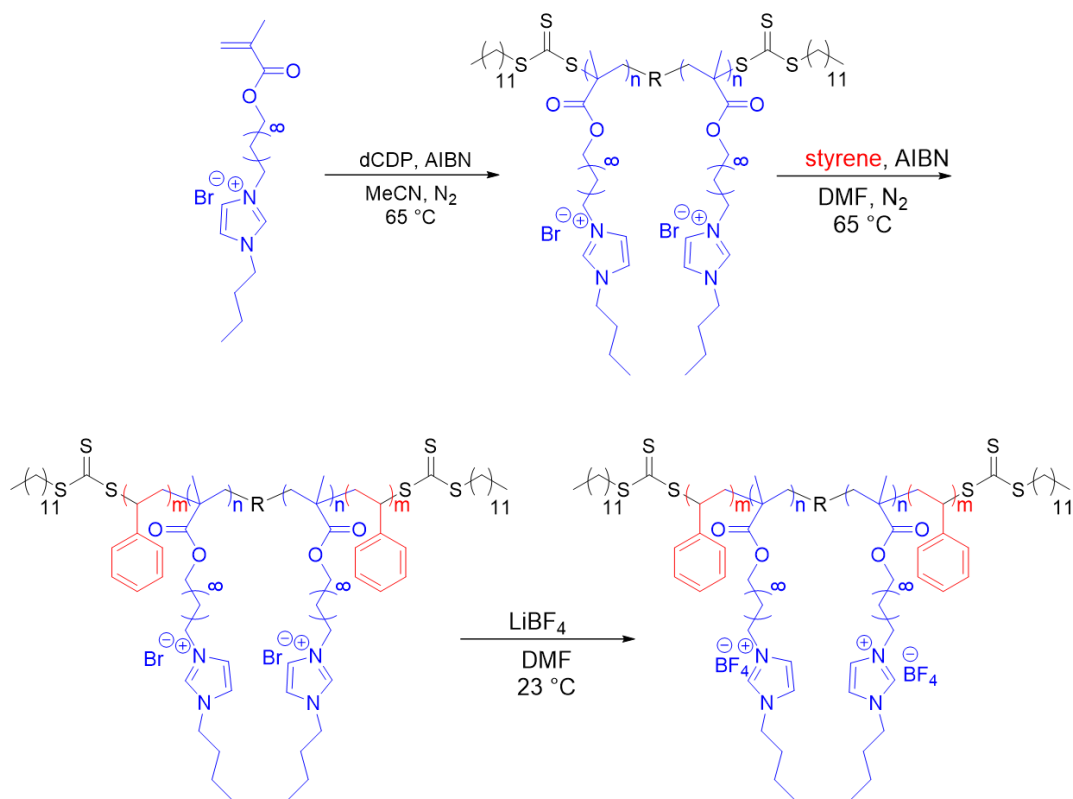


**Figure 9.1** Synthesis of poly(S-*b*-1BDIMABr-*b*-S) triblock copolymers through RAFT polymerization.

**Figure 9.2a** shows the shift of triblock copolymer elution time in size exclusion chromatography (SEC). Increasing polymerization time of styrene monomers lead to a shift to lower elution time (higher molecular weight) as well as an improvement in signal-to-noise ratios. Poly(1BDIMABr) macroCTA exhibited a lower refractive index value ( $dn/dc$ ) than mobile phase (DMF + 0.05 M LiBr), and the incorporation of styrene blocks increased the refractive index value resulting in a better signal-to-noise ratios. The triblock copolymers were not soluble in any other common SEC solvents (i.e. chloroform, THF, and water). The absolute molecular weights of three different triblock copolymers were determined using  $dn/dc$  values measured offline, and the relative ratios between two blocks were calculated using <sup>1</sup>H NMR spectroscopy. **Table 9.1** summarizes the molecular weights of three block copolymers: 3-34-3 kg/mol, 9-34-9 kg/mol, and 15-

34-15 kg/mol. Polydispersity index (PDI) of block copolymers decreased with increasing polymerization time which is typical of RAFT polymerizations. In order to achieve reasonable conversions during chain extension with styrene, a relatively low chain transfer agent/initiator (CTA/I) ratio of 3 was employed, leading to higher overall dispersity.

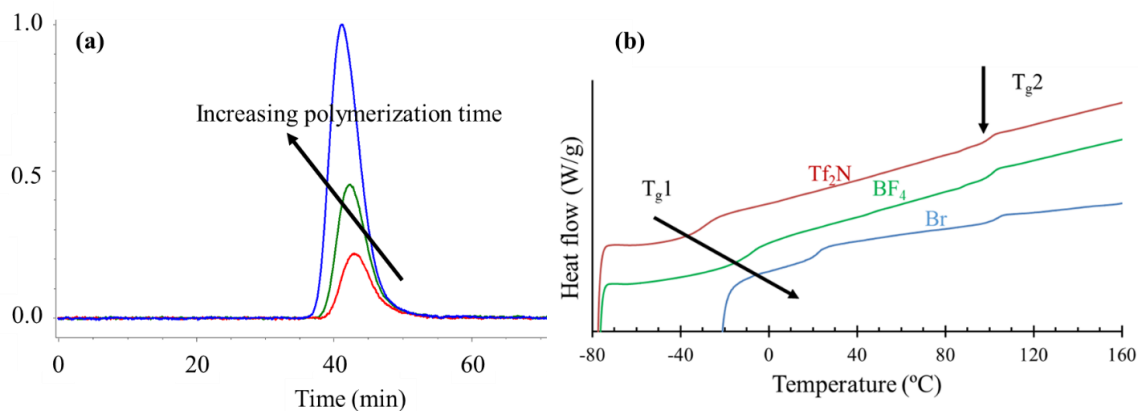


**Figure 9.2** (a) SEC traces of poly(*S-b-1BDIMABr-b-S*) triblock copolymers with different polymerization time; (b) thermal transitions monitored via DSC (15-34-15 kg/mol samples shown).

The thermal transitions of poly(*S-b-1BDIMABr-b-S*) with molecular weight of 15-34-15 kg/mol is shown in **Figure 9.2b**.  $T_{g1}$  (from -30 to 20 °C) is assigned as the  $T_g$  of the PIL block as the long alkyl spacer linkages between polymer backbones and imidazolium groups offered extra mobility, decreasing  $T_g$ .  $T_{g2}$  at around 100 °C corresponds well with the  $T_g$  of polystyrene. When comparing the effect of counter anions, bulkier anions tend to plasticize polymer matrices and induce weaker electrostatic interactions which corresponds to the DSC measurements.  $T_{g1}$  decreased from 22 °C (Br) to -10 °C ( $BF_4$ ) and -31 °C ( $Tf_2N$ ). Exchanging the counter anions exhibited no appreciable effect on the  $T_g$  of polystyrene block ( $T_{g2}$ ). Of note is that for block copolymers with the same counter anion but different polystyrene block lengths, only

minimal changes for both  $T_{g1}$  and  $T_{g2}$  were observed (See **Table 9.1**). In the lowest molecular weight block copolymers, 3-34-3 kg/mol, the polystyrene blocks were too short to show a prominent  $T_{g2}$  in DSC. Both 9-34-9 and 15-34-15 showed two distinct  $T_{gs}$  indicative of microphase separation.

**Table 9.1** Molecular weights and  $T_{gs}$  of triblock copolymers with different counter anions

$M_n$ (kg/mol)	3-34-4			9-34-9			15-34-15		
PDI	1.55			1.35			1.35		
Counter ions	Br	BF <sub>4</sub>	Tf <sub>2</sub> N	Br	BF <sub>4</sub>	Tf <sub>2</sub> N	Br	BF <sub>4</sub>	Tf <sub>2</sub> N
$T_{g1}$ (°C)	21	-12	-33	22	-9	-35	22	-10	-31
$T_{g2}$ (°C)	N	N	N	100	98	91	103	101	101

N: not observed

Broadband dielectric spectroscopy was used to determine the real and imaginary parts of the complex conductivity,  $\sigma^* = \sigma' + i\sigma''$ . As shown in **Figure 9.3a**, ionic conductivity in polymerized ionic liquids typically exhibit three key frequency regions in  $\sigma'$ : frequency dependence in the high frequency regime, an intermediate DC-ionic conductivity plateau, and low frequency interfacial/electrode polarization. This is typically described well by the random barrier model, in which the counter ion is thought to travel through a random landscape of potential energy barriers. In order to contribute to DC-ionic conductivity,  $\sigma_0$ , the counter ion has to overcome the highest energy barrier and participate in long range ion conduction. The rate at which this occurs is the characteristic ion hopping rate, which marks the transition from frequency dependent to independent  $\sigma'$ . Aggregation of charges at the electrodes causes a shielding effect at

sufficiently long time scales through Coulombic repulsion, which decreases ionic conductivity at low frequencies.

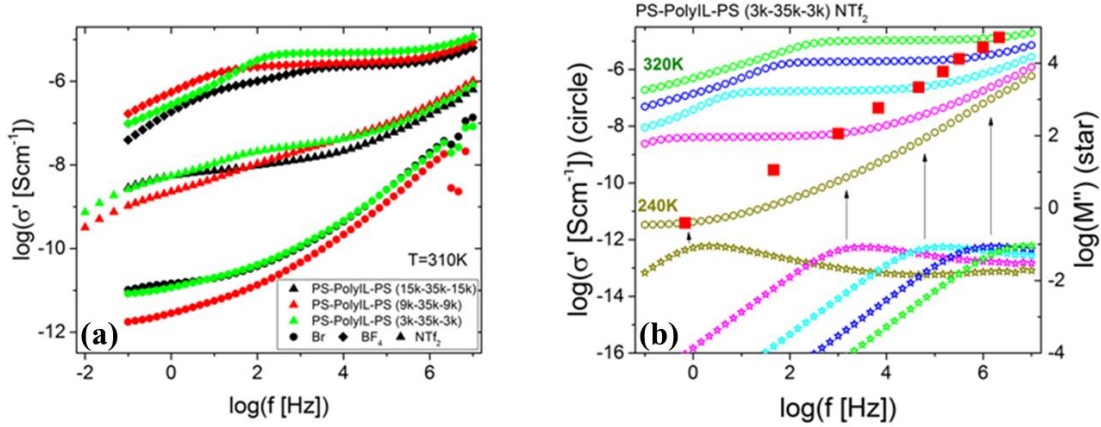


**Figure 9.3** Real part (a) of complex conductivity  $\sigma = \sigma' + i\sigma''$  as a function of frequency for triblock copolymers with bromide (Br), tetrafluoroborate (BF<sub>4</sub>), and bis(trifluoromethyl sulfonyl)imide (Tf<sub>2</sub>N) anions at 310 K. Figure b) shows  $\sigma'$  and the dielectric loss modulus  $M''$  as a function of frequency. Red square mark the magnitude of the DC-ionic conductivity,  $\sigma_0$ , corresponding to the peak frequency of  $M''$ .

Due to interfacial polarization effects between charged and non-charged blocks in these ionic block copolymers, the DC-plateau was not clearly visible in all compositions studied. Therefore, an alternative analysis involving the dielectric loss modulus  $M'' = \frac{\omega \epsilon_0 \sigma''}{(\sigma')^2 + (\sigma'')^2}$  was used, in which the characteristic ion hopping rate appears as a peak. The DC-ionic conductivity,  $\sigma_0$ , is then extracted from  $\sigma'$ , at the time scale of the characteristic ion hopping rate corresponding to the peak in  $M''$ , indicated by red squares in **Figure 9.3b**.

Comparing the temperature dependence of  $\sigma_0$  for samples with different anions and polystyrene (PS) block molecular weight, as done in **Figure 9.4**, reveals several interesting aspects of charge transport. At room temperature (blue dashed line) ionic conductivity increased by over 6 orders of magnitude by substituting the Br anion with NTf<sub>2</sub>. It is known that size and charge distribution of the anion has a large impact on

charge transport and  $T_g$  in PILs<sup>21</sup>. Generally, small counter ions, such as Br, are known to have stronger coulombic interactions with the cations, resulting in a higher  $T_g$  and lower ionic conductivity than larger counter ions such as  $Tf_2N$ . However, to our knowledge, an increase by as high as 6 orders of magnitude in the conductivity spectrum has not been reported before. The possibility is therefore presented here to tune the conductivity curve with respect to temperature, i.e., achieving a desired conductivity value over a temperature span of nearly 100 K by merely changing the anion.

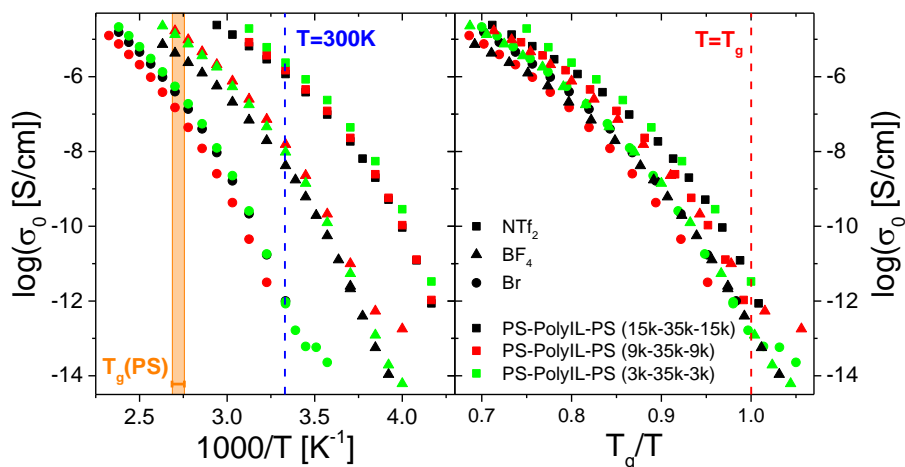


**Figure 9.4** DC-ionic conductivity as a function of inverse temperature and  $T_g$ -normalized temperature (ionic block  $T_g$ ). Blue and red lines indicate room temperature and the calorimetric glass transition temperature, respectively. An orange bar marks the range of  $T_g$ s of polystyrene.

Secondly, the presence of the non-charged block does not play a significant role in ion transport properties. The temperature dependence of ionic conductivity in PIL homopolymers typically follows a Vogel-Fulcher-Tammann (VFT)-like temperature dependence above  $T_g$  where the motion of ions is aided by the structural relaxation of the polymer. Below  $T_g$ , molecular motion of the polymer is frozen and ion transport becomes a thermally activated process with Arrhenius temperature dependence. Interestingly, for these ionic block copolymers, there is only a weak change of temperature dependence

across the glass transition of the PS block. Samples with the Br anion are the only ones in the measured temperature range which display a slight change in temperature dependence above and below the  $T_g$  of the polystyrene block. Increasing the molecular weight of the non-charged block, while keeping the anion consistent, does not have a significant impact on ionic conductivity, indicating that ion transport only occurs through the PIL block and is generally unaffected by the non-charged segments.

Plotting ionic conductivity as a function of normalized temperature reveals the  $T_g$ -independent ionic conductivity (**Figure 9.4b**). This representation compares conductivity in terms of the structural relaxation of the polymer matrix, and so excludes parameters such as  $T_g$  differences, molecular weight differences, and other material aspects and allows for a direct comparison of ion transport with respect to the structural relaxation.  $T_g$ -independent ionic conductivity does not show the decoupling of ion dynamics from the structural relaxation, characteristic for polymerized ionic liquids, which typically exhibit  $\sigma_0$  values of  $10^{-7}$  to  $10^{-8}$  S/cm.<sup>21</sup> Instead, the  $T_g$ -independent values of these systems rather resemble those of low molecular weight ionic liquid systems with  $\sigma_0$  values of  $10^{-12}$  to  $10^{-13}$  S/cm (at  $T_g$ ).<sup>22</sup> This is due to the long spacer length separating the bound cationic groups from the structural relaxation of the polymer backbone, giving the imidazolium cation enough space to diffuse, just as it would in a low molecular weight ionic liquid system, while still being remotely connected, as recently been demonstrated.<sup>18</sup>

Considering  $T_g$ -independent ionic conductivity reveals an interesting – albeit subtle - trend: samples with the Tf<sub>2</sub>N anion appear to have higher  $T_g$ -independent ionic conductivity compared to the other anions. It is worth noting that in low-molecular

weight ionic liquids and PIL homopolymers, smaller ions exhibit higher  $T_g$ -independent ionic conductivity when the effects of  $T_g$  changes are taken into account; a phenomenon that is attributed to the fact that it is easier for small anions to diffuse. Therefore, large ions such as  $Tf_2N$  usually have the lowest  $T_g$ -independent ionic conductivity. Since the differences in ionic conductivity observed in the current work are minimal, this aspect will require further studies for ionic block copolymers, with a focus on considerably varying the size of the anion and probing the resulting transport characteristics.

The composition independent ion conduction promised a facile approach to alter polymer viscoelastic properties through compositional changes without deteriorating ionic conductivity. Dynamic mechanical analysis (DMA) in **Figure 9.5a** showed the elastic storage modulus ( $E'$ ) as a function of increasing temperature. The block copolymers with  $BF_4$  counter anions showed different rubbery plateau depending on styrene content. Higher styrene content increased the plateau modulus from  $\sim 8$  MPa (9-34-9 kg/mol) to  $\sim 60$  MPa (15-34-15 kg/mol). Block copolymers with  $Tf_2N$  counter anions formed no free standing films, and block copolymers with Br counter anions experienced severe water sorption during the DMA tests and exhibited no repeatable data.

Due to the difficulty of thermomechanical tests on free-standing films, we employed rheometer to investigate the rheological behaviors of the block copolymers. **Figure 9.5b** showed the changes of shear storage modulus ( $G'$ ) with increasing frequency in block copolymers with  $BF_4$  counter anions at 180 °C.  $G'$  exhibited over a decade difference between 3-34-3 kg/mol and 9-34-9 kg/mol samples while their ionic conductivities were similar. The  $G'$  at a given frequency followed the following trend: 3-

34-3 > 15-34-15 > 9-34-9 kg/mol. This trend is presumably due to the competition between ion concentration dilution and the hard block content increase. Incorporation of more styrene monomers effectively dilutes the ion concentration of polymer matrices, reducing the electrostatic interactions. As a result, inter-molecular interaction decreases, and so does  $G'$ . In contrast, longer polystyrene block increases  $G'$  as the rigid domains elongate. Hence, a minimal value of  $G'$  appears in **Figure 9.5b**. The ion concentration dilution effect was responsible for the decrease of  $G'$  between 3-34-3 kg/mol and 9-34-9 kg/mol block copolymers. However, further increase of styrene content led to significant  $G'$  increase which overcame ion concentration dilution when increasing polystyrene block length from 9 kg/mol to 15 kg/mol.

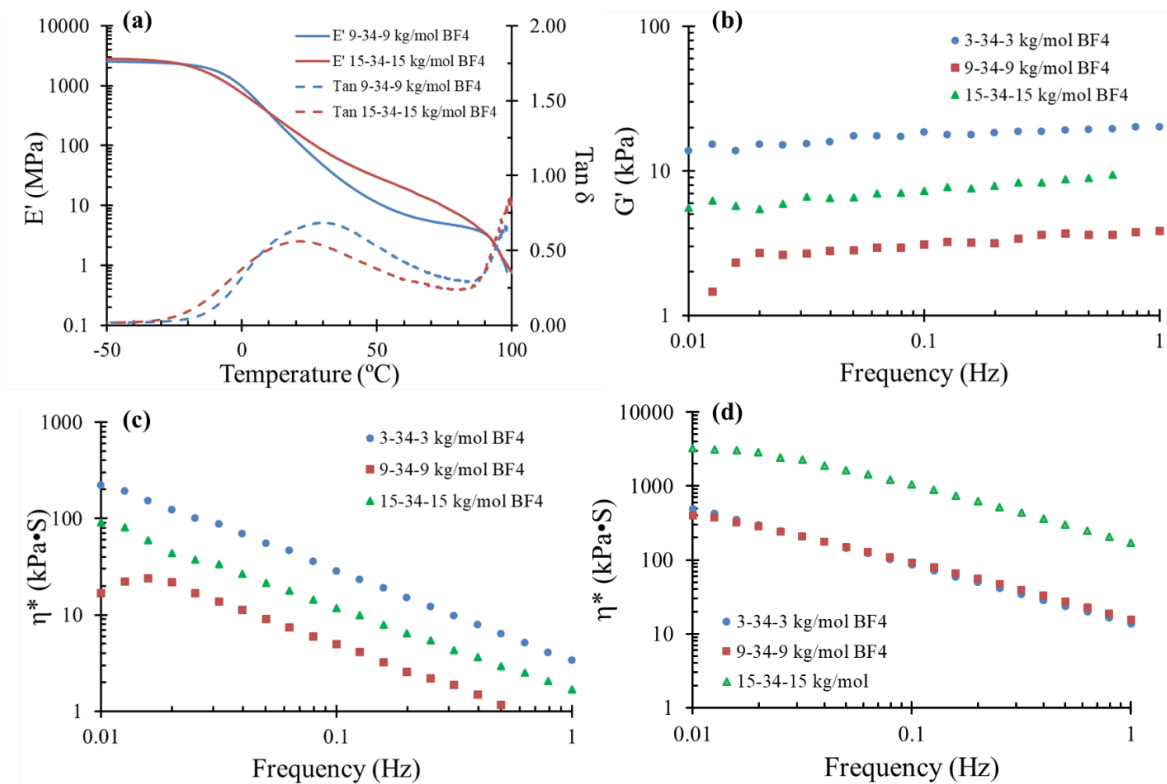


**Figure 9.5** (a) Thermomechanical property of block copolymers with BF<sub>4</sub> counter anions in DMA; (b) shear storage modulus ( $G'$ ) as a function of frequency in block copolymers with BF<sub>4</sub> counter anions; (c) & (d) complex viscosity ( $\eta^*$ ) as a function of frequency at 180 °C (c) and 100 °C (d).

**Figure 9.5c** and **9.5d** showed the changes of the complex viscosity ( $\eta^*$ ) of triblock copolymers with  $\text{BF}_4$  counter anions as a function of frequency at 180 °C and 100 °C, respectively. At both temperature, polymers demonstrated shear thinning at low frequency, which corresponded with previous literature report.<sup>23</sup> At 180 °C,  $\eta^*$  followed similar trend as in **Figure 9.5b** for the same reason. At 100 °C, all  $\eta^*$  increased significantly compared to 180 °C as expected. Low temperature significantly restricted the ion mobility and thus diminished the ion concentration dilution effect. As a result, incorporation of more styrene units led to a prominent increase of  $\eta^*$  from ~400 kPa•S to ~3000 kPa•S.

To further investigate the viscoelastic property differences due to composition changes, time temperature superposition (TTS) allowed the calculation of Vogel temperature ( $T_0$ ), fragility ( $m$ ) and fractional free volume at  $T_g$  ( $f_g$ ). **Figure 9.6a** showed the TTS traces of all three block copolymers with  $\text{BF}_4$  counter anions. Due to extra electrostatic interactions, the TTS shift was not as smooth as common polymeric matrices without secondary interactions. Nevertheless, **Figure 9.6b** demonstrated excellent agreement between Williams–Landel–Ferry (WLF) equation<sup>24</sup> (**Equation 1**) and the experimental superposition parameter ( $\alpha_T$ , the ratio of any mechanical relaxation time at temperature  $T$  and reference temperature  $T_{\text{ref}}$ ),

$$\log \alpha_T = -c_1 (T - T_{\text{ref}}) / (c_2 + T - T_{\text{ref}}) \quad 1$$

where  $c_1$  and  $c_2$  are experimentally determined constants. We chose  $T_g$  (100 °C) as  $T_{\text{ref}}$  for the rest of the discussion. Based on the original Doolittle equation<sup>25</sup> and the

assumption that the fractional free volume scales linearly with temperature<sup>24</sup>, **Equation 2** enabled the calculation of fractional free volume at  $T_g$  ( $f_g$ ):

$$c_1 = B'(1/2.303 f_g) \quad 2$$

where  $B'$  is a constant which often equals to unity.

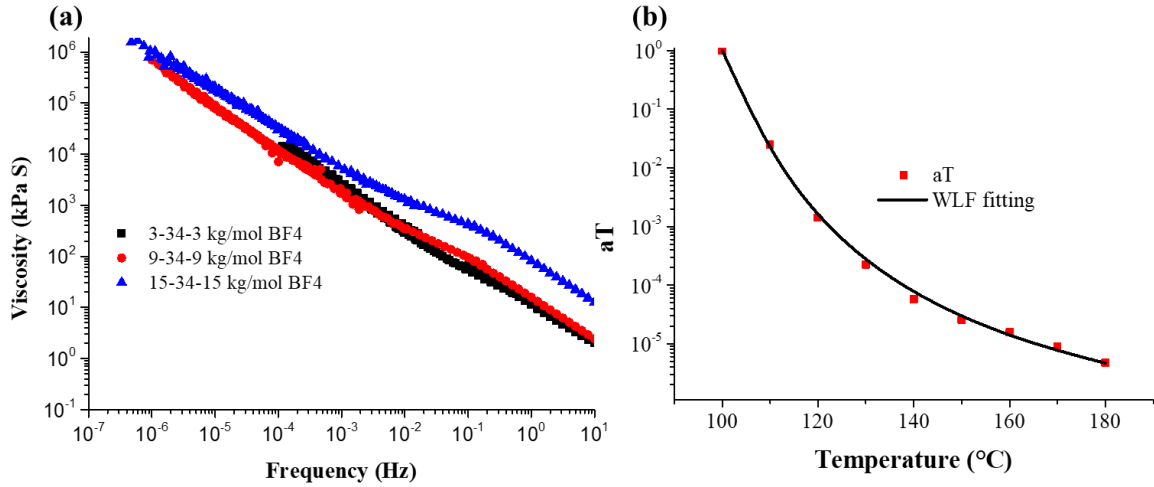


**Figure 9.6** Time temperature superposition (TTS) of block copolymers with BF4 counter anions (a) as a function of frequency and the WLF fitting (b) of TTS data (shown only 15-34-15 samples).

Liu *et al.* demonstrated that WLF equation and Vogel-Fulcher-Tammann (VFT) equation<sup>26</sup> (Equation 3) were mathematically equivalent.<sup>27</sup> Comparing WLF equation and VFT equation allows the calculation of Vogel temperature ( $T_0$ ) and eventually fragility ( $m$ )<sup>28</sup> through **Equation 3** to **Equation 6**.

$$\eta(T) = \eta_0 \exp(B/(T - T_0)) \quad 3$$

$$T_0 = c_2 - T_{ref} \quad 4$$

$$B = 2.303c_1c_2 \quad 5$$

$$m = \left(\frac{B}{2.303}\right) \frac{T_g}{(T_g - T_0)^2} \quad 6$$

where  $\eta(T)$  and  $\eta_0$  are zero-shear viscosity at temperature  $T$  and  $T_0$ , respectively.  $B$  is an experimentally determined constant.

**Table 9.2** summarized the viscoelastic properties from WLF equation (**Equation 2**) and VFT equation (**Equation 3**).  $T_0$ ,  $m$  and  $f_g$  all demonstrated minimal values in 9-34-9 kg/mol samples similar to the results in the frequency sweep (**Figure 9.5**) due to the competition between ion concentration dilution and the hard block content. With increasing styrene content, fragility decreased first from 91.0 to 85.6 and increased to 102.9. Similarly, fractional free volume decreased from 0.122 to 0.058 then increased back to 0.067 with increasing polystyrene block length.

**Table 9.2** WLF fitting parameters and calculated viscoelastic properties from WLF equation and VFT equation of block copolymers with  $\text{BF}_4$  counter anions. ( $T_{\text{ref}} = T_g = 100\text{ }^\circ\text{C}$ )

$M_n$ (kg/mol)	$C_1$	$C_2$ (K)	$T_0$ (K)	B	m	$f_g$
3-34-3	3.55	14.55	359	119.0	91.0	0.122
9-34-9	7.52	32.80	340	568.0	85.6	0.058
15-34-15	6.45	23.40	350	347.6	102.9	0.067

## 9.5 Conclusions

Novel triblock PIL copolymers were synthesized by RAFT polymerization in order to investigate if ion dynamics and mechanical integrity could be independently. The IL monomer was designed with a long alkyl spacer to separate the charged imidazolium moiety from the polymer, which resulted in the ionic conductivity of the PIL block copolymer to span 6 orders of magnitude through facile counter ion exchange. The long alkyl linkage also led to  $T_g$ -independent ionic conductivities in the block copolymer that more closely resembled that of small ILs. For PIL triblock copolymers with the same counter anions, the ionic conductivity was not dependent on the length of the polystyrene

block while viscoelastic properties was dominated by the polystyrene content. These results suggest a significant advancement in the use of PILs. Collectively, these results represent a significant advancement in the use of PILs for applications where conductivity typically comes at the expense of mechanical integrity and establishes a prominent path forward for this exciting class of materials.

## 9.6 References

1. Hall, C. C.; Zhou, C.; Danielsen, S. P. O.; Lodge, T. P., Formation of Multicompartment Ion Gels by Stepwise Self-Assembly of a Thermoresponsive ABC Triblock Terpolymer in an Ionic Liquid *Macromolecules* **2016**, *49*, 2298-2306.
2. Lee, J. H.; Lee, A. S.; Hong, S. M.; Hwang, S. S.; Koo, C. M., Hybrid ionogels derived from polycationic polysilsesquioxanes for lithium ion batteries *Polymer* **2017**, *117*, 160-166.
3. Lodge, T. P., Materials science - A unique platform for materials design *Science* **2008**, *321*, 50-51.
4. Lodge, T. P.; Ueki, T., Mechanically Tunable, Readily Processable Ion Gels by Self-Assembly of Block Copolymers in Ionic Liquids *Acc. Chem. Res* **2016**, *49*, 2107-2114.
5. Moon, H. C.; Kim, C. H.; Lodge, T. P.; Frisbie, C. D., Multicolored, Low-Power, Flexible Electrochromic Devices Based on Ion Gels *ACS Appl. Mater. Interfaces* **2016**, *8*, 6252-6260.
6. Jo, G.; Ahn, H.; Park, M. J., Simple Route for Tuning the Morphology and Conductivity of Polymer Electrolytes: One End Functional Group is Enough *ACS Macro Lett.* **2013**, *2*, 990-995.
7. Cotanda, P.; Petzetakis, N.; Jiang, X.; Stone, G.; Balsara, N. P., Hydroxide-ion transport and stability of diblock copolymers with a polydiallyldimethyl ammonium hydroxide block *J. Polym. Sci. Pol. Chem.* **2017**, *55*, 2243-2248.
8. Jyothi, M. S.; Soontarapa, K.; Padaki, M.; Balakrishna, R. G.; Isloor, A. M., Favorable influence of mPIAM on PSf blend membranes for ion rejection *J. Membr. Sci.* **2017**, *533*, 229-240.
9. Gao, R. L.; Wang, D.; Heflin, J. R.; Long, T. E., Imidazolium sulfonate-containing pentablock copolymer-ionic liquid membranes for electroactive actuators *J. Mater. Chem.* **2012**, *22*, 13473-13476.
10. Jangu, C.; Wang, J. H. H.; Wang, D.; Sharick, S.; Heflin, J. R.; Winey, K. I.; Colby, R. H.; Long, T. E., Well-Defined Imidazolium ABA Triblock Copolymers as Ionic-Liquid-Containing Electroactive Membranes *Macromol. Chem. Phys.* **2014**, *215*, 1319-1331.
11. Margaretta, E.; Fahs, G. B.; Inglefield, D. L.; Jangu, C.; Wang, D.; Heflin, J. R.; Moore, R. B.; Long, T. E., Imidazolium-Containing ABA Triblock Copolymers as Electroactive Devices *ACS Appl. Mater. Interfaces* **2016**, *8*, 1280-1288.

12. Bara, J. E.; Lessmann, S.; Gabriel, C. J.; Hatakeyama, E. S.; Noble, R. D.; Gin, D. L., Synthesis and Performance of Polymerizable Room-Temperature Ionic Liquids as Gas Separation Membranes *Ind. Eng. Chem. Res.* **2007**, *46*, 5397-5404.
13. Bara, J. E.; Hatakeyama, E. S.; Gin, D. L.; Noble, R. D., Improving CO<sub>2</sub> permeability in polymerized room-temperature ionic liquid gas separation membranes through the formation of a solid composite with a room-temperature ionic liquid *Polym. Adv. Technol.* **2008**, *19*, 1415-1420.
14. Moghadam, F.; Kamio, E.; Yoshioka, T.; Matsuyama, H., New approach for the fabrication of double-network ion-gel membranes with high CO<sub>2</sub>/N<sub>2</sub> separation performance based on facilitated transport *J. Membr. Sci.* **2017**, *530*, 166-175.
15. Hemp, S. T.; Zhang, M. Q.; Allen, M. H.; Cheng, S. J.; Moore, R. B.; Long, T. E., Comparing Ammonium and Phosphonium Polymerized Ionic Liquids: Thermal Analysis, Conductivity, and Morphology *Macromol. Chem. Phys.* **2013**, *214*, 2099-2107.
16. Wang, S. W.; Liu, W. J.; Colby, R. H., Counterion Dynamics in Polyurethane-Carboxylate Ionomers with Ionic Liquid Counterions *Chem. Mat.* **2011**, *23*, 1862-1873.
17. Jourdain, A.; Serghei, A.; Drockenmuller, E., Enhanced Ionic Conductivity of a 1,2,3-Triazolium-Based Poly(siloxane ionic liquid) Homopolymer *ACS Macro Lett.* **2016**, *5*, 1283-1286.
18. Chen, M.; Dugger, J. W.; Li, X.; Wang, Y.; Kumar, R.; Meek, K. M.; Uhrig, D. W.; Browning, J. F.; Madsen, L. A.; Long, T. E.; Lokitz, B. S., Polymerized ionic liquids: Effects of counter-anions on ion conduction and polymerization kinetics *J. Polym. Sci. Pol. Chem. O.*
19. Allen, M. H.; Hemp, S. T.; Zhang, M. S.; Zhang, M. Q.; Smith, A. E.; Moore, R. B.; Long, T. E., Synthesis and characterization of 4-vinylimidazole ABA triblock copolymers utilizing a difunctional RAFT chain transfer agent *Polym. Chem.* **2013**, *4*, 2333-2341.
20. Anastasaki, A.; Nikolaou, V.; McCaul, N. W.; Simula, A.; Godfrey, J.; Waldron, C.; Wilson, P.; Kempe, K.; Haddleton, D. M., Photoinduced Synthesis of alpha,omega-Telechelic Sequence-Controlled Multiblock Copolymers *Macromolecules* **2015**, *48*, 1404-1411.
21. Iacob, C.; Matsumoto, A.; Brennan, M.; Liu, H.; Paddison, S. J.; Urakawa, O.; Inoue, T.; Sangoro, J.; Runt, J., Polymerized Ionic Liquids: Correlation of Ionic Conductivity with Nanoscale Morphology and Counterion Volume *ACS Macro Letters* **2017**, *6*, 941-946.
22. Sangoro, J., Charge transport and dipolar relaxations in an alkali metal oligoether carboxylate ionic liquid *Colloid Polym Sci* **2014**, *292*, 1933-1938.
23. Bagrodia, S.; Pisipati, R.; Wilkes, G. L.; Storey, R. F.; Kennedy, J. P., Melt rheology of ion-containing polymers. I. Effect of molecular weight and excess neutralizing agent in model elastomeric sulfonated polyisobutylene-based ionomers *J. Appl. Polym. Sci.* **1984**, *29*, 3065-3073.
24. Williams, M. L.; Landel, R. F.; Ferry, J. D., The Temperature Dependence of Relaxation Mechanisms in Amorphous Polymers and Other Glass-forming Liquids *J. Am. Chem. Soc.* **1955**, *77*, 3701.
25. Doolittle, K., Studies in Newtonian Flow. II. The Dependence of the Viscosity of Liquids on Free-Space *J. Appl. Phys.* **1951**, *22*, 1471.

26. Fulcher, G. S., Analysis of Recent Measurements of The Viscosity of Glasses - Reprint *J. Am. Ceram. Soc.* **1992**, 75, 1043-1059.
27. Liu, C.-Y.; He, J.; Keunings, R.; Bailly, C., New Linearized Relation for the Universal Viscosity–Temperature Behavior of Polymer Melts *Macromolecules* **2006**, 39, 8867-8869.
28. Pogodina, N. V.; Nowak, M.; Lauger, J.; Klein, C. O.; Wilhelm, M.; Friedrich, C., Molecular dynamics of ionic liquids as probed by rheology *J. Rheol* **2011**, 55, 241-256.

## Chapter 10: Polymerized Phosphonium Ylide: Fast Solid-State Charge Transfer

*(Ongoing project)*

*Mingtao Chen, Christopher R. Kasprzak, Meng Cai, Amanda J. Morris and Timothy E. Long\**

*Department of Chemistry, Virginia Tech, Blacksburg, VA 24061*

*Macromolecules Innovation Institute, Virginia Tech, Blacksburg, VA 24061*

*\*To whom correspondence should be addressed: [telong@vt.edu](mailto:telong@vt.edu)*

### 10.1 Abstract

In this work, we report the first synthesis of polymerized phosphonium ylide monomers. A facile reaction between 4-(diphenylphosphino)styrene (DPPS) and maleic anhydride (MA) exhibited fast charge transfer, even in the solid state, as evidenced through a color change upon blending. Different stoichiometry of DPPS and MA controls the final phosphonium ylide monomer structures, which showed drastically different solution colors. Conventional free radical polymerization afforded phosphonium ylide homopolymers with no glass transition temperature ( $T_g$ ) before degradation. Solution of both monomers and polymers showed prominent light absorption within the range of visible light and strong fluorescence after excitation. Both excitation and emission maxima of the monomer and polymer solutions fell within the range of commonly studied fluorescent dyes, whose synthesis was complicated compared to phosphonium ylides. Due to the lack of a long-conjugated system, the fluorescence lifetime of phosphonium ylide monomers and polymers were relatively short and required further optimization. Nevertheless, poly(phosphonium ylide)s demonstrated great potential as fluorescent dyes with easy synthesis and storage.

## 10.2 Introduction

In the present study, a facile reaction between 4-(diphenylphosphino)styrene (DPPS) and maleic anhydride (MA) enabled the synthesis of unprecedented polymerizable phosphonium ylide (PY) monomers (where a carbanion is directly bonded to a phosphonium cation) and their corresponding homopolymers. The synthesis of PY monomers involved fast solid-state charge transfer, and the resulting poly(phosphonium ylide) (PPY) demonstrated promising fluorescence within visible light range.

Phosphonium ionic liquids (ILs) and poly(ionic liquid)s (PILs) possess advantageous attributes, such as improved thermal stability<sup>1-3</sup> and ion conductivity,<sup>3-4</sup> compared to ammonium analogs, due to the difference in electronegativity.<sup>5</sup> The applications of phosphonium ILs and PILs ranges from biomolecule binding,<sup>6</sup> antimicrobial coatings,<sup>7-8</sup> gas molecule capture,<sup>9</sup> to conductive materials.<sup>10-15</sup> Yet, the understanding of phosphonium ILs and PILs are still underdeveloped compared to commonly used nitrogen-based (ammonium,<sup>16</sup> imidazolium,<sup>17-19</sup> triazolium,<sup>20</sup> etc.) counterparts.

Current research of phosphonium PILs primarily focus on cation-containing polymers and zwitter-ion polymers. Colby *et al.* achieved ion conductivity as high as  $2 \times 10^{-5}$  S/cm at 30 °C using siloxane based phosphonium-containing polymers<sup>5</sup>. Siloxane based polymer backbones provided mobile matrices ( $T_g = -80$  °C) while phosphonium cations and Tf<sub>2</sub>N counter anions (bis(trifluoromethylsulfonyl)imide) demonstrated weak electrostatic interaction compared to ammonium analogs due to the difference in electronegativity. Both attributes contributed to the high ion conductivity at 30 °C. Long *et al.* demonstrated the first example of 3D printing IL monomers due to the relatively low viscosity of phosphonium IL monomers comparing to nitrogen-based ILs.<sup>21</sup> 3D

printing of phosphonium IL monomers enabled complex three-dimensional objects with high thermal stability, ion conductivity, and optical clarity. In phosphonium zwitter-ion polymers, Ohno and coworkers reported anisotropic proton conduction using liquid crystal materials.<sup>22</sup> Aligned samples improved ion conductivity at least an order of magnitude than isotropic samples. For the best of the authors' knowledge, this manuscript is the first investigation of polymerizable phosphonium ylide monomers and their fluorescent properties.

## **10.3 Experimental**

### **10.3.1 Materials**

4-(diphenylphosphino)styrene (DPPS) and maleic anhydride (MA) were purchased from Sigma-Aldrich and stored under argon in an anhydrous condition prior to use. Azobisisobutyronitrile (AIBN) was purchased from Sigma-Aldrich and recrystallized from methanol before use. All organic solvents were purchased from Sigma-Aldrich and used without further purification.

### **10.3.2 Instrumentation**

<sup>1</sup>H, <sup>13</sup>C, <sup>31</sup>P nuclear magnetic resonance (NMR) spectroscopies were conducted on a Varian Unity NMR spectrometer (400 Hz). Mass spectrometry was performed on an Agilent 6220 Accurate Mass-TOF. Thermal degradation temperature was determined using a Q500 thermogravimetric analysis (TGA) from TA Instruments (nitrogen purge, 10 °C/min heating rate). Thermal transitions were investigated through a TA Q2000 differential scanning calorimetry (DSC) from TA Instruments. The glass transition temperatures were reported as the midpoint of the thermal transition in the second heat cycle of a heat/cool/heat procedure (10 °C/min heat rate and quench cool). Light absorption properties were tested through an Agilent Technologies Cary Series UV-Vis-

NIR spectrophotometer. The spectra range was set to 200 to 800 nm with baseline correction using blank solvent. Fluorescence study was carried out using an ASOC-10 fluorometer from Photon Technology International Inc. Before performing the lifetime study, sealed sample solutions were sparged with argon for 15 min.

### 10.3.3 Solid-state charge transfer

DPPS and MA (both white solids) were directly blended together using a plastic spatula. No strict stoichiometry was required. An orange color started to appear after ~ 5 s. The color became darker with time and eventually appeared as a dark brown solid after a week.

### 10.3.4 Synthesis of PY monomers

All PY monomer synthesis followed the same procedures but different DPPS/MA ratios. For instance, the synthesis of PY monomer (DPPS/MA = 1/2) were performed as follows: DPPS (2.98 g, 0.01 mol), MA (2.02g, 0.02 mol), and dimethylformamide (DMF, 5 g) were charged in a 25 mL, round-bottomed flask. Black color appeared instantly. The reaction was performed overnight at 23 °C with stirring after purging with Argon for 5 min. The resulting PY monomers were precipitated into diethyl ether and washed with diethyl ether once. The precipitated product was further dried under vacuum at 23 °C for 24 h, yielding a black solid (~80% isolation yield). <sup>1</sup>H NMR spectroscopy (400Hz, DMSO-*d*<sub>6</sub>): 3.32 ppm (P=C-CH<sub>2</sub>-C=O, s), 5.45 ppm (H-CH=CH-, dd), 6.01 ppm (H-CH=CH-, dt), 6.81 ppm (-CH<sub>2</sub>=CH-, dd), 7.52-7.87 ppm (aromatic protons, m). MS-TOF (ESI+, (M+H)<sup>+</sup>): Theoretical value = 387.1072 g/mol; Experimental value = 387.1080 g/mol.

### 10.3.5 Free radical polymerization of PY monomers

PY monomers (1 g, 2.6 mmol, DPPS/MA = 1/2) and AIBN (2.12 mg, 0.013 mmol) were dissolved in 5.18 mL DMSO. The solution were sparged with Argon for 10 min to remove oxygen. Polymerization was performed at 65 °C for 24 h with stirring. The reaction was quenched with air, and the product was purified through dialysis against tetrahydrofuran (THF). The final product was a black solid after drying under vacuum at 23 °C for 24 h. <sup>1</sup>H NMR spectroscopy (400Hz, DMSO-*d*<sub>6</sub>): 3.38 ppm ((P=C-CH<sub>2</sub>-C=O and polymer backbone, m), 7.69 (aromatic protons, m).

#### 10.4 Results and Discussions

A simple physical blending of solid reactants DPPS and MA using a laboratory spatula led to fast color change from white to orange (**Figure 10.1**). Both DPPS and MA started as white solids, and within 10 s after physical blending orange color appeared (Supplementary video). Tohamy *et al.* reported the charge transfer between MA and triphenylphosphine (TPP) in chloroform solution evidenced by the fast color change as well<sup>23</sup>. The authors claimed the formation of a phosphonium ylide (PY) between one MA and one TPP molecule. Hence we proposed the products of DPPS and MA as a polymerizable PY monomers depicted in **Figure 10.1**. PY monomers tautomerized between P=C and ylide formation, which is well known as Wittig reagents.

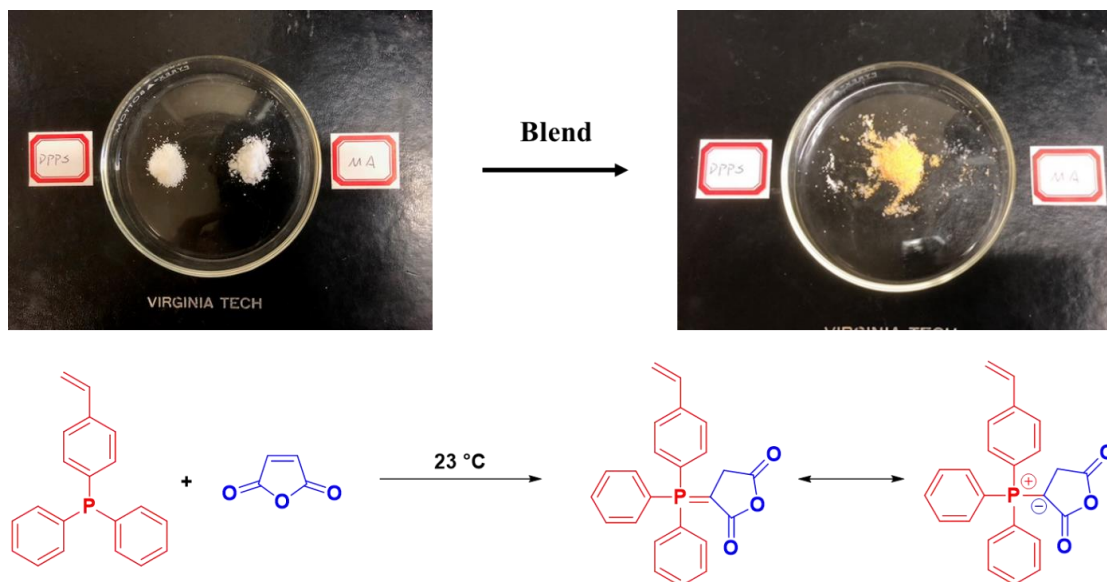


**Figure 10.1** Fast solid-state charge transfer between DPPS and MA.

To ensure complete reaction, reactions between MA and DPPS were further carried out in chloroform solution. The solution of individual reactants started colorless, and instant color appeared when combining two solutions together. Different molar ratios of MA and DPPS demonstrated different colors in solution, as shown in **Figure 10.2**. Increasing equivalents of MA progressively deepened solution color from orange to dark purple. The purified products appeared as solids with similar color to the corresponding reaction solution.  $^1\text{H}$  NMR spectroscopy confirmed the structures of PY monomers with different feed ratios (**Figure S10.1**). The integral of MA protons (c in **Figure S10.1**) and styrenic protons (a or b in **Figure S10.1**) allowed the calculation of actual DPPS/MA ratio in the products. Stoichiometry readily controlled the product DPPS/MA ratios. For  $\text{DPPS/MA} > 0.5$  (PY2 and PY3 in **Figure 10.2**), a complex between two DPPS molecules and one MA molecule was formed<sup>23</sup>. In contrast, when MA was in excess ( $\text{DPPS/MA} = 0.5$ , PY1 in **Figure 10.2**), the conversion of DPPS to PY monomers was quantitative. This finding corresponded with Tohamy *et al.*'s conclusion that an

intermediate with two MA molecules and one TPP molecule was responsible for the formation of one PY molecule.  $^{13}\text{C}$  NMR spectroscopy further confirmed the successful synthesis of PY monomers (**Figure S10.2**). As expected, the presence of the phosphorus atom splitted all carbon signals into doublets.

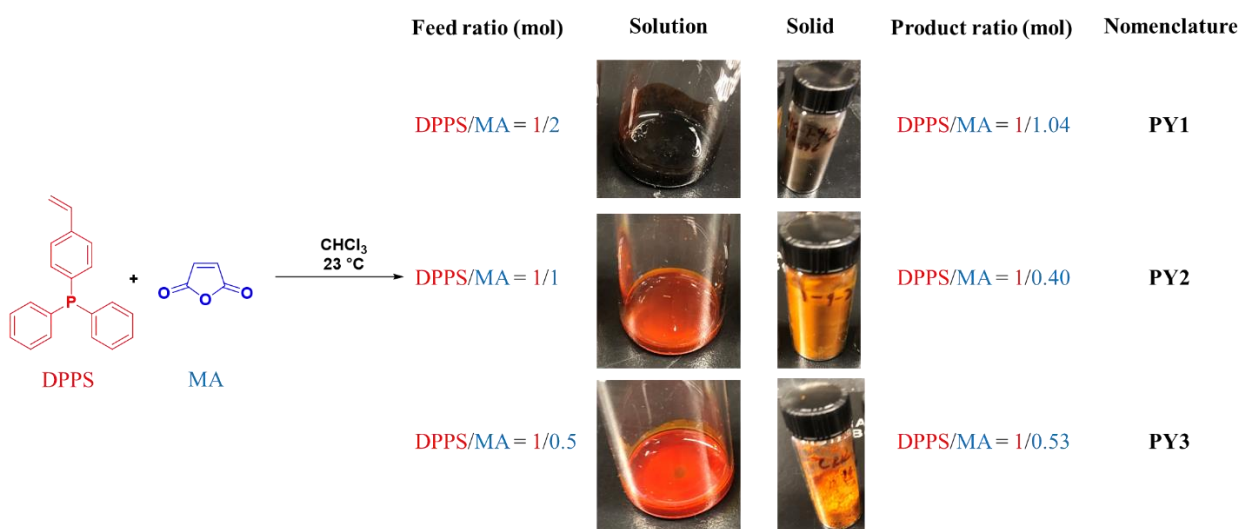


**Figure 10.2** Synthesis of PY monomers with different DPPS/MA feed ratios.

Phosphine species are prone to oxidation. Hence, to evaluate the degree of oxidation during the synthesis of PY monomers, we employed  $^{31}\text{P}$  NMR spectroscopy. We intentionally oxidized DPPS following the procedure adapted from a previous literature<sup>24</sup>. Comparing the phosphorus signals of PY monomers and both DPPS and oxidized DPPS, PY monomers showed negligible oxidation and residual unreacted DPPS (**Figure 10.3**). All three PY monomers showed limited DPPS residual signal, indicating that no unreacted DPPS even in PY2 and PY3 remained after purification.

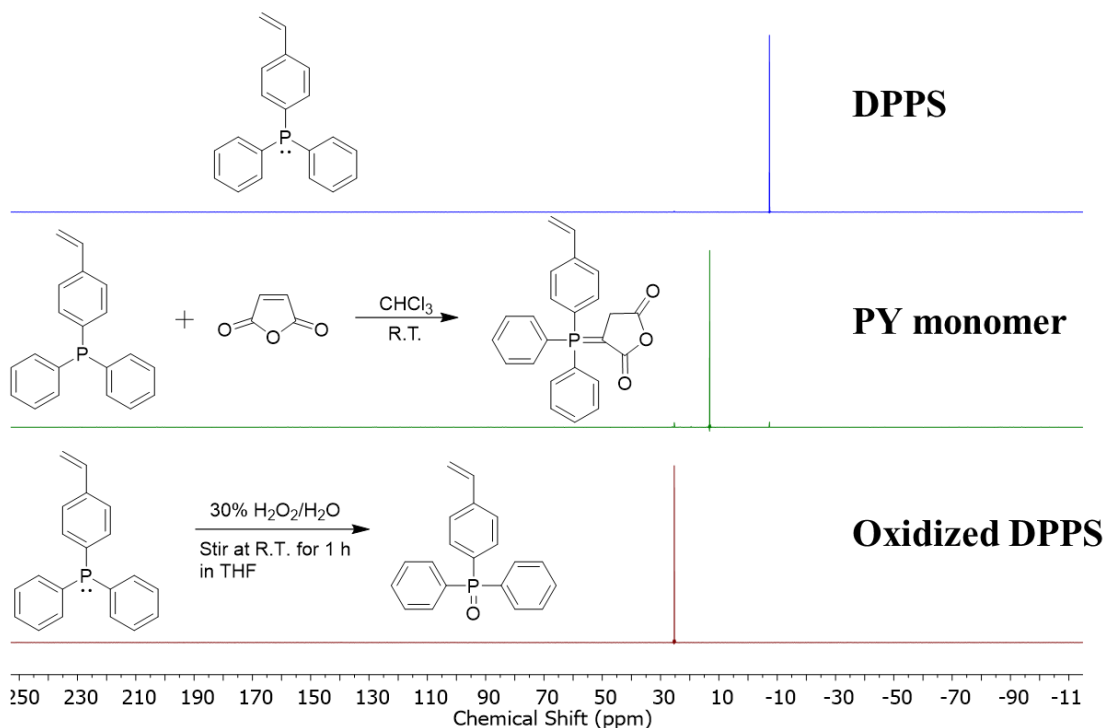
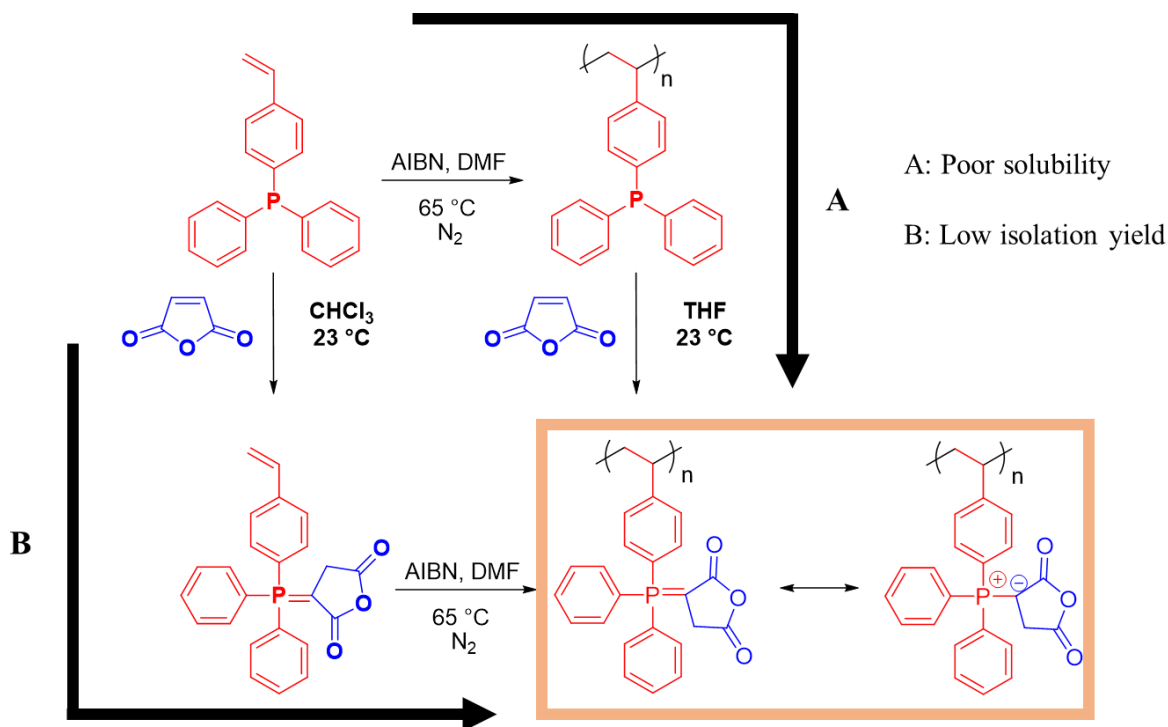


**Figure 10.3** Comparison of DPPS, ylide, and oxidized DPPS in  $^{31}\text{P}$  NMR spectroscopy.

Conventional free radical polymerization afforded poly(phosphonium ylide)s (PPYs). **Scheme 10.1** described the synthesis of PPYs through either direct polymerization of PY monomers or post-polymerization functionalization of poly(DPPS). Route A applied the homopolymerization of DPPS first, and post-polymerization functionalization between poly(DPPS) and MA presumably generated PPYs; however, no common solvent or solvent mixture dissolved the obtained PPYs. We ascribed the potential crosslinking between two DPPS units and one MA molecule to the poor solvent solubility. Route B featured direct polymerization of pre-made PY monomers and afforded polymers readily soluble in dimethyl formamide (DMF). Yet, the isolation yield after dialysis was low ( $< 20\%$ ), presumably due to low monomer conversion under current polymerization conditions. Nevertheless, further thermal characterization and fluorescence studies were carried out using polymers synthesized from Route B.



**Scheme 10.1** Polymerization of PPYs through different synthetic strategies.

Free radical polymerization of PY1 and PY3 afforded black poly(phosphonium ylide) (PPY1 and PPY3), respectively.  $^1\text{H}$  NMR spectroscopy confirmed the successful polymerization and the retention of DPPS/MA ratios (**Figure S10.3**). PPY1 and PPY3 were only soluble in dimethylformamide (DMF) for molecular weight characterization. Size exclusion chromatography (SEC) revealed severe binding between PPY polymers and SEC columns evidenced by the polymer elution peak after solvent front. Attempt to employ lithium bromide (LiBr) in DMF to screen polymer-column interaction exhibited no detectable polymer elution peaks. Thermogravimetric calorimetry (TGA) showed continuous thermal degradation starting at  $\sim 180$  °C, which we attributed to the release of MA from phosphonium ylide sites. Differential scanning calorimetry (DSC) revealed no glass transition temperature ( $T_g$ ) before degradation, preventing the utilization of melt viscosity to characterize molecular weights.

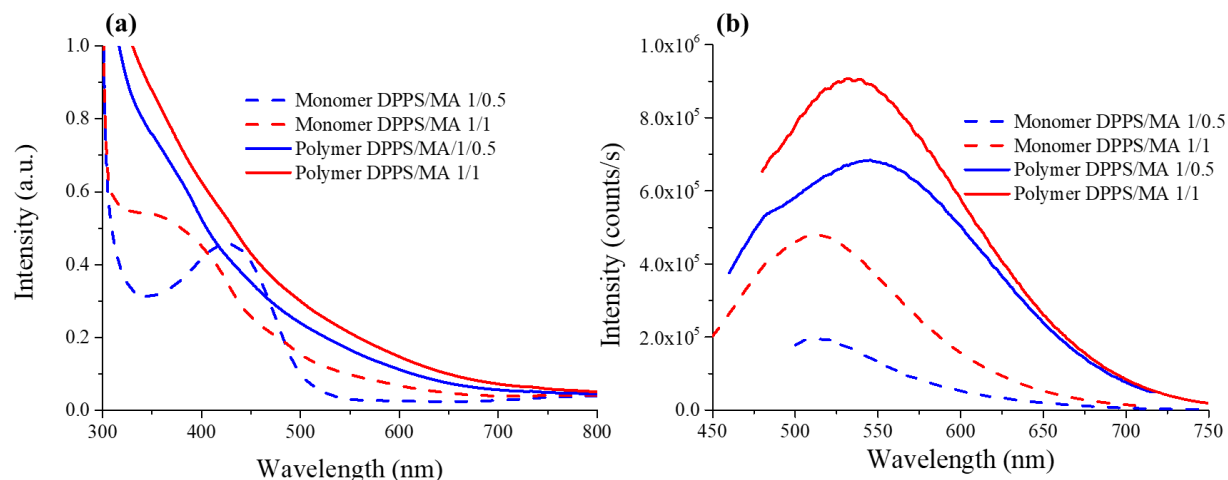


**Figure 10.4** Light absorption (a) and fluorescence (b) of PPY1 and PPY3.

Both phosphonium ylide monomers and homopolymers demonstrated promising visible light absorption and fluorescence. **Figure 10.4a** depicted the visible light absorption as a function of incident light wavelength. PY1 and PY3 monomers exhibited absorption maximum at 420 and 360 nm in methanol (0.5 mg/mL), respectively (**Table 10.1**). PPY1 and PPY3 homopolymers absorbed more light than corresponding monomers at only half of the concentration (0.25 mg/mL in DMSO) and showed no prominent absorption maximum. Instead, shoulder peaks at 362 nm (PPY1) and 398 nm (PPY3) served as the excitation wavelength for the following fluorescence study (**Table 10.1**). Both blank methanol and DMSO solvent demonstrated no absorption within tested wavelength range. Fluorescence study was carried out using monochromic UV lamp with the closest wavelength to the absorption maximum: 340 nm for PY3 and PPY1; 415 nm for PY1 and PPY3. **Figure 10.4b** showed strong fluorescence for all four solutions with maximum emission between 510 nm and 545 nm. Similar to absorption spectrum, homopolymers (PPY1 and PPY3) exhibited higher emission intensity than their corresponding monomers even at half of the concentration. Using the ExpDecay1 curve

fitting in Origin software, phosphonium ylide monomers and polymers showed short fluorescence lifetime ( $\tau$ ) ranging from 0.65 ns to 3.02 ns due to the lack of long conjugated system in the styrenic backbones. Commonly studied fluorescent dyes demonstrate excitation maximum ranging from 354 to 434 nm and emission maximum ranging from 445 to 551 nm.<sup>25</sup> Both PYs and PPYs fell within this range, promising great potential as organic photo-sensitized dyes.

**Table 10.1** Excitation and emission properties of phosphonium ylide monomers and polymers

<b>Materials (DPPS/MA) (mol/mol)</b>	<b>Absorption max (nm)</b>	<b>Emission max (nm)</b>	<b>Emission lifetime (ns)</b>
PY1 (1/0.5)	420	510	0.65
PY2 (1/1)	360	510	2.80
PPY1 (1/0.5)	362	545	2.88
PPY (1/1)	398	535	3.02

PY1 and PY3: 0.5 mg/mL in methanol; PPY1 and PPY3: 0.25 mg/mL in DMSO.

## 10.5 Conclusions

DPPS and MA demonstrated fast charge transfer in both solid state and solution. Different stoichiometry of DPPS and MA altered the solution color and the structure of phosphonium ylide monomer (PY). Direct free radical polymerization of PY monomers generated poly(phosphonium ylide)s (PPY) homopolymers. PPYs showed no prominent  $T_g$  before degradation. The solution of PYs and PPYs exhibited fluorescence using visible light excitation and matched the performance of commonly studied organic fluorescent dyes; however, the fluorescence lifetime was relatively short due to the lack of long-conjugated systems. With further improvement of the fluorescence lifetime, PPYs will serve as promising fluorescent dyes that are easy to synthesize and store.

## 10.6 References

1. Janikowski, J.; Razali, M. R.; Forsyth, C. M.; Nairn, K. M.; Batten, S. R.; MacFarlane, D. R.; Pringle, J. M., Physical Properties and Structural Characterization of Ionic Liquids and Solid Electrolytes Utilizing the Carbamoylcyano(nitroso)methanide Anion *ChemPlusChem* **2013**, *78*, 486-497.
2. Tsunashima, K.; Niwa, E.; Kodama, S.; Sugiya, M.; Ono, Y., Thermal and Transport Properties of Ionic Liquids Based on Benzyl-Substituted Phosphonium Cations *J. Phys. Chem. B* **2009**, *113*, 15870-15874.
3. Hemp, S. T.; Zhang, M. Q.; Allen, M. H.; Cheng, S. J.; Moore, R. B.; Long, T. E., Comparing Ammonium and Phosphonium Polymerized Ionic Liquids: Thermal Analysis, Conductivity, and Morphology *Macromol. Chem. Phys.* **2013**, *214*, 2099-2107.
4. Noonan, K. J. T.; Hugar, K. M.; Kostalik, H. A.; Lobkovsky, E. B.; Abruna, H. D.; Coates, G. W., Phosphonium-Functionalized Polyethylene: A New Class of Base-Stable Alkaline Anion Exchange Membranes *J. Am. Chem. Soc.* **2012**, *134*, 18161-18164.
5. Liang, S. W.; O'Reilly, M. V.; Choi, U. H.; Shiau, H. S.; Bartels, J.; Chen, Q.; Runt, J.; Winey, K. I.; Colby, R. H., High Ion Content Siloxane Phosphonium Ionomers with Very Low T-g *Macromolecules* **2014**, *47*, 4428-4437.
6. Rose, V. L.; Mastrotto, F.; Mantovani, G., Phosphonium polymers for gene delivery *Polymer Chemistry* **2017**, *8*, 353-360.
7. Lukac, M.; Devinsky, F.; Pisarcik, M.; Papapetropoulou, A.; Bukovsky, M.; Horvath, B., Novel Phosphonium-Type Cationic Surfactants: Synthesis, Aggregation Properties and Antimicrobial Activity *J. Surfactants Deterg.* **2017**, *20*, 159-171.
8. Xue, Y.; Xiao, H. N.; Zhang, Y., Antimicrobial Polymeric Materials with Quaternary Ammonium and Phosphonium Salts *International Journal of Molecular Sciences* **2015**, *16*, 3626-3655.
9. Zhang, Y. Q.; Zhang, S. J.; Lu, X. M.; Zhou, Q.; Fan, W.; Zhang, X. P., Dual Amino-Functionalised Phosphonium Ionic Liquids for CO<sub>2</sub> Capture *Chem.-Eur. J.* **2009**, *15*, 3003-3011.
10. Choi, U. H.; Mittal, A.; Price, T. L.; Gibson, H. W.; Runt, J.; Colby, R. H., Polymerized Ionic Liquids with Enhanced Static Dielectric Constants *Macromolecules* **2013**, *46*, 1175-1186.
11. Wang, S. W.; Liu, W. J.; Colby, R. H., Counterion Dynamics in Polyurethane-Carboxylate Ionomers with Ionic Liquid Counterions *Chem. Mat.* **2011**, *23*, 1862-1873.
12. Parent, J. S.; Penciu, A.; Guillén-Castellanos, S. A.; Liskova, A.; Whitney, R. A., Synthesis and Characterization of Isobutylene-Based Ammonium and Phosphonium Bromide Ionomers *Macromolecules* **2004**, *37*, 7477-7483.
13. Cowan, M. G.; Masuda, M.; McDanel, W. M.; Kohno, Y.; Gin, D. L.; Noble, R. D., Phosphonium-based poly(Ionic liquid) membranes: The effect of cation alkyl chain length on light gas separation properties and Ionic conductivity *Journal of Membrane Science* **2016**, *498*, 408-413.
14. Gu, S.; Cai, R.; Luo, T.; Chen, Z.; Sun, M.; Liu, Y.; He, G.; Yan, Y., A Soluble and Highly Conductive Ionomer for High-Performance Hydroxide Exchange Membrane Fuel Cells *Angewandte Chemie International Edition* **2009**, *48*, 6499-6502.
15. Womble, C. T.; Coates, G. W.; Matyjaszewski, K.; Noonan, K. J. T., Tetrakis(dialkylamino)phosphonium Polyelectrolytes Prepared by Reversible Addition-Fragmentation Chain Transfer Polymerization *ACS Macro Lett.* **2016**, *5*, 253-257.

16. Shaplov, A. S.; Lozinskaya, E. I.; Losada, R.; Wandrey, C.; Zdvizhkov, A. T.; Korlyukov, A. A.; Lyssenko, K. A.; Malyshkina, I. A.; Vygodskii, Y. S., Polymerization of the new double-charged monomer bis-1,3(N,N,N-trimethylammonium dicyanamide)-2-propylmethacrylate and ionic conductivity of the novel polyelectrolytes *Polym. Adv. Technol.* **2011**, *22*, 448-457.
17. Allen, M. H.; Wang, S.; Hemp, S. T.; Chen, Y.; Madsen, L. A.; Winey, K. I.; Long, T. E., Hydroxyalkyl-Containing Imidazolium Homopolymers: Correlation of Structure with Conductivity *Macromolecules* **2013**, *46*, 3037-3045.
18. Green, M. D.; Long, T. E., Designing Imidazole-Based Ionic Liquids and Ionic Liquid Monomers for Emerging Technologies *Polymer Reviews* **2009**, *49*, 291-314.
19. Green, M. D.; Salas-de la Cruz, D.; Ye, Y. S.; Layman, J. M.; Elabd, Y. A.; Winey, K. I.; Long, T. E., Alkyl-Substituted N-Vinylimidazolium Polymerized Ionic Liquids: Thermal Properties and Ionic Conductivities *Macromol. Chem. Phys.* **2011**, *212*, 2522-2528.
20. Obadia, M. M.; Jourdain, A.; Serghei, A.; Ikeda, T.; Drockenmuller, E., Cationic and dicationic 1,2,3-triazolium-based poly(ethylene glycol ionic liquid)s *Polym. Chem.* **2017**, *8*, 910-917.
21. Schultz, A. R.; Lambert, P. M.; Chartrain, N. A.; Ruohoniemi, D. M.; Zhang, Z. Y.; Jangu, C.; Zhang, M.; Williams, C. B.; Long, T. E., 3D Printing Phosphonium Ionic Liquid Networks with Mask Projection Microstereolithography *ACS Macro Lett.* **2014**, *3*, 1205-1209.
22. Ueda, S.; Kagimoto, J.; Ichikawa, T.; Kato, T.; Ohno, H., Anisotropic Proton-Conductive Materials Formed by the Self-Organization of Phosphonium-Type Zwitterions *Advanced Materials* **2011**, *23*, 3071-3074.
23. Awad, W. I.; Kandile, N. G.; Wassef, W. N.; Tohamy, F. A., Charge-transfer complexes with trivalent phosphorus compounds *Spectrochimica Acta Part A: Molecular Spectroscopy* **1990**, *46*, 1163-1167.
24. Zhang, S.; Xu, Q. L.; Xia, J. C.; Jing, Y. M.; Zheng, Y. X.; Zuo, J. L., Highly efficient yellow phosphorescent organic light-emitting diodes with novel phosphine oxide-based bipolar host materials *J. Mater. Chem. C* **2015**, *3*, 11540-11547.
25. Rozario, J.; Khan, W. A.; Mallik, F. F.; Mominuzzaman, S. M. In *Incorporation of fluorescent dyes for efficient organic photovoltaic cell*, 2nd International Conference on the Developments in Renewable Energy Technology (ICDRET 2012), 5-7 Jan. 2012; 2012; pp 1-4.

## 10.7 Supplementary information

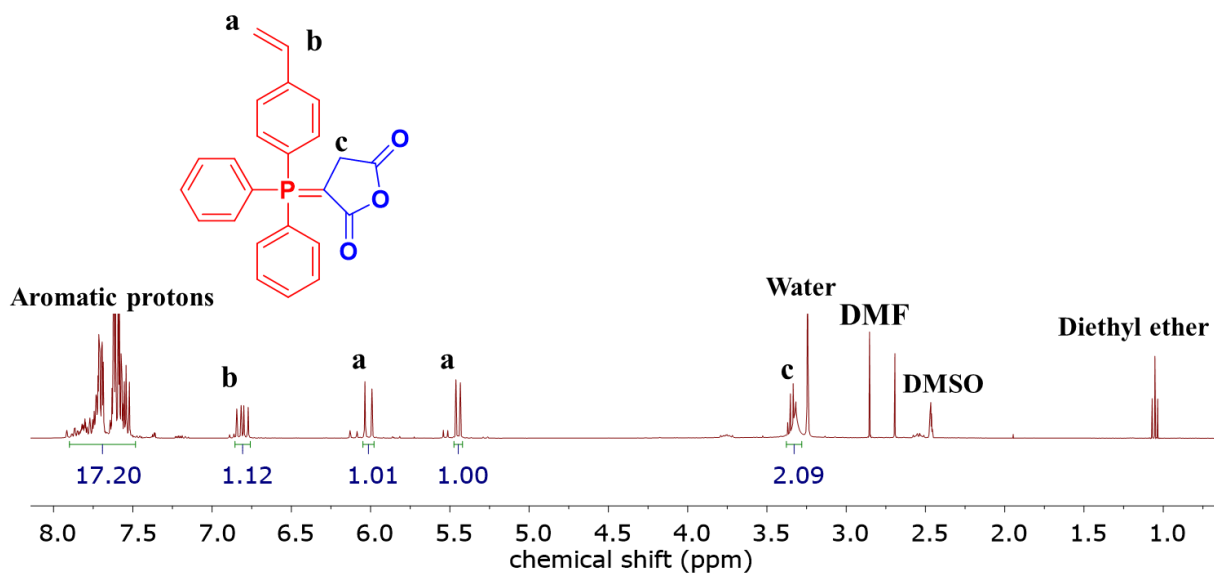


Figure S10.1 <sup>1</sup>H NMR spectroscopy of PY3 monomer.

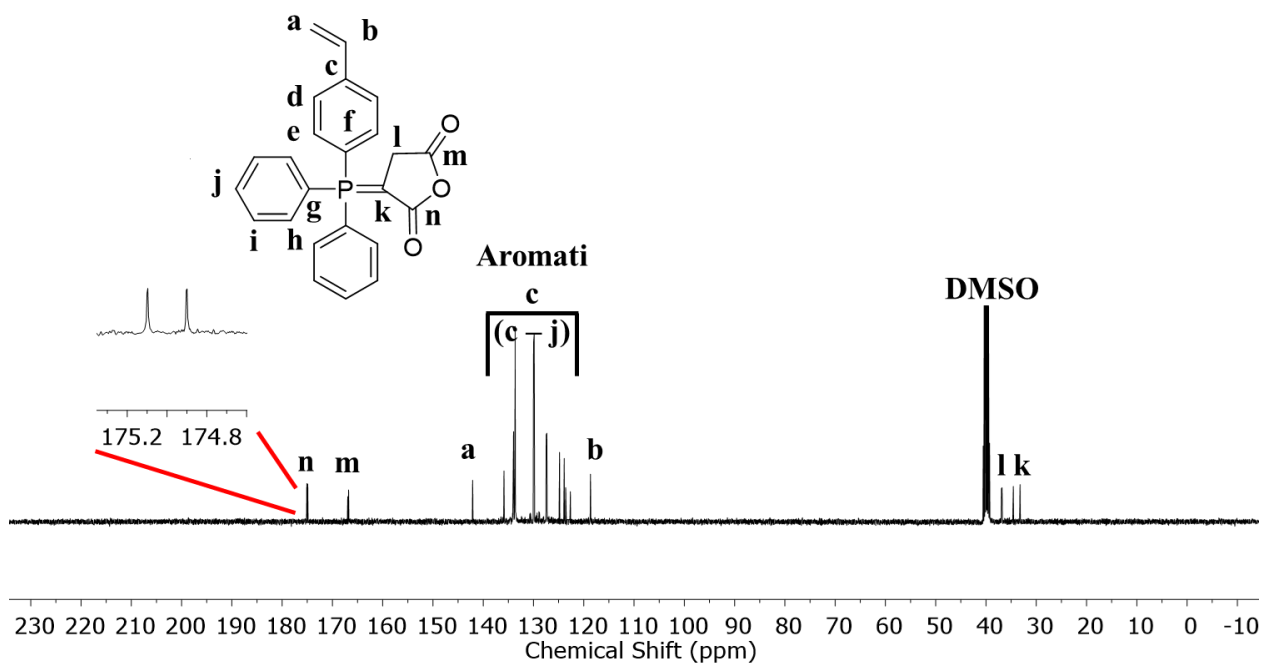
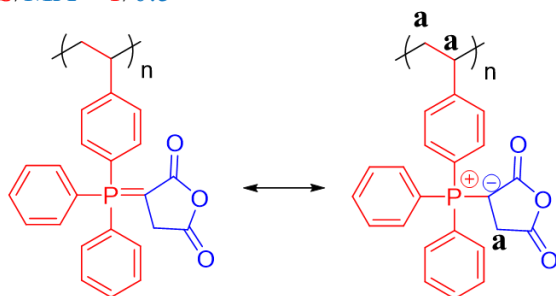


Figure S10.2 <sup>13</sup>C NMR spectroscopy of PY3 monomer.

DPPS/MA = 1/0.5



Theoretical integral of a: 4.06  
Experimental integral of a: 3.72

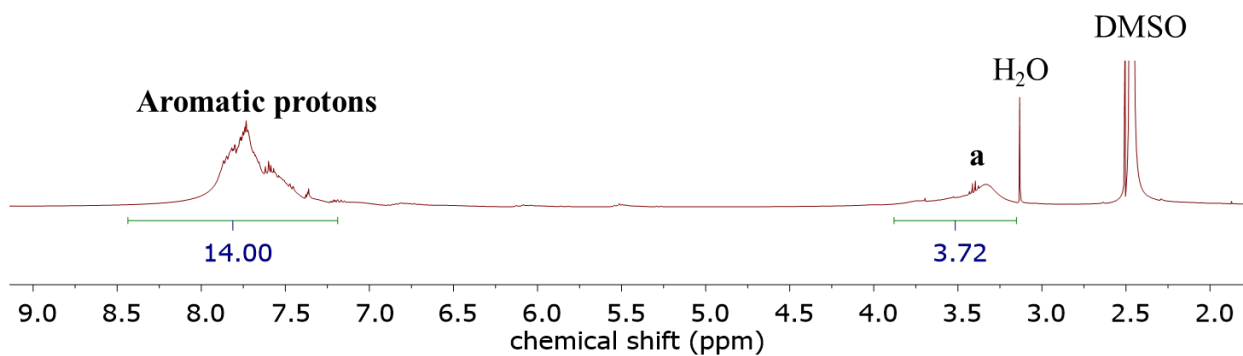


Figure S10.3 <sup>1</sup>H NMR spectroscopy of PPY3 homopolymers.

## Chapter 11: Overall Conclusions

The oligomer-based Michael addition chemistry between DA and bisAcAc generated solvent-free, reactive rooftop adhesives (Chapter 4). The variation in catalyst concentration, temperature, molecular weight, and oligomer chemical structure readily controlled the crosslinking kinetics, achieving  $G'/G''$  crossover time ranging from 8 min to > 300 min. Comparing to solvent-based adhesives, the Michael networks showed comparable or better adhesive properties at the interfaces of three different commercial rubber membranes (EPDM, PVC, and TPO). The addition of 10 wt% tackifiers further improved the adhesive performance while increasing  $G'/G''$  crossover time from ~80 min to ~120 min. At the interfaces of rubber membranes and plywood, the Michael networks at least doubled the maximum adhesive load compared to commercial adhesive control. These Michael networks promised good and consistent adhesive properties across different interfaces and represented a successful example as next-generation environment-friendly adhesives.

Anionic polymerization of 4VBP, isoprene, and styrene synthesized novel ABC triblock copolymers using poly4VBP as internal polar additives to control polyisoprene microstructures (Chapter 5). The presence of poly4VBP segment promoted the 3,4 addition in polyisoprene from 8% to > 35%. In contrast, when polymerizing 4VBP after the isoprene monomers, the 3,4 addition remained at low level (8%). As a result, the monomer addition sequence enabled different polyisoprene microstructures without polar additives for the first time. High 3,4 addition increased the  $T_g$  of polyisoprene from -60 °C to -20 °C due to promoted chain entanglement. Increased 3,4 addition content also led

to an increase of polyisoprene polarity allowing microphase mixing instead of microphase separation according to DSC.

Reversible addition-fragmentation chain transfer (RAFT) polymerization produced ABA triblock copolymers with pendant urea sites to investigate the temperature response of pendant hydrogen bonding and its corresponding influence on polymer physical properties (Chapter 6). Random copolymerization of HUrMA and PhUrMA generated external hard blocks with tunable  $T_g$ s through compositional control. The pendant hydrogen bonding promoted microphase separation forming short-range ordered morphologies. As a result, ABA triblock copolymers demonstrated extended modulus plateaus above the  $T_g$  of the hard blocks. However, unlike backbone hydrogen bonding, most pendant hydrogen bonding retained ordered structure at temperatures as high as 165 °C according to VT-FTIR, presumably due to the lack of cooperativity when “unzipping” hydrogen bonding. Further investigation employed pyridine substituents on urea groups to preorganized hydrogen bonding, achieving exceptionally ordered microphase separated lamella morphology according to SAXS (Chapter 7). The modulus plateau in DMA exhibited 80 °C extension above the hard block  $T_g$  due to strong and ordered hydrogen bonding. Quaternization of pyridine groups allowed the introduction of electrostatic interaction serving as a second physical crosslinking mechanism besides hydrogen bonding. Electrostatic interactions disrupted the ordered, long range hydrogen bonding, adopting local compact packing. As a result, higher order scattering peaks disappeared in SAXS and flow temperature ( $T_f$ ) in DMA decreased from 180 °C to 100 °C. Yet, extra physical crosslinking from electrostatic interaction delayed the dissociation of hydrogen bonding at high temperatures and showed no stress relaxation after 60 min.

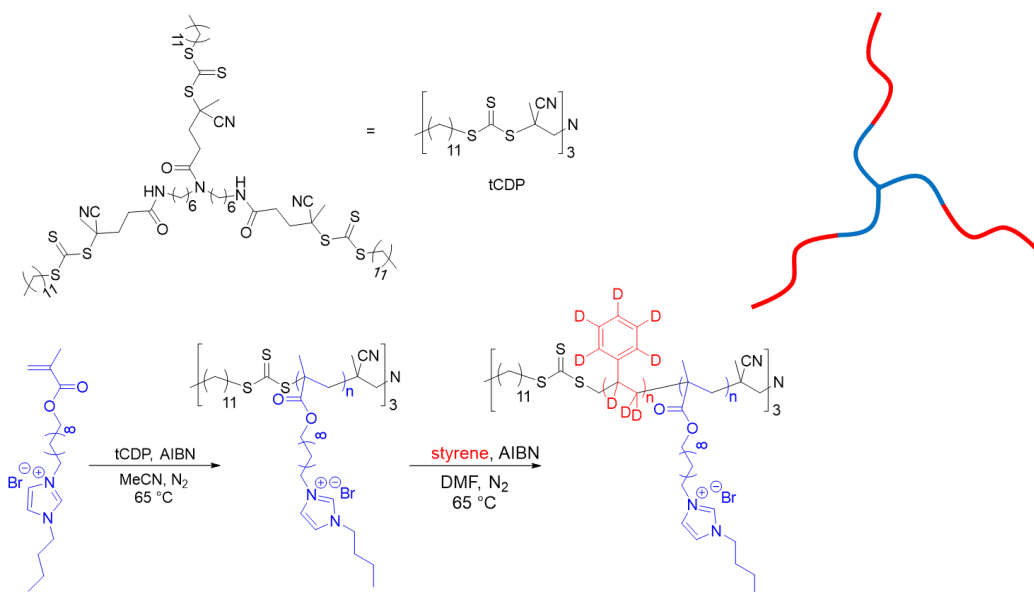
Ion-containing polymers were readily synthesized through conventional free radical polymerization and RAFT polymerization. A novel ionic liquid monomers with a long alkyl spacer between imidazolium moieties and polymerizable methacrylate groups enabled the synthesis of poly(ionic liquid)s (PILs) homopolymers (Chapter 8). After ion exchange, PILs with four different counter anions showed decreasing  $T_g$ s with increasing anion size, and the ion conductivity exhibited strong dependence on  $T_g$ . PILs with Tf<sub>2</sub>N counter anions showed conductivity as high as  $2.45 \times 10^{-5}$  S/cm at 30 °C. The counter anions also demonstrated strong influence on polymerization kinetics during RAFT polymerization. Monomers with Br counter anions polymerized readily while monomers with Tf<sub>2</sub>N counter anions showed no monomer conversion after 24 h. We proposed Marcus theory to explain the kinetic differences resulting from counter ion identity and solvent polarizability. RAFT polymerization produced AB and ABA block copolymers using the ionic liquid monomer discussed above (Chapter 9). When using deuterated styrene as the second monomer, neutron reflectometry enabled the first ever investigation of *in situ* morphology changes during an actuation process. BDS study of ABA triblock copolymers with polystyrene as a mechanical reinforcement block concluded over 8 decades of ion conductivity change through counter ion exchange. In ABA triblock copolymers with the same counter ions, the polystyrene content had limited influence on ion conductivity. The insensitivity of ion conduction to the composition of block copolymers promised a facile approach to achieve tunable viscoelastic properties without altering ion conductivity. TTS study confirmed the different viscoelastic properties (viscosity, fragility, Vogel temperature, and fractional free volume) of block copolymers with different composition but same counter ions.

A facile reaction between 4-(diphenylphosphino)styrene (DPPS) and maleic anhydride (MA) generated a new class of monomers: phosphorus ylide monomers (PY). The reaction showed fast charge transfer in solid state at ambient condition evidenced by the instant coloring upon physical blending of two solid reactants. Direct polymerization of PY monomers or post-polymerization functionalization of poly(DPPS) produced poly(phosphorus ylide)s (PPYs). Both PY monomers and PPYs showed strong visible light absorption and fluorescence in solution, promising their application as dyes in solar cells. Further investigation required improvement of the fluorescence lifetime.

## Chapter 12 Suggested Future Work

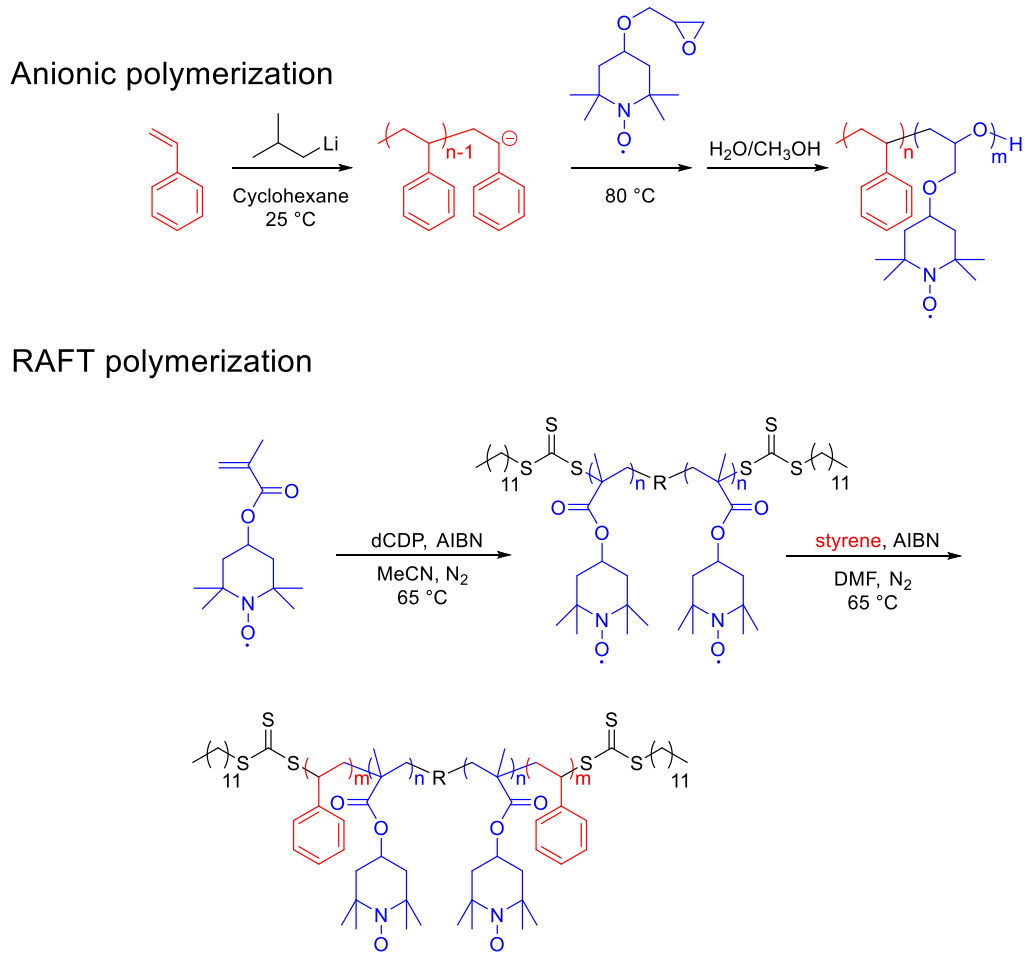
### 12.1 Ion-Containing 3-Arm (AB)<sub>3</sub> Diblock Copolymers Synthesis

Ion-containing block copolymers represent ideal materials for electric actuation, which is crucial for artificial muscles and soft robots. ABA triblock copolymers provide good mechanical properties required for actuators while AB diblock copolymers offer better microphase separation, which is beneficial for the actuation process. To resolve this dilemma between ABA triblock copolymers and AB diblock copolymers, RAFT polymerization of ionic liquid monomers and deuterated styrene monomers generated (AB)<sub>3</sub> diblock copolymers, aiming to achieve ordered morphologies and mechanical integrity simultaneously. Trifunctional RAFT CTA successfully synthesized (AB)<sub>3</sub> diblock copolymers with low molecular weight distribution (**Scheme 12.1**). Future investigation will include BDS measurement of ion conductivity as a function of temperature and frequency and neutron reflectometry study to elucidate *in situ* morphological changes under external field.



**Scheme 12.1** Synthesis of (AB)<sub>3</sub> diblock copolymers using RAFT polymerization.

## 12.2 Synthesis of Radical Block Copolymers



**Scheme 12.2** Synthesis of radical-containing block copolymers through anionic polymerization and RAFT polymerization.

Radical polymers, non-conjugated macromolecules with stable radicals presented in the pendant groups, represent great advantages, such as high conductivity and facile preparation, compared to conjugated conductive polymers and poly(ionic liquid)s (PILs). Most radical polymer research focuses on homopolymers, which form percolating domains to conduct electrons after annealing.<sup>1</sup> The percolating domains promoted electron conductivity for around 7 orders of magnitude. Yet, radical-containing block copolymers remains underexploited, even though they potentially provide mechanical integrity and ordered morphology. The latter showed efficient mass transfer as ordered

percolating domains.<sup>2</sup> Various commercially available radical-containing monomers<sup>1, 3</sup> will enable the synthesis of radical-containing block copolymers through either anionic polymerization or RAFT polymerization (**Scheme 12.2**). The resulting polymer films should form free standing films while maintaining fast and high electron conduction.

### **12.3 UV-Assisted Direct Writing of Ion Conduction Pathways**

Directional control of anisotropic ion conduction to achieve complex current pathways is of great importance in areas such as solid-state batteries<sup>4</sup>, soft robotics<sup>5</sup>, and high throughput barriers<sup>6</sup>. Current industrial application relies on surface lithography of inorganic materials to offer feature resolution down to 12 nm. Researchers have investigated the surface-directed self-assembly of block copolymers to access resolution below 10 nm.<sup>7</sup> However, block copolymer self-assembly requires an annealing step, is prone to defects, and only provides limited choices of morphologies. Herein, we propose the synthesis of poly(ionic liquid)s (PILs) embedded into photo-degradable poly(ethylene glycol) (PEG) crosslinked matrices. Using ultra-violet (UV) light to selectively degrade the crosslinked PEG networks enables the fabrication of complex conductive pathways. This method will provide a facile means to achieve complex and conductive patterns otherwise inaccessible through both surface lithography and surface-directed self-assembly mentioned above.

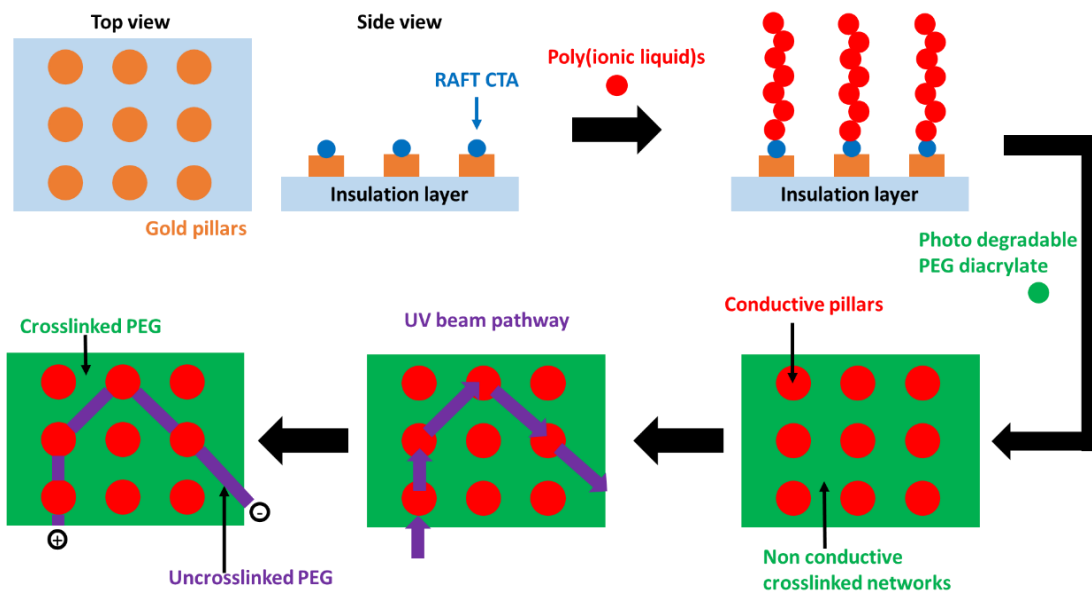


**Figure 12.1** Schematic description of UV assisted direct writing of ion conduction pathways.

**Figure 12.1** depicted the fabrication of UV responsive crosslinked materials embedded with isolated, conductive pillars. Binding of chain transfer agents (CTAs) to the gold pillar surfaces enables the reversible addition-fragmentation chain transfer (RAFT) polymerization of conductive PIL homopolymers from these surfaces, yielding isolated, conductive pillars (red region).<sup>8</sup> The rest of the matrices were filled with a combination of PEG monoacrylates and photo-degradable PEG diacrylates (crosslinkers) and crosslinked through upon heating (green matrix).<sup>9</sup> The ion conduction of the crosslinked materials will be limited as PIL pillars were isolated by immobile PEG networks. Use of a focused UV beam enables the selective degradation of the crosslinked PEG networks to connect isolated PIL pillars (purple line). The degraded PEG matrices will promote ion migration between pillars due to increased mobility. As a result, this strategy achieves various complex conductive pathways in a mechanically robust film. We will focus on the optimization of PIL chemical structures, crosslink density of PEG

matrices, and the wavelength and intensity of UV light. Further investigation will involve different crosslinked matrices other than PEG to achieve even more drastic conductivity changes before and after degradation.

## 12.4 Tunable Anisotropy in Ion Conduction: Electro- and Light-Responsive Block Copolymers

Ion-containing polymers are at the verge of a major breakthrough in energy-related applications. Particularly, materials with anisotropic ion conduction upon external stimulus is of great interest due to their potential to recognize and convert external signals to electric signals. However, modern research focuses primarily on macroscopic properties with limited interest in understanding the microscopic phenomena that dictates bulk properties. Our study will focus on connecting the “dots” in stimuli-responsive electro-processes: from rational design of molecular structure and mesoscale morphology to macroscopic performance, facilitating the development of tailored ion-containing materials across all length scales.

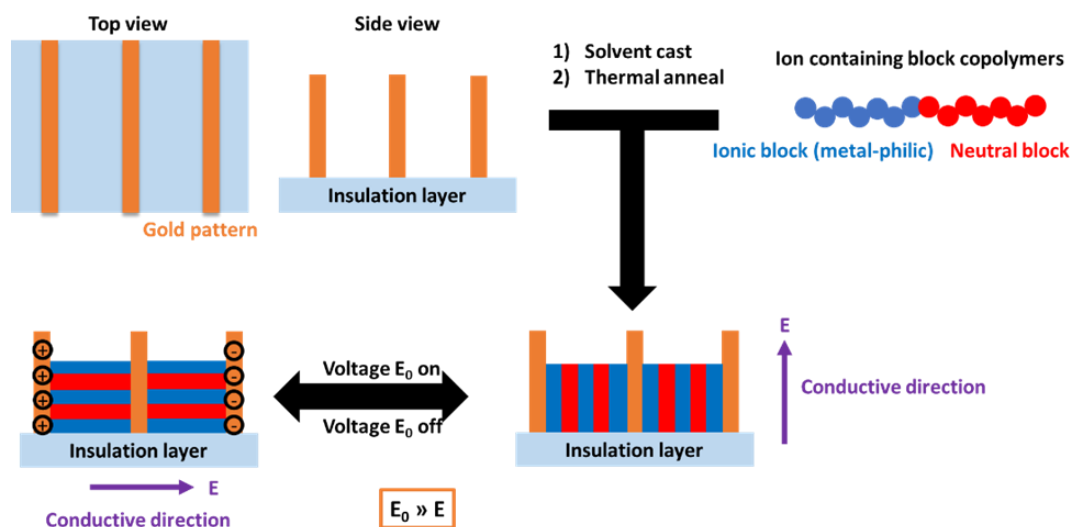


**Figure 12.2** Fabrication of electro-switchable anisotropic conductive device.

**Figure 12.2** depicts a self-assembled block copolymer with tunable anisotropic ion

conduction. To provide microphase separated morphology, the block copolymers consist of two immiscible blocks: an ion-containing block with lower  $T_g$  to facilitate mass transfer (ion conduction) and a neutral block to provide mechanical integrity. In order to control the orientation of the lamellar morphology, incorporation of “metal-philic” groups, such as urea linkage, imparts preferential binding of ionic blocks to patterned gold surfaces.<sup>10</sup> The favored binding between ionic blocks and gold surface will direct the orientation of lamellar morphology. Under working voltage  $E$  (**Figure 12.2**), block copolymers may exhibit higher conductivity when the orientation of lamellar aligns with current direction. In contrast, after applying strong perpendicular voltage  $E_0$ , block polymers will experience a change of lamellar orientation with respect to the insulation substrate from normal to parallel. The anisotropy of ion conduction remains, but the highly conductive direction alters by  $90^\circ$ .  $E_0$  is significantly higher than  $E$ , guaranteeing no morphological changes under working voltage  $E$ . The scope of this proposal will cover material optimization ( $T_g$ , ion conductivity, and molecular weight),  $E_0/E$  ratios, and the durability of the system. Eventually, this system will serve as a model study to develop soft diodes with switchable conductive direction.

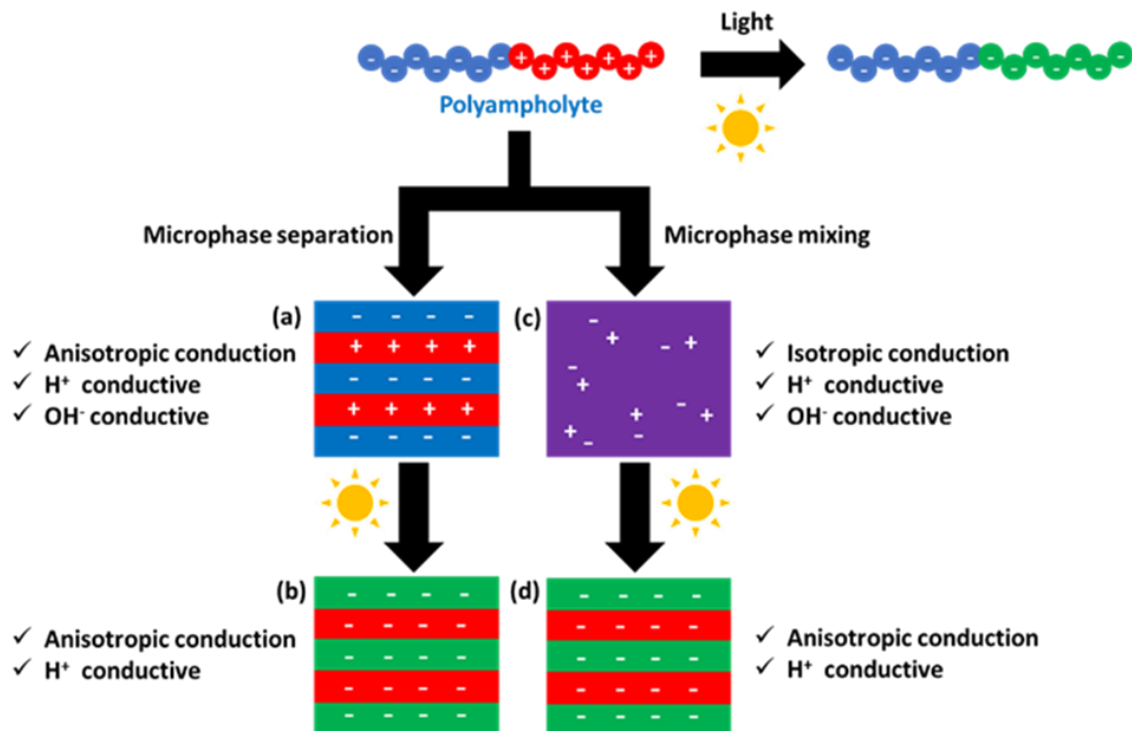


**Figure 12.3** Schematic description of light-responsive polyampholytes.

Instead of using an external field as a stimuli, light provides a safer, more energy efficient, and more readily available approach to trigger *in situ* ion conduction changes.

**Figure 12.3** demonstrates the application of a polyampholyte as a light-responsive conductive materials. Depending on specific chemical structures, polyampholytes will either undergo microphase mixing or separation. In the case of microphase-separated systems (**Figure 12.3a**), cationic and anionic domains will adopt microphase separated morphologies (preferably lamellar morphology), affording anisotropic ion conduction at the direction of lamellar orientation. As the polyampholytes exhibited both positive and negative charges, H<sup>+</sup> and OH<sup>-</sup> conduction will benefit from their affinity to the polyampholytes. When exposing to visible light (**Figure 12.3b**), the cationic domains will undergo heterolytic cleavage and produce anionic polymer backbones.<sup>11</sup> Due to ionic repulsion, the lamellar morphology will only undergo limited morphology. However, the

polymer backbones bear mostly negative charges, preventing the ion conduction of OH<sup>-</sup>. Similarly, in a microphase-mixed matrices (**Figure 12.3c**), polyampholytes will exhibit both H<sup>+</sup> and OH<sup>-</sup> ion conduction with no preferential conduction direction. Upon light exposure (**Figure 12.4d**), OH<sup>-</sup> conduction decreases significantly. Selection of charged moieties, optimization of the morphology, and electro-stability will be the keys to the successful construction of such system, which will serve as a prototype of both ion selective and directional specific ion exchange membranes.

## 12.5 References

1. Joo, Y.; Agarkar, V.; Sung, S. H.; Savoie, B. M.; Boudouris, B. W., A nonconjugated radical polymer glass with high electrical conductivity *Science* **2018**, *359*, 1391-1394.
2. Jo, G.; Ahn, H.; Park, M. J., Simple Route for Tuning the Morphology and Conductivity of Polymer Electrolytes: One End Functional Group is Enough *ACS Macro Lett.* **2013**, *2*, 990-995.
3. Baradwaj, A. G.; Wong, S. H.; Laster, J. S.; Wingate, A. J.; Hay, M. E.; Boudouris, B. W., Impact of the Addition of Redox-Active Salts on the Charge Transport Ability of Radical Polymer Thin Films *Macromolecules* **2016**, *49*, 4784-4791.
4. Lodge, T. P., Materials science - A unique platform for materials design *Science* **2008**, *321*, 50-51.
5. Wehner, M.; Truby, R. L.; Fitzgerald, D. J.; Mosadegh, B.; Whitesides, G. M.; Lewis, J. A.; Wood, R. J., An integrated design and fabrication strategy for entirely soft, autonomous robots *Nature* **2016**, *536*, 451-+.
6. Fan, Y.; Zhang, M.; Moore, R. B.; Lee, H.-S.; McGrath, J. E.; Cornelius, C. J., Viscoelastic and gas transport properties of a series of multiblock copolymer ionomers *Polymer* **2011**, *52*, 3963-3969.
7. Jeong, S.-J.; Kim, J. Y.; Kim, B. H.; Moon, H.-S.; Kim, S. O., Directed self-assembly of block copolymers for next generation nanolithography *Materials Today* **2013**, *16*, 468-476.
8. Cimen, D.; Caykara, T., Micro-patterned polymer brushes by a combination of photolithography and interface-mediated RAFT polymerization for DNA hybridization *Polym. Chem.* **2015**, *6*, 6812-6818.
9. Yang, C.; Tibbitt, M. W.; Basta, L.; Anseth, K. S., Mechanical memory and dosing influence stem cell fate *Nat. Mater.* **2014**, *13*, 645-652.
10. Das, P.; Mahato, P.; Ghosh, A.; Mandal, A. K.; Banerjee, T.; Saha, S.; Das, A., Urea/thiourea derivatives and Zn(II)-DPA complex as receptors for anionic recognition- A brief account *J. Chem. Sci.* **2011**, *123*, 175-186.
11. Zhou, T.; Lei, Y.; Zhang, H.; Zhang, P.; Yan, C.; Zheng, Z.; Chen, Y.; Yu, Y., Visible-Light Photolabile, Charge-Convertible Poly(ionic liquid) for Light-degradable Films and Carbon-Based Electronics *ACS Appl. Mater. Interfaces* **2016**, *8*, 23431-23436.

